Dynamics and Flow Behaviour of Colloidal Rod-like Particles

Minne Paul Lettinga

Dynamics and Flow Behaviour of Colloidal Rod-like Particles

Minne Paul Lettinga

Forschungszentrum Jülich
Institut für Festkörperforschung

Weiche Materie

Habilitationsschrift

Jülich, April 2010

Contents

Chapter 1

Introduction

1.1 Colloids

The mere observation of a small particle moving criss-cross through the solvent, as done by the botanist Brown in the early 19th century using a simple microscope, finally led Jean-Baptist Perrin to the first experimental proof of the existence of molecules and the determination of the number of Avogadro[1]. For this he was rewarded the Nobel prize in 1926. Particles, so called colloids, display this random motion due to the continuous bombardment of solvent molecules. As a result of this thermal motion they are not much affected by gravity. Perrin realized that colloidal particles could mimic the behavior of atoms, given that the Brownian motion of the colloids is very similar to the random motion of atoms. Thus dispersions of colloidal particles can be considered as being thermodynamic systems which display, as molecular systems, phenomena like phase transitions. With this analogy a very rich experimental tool is given to explore the phase behavior of particles with a huge variety of interactions, taking advantage of a few very practical features of colloidal particles:

The most obvious feature is that colloids are very big and slow as compared to molecules. This means that processes, which are too fast and small to be probed at the molecular scale, can be easily accessed on the colloidal scale using light microscopy and scattering. Apart from the length and time scales that are experimentally easily accessible, there is also a wealth of physical and chemical tricks that can be used to tailor the interactions between the particles. This is very important because the interactions between the particles determine if a given system is stable or not. This phase behavior can be theoretically predicted provided that the interaction potential between the particles is known. Thus, Colloidal systems provide the experimentalist the tools to study the effect of the interaction between the particles on the overall behavior of the system, so that theory can be directly tested.

The most simple *interaction* between two particles is the so-called 'hard core' interaction. With 'hard' we mean that there is no interaction when the particles do not overlap and an infinite interaction when they do overlap. The simplest *morphology* of a particle is a spherical particle. Considering a system of hard spheres is thus like considering a system of billiard balls, except that billiard balls do not undergo brownian motion. Dispersions of colloidal hard spheres have been subject of extensive study over the past decades although the phase behavior is limited to the crystallization at a volume fraction of 0.49 and the vitrification at a volume fraction of 0.64[2]. Colloidal particles can also be made attractive by grafting them with a thin layer of polymer. The attraction can then be tuned by changing the solvent quality of the polymer. Such systems show a 'gas-liquid' transition including the critical behavior just before the phase transition, very similar to molecular systems[3]. These 'sticky spheres' can also form gels at very low concentrations. To understand the behavior of dispersion of spheres one only needs to consider the position of the particles or, on a more coarse grained scale, the fluctuations in the density.

1.2 Lyotropic liquid crystals

However important atoms are, and their colloidal spherical equivalents, almost all molecules or proteins that are present in nature are not spherical. The most simple non-spherical particles are rods. Compared to spheres, rods have a far more rich phase behavior since it depends on both the positional and orientational degrees of freedom of the rods. The simples transition of rod-like particles is between between the *isotropic* phase (I), displaying orientational and positional disorder, to the *nematic* phase (N), displaying a mean averaged orientation but still no long-ranged positional order. Orientational order manifests itself when the dispersion is birefringent due to the difference in the refractive index parallel and perpendicular to the average orientation of the rods. Observations of birefringent structures have been first described by Zocher[4] who studied dispersions of V_2O_5 and FeOOH. These systems consist of inorganic needle shaped particles, as was found by ultramicroscopy, introduced by Zsigmondy in the early 20th century. Not much later, in 1936, similar observations were made on dispersions of Tobacco Mosaic Virus by Bawden et al. [5]. At that time it was surprising that dilute low viscous dispersions of colloidal particles could show birefringence, since birefringence was associated with mineral crystals or thermotropic liquid crystals. The latter is a class of systems consisting of small anisometric molecules that form a nematic phase at low temperature which can be melted into *isotropic* phase at high temperatures. For these thermotropic liquid crystals the interactions between the molecules play an important role. For colloidal dispersions, which are two-component systems, this is not obvious.

It was Onsager who reasoned on the basis of purely geometrical considerations that dispersions of hard rods should also undergo a phase transition from the isotropic phase to the nematic phase[6]. At this phase transition the system will gain positional entropy, since the accessible volume is higher when rods are aligned in the nematic phase, at the cost of orientational entropy. Since temperature does not play a role for such systems, dispersions of aligned hard rods are called *lyotropic* liquid crystals, indicating that only the number of dispersed particles

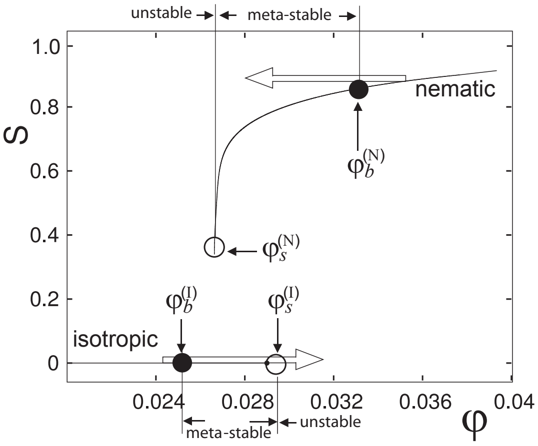

Figure 1.1: Bifurcation diagram of the nematic order parameter S for hard rods ($\varphi_p^R = 0$) with $L/D = 133$. Open circles indicate spinodal points, separating the unstable and metastable region, while the filled circles indicate binodal points, separating the metastable and the stable region. The arrows indicate concentration quenches that would render the system in a supersaturated state.

is important. He predicted that this is a first order phase transition, which means in the case of rods that there is a discontinuity in orientation as well as concentration. As a result there is a concentration range where the isotropic and nematic phases coexist. The concentration and orientational order parameter of the coexisting phases characterize the *binodal* points. These are also the points after which the dispersion becomes metastable to fluctuations in the orientation, when increasing the concentration from an initially isotropic phase or decreasing the concentration from an initially nematic phase. Similarly, spinodal points can be defined and calculated, which mark the concentration where the dispersion becomes unstable and each fluctuation in orientation will result in phase separation. The full bifurcation diagram consisting of the metastable and unstable isotropic and nematic phase have been calculated by Kayser and Raveché[7] and is plotted in Fig. 1.1.

If the concentration of rods is further increased then a sequence of transitions where rods are positionally ordered take place: the *smectic* phase, which consists of regularly spaced layers of rods that show a liquid-like order within the layer; the *columnar* phase, where columns of rods are hexagonally ordered; the 3-D ordered *crystalline* phase[8, 9]. This is again very different from dispersions of spheres, that either have liquid-like order or crystalline order. This sequence of phase transitions makes that lyotropic liquid crystals are of fundamental interest. They form the most simple system where randomly diffusing particles can self-assemble into these structures with higher architecture. As mentioned before it is straightforward to see if a nematic phase has formed by detecting the birefringence of the system. Similarly, if rods are longer than the optical resolution then the smectic phase can be observed by Differential

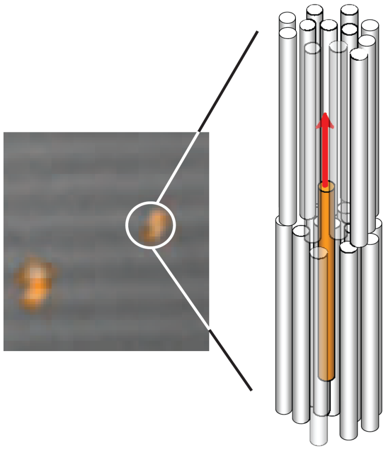

Figure 1.2: Artist impression of a labeled particle jumping between adjacent smectic layers .

Interference Contrast microscopy, using the regular fluctuations in the refractive index. In both cases one observes features that are a signature for the reduced entropy. In the case of the nematic phase orientational order is detected, while for the smectic phase positional order in one dimension is detected. Signature for the increase in positional entropy has not been given so far. This raises the question of how the underlying dynamics of the rods behaves throughout phase space. Dynamic light scattering, which still is the working horse in colloidal physics, is very inconclusive, even in the isotropic phase, because of the complexity of the interpretation of the measurements. Some measurements have been performed using fluorescence recovery after photon bleaching, but the results are limited in the concentration range and information that can be extracted[10]. By monitoring the motion of individual rods one could directly observe the effect a phase transition has on the motion of particles, but likewise also it could give direct information on the nature of the different phases. The wealth of information contained in such observations is not yet sufficiently appreciated. '***Diffusion of rods in dispersions of rods***' is the subject of ***part I*** of this Habilitationsschrift . For these measurements *fd* viruses are used in combination with fluorescence video microscopy. This virus is a bacteriophage which are very long (880 nm) and thin (6.6 nm) and quite stiff with a persistence length of 3.3 μm which therefore constitute the most ideal systems available. In chapter 2 and 3 (Ref. [11, 12]) the focus is on the nematic phase and the I-N transition, where in chapter 3 in addition the influence of hydrodynamic interactions is addressed. For this we relied also on Multi-Particle Collision dynamics simulations to implement hydrodynamic interactions. In chapter 4 and 5(Ref. [13, 14]) the self-diffusion in the smectic phase is studied, see Fig. 1.2.

So far experimental studies of I-N transition have mostly focused on the location of the I-N binodal points. Experimentally these points are easily found since the nematic phase can be clearly distinguished from the isotropic phase using its birefringence. The challenge has been to find systems that actually fulfil the requirements set by the Onsager theory, namely that they have to be very long (at least 40 time longer than they are thick) and infinitely stiff. Since this turned out not to be an easy task, extensions of Onsager theory have been proposed in order to incorporate the effect of flexibility[15, 16], small aspect ratio[17, 18],polydispersity[19, 20, 21]. Very little attention has been paid sofar to the kinetic pathway of this transition. If one is able to monitor the phase separation, then one has access to a rich source of information. First, it would be possible to study supercooled and superheated fluids, because this is effectively what metastable nematic and isotropic phases are, respectively. For dispersions of colloidal spheres this is difficult because the spinodal and binodal line are located very close to each other, while the energy barrier for phase separation to take place is low. Second, systems might be arrested in the metastable state[3]. Once phase separation sets in the question arises which features characterize the phase separation of colloidal rods. Where for phase separating spheres one needs to consider density concentrations, for rods both the orientation and concentration fluctuations need to be considered. The question is which parameter is enslaved by which. Also the morphology of the formed structures during the phase separation are possibly much different from the usually observed features observed for spheres. In short, the mechanism of phase separating rods is still unclear and the bifurcation diagram, including the unstable and metastable regions, has been merely a theoretical concept until recently. Some hints of different phase separation pathways were found for a system of Boehmite rods[22] and actin filaments[23]. In ***Part II*** of this Habilitationsschrift the '***Isotropic-nematic Phase separation kinetics***' of *fd* virus is described. Shear flow is used to stabilize the nematic phase of an initially biphasic sample, again consisting of dispersed *fd* virus. The phase separation kinetics that sets in after cessation of the shear flow is set by the concentration of the sample. In this way the I-N spinodal point was determined. In chapter 6 (Ref. [24]) we focus our attention to the morphology during phase separation, while in chapter 7 (Ref. [25]) we focus on the spinodal decomposition and compare results to theory. In chapter 8 (Ref. [26]) we study the influence of attraction to the location of the N-I spinodal point, but also on the growth rate of the formed structures. In addition we determined also the I-N spinodal point by using pressure quenches. With this technique we instantaneously concentrated the sample making use of the compressibility of water.

1.3 Dispersions of rod-like particles under shear flow

As described above, the mesoscopic length scale of colloids has the advantage that physical processes in equilibrium become more accessible. Another consequence of the length scale is that the shear modulus of colloidal dispersions is very low, so that moderate external fields are sufficient to affect the behavior of the system. That is why colloidal dispersions are typical examples of 'soft matter' systems. The phase behavior of colloidal dispersion in external fields is still a very immature area of research as compared to the equilibrium phase behavior. This despite of the fact that in nature and industry systems are almost always subjected to external fields, like shear flow, EM fields, temperature gradients and confinement. In recent years colloids in external fields were subject of increasing interest. Exemplarily are the intensive studies within the transregio network TR6 "Colloids in external fields"[27, 28]. Our contribution to this network was in the area of colloidal dispersions in shear flow. A well known biological example is blood circulation, where effectively highly concentrated dispersions of more or less deformable cells are pushed through narrow channels[29]. A well known industrial example is paint, of which the flow behavior sets the final product[30]. Already the simplest case of dispersions of colloidal hard spheres in the fluid phase in shear flow displays a very rich scale of features: divergent viscosity with increasing concentration[31] as seen in blood rheology[32] and extreme shear thickening[33] as used for body armor[34]. To understand the flow behavior of colloidal dispersions it is important to understand how the system is structurally changed when it is submitted to the flow. Vise versa, shear flow can also affect the phase behavior of the colloidal dispersion. For attractive colloidal spheres it has been shown for example theoretically[35] and experimentally[36] that the critical structure factor is strongly affected by shear flow and that, as a result, the location of the location of the phase transition shifts. Here it plays an important role that the critical structure is much bigger than the particle size and moreover that the dynamics of the system is very slow close the critical point. In other words, one should scale the shear rate with the dominating length and time scale of the system. Also for repulsive charged spheres we have shown how the crystallization kinetics changes when the dispersion is submitted to a shear flow[37]. Here again a thermodynamically driven phase transition competes with shear flow that erodes the formed crystals. In this case, however, shear also can accelerate the phase transition, because of convection by shear flow. For hard spheres the shear induced transition from a glass state to a crystalline state[38].

For dispersions of rods one expects that external fields will affect the behavior even of single particle. When the applied field, and therefore the applied torque on the rod, is high enough as compared to the rotational diffusion of the rod then this induces an average orientation. This has been observed already in 1902 by Majorana who observed that dispersions of colloidal of Ferroxides become birefringent when subjected to a magnetic field[39]. Not much later, in 1912, Zocher found that also flow could induce birefringence. This was before the steady state birefringence structures were found. To demonstrate the peculiarity of the fact that fluids can show birefringence Bawden et al. [5] published a photo of a goldfish in a bowl with a 'dilute solution of protein from infected sap' between crossed polarizers. These 'proteins' were in fact the tobacco mosaic virus we introduced earlier. These examples show that the flow behavior of colloidal rods was already a subject of interest in the early days of colloidal physics. They show that alignment can be induced by shear flow.

The obvious question is how flow alignment influences the location of the I-N transition, since fluctuations in the orientation are not needed anymore to form a nematic phase from the isotropic phase when rods are already aligned by shear flow. In other words, the phase diagram of colloidal rods might change when rods are submitted to an external field like shear

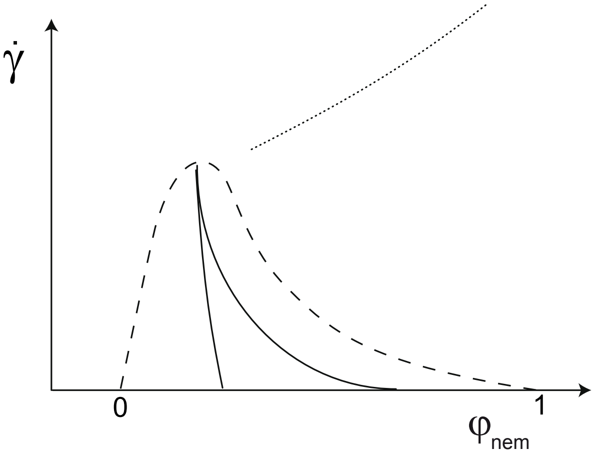

Figure 1.3: Expected non-equilibrium phase diagram with the I-N and N-I spinodal, the right and left solid line respectively, the binodal line (dashed) and the tumbling-flow alignment line (dotted). .

flow. For *fd* virus this has been studied using a magnetic field[40], where it was shown that indeed the I-N spinodal point shifts to lower concentrations. In other words, the external field stabilizes the nematic phase. Theoretically it has been shown that shear has the same effect on the location of the I-N and N-I spinodal point [41, 42], see the solid lines in Fig. 1.3. There are very few experimental examples where the flow induced I-N transition has been studied. The spinodal line has also been determined indirectly for *fd* virus dispersions using flow hysteresis experiments[41].

To predict the I-N binodal line (dashed line in Fig. 1.3) is a far more difficult task which has not been fulfilled sofar. To get a sense of the physics that is at hand one should first ask the question how the isotropic and the nematic phase respond independently to shear flow. For infinite dilute rods it is known that they perform rotations in the so called Jeffrey orbits. Brownian rods have on average a small angle with the flow direction, depending on the size of the particle[43]. The flow alignment in the highly entangled isotropic phase has been studied for a large variety of samples. The alignment of the rods or rodlike particles reduces the degree of entanglement and therefore the viscosity is decreased[44, 45, 46]. The flow behavior of the nematic phase is more complex. Theoretical predictions have shown already quite some time ago that the nematic phase might undergo a tumbling motion where the nematic director leaves the initial flow alignment and makes a full turn in the flow-gradient plane to return again at the flow direction[47]. Later it was shown that the trajectory of a tumbling nematic phase strongly depends on shear rate and initial orientation[48, 49]. The director will only be fully flow aligned at sufficiently high shear rates. First experimental evidence of such a process was given for sheared polymeric liquid crystals[50]. The problem of this type of systems is that they only form a nematic phase at rather high volume fractions, due to the flexibility and polydispersity of the particles. The viscosity of such dispersions is dominated by the stress between the nematic domains, i.e. the texture of the nematic phase. Comparison with theory for such systems can only be done when the system is close to flow alignment[51]. The advantage of *fd* viruses is that the I-N phase transition already takes place at very low concentrations, so that the contribution of the texture to the stress is expected to be low. Moreover, the equilibrium phase behavior of *fd* virus, see part I and II, as well as the flow behavior of the isotropic phase, see Ref. [45], can be theoretically understood. Thus the goal of ***part III*** of this Habilitationsschrift is to study the effect of shear flow on the phase behavior of dispersions of rod-like colloidal particles, i.e. more specifically on the '***Isotropic-nematic Phase Transition under shear flow***', using *fd* virus as a model system. First, in chapter 9 (Ref. [52]) an overview is given of all the important transition lines, i.e. the spinodal and binodal line and the tumbling-to-flow alignment line. Also it is shown here that within a distinct part of the biphasic region bands are formed that are stacked in the vorticity or neutral direction. In the following chapters each aspect is treated separately. Chapter 10 (Ref. [53]) focuses on the rheological response of the pure nematic phase of *fd* viruses, as studied over a wide concentration range. The results correspond nicely with calculations using Smoluchowski theory. Thus the flow behavior of the full nematic phase is well characterized. Next, in Chapter 11 (Ref. [54]) it is shown how the two different dynamic states, i.e. the tumbling nematic and the flow aligning isotropic phase, and which parameters set the non-equilibrium phase behavior. Again, as in chapter 3, experiments are combined with Multi-Particle Collision dynamics, thus giving a microscopic insight of the physics at hand.

The formation of shear bands stacked in the vorticity or neutral direction, as introduced in chapter 9, is strongly connected to the presence of biphasic structures in the dispersion. Structure formation in the neutral direction falls under a class of hydrodynamic instabilities within a broad range of instabilities. In general one can distinguish between shear banding in the vorticity direction and in the gradient direction, see top and bottom panel of Fig. 1.4[55]. The 'classical' picture of vorticity band formation is that the fluid splits up in rings of different viscosity which are both subjected to the same shear rate, i.e. with different stress[56, 42] as shown schematically in Fig. 1.4. Vorticity banding thus would occur at a constant shear rate and for shear thickening fluids. This is however not at all generally true. There is experimental evidence[57, 58, 59] and theoretical justification[60] that vorticity bands are formed due to instabilities in the interface between two gradient bands. Also it was shown theoretically that a coupling between flow and concentration can induce vorticity bands.

In recent years another class of fluids showing vorticity bands developed. The common feature of these systems is that the fluid contains inhomogeneities, such as polymers [61], self-assembled structures like in worm-like micellar[62], clay gels[63], and emulsion droplets[64]. These structures will be non-uniformly stretched due to the curved streamlines that are present in most rheological devices, thus generating hoop-stresses that give rise to elastic normal forces[65] which set the fluid in weakly rolling motion. In Fig. 1.4 this effect is schemati-

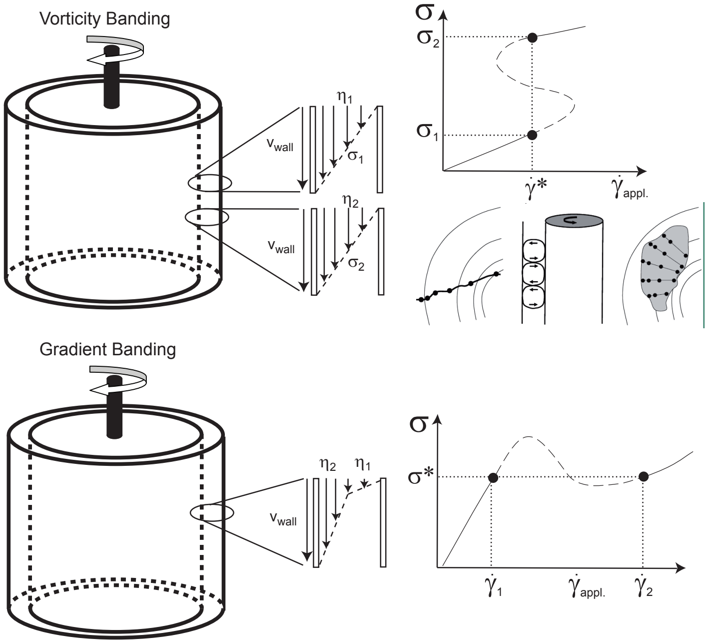

Figure 1.4: Two types of shear banding: in the vorticity direction (top) and in the gradient direction (bottom). The flow profiles are indicated in the middle by the different lengths of the arrows. To the right possible causes of shear band formation are indicated in the form of different flow curves 8top and bottom) and droplet deformation (middle).

cally drawn for a polymer and a droplet. The mechanism underlying the vorticity-banding instability is thus analogous to the well known elastic instability of polymer systems, leading to the Weissenberg effect (see Weissenberg 1947), where the role of polymer chains is now played by the inhomogeneities. Note that this is a pure elastic instability and that inertia does not play a role as is the case for the also wellknown Taylor instability[66]. In chapter 12 and 13 it is shown that the vorticity banding that is observed in the I-N phase separating system of *fd* virus, see chapter 11, belongs to this class of fluids. The kinetics of the shear band formation and its dependence on the location within the non-equilibrium phase diagram and on the used geometry is described in chapter 12(Ref. [67]), while in chapter 13 a mechanism is proposed to explain the shear band formation(Ref. [68]).

1.4 Flow instabilities in dispersions of worm-like particles

Gradient banding in shear flow is far better documented [69] and understood[55, 70] than vorticity banding. The 'classical' picture of gradient band formation is that an extreme shear thinning fluid becomes mechanically unstable and splits up in a region of a low viscosity and high shear rate close to the moving wall and a region with a high viscosity and low shear rate close to the static wall such that the stress in both bands is constant, see Fig. 1.4. From a theoretical point of view this is very similar to an equilibrium gas-liquid phase separation[71, 72]. Where in the latter case one is interested how fluctuations in the density become unstable and grow, in the case of shear banding one is interested in small deviations from the linear velocity profile that grow. In principle its occurrence is independent of the structural changes in the fluid underlying the shear thinning behavior, as long as the shear thinning is substantial. Thus gradient banding has been observed for systems ranging from hard sphere colloidal crystals[73] and soft colloidal glasses[74] to associative polymer networks[75], entangled polymer solutions[76, 77] and DNA solutions[78, 79].

The mechanism underlying shear thinning in the case of DNA solutions is the shear induced disentanglement of the polymers, which depends on the reptation dynamics of the polymers. A disentangled polymer system will have much lower viscosity than an entangled polymer system. It is still a matter of debate if shear banding really occurs in such systems, i.e. if these systems show two distinct bands with different shear rates or a continuous distribution of shear rates[80]. Shear thinning behavior is far more pronounced for dispersions of living polymers, which are self-assembled particles. This class of polymers has two mechanisms to release stress: reptation and the break up and recombination of the polymers. In the case that the average breaking time is much faster than the reptation time it can be shown that this results in a unique relaxation mechanism and strong shear thinning[81, 82]. Surfactant wormlike micelles are self-assembled particles consisting of lipids, which are continuously exchanged between the different micelles. The first rheological studies showing the potential of such systems are due to Rehage and Hoffmann, see e.g. Ref. [83, 84]. Indeed strong shear thinning was found, depending on the exact constitution of the sample. Therefore wormlike micelles are the 'working horse' for experimentalists in the field of flow instabilities. It should also be mentioned that strong shear thinning is a very desirable feature for industrial applications. The flow behavior of shampoo, for example, is mainly engineered by using surfactant wormlike micelles. It goes without saying why for this application shear thinning is useful: at low shear it behaves like a gel, at high shear it flows very easily. The same features are also very useful in, e.g. the oil industry[85]. The first experimental proof for the occurrence of structure formation in the fluid were birefringence measurements showing the split up of fluid into regions with low and high birefringence, i.e. probably into regions with high and low viscosity respectively[86]. This strongly hinted that also the shear rate in both regions is different. The existence of shear banding in this class of systems has first been found by Callaghan et al. in a pipe-flow geometry using Nuclear Magnetic Resonance Microscopy[87]. Using Heterodyne Dynamic Light Scattering Salmon et al[88] demonstrated for the first time that indeed a scenario is at hand where the systems splits up in two bands with shear rates of $\dot{\gamma}_1$ and $\dot{\gamma}_2$. The contribution of both bands is set by the lever rule, similar to the lever rule for gas-liquid phase separation. The mechanisms of how the shear bands are formed after starting up the flow and how the shear bands are related with the birefringent structures was nicely demonstrated both by Hu and Lips[89] and Miller and Rotstein[90]. Both groups used Particle Imaging Velocimetry (PIV) in combination with small angle light scattering and birefringence imaging. The system that was used in the latter three studies, but also by Rehage and Hoffmann and many others, was a 6 wt. % cetylpyridinium chloride/sodium salicylate (CPyCl–NaSal) micellar solutions. The kinetics of the shear band formation is very interesting from a fundamental point of view. Again, as for the I-N transition discussed in Part II of this Habilitationsschrift, the question can be asked whether the velocity profile is meta-stable or unstable for fluctuations in the velocity. In the literature on shear band formation it is often stated that a shear induced nematic phase 'nucleates' on the moving inner wall. This implies two things: first, that shear flow induces a phase transition and second, that the shear bands 'grow' from the wall. The PIV experiments eliminated these implications since the shear bands form instantaneously so that no mass transport can take place, i.e. no phase separation, and they also from from the middle of the gap. Both features imply that the flow is unstable after start up, although features for a spinodal-like decomposition could not be found. The flow behavior is much more complex for somewhat higher concentrations than 6 wt. % CPyCl–NaSal, where the flow profile shows strong oscillations[91]. This is one of many examples of temporal fluctuations[92, 93, 94]. There are equally many mechanisms that could play a role: the system could be metastable for shear band formation, there could be dynamic stick-slip behavior, it could be that the system jumps between two states $\dot{\gamma}_1$ and $\dot{\gamma}_2$ without formation of shear bands, the system might undergo a tumbling motion, or the interface between the shear bands might fluctuate, which is difficult to recognize when using 1-D experiments. Here it should be mentioned that most of these effects have been observed for shear thickening wormlike micelles like cetyl trimethylammonium tosilate[93] and cetyl trimethyl ammonium bromide[94]. A nice overview of the different reported effects is given in Ref. [69].

In spite of the extended literature there are still fundamental questions to be answer for a full understanding of gradient shear banding. First of all, the microscopic arguments underlying the predicted shear thinning behavior for living polymers as described in Ref. [81] do not have an experimental counterpart. Thus it is not at all clear what the actual reason is for the extreme shear thinning of these surfactant systems and whether this is a generic feature for living polymers. Second, in the debate on the stability of the gradient bands there is still no direct link between theory and experiments. Here the meta- or unstabile flow might play an important role but also practical aspects like the stick-slip boundary conditions. These questions need to be answered for a thorough understanding of ***Flow instabilities in dispersions of wormlike particles***, as described in ***Part IV*** of this Habilitationsschrift.

In chapter 14 the flow behavior of bis-urea substituted toluene (EHUT) is described (Ref. [95]). This is a bifunctional monomer that assembles reversibly into long, semiflexible polymer chains by multiple hydrogen bonds[96] with a total persistence length of at least 100 nm[97]. Similar to the traditional wormlike micelles, this system also shows strong shear thinning behavior[98]. Using heterodyne dynamic light scattering not less than three different shear banding regimes are observed. At low shear rates the system shows 'classical' shear banding, as described above. The shear banding regime at higher shear rates, however, is related to a shear-induced phase transition and the appearance of texture. Hence, EHUT is the the first living polymer system which was not a surfactant wormlike micellar system that showed shear banding. Moreover, the experiments on this system hint to different mechanisms and reasons for shear thinning and shear band formation. First, as mentioned earlier, the living character of the polymer plays an important role. In the initial paper (Ref. [81]) it is assumed that shear does not influence the breaking or recombination time. If the breaking time decreases with shear then one could argue that entanglements disappear, causing shear thinning. On the other hand one could argue that living polymers merge due to imposed flow, such that they elongate. Because long rods have a low rotational diffusion coefficient, they will more easily flow-align, causing shear thinning. For both mechanisms there is some support from simulations[99, 100]. The advantage of the EHUT system is that so called 'chain stoppers' can be used, such that recombination is inhibited. Doing so the characteristic maximum in the stress at the start of the shear thinning plateau becomes less pronounced, hinting that the shear thinning is somehow related to a coupling of chain alignment and growth[98]. Also for surfactant wormlike micelles some experimental justification for shear induced structural changes is found[101]. Both mechanisms describe a mechanical origin of shear thinning. Another reason for shear thinning could be the proximity of an I-N transition as described in Part I and II, because the collective rotational diffusion coefficient goes to zero approaching the I-N spinodal[102, 42]. Most systems described here can in principle form a nematic phase. The I-N transition is, however, in most cases located at quite high concentrations due to the flexibility and polydispersity of the systems.

Both the influence of the proximity of the I-N transition and the microscopic behavior of the living polymers can in principle be studied by using systems that can be imaged and that also show the I-N transition. Poly(butadiene) poly(ethylene oxide) (PbPeo) diblock copolymers with a 50-50 block composition form wormlike micelles that fulfil both criteria[103, 104]. In chapter 15 (Ref. [105]) it is shown that this system displays a gradient shear banding transition, purely due to proximity of the I-N spinodal. Step rate quenches was used to locate the non-equilibrium I-N binodal, as in chapter 9. The equilibrium I-N spinodal was found by dynamic shear experiments where we simultaneously probed the stress and the ordering of the Kuhn segments using time-resolved rheo-SANS and fitting the data using the equation of motion for the ordering tensor of rods. This in itself is an unique combination where the macroscopic stress can be related with the microscopic orientational behavior of the rods. With heterodyne dynamic light scattering, as used in chapter 14, we identified a small region close to the I-N spinodal where shear bands form. Our findings were confirmed later for surfactant wormlike micelles[106]. Observations using fluorescence microscopy in combination with a counter rotating cone-plate shear cell did not reveal any breaking or recombination (not published), so that the future challenge is to find a system that does show the breaking-recombining dynamics, but that can still be imaged.

The second issue that should be addressed is the stability of the gradient bands. In the original theory on gradient shear band formation there is only one parameter that is needed to select the two stresses at the beginning and the end of the stress plateau and that also drives fluctuations in the flow profile into a shear banded state. This term is called the 'shear-curvature viscosity'[72] and the 'stress diffusion coefficient'[107] in two very similar theories that were developed at the same time. Where this was for some time only a mathematical concept needed to describe shear banding, it could actually be determined by monitoring the 'interface travel' of the birefringent band[108] and also by analyzing the flow profile of 6 wt. % CPyCl–NaSal in microfluidic cells[109]. In chapter 16 (Ref. [110]) the interface travel in the latter system is probed by a step rate experiment within the stress plateau, directly recording the interface displacement using Ultra-Sonic Velocimetry (USV) coupled to standard rheology in Couette geometry. The main goal of this paper was however to show how the existence of shear bands in a sheared dispersion can be proven with a standard rheometer superimposing a shear oscillation on a steady shear flow in the shear banding regime.

The only time constant that sets the response of the system described in chapter 16 is the 'shear-curvature viscosity' or the 'stress diffusion coefficient'. Here it is assumed that the gradient bands in this system are well behaved, i.e. stable. As mentioned above this is not generally true. Even when considering purely shear thinning systems, still strong fluctuations are reported, like for 10 wt. % CPyCl–NaSal[91]. The occurrence of these fluctuations depended, however, on which batch of material is used. One possible explanation for the fluctuations is given by the group of Lerouge, where it was shown how vorticity bands grow from instabilities in the interface between high and low viscous gradient bands[57, 58, 59]. The same observations were also made for shear thinning CPyCl–NaSal dispersions[111]. If the instability of the interface is a generic feature it does not explain the dependence on which batch of materials is used. So the question is if there could be another mechanism at hand. In the paper by Lopez et al it was mentioned that the system slips or, in other words, that the mechanically applied shear rate is not the actual shear rate[91]. The experiments lack, however, time resolution, which is a problem when using NMR. A high time resolution is also needed to distinguish between an metastable or unstable flow, as mentioned earlier [89, 90]. If the flow is unstable then bands could nucleate and melt, which is also a possible reason for the observed fluctuations. In chapter 17 (ref. [112] we perform measurements very similar to and on the same system as the experiments described in Ref. [89, 90], i.e. recording time-resolved velocity profiles during transient strain-controlled experiments, in this case using USV as in chapter 16. To access the effect of the boundary conditions we used smooth and sandblasted geometries, something that is not possible with optical techniques like PIV. For stick boundary conditions standard shear banding is observed, although depending on the degree of micellar entanglement temporal fluctuations are observed in the highly sheared band. For slip boundary conditions wall slip occurs only for shear rates larger than the start of the stress plateau. At low entanglement, shear band formation is shifted by a constant, while for more entangled systems shear bands constantly nucleate and melt. This has the important implication that for both concentrations wall slip acts as to stabilize the bulk flow. Micellar orientation gradients at the walls may account for these original features. If the boundary conditions are not well controlled then fluctuations may occur, especially for those systems that have a high barrier to form shear bands.

Bibliography

[1] J. Perrin. *Atoms.* Constable, London, 1916.

[2] P. N. Pusey and W. van Megen. Phase behavior of concentrated suspensions of nearly hard colloidal spheres. *Nature*, 320:340–342, 1986.

[3] H. Verduin and J. K. G. Dhont. Phase diagram of a model adhesive hard-sphere dispersion. *J. Colloid Int. Sci.*, 172:425–437, 1995.

[4] H. Zocher. Über freilwillige strukturbildung in solen. *Anorg. Allg. Chem.*, 147:91–110, 1925.

[5] F. C. Bawden, N. W. Pirie, J. D. Bernal, and I. Fankuchen. Liquid crystalline substances from virus-infected plants. *Nature*, pages 1051–1052, 1936.

[6] L. Onsager. The effect of shape on the interaction of colloidal particles. *Ann. N.Y. Acad. Sci.*, 51:627–659, 1949.

[7] R. F. Kayser and H. J. Raveché. Bifurcation in onsager's model of the isotropic-nematic transition. *Phys. Rev. A*, 17:2067–2072, 1978.

[8] E. Grelet. Hexagonal order in crystalline and columnar phases of hard rods. *Phys. Rev. Lett.*, 100:168301, 2008.

[9] A. Stroobants, H. N. W. Lekkerkerker, and D. Frenkel. Evidence for one-, two-, and three-dimensional order in a system of hard parallel spherocylinders. *Phys. Rev. A.*, 36(6):2929–2945, 1987.

[10] M. P. B. van Bruggen, H. N. W. Lekkerkerker, G. Maret, and J. K. G. Dhont. Long-time translational self-diffusion in isotropic and nematic dispersions of colloidal rods. *Phys. Rev. E*, 58(6):7668–7677, 1998.

[11] M. P. Lettinga, E. Barry, and Z. Dogic. Self-diffusion of rod-like viruses in the nematic phase. *Europhys. Lett.*, 71(4):692698, 2005.

[12] M. P. Lettinga, Z. Zhang, J.K.G. Dhont, S. Messlinger, and G. Gompper. Hydrodynamic interactions in dense rod suspensions. *Soft Matter*, 6:4556–4562, 2010.

[13] M. P. Lettinga and E. Grelet. Self-diffusion of rodlike viruses through smectic layers. *Phys. Rev. Lett.*, 99:197802, 2007.

[14] E. Grelet, M. P. Lettinga, M. Bier, R. van Roij, and P. van der Schoot. Dynamical and structural insights into the smectic phase of rod-like particles. *J. Phys.: Condens. Matter*, 20:494213, 2008.

[15] A. R. Khokhlov and A. N. Semenov. Liquid-crystalline ordering in the solution of partially flexible macromolecules. *Physica A*, 112(3):605–614, 1982.

[16] Z. Y. Chen. Nematic ordering in semiflexible polymer chains. *Macromolecules*, 26:3419–3423, 1993.

[17] H. Hansen-Goos and K. Mecke. Fundamental measure theory for inhomogeneous fluids of nonspherical hard particles. *Phys. Rev. Lett.*, 102:018302, 2009.

[18] M. A. Cotter and D. C. Wacker. van der waals theory of nematogenic solutions. i. derivation of general equations. *Phys. Rev. A*, 18:2669, 1978.

[19] T. J. Sluckin. Polydispersity in liquid crystal systems. *Liquid Crystals*, 6(1):111–131, 1989.

[20] H. N. W. Lekkerkerker, Ph. Coulon, R van der Haegen, and R. Deblieck. On the isotropic-liquid crystal phase separation in a solution of rodlike particles of differnt lengths. *J. Chem. Phys.*, 80(7):3427–3433, 1984.

[21] H. H. Wensink and G. J. Vroege. Isotropic-nematic phase behavior of length-polydisperse hard rods. *J. Chem. Phys.*, 119(13):6868–6828, 2003.

[22] M. P. B. van Bruggen, J. K. G. Dhont, and H. N. W. Lekkerkerker. Morphology and kinetics of the isotropic-nematic phase transition in dispersions of hard rods. *Macromolecules*, 32:2256–2264, 1999.

[23] P. W. Oakes, J. Viamontes, and J. X. Tang. Growth of tactoidal droplets during the first-order isotropic to nematic phase transition of f-actin. *Phys. Rev.E*, 75:061902, 2007.

[24] M. P. Lettinga, K. Kang, A. Imhof, D. Derks, and J. K. G. Dhont. Kinetic pathways of the nematic-isotropic phase transition of rod-like viruses. *J. Phys.: Condens. Matter*, 17:S3609–S3681, 2005.

[25] M. P. Lettinga, K. Kang, P. Holqvist, A. Imhof, D. Derks, and J. K. G. Dhont. Nematic-isotropic spinodal decomposition of rod-like viruses. *Phys. Rev. E*, 73:011412, 2006.

[26] P. Holmqvist, M. Ratajczyk, G. Meier, H. H. Wensink, and M. P. Lettinga. Supersaturated dispersions of rod-like viruses with added attraction. *Phys. Rev. E*, 21:10976–10982, 2009.

[27] H. Löwen. Colloidal soft matter under external control. *J. Phys.: Condens. Matter*, 13:R415–R432, 2001.

[28] H. Löwen. Colloidal dispersions in external fields: recent developments. *J. Phys.: Condens. Matter*, 20:404201, 2008.

[29] E. W. Merrill. Rheology of blood. *Physiological reviews*, 49(4):863–887, 1969.

[30] L. de Viguerie, G. Ducouret, F. Lequeux, T. Moutard-Martin, and P. Walter. Historical evolution of oil painting media: A rheological study. *C. R. Physique*, 10:612621, 2009.

[31] Z. Cheng, J. Zhu, and P. M. Chaikin. Nature of the divergence in low shear viscosity of colloidal hard-sphere dispersions. *Phys. Rev.*, 65:041405, 2002.

[32] R. Pal. Rheology of concentrated suspensions of deformable elastic particles such as human erythrocytes. *J. of Biomech.*, 36(7):981–989, 2003.

[33] W. J. Frith, P. dHaene, R. Buscall, and J. Mewis. Shear thickening in model suspensions of sterically stabilized particles. *J. Rheol.*, 40(4):531–548, 1996.

[34] N. J. Wagner and J. F. Brady. Shear thickening in colloidal dispersions. *Physics Today*, pages 27–32, 2009.

[35] J. K. G. Dhont. *An Introduction to Dynamics of Colloids.* Elsevier, Amsterdam, 1996.

[36] M. P. Lettinga, H. Wang, and J. K. G. Dhont. Microstructural response of a near-critical colloid-polymer mixture to shear flow. *Phys. Rev. E*, 70:061405, 2004.

[37] P. Holmqvist, M. P. Lettinga, J. Buitenhuis, and J. K. G. Dhont. Crystallization kinetics of colloidal spheres under stationary shear flow. *Langmuir*, 21:10976–10982, 2005.

[38] B. J. Ackerson and P. N. Pusey. Shear-induced order in suspension of hard-sphere. *Phys. Rev. Lett.*, 61:1033, 1988.

[39] Q. Majorana. Nuovi fenomeni magneto-ottici presentati da speciali soluzioni magnetiche. *Il Nuovo Cimento*, 4(1):374–376, 1902.

[40] J. Tang and S. Fraden. Magnetic-field-induced phase transition in a colloidal suspension. *Phys. Rev. Lett.*, 71(21):3509–3512, 1993.

[41] T. A. J. Lenstra, Z. Dogic, and J. K. G. Dhont. Shear-induced displacement of isotropic-nematic spinodals. *J. Chem. Phys.*, 114(22):10151–10162, 2001.

[42] P.D. Olmsted and C.-Y.D. Lu. Phase separation of rigid-rod suspensions in shear flow. *Phys. Rev. E*, 60(4):4397–4415, 1999.

[43] J. Vermant, H. Yang, and G. G. Fuller. Rheooptical determination of aspect ratio and polydispersity of nonspherical particles. *AICHE Journal*, 47(4):790–798, 2001.

[44] M. Doi and S. F. Edwards. *The Theory of Polymer Dynamics*. Oxford, 1986.

[45] C. Graf, H. Kramer, M. Deggelmann, M. Hagenbüchle, Ch. Johner, Ch. Martin, and R. Weber. Rheological properties of suspensions of interacting rodlike fd-virus particles. *J. Chem. Phys.*, 98(6):4921–4928, 1993.

[46] S. Förster, M. Konrad, and P. Lindner. Shear thinning and orientational ordering of wormlike micelles. *Phys. Rev. Lett.*, 94:017803, 2005.

[47] S. Hess. Fokker-planck-equation approach to flow alignment in liquid crystals. *Z. Naturforsch.*, 31(a):1034–1037, 1976.

[48] R.G. Larson. Arrested tumbling in shearing flows of liquid crystal polymers. *Macromolecules*, 23:3983–3992, 1990.

[49] M. G. Forest and Q. Wang. Monodomain response of finit-aspect-ratio macromolecules in shear and realted linear flows. *Rheol. Acta*, 42:20–46, 2003.

[50] W. R. Burghardt and G. G. Fuller. Role of director tumbling in the rheology of polymer liquid crystal solutions. *Macromolecules*, 24:2546, 1991.

[51] M. Grosso, S. Crescitelli, E. Somma, J. Vermant, P. Moldeaers, and P. L. Maffettone. Prediction and observation of sustained in a shear liquid crystalline polymer. *Phys. Rev. Lett.*, 90:098304, 2003.

[52] M. P. Lettinga, G.H. Koenderink, B.W.M. Kuipers, E. Bessels, and A.P. Philipse. Rotational dynamics of colloidal spheres probed with fluorescence recovery after photobleaching. *J. Chem. Phys.*, 120(9):4517–4529, 2004.

[53] M. P. Lettinga, Z. Dogic, H. Wang, and J. Vermant. Flow behavior of colloidal rodlike viruses in the nematic phase. *Langmuir*, 21:8048–8057, 2005.

[54] M. Ripoll, P. Holmqvist, R. G. Winkler, G. Gompper, J. K. G. Dhont, and M. P. Lettinga. Attractive colloidal rods in shear flow. *Phys. Rev. Lett.*, 101:168302, 2008.

[55] J. K. G. Dhont and W. J. Briels. Gradient and vorticity banding. *Rheol. Acta*, 47(3):257–281, 2008.

[56] P. Boltenhagen, Y. Hu, E. F. Matthys, and D. J. Pine. Observation of bulk phase separation and coexistence in a sheared micellar solution. *Phys. Rev. Lett.*, 79(12):2359–2362, 1997.

[57] S. Lerouge, M. Argentina, , and J. P. Decruppe. Interface instability in shear-banding flow. *Phys. Rev. Lett.*, 96:088301, 2006.

[58] S. Lerouge, M. A. Fardin, M. Argentina, G. Grégoire, and O. Cardoso. Interface dynamics in shear-banding flow of giant micelles. *Soft Matter*, 4:18081819, 2008.

[59] M. A. Fardin, B. Lasne, O. Cardoso, G. Grégoire, M. Argentina, J. P. Decruppe, and S. Lerouge. Taylor-like vortices in shear-banding flow of giant micelles. *Phys. Rev. Lett.*, 103:028302, 2009.

[60] S. M. Fielding. Vorticity structuring and velocity rolls triggered by gradient shear bands. *Phys.Rev. E*, 76:016311, 2007.

[61] R.G. Larson, E. S. G. Shaqfeh, and S. J. Muller. A purely elastic instability in taylor-couette flow. *J. Fluid Mech.*, 218:573–600, 1990.

[62] D. Bonn, J. Meunier, O. Greffier, A. Al-Kahwaji, and H. Kellay. Bistability in non-newtonian flow: Rheology of lyotropic liquid crystals. *Phys. Rev. E*, 58(2):2115–2118, 1998.

[63] F. Pignon, A. Magnin, and J.-M. Piau. Butterfly light scattering pattern and rheology of a sheared thixotropic clay gel. *Phys. Rev. Lett.*, 79(23):4689–4673, 1997.

[64] R. H. Tromp and E. H. A. De Hoog. Band formation on shearing in phase-separated polymer solutions. *Phys. Rev. E*, 77:031503, 2008.

[65] P. Pakdel and G. H. McKinley. Elastic instability and cruved streamlines. *Phys. Rev. Lett.*, 77(12):2459–2462, 1996.

[66] R.G. Larson. Instabilitiesin viscoelastic flows. *Rheol. Acta*, 31:213–263, 1992.

[67] K. Kang, M. P. Lettinga, Z. Dogic, and J. K. G. Dhont. Vorticity banding in rodlike virus suspensions. *Phys. Rev. E*, 74:026307, 2006.

[68] K. Kang, M. P. Lettinga, and J. K. G. Dhont. Is vorticity-banding due to an elastic instability? *Rheol Acta*, 47:499–508, 2008.

[69] S. Manneville. Recent experimental probes of shear banding. *Rheol. Acta*, 47(1):301318, 2008.

[70] P. D. Olmsted. Perspectives on shear banding in complex fluids. *Rheol. Acta*, 47(3):283–300, 2008.

[71] P. D. Olmsted. Two-state shear diagrams for complex fluids in shear flow. *Europhys. Lett.*, 48:399, 1999.

[72] J. K. G. Dhont. A constitutive relation describing the shear-banding transition. *Phys. Rev. E*, 60(4):4534–4544, 1999.

[73] A. Imhof, A. van Blaaderen, and J. K. G. Dhont. Shear melting of colloidal crystals of charged spheres studied with rheology and polarizing microscopy. *Langmuir*, 10:3477–3484, 1994.

[74] W. M. Holmes, P. T. Callaghan, D. Vlassopoulos, and J. Roovers. Shear banding phenomena in ultrasoft colloidal glasses. *J. Rheol.*, 48(5):1085–1102, 2004.

[75] J. Sprakel, E. Spruijt, M. A. Cohen Stuart, N. A. M. Besseling, M. P. Lettinga, and J. van der Gucht. Shear banding and rheochaos in associative polymer networks. *Soft Matter*, 4:16961705, 2008.

[76] P. Tapadia and S.-Q. Wang. Yieldlike constitutive transition in shear flow of entangled polymeric fluids. *Phys. Rev. Lett.*, 91(19):198301, 2003.

[77] P. Tapadia, S. Ravindranath, and S.-Q. Wang. Banding in entangled polymer fluids under oscillatory shearing. *Phys. Rev. Lett.*, 96:196001, 2006.

[78] P. E. Boukany, Y. T. Hu, and S.-Q. Wang. Observations of wall slip and shear banding in an entangled dna solution. *Macromolecules*, 41:2644–2650, 2008.

[79] Y. T. Hu, C. Palla, and A. Lips. Role of electrostatic interactions in shear banding of entangled dna solutions. *Macromolecules*, 41:6618–6620, 2008.

[80] Y. T. Hu, L. Wilen, A. Philips, and A. Lips. Is the constitutive relation for entangled polymers monotonic? *J. Rheol.*, 51(2):275–295, 2007.

[81] N. A. Spenley, M. E. Cates, and T. C. B. McLeish. Nonlinear rheology of wormlike micelles. *Phys. Rev. Lett.*, 71(939), 1993.

[82] M. E. Cates. Reptation of living polymers: Dynamics of entangled polymers in the presence of reversible chain-scission reactions. *Macromolecules*, 20(9):2289, 1987.

[83] H. Rehage and H. Hoffmann. Rheological properties of viscoelastic surfactant systems. *J. Phys. Chem.*, 92:4712–4719, 1988.

[84] H. Rehage and H. Hoffmann. Viscoelastic surfactant solutions: model systems for rheological researchs. *Mol. Phys.*, 74:933973, 1991.

[85] G. C. Maitland. Oil and gas production. *Curr. Opinion Colloid Interface Sci.*, 5:301 –311, 2000.

[86] J. P. Decruppe, R. Cressely, R. Makhloufi, and E. Cappelaere. Flow birefringence experiments showing a shear-banding structure in a ctab solution. *Colloid Polym. Sci.*, 273(4):346–351, 1995.

[87] P. T. Callaghan, M. E. Cates, C. J. Rofe, and J. B. A. F. Smeulders. A study of the "spurt elfect" in wormlike micelles using nuclear magnetic resonance microscopy. *J. Phys. II France*, 6:375–393, 1996.

[88] J.-B. Salmon, A. Colin, and S. Manneville. Velocity profiles in shear-bandingwormlike micelles. *Phys. Rev. Lett.*, 90(22):228303, 2003.

[89] Y. T. Hu and A. Lips. Kinetics and mechanism of shear banding in an entangled micellar solution. *J. Rheol.*, 49(5):1001–1027, 2005.

[90] E. Miller and J. P. Rothstein. Transient evolution of shear-banding wormlike micellar solutions. *J. Non-Newtonian Fluid Mech.*, 143(1):22–37, 2007.

[91] M. R. López-González, W. M. Holmes, P. T. Callaghan, and P. J. Photinos. Shear banding fluctuations and nematic order inwormlike micelles. *Phys. Rev. Lett.*, 93:268302, 2004.

[92] V. Herle, J. Kohlbrecher, Bruno Pfister, P. Fischer, and E. J. Windhab. Alternating vorticity bands in a solution of wormlike micelles. *Phys. Rev. Lett.*, 99:158302, 2007.

[93] R. Bandyopadhyay, G. Basappa, and A. K. Sood. Observation of chaotic dynamics in dilute sheared aqueous solutions of ctat. *Phys. Rev. Lett.*, 84(9):2022–2025, 2000.

[94] L. Bécu, S. Manneville, and A. Colin. Spatiotemporal dynamics of wormlike micelles under shear. *Phys. Rev. Lett.*, 93(1):018301, 2004.

[95] J. van der Gucht, M. Lemmers, W. Knoben, N. A. M. Besseling, and M. P. Lettinga. Multiple shear-banding transitions in a supramolecular polymer solution. *Phys. Rev. Lett.*, 97:108301, 2006.

[96] S. Boileau, L. Bouteiller, F. Lauprêtre, and F. Lortie. Soluble supramolecular polymers based on urea compounds. *New J. Chem., 2000, 24,*, 24:845–848, 2000.

[97] J. van der Gucht, N. A. M. Besseling, W. Knoben, L. Bouteiller, M. P. Lettinga, and M. A. Cohen Stuart. Brownian particles in supramolecular polymer solutions. *Phys. Rev. E*, 67:051106, 2003.

[98] W. Knoben, N. A. M. Besseling, and M. A. Cohen Stuart. Rheology of a reversible supramolecular polymer studied by comparison of the effects of temperature and chain stoppers. *J. Chem. Phys.*, 126:024907, 2007.

[99] J. T. Padding, E. S. Boek, and W. J. Briels. Dynamics and rheology of wormlike micelles emerging from particulate computer simulations. *J. Chem. Phys.*, 129:074903, 2008.

[100] W. J. Briels, P. Mulder, and W. K. den Otter. Simulations of elementary processes in entangled wormlike micelles under tension: a kinetic pathway to y-junctions and shear induced structures. *J. Phys.: Condens. Matter*, 16(38):S3965–S3974, 2004.

[101] J. Dehmoune and J.-P. Decruppe O. Greffier H. Xu. Rheometric and rheo-optical investigation on the effect of the aliphatic chain length of the surfactant on the shear thickening of dilute worm-like micellar solutions. *Rheol. Acta*, 46:11211129, 2007.

[102] J. K. G. Dhont and W. J. Briels. Viscoelasticity of suspensions of long, rigid rods. *Colloid Surface A*, 213(2-3):131–156, 2003.

[103] P. Dalhaimer, F. S. Bates, and D. E. Discher. Single molecule visualization of stable, stiffness-tunable, flow-conforming worm micelles. *Macromolecules*, 36:6873–6877, 2003.

[104] Y.-Y. Won, H. T. Davis, and F. S. Bates. Giant wormlike rubber micelles. *Science*, 283:960–963, 1999.

[105] B. Lonetti, J. Kohlbrecher, L. Willner, J. K. G. Dhont, and M. P. Lettinga. Dynamic response of block copolymer wormlike micelles to shear flow. *J. Phys.: Condens. Matter*, 20:404207, 2008.

[106] M. E. Helgeson, M. D. Reichert, Y. T. Hub, and N. J. Wagner. Relating shear banding, structure, and phase behavior in wormlike micellar solutions. *Soft Matter*, 5:3858–3869, 2009.

[107] C.-Y. D. Lu, P. D. Olmsted, and R. C. Ball. Effects of nonlocal stress on the determination of shear banding flow. *Phys. Rev. Lett.*, 84(4):642–645, 2000.

[108] O. Radulescu, P. D. Olmsted, J. P. Decruppe, S. Lerouge, J.-F. Berret, and G. Porte. Time scales in shear banding of wormlike micelles. *EPJE*, 62:230–237, 2003.

[109] C. Masselon, J.-B. Salmon, and A. Colin. Nonlocal effects in flows of wormlike micellar solutions. *Phys. Rev. Lett*, 100:038301, 2008.

[110] P. Ballesta, M. P. Lettinga, and S. Manneville. Superposition rheology of shear-banding wormlike micelles. *J. Rheol.*, 51(5):1047–1072, 2007.

[111] S. Lerouge. *Personal communication with S. Lerouge*, 2009.

[112] M. P. Lettinga and S. Manneville. Competition between shear banding and wall slip inwormlike micelles. *Phys. Rev. Lett.*, 103:248302, 2009.

Part I

Diffusion of rods in concentrated dispersions of rods

Chapter 2

Self-diffusion of rod-like viruses in the nematic phase

EUROPHYSICS LETTERS 15 August 2005

Europhys. Lett., **71** (4), pp. 692–698 (2005)
DOI: `10.1209/epl/i2005-10127-x`

Self-diffusion of rod-like viruses in the nematic phase

M. P. LETTINGA[1], E. BARRY[2] and Z. DOGIC[2]

[1] *IFF, Institut Weiche Materie, Forschungszentrum Jülich - D-52425 Jülich, Germany*
[2] *Rowland Institute at Harvard, Harvard University - Cambridge, MA 02142, USA*

received 21 March 2005; accepted 17 June 2005

PACS. `82.70.-y` – Disperse systems; complex fluids.
PACS. `61.30.-v` – Liquid crystals.
PACS. `66.10.-x` – Diffusion and ionic conduction in liquids.

Abstract. – We measure the self-diffusion of colloidal rod-like virus fd in an isotropic and nematic phase. A low-volume fraction of viruses are labelled with a fluorescent dye and dissolved in a background of unlabelled rods. The trajectories of individual rods are visualized using fluorescence microscopy from which the diffusion constant is extracted. The diffusion parallel ($D_{\|}$) and perpendicular ($D_{\perp}$) to the nematic director is measured. The ratio ($D_{\|}/D_{\perp}$) increases monotonically with increasing virus concentration. Crossing the isotropic-nematic phase boundary results in increase of $D_{\|}$ and decrease of $D_{\perp}$ when compared to the diffusion in the isotropic phase (D_{iso}).

Introduction. – Suspensions of semi-flexible polymers exhibit a variety of dynamical phenomena, of great importance to both physics and biology, that are still only partially understood. Advances over the past decade include direct visual evidence for a reptation-like diffusion of polymers in a highly entangled isotropic solution and shape anisotropy of an isolated polymer [1–4]. If the concentration of the polymers is increased, a suspension undergoes a first-order phase transition to a nematic phase, which has long-range orientational order but no long-range positional order. As a result of the broken orientational symmetry, it is expected that the diffusion of polymers in the nematic liquid crystals will be drastically different from that in concentrated isotropic solutions. While the static phase behavior of semi-flexible nematic polymers is well understood in terms of the Onsager theory and its extensions by Khoklov and Semenov [5, 6], the dynamics of semi-flexible polymers in the nematic phase is much less explored [7].

In this paper, we determine the concentration dependence of the anisotropic diffusion of semi-flexible viruses in a nematic phase and compare it to the diffusion in the isotropic phase. Experimentally, the only data on the translational diffusion of colloidal rods in the nematic phase was taken in a mixture of labelled and unlabelled polydysperse boehmite rods using fluorescence recovery after photobleaching (FRAP) [8]. Theoretically, molecular-dynamics simulations were performed on hard spherocylinder and ellipsoidal systems from which the anisotropic diffusion data was extracted [9–11]. The unisotropic diffusion has also been studied in low-molecular-weight thermotropic liquid crystals using NMR spectroscopy or inelastic scattering of neutrons [12].

Real-space microscopy is a powerful method that can reveal dynamics of colloidal and polymeric liquid systems that are inaccessible to other traditional techniques [3, 7]. We use digital microscopy to directly visualize the dynamics of fluorescently labelled fd in a nematic background of unlabelled fd. The advantage of this method is an easy interpretation of data and no need to obtain macroscopically aligned monodomains in magnetic fields. The advantages of using fd are its large contour length which can be easily visualized with optical microscope and its phase behavior which can be quantitatively described with the Onsager theory extended to account for electrostatic repulsive interactions and semi-flexibility [13, 14]. Viruses such as fd and TMV have been used earlier to study the rod dynamics in the isotropic phase [15].

Experimental methods. – The physical characteristics of the bacteriophage fd are its length $L = 880\,\text{nm}$, diameter $D = 6.6\,\text{nm}$, persistence length of 2200 nm and a surface charge of $10\,\text{e}^-/\text{nm}$ at pH 8.2 [16]. Bacteriophage fd suspension forms isotropic, cholesteric and smectic phases with increasing concentration [16–18]. The free energy difference between the cholesteric and nematic phase is very small and locally the cholesteric phase is identical to nematic. We expect that at short time scales the diffusion of the rods for these two cases would be the same. Hereafter, we refer to the liquid crystalline phase at intermediate concentration as a nematic instead of a cholesteric.

The fd virus was prepared according to a standard biological protocol using XL1-Blue strain of *E. coli* as the host bacteria [19]. The yields are approximately 50 mg of fd per liter of infected bacteria and the virus is typically grown in 6 liter batches. Subsequently, the virus is purified by repetitive centrifugation (108000 g for 5 hours) and re-dispersed in a 20 mM phosphate buffer at $p\text{H} = 7.5$. First-order isotropic-nematic (I-N) phase transition for fd under these conditions takes place at a rod concentration of 15.5 mg/ml.

Fluorescently labelled fd viruses were prepared by mixing 1 mg of fd with 1 mg of succinimidyl ester Alexa-488 (Molecular Probes) for 1 hour. The dye reacts with free amine groups on the virus surface to form irreversible covalent bonds. The reaction is carried out in small volume (100 μl, 100 mM phosphate buffer, $p\text{H} = 8.0$) to ensure a high degree of labelling. Excess dye was removed by repeated centrifugation steps. Absorbance spectroscopy indicates that there are approximately 300 dye molecules per each fd virus. Viruses labelled with fluorescein isothiocynante, a dye very similar to Alexa 488, exhibit the phase behavior identical to that of unlabelled virus. Since liquid crystalline phase behavior is a sensitive test of interaction potential, it is reasonable to assume that the interaction potential between labelled viruses is very similar to that between unlabelled viruses.

The samples were prepared by mixing one unit of anti-oxygen solution (2 mg/ml glucose oxidase, 0.35 mg/ml catalase, 30 mg/ml glucose and 5% β-mercaptoethanol), one unit of a dilute dispersion of Alexa 488 labelled viruses and eight units of the concentrated fd virus suspension at the desired concentration. Under these conditions the fluorescently labelled viruses are relatively photostable and it is possible to continuously observe rods for 3-5 minutes without significant photobleaching. The ratio of labelled to unlabelled particles is roughly kept at 1 : 30000. The samples were prepared by placing 4 μl of solution between a No 1.5 cover slip and coverslide. The thickness of the samples is about 10 μm. Thin samples are important to reduce the signal of out-of-focus particles. Samples are equilibrated for half an hour, allowing flows to subside and liquid crystalline defects to anneal. We have analyzed data at various distances from the wall and have not been able to observe a significant influence of wall on the diffusion of viruses.

For imaging we used an inverted Nikon TE-2000 microscope equipped with 100 × 1.4 NA PlanApo oil immersion objective, a 100 W mercury lamp and a fluorescence cube for Alexa 488 fluorescent dye. The images where taken with a cooled CCD Camera (CoolSnap HQ,

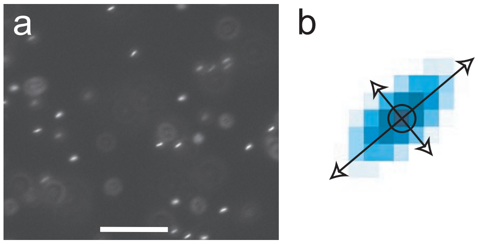

Fig. 1 – (a) Image of fluorescently labelled rods dissolved in a background nematic phase of unlabelled rods. The scale bar is 5 μm. (b) Two-dimensional Gaussian fit to an individual rod. Arrows indicate the long and short axis. The circle indicates the center of mass. From this fit it is possible to obtain the orientation of an individual fd rod. The pixel size is 129 nm.

Roper Scientific) set to an exposure time of 60 ms, running in a overlap mode at a rate of 16 frames per second with 2×2 binning. The pixel size was 129 nm and the field of view was 89 μm × 66 μm. Typically there were around hundred fluorescently labelled rods in the field of view. For each fd concentration ten sequences of four hundred images were recorded.

Analysis method. – Figure 1a shows a typical image of fluorescently labelled rods in a background nematic of unlabelled rods. Due to limited spatial and temporal resolution of the optical microscope, labelled fd appear as a slightly anisotropic rod, although the actual aspect ratio is larger than 100. To measure the anisotropic diffusion in the nematic phase, it is first necessary to determine the nematic director which has to be uniform within a field of view. Spatial distortion of the nematic would significantly affect our results. The centers of mass and orientation of rods are obtained sequentially. In a first step, a smoothed image is used to identify the rods and obtain the coordinates of its center of mass using image processing code written in IDL [20]. Subsequently, a two-dimensional Gaussian fit around the center of mass of each rod is performed (fig. 1b). From this fit the orientation of each rod-like virus is obtained. This procedure is then repeated for a sequence of images.

The length of a trajectory is usually limited to a few seconds, after which the particles diffuse out of focus. In fig. 2a and b we plot the trajectories of an ensemble of particles for both isotropic and nematic sample. As expected, the trajectories in the isotropic phase are spherically symmetric (fig. 2a) while those in the nematic phase exhibit a pronounced anisotropy (fig. 2a). The symmetric nature of the distribution indicates that there is no drift or flow in our samples. We obtain the orientation of the nematic director using two independent methods. One method is to measure the main axis of the distribution shown in fig. 2b. This procedure assumes that the diffusion is largest along the nematic director. An alternative method is to plot a histogram of rod orientations which are obtained from 2D Gaussian fits to each rod (fig. 1b). The resulting orientational distribution function (ODF) is shown in fig. 2c. In principle, it should be possible to obtain both the nematic director and order parameter from ODF shown in fig. 2c. We find that the order parameter obtained in such a way is systematically higher than the order parameter obtained from more reliable X-ray experiments [14]. This is due to significant rotational diffusion each rod undergoes during an exposure time of 60 ms.

The differences in the orientation of the nematic director obtained using these two methods is always less than 5 degrees. For the example shown in fig. 2, from the anisotropy of the diffusion we obtain a nematic director at an angle of 31.2° (fig. 2b), while the peak of the orientational distribution function lies at 30.2° (fig. 2c). The director can be "placed" along

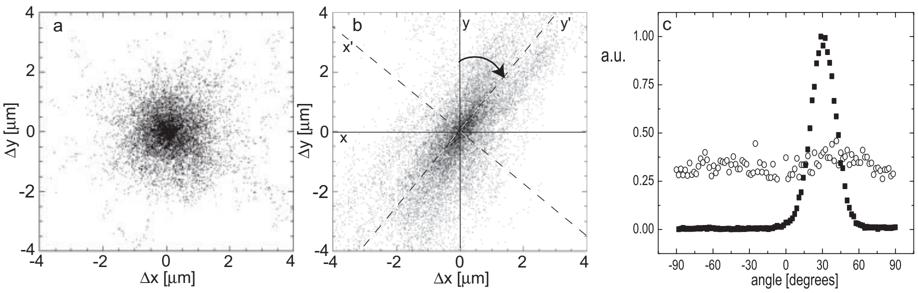

Fig. 2 – (a) A collection of trajectories of fluorescently labelled virus particles in the isotropic phase. All trajectories are translated so that the first point is located at the origin. For clarity we only show the center of mass and not the line connecting subsequent points in a particle trajectory. The concentration of virus in this sample was 14 mg/ml. (b) Anisotropic trajectories of the fluorescently labelled viruses diffusing in the nematic phase. The concentration of the background virus in this sample was 21 mg/ml. x' and y' indicate a new lab-frame in which the director is aligned along the y'-axis. (c) The orientational distribution function obtained by plotting the probability distribution function of the virus orientation for isotropic (open circles) and nematic phase (full squares). The orientation of the virus is obtained from two-dimensional Gaussian fits, an example of which is shown in fig. 1b. The nematic directors obtained from (b) and (c) are almost identical.

one of the two main axes by rotating the lab-frame.

The diffusion coefficients of the rods parallel ($D_\parallel$) and perpendicular ($D_\perp$) to the director are calculated from the x'- and y'-component of the mean-square displacement. When the director lies along the y'-axis, $D_\parallel$ and $D_\perp$ are given by

$$D_\parallel = \frac{1}{N}\frac{1}{2}\sum\{y'_i(t) - y'_i(0)\}^2, \tag{1}$$

$$D_\perp = \frac{1}{N}\frac{1}{\sqrt{2}}\sum\{x'_i(t) - x'_i(0)\}^2, \tag{2}$$

where N is the number of traced particles. To obtain $D_\perp$, D_x is multiplied with $\sqrt{2}$ since only one component of the diffusion perpendicular to the director is measured. The underlying assumption of our analysis is that the nematic director is oriented in the field of view. For 10 μm thin samples this is reasonable.

Results and discussion. – Typical mean-square displacements (MSD) are shown in fig. 3 for samples in an isotropic and nematic phase. On average, the mean-square displacement was linear over fifty frames in the nematic phase, but only over twenty-five frames in the isotropic phase. The diffusion perpendicular to the director is slower in the nematic phase as compared to the isotropic phase. Therefore in the nematic phase, the particles stay longer in focus and can be tracked for a longer time. Because the MSDs are linear over the entire time range and displacements are up to a few times the particle length, we are measuring pure long-time self-diffusion. Visual inspection of the trajectories in the concentrated isotropic phase, just below I-N coexistence shows no characteristics of the reptation observed in suspensions of long DNA fragments or actin filaments [2, 3]. This points to the fact that fd is very weakly entangled in a concentrated isotropic suspension. This is in agreement with recent microrheology measurements of fd suspensions [21]. We note that MSDs obtained from few hundred trajectories within a single field of view are very accurate. However, if we move to

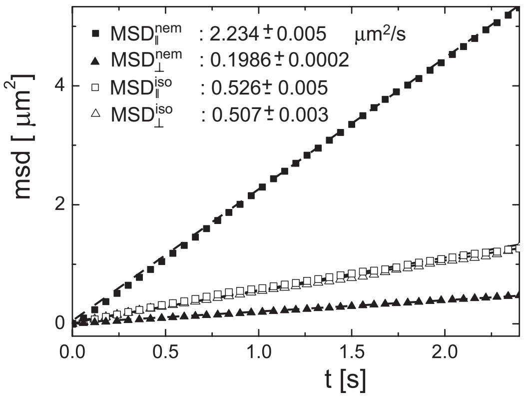

Fig. 3 – The mean-square displacements of rods along the director (full squares) and perpendicular to the director (full triangles) obtained for a nematic sample at virus concentration of 21 mg/ml. The isotropic data are given by the open squares and were taken just below the I-N phase transition at virus concentration of 14 mg/ml. The diffusion along the director is significantly enhanced when compared to the diffusion in the isotropic phase, while the diffusion perpendicular to the director is significantly suppressed. The mean-square displacements shown in this figure are measured from a single field of view.

another region of the sample we obtain MSD with a slightly different slope. This leads to the conclusion that the largest source of error in measuring the anisotropic diffusion coefficient is the uniformity of the nematic director within the field of view.

The concentration dependence of the anisotropic diffusion constants is shown in fig. 4a. The nematic phase melts into an isotropic phase at low concentrations and freezes into a

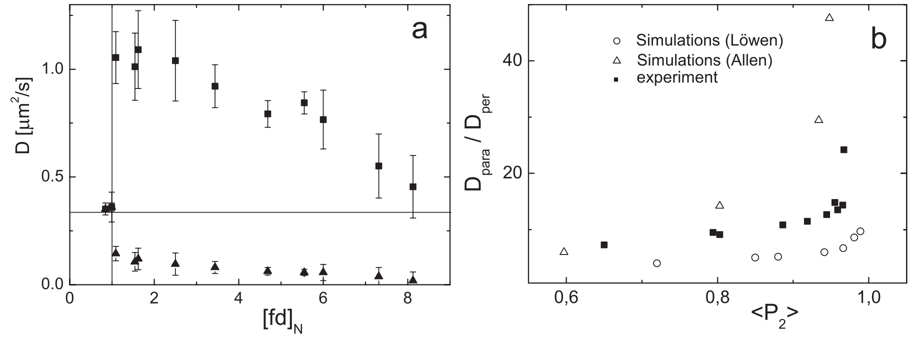

Fig. 4 – (a) The concentration dependence of the translational diffusion parallel to ($D_{\parallel}$) and perpendicular to ($D_{\perp}$) the nematic director are indicated by squares and triangles, respectively. The nematic phase in coexistence with the isotropic phase occurs at $c_{fd} = 15.5$ mg/ml and is indicated by a vertical line. The x-axis is rescaled so that I-N transition takes place at $[fd]_N$=1. (b) The plot of the dimensionless ratio of the parallel to perpendicular diffusion constant $D_{\parallel}/D_{\perp}$ as a function of the nematic order parameter. The concentration dependence of the nematic order parameter is taken from ref. [14]. Open triangles are data for hard spherocylinders with aspect ratio of 10 taken from ref. [11] while open circles are data for ellipsoids with aspect ratio 10 taken from [9].

smectic phase at high concentrations. We made an attempt to measure the diffusion of rods in the smectic phase, but have not seen any appreciable diffusion on optical length scales over a time period of minutes. The most strinking feature of our data is a strong discontinuity in the behavior of the diffusion constant at the I-N phase transition. Compared to diffusions in isotropic case D_{iso}, $D_{\|}$ is larger by a factor of four, while $D_{\perp}$ is smaller by a factor of two. The concentration dependence of $D_{\|}$ and $D_{\perp}$ exhibit different behavior. With increasing concentration, for $D_{\|}$ we measure an initial plateau, which is followed by a broad region where the diffusion rate decreases monotonically. $D_{\perp}$, however, shows a monotonic decrease of the diffusion constant over the whole concentration range where nematic phase is stable.

It is useful to compare our results to previous theoretical and experimental work, especially the measurements of the diffusion coefficient for silica-coated boehmite rods [8]. In this work the authors measure $D_{\|}/D_{\perp} \approx 2$ for monodomain nematic samples which are in coexistence with the isotropic phase. This is significantly different from $D_{\|}/D_{\perp} \approx 7.5$ for fd virus. Another significant difference is that results on boehmite indicate that both $D_{\|}$ and $D_{\perp}$ are smaller than D_{iso}, in contrast to our measurements, where $D_{\|}$ is much larger and $D_{\perp}$ is much smaller than D_{iso}.

When comparing our data to simulations of the diffusion of hard spherocylinders and ellipsoids [9, 11], one needs to compare equivalent samples. Scaling to rod concentration where the I-N transition takes place would be erroneous, since fd virus is a semi-flexible rod. The semi-flexibility of the virus drives the isotropic-nematic phase transition to higher concentrations and it significantly decreases the order parameter of the nematic phase in coexistence with the isotropic phase [13, 14]. We choose to compare data and simulations at the same value of the nematic order parameter which is determined independently [14]. For fd, the nematic order parameter is 0.65 at the I-N coexistence, it monotonically increases with increasing rod concentration and saturates at high rod concentration. Experiment and simulation qualitatively agree and both show a rapid increase of $D_{\|}/D_{\perp}$ ratio with increasing nematic order parameter (fig. 4b). We note that there is a discrepancy between the simulations results obtained in refs. [9, 11] which might be due to different systems studied in these two papers.

Interestingly, simulations predict that upon increasing rod concentration beyond I-N coexistence $D_{\|}$ initially increases and subsequently upon approaching the smectic phase decreases. The author argues that the non-monotonic behavior of $D_{\|}$ is the result of the interplay between two effects. First, with increasing rod concentration the nematic order parameter increases which enhances $D_{\|}$. Second, with increasing rod concentration there is less free volume which leads to decrease of $D_{\|}$. The author further argues that the first effect dominates at low rod concentrations where the nematic order parameter rapidly increases while the second effect dominates at high rod concentrations where the nematic order parameter is almost saturated. In contrast, both of these effects contribute to a monotonic decrease in $D_{\perp}$ with increasing concentration, which is observed in simulations. Due to relatively large error in our experimental data, it is not clear if the behavior of $D_{\|}$ is non-monotonic. There is an initial hesitation, but $D_{\|}$ decreases over most of the concentration range. This difference between simulations and experiment might be because we compare experiments of semi-flexible fd to simulations of perfectly rigid rods. Compared to semi-flexible rods, the order parameter of rigid rods increases much faster with increasing rod concentration [14].

It would be of interest to extend our measurements to rotational diffusion in the isotropic and nematic phase. At present the rod undergoes significant rotational diffusion during each exposure which reduces resolution and prevents accurate determination of the instantaneous orientation of a rod. It might be possible to significantly reduce the exposure time by either using a more sensitive CCD camera or a more intense laser as an illumination source.

Conclusions. – Using fluorescence microscopy we have visualized rod-like viruses and measured the anisotropic long-time self-diffusion coefficients in the isotropic and nematic phase. In the nematic phase the diffusion along the director and the diffusion perpendicular to the director decrease monotonically with increasing rod concentration. The ratio of parallel to perpendicular diffusion increases monotonically with increasing rod concentration. The results compare qualitatively with simulations on hard rods with moderate aspect ratios.

Note added in proofs. – Our experiments coupled with recent observations of sub-diffusive behavior of ellipsoidal particles in a nematic fd illustrate that much remains to be understood about the dynamics of colloidal liquid crystals [22].

* * *

PL is supported in part by Transregio SFB TR6, "Physics of colloidal dispersions in external fields". ZD is supported by a Junior Fellowship from Rowland Institute at Harvard.

REFERENCES

[1] Perkins T. T., Smith D. E. and Chu S., *Science*, **264** (1994) 819.
[2] Smith D. E., Perkins T. T. and Chu S., *Phys. Rev. Lett.*, **75** (1995) 4146.
[3] Kas J. *et al.*, *Biophys. J.*, **70** (1996) 609.
[4] Haber C., Ruiz S. A. and Wirtz D., *Proc. Natl. Acad. Sci. U.S.A.*, **97** (2000) 10792.
[5] Onsager L., *Ann. N.Y. Acad. Sci.*, **51** (1949) 627.
[6] Khokhlov A. R. and Semenov A. N., *Physica A*, **108** (1981) 546.
[7] Dogic Z. *et al.*, *Phys. Rev. Lett.*, **92** (2004) 125503.
[8] Van Bruggen M. P. B. *et al.*, *Phys. Rev. E*, **58** (1998) 7668.
[9] Allen M. P., *Phys. Rev. Lett.*, **65** (1990) 2881.
[10] Hess S., Frenkel D. and Allen M. P., *Mol. Phys.*, **74** (1991) 765.
[11] Lowen H., *Phys. Rev. E*, **59** (1989) 1999.
[12] Kruger G. J., *Phys. Rep.*, **82** (1982) 230.
[13] Tang J. and Fraden S., *Liq. Cryst.*, **19** (1995) 459.
[14] Purdy K. R. *et al.*, *Phys. Rev. E*, **67** (2003) 031708.
[15] Cush R. C. and Russo P. S., *Macromolecules*, **35** (2002) 8659.
[16] Dogic Z. and Fraden S., *Philos. Trans. R. Soc. London, Ser. A*, **359** (2001) 997.
[17] Dogic Z. and Fraden S., *Phys. Rev. Lett.*, **78** (1997) 2417.
[18] Dogic Z. and Fraden S., *Langmuir*, **16** (2000) 7820.
[19] Maniatis T., Sambrook J. and Fritsch E. F. E., *Molecular Cloning* (Cold Spring Harbor University Press) 1989.
[20] The code used for tracking particles is available online at the following address: `http://www.physics.emory.edu/~weeks/idl/`.
[21] Addas K. M., Schmidt C. F. and Tang J. X., *Phys. Rev. E*, **70** (2004) 021503.
[22] Islam M/ F. and Yodh A. G., in preparation.

Chapter 3

Hydrodynamic interactions in dense rod suspensions

Hydrodynamic interactions in rod suspensions with orientational ordering

M. P. Lettinga,*[a] J. K. G. Dhont,[a] Z. Zhang,[a] S. Messlinger[b] and G. Gompper*[b]

Received 9th March 2010, Accepted 24th May 2010
DOI: 10.1039/c0sm00081g

The effect of hydrodynamic interactions on the diffusion of rods in the nematic phase is studied, both experimentally by time-resolved fluorescence video microscopy and theoretically by mesoscale-hydrodynamics simulations. The aspect ratio of the rods and the relative importance of hydrodynamic interactions—compared to direct interactions—are varied independently. This is achieved in experiments by using charged rod-like viruses (*fd*-virus) with varying ionic strength, both for the wild-type virus and viruses coated with a brush of polymers. In computer simulations, hydrodynamic interactions are incorporated by a particle-based mesoscopic simulation technique. It is found that translational long-time diffusion coefficients for parallel motion along the nematic director, scaled with the diffusion coefficient at infinite dilution, are significantly affected by hydrodynamic interactions, but are insensitive to the aspect ratio. In contrast, the diffusion anisotropy—defined as the ratio of the diffusion coefficients parallel and perpendicular to the nematic director—shows only a weak dependence on hydrodynamic interactions, but strongly varies with the aspect ratio.

1 Introduction

The diffusion of colloidal particles in complex environments is of interest for a large variety of soft-matter and biological systems. Diffusion in concentrated suspensions of spheres has been extensively studied, and is known to be strongly affected both by direct and hydrodynamic interactions (see, for example, ref. 1). Likewise, diffusive transport within cells is strongly affected by the densely packed environment. Here, the environment is a complicated mixture of many macro-molecular components, part of which is a network formed by microtubules and F-actin. Diffusion of spherical macromolecules through similar isotropic networks of very long and thin biopolymers has been studied in detail.[2–6] However, only a few experimental studies have been devoted to diffusion of spherical colloids through nematically ordered networks,[7–9] despite the fact that orientationally-ordered structures are found in abundance in nature.[10] Even less is known about the diffusion of rod-like colloids in concentrated suspensions. Experiments on thermotropic[11,12] and lyotropic systems[13–16] as well as computer simulations[17–19] show that in the nematic phase, diffusion along the director can be orders of magnitudes faster than diffusion in the perpendicular direction.

For diffusion of relatively small spheres through rod networks, hydrodynamic interactions (HI) are essential.[7] However, there is so far little understanding of the role played by hydrodynamic interactions for the diffusion of rods in rod networks, both in the isotropic and nematic phases. In particular, the importance of hydrodynamic interactions—in comparison with direct interactions—for the diffusive properties of rods in the nematic phase parallel and perpendicular to the director is not known.

The understanding of the diffusion in dispersions of sterically interacting rods in the semi-dilute regime has greatly profited from the tube model of Doi.[20,21] With the work of Fixman,[22] Edwards and Evans[23] and Teraoka and Hayakawa,[24,25] the validity of the Doi theory has been extended to apply over a large concentration range. These theories have been verified on a qualitative level in ref. 26 experimentally and in ref. 27–29 by simulations. Possible deviations from experimental results might be related to the neglect of HI in both theory and simulation. Hydrodynamic interactions have been described in terms of hydrodynamic screening, due to entanglement of the long and thin rods in the network.[5,7,30,31] These descriptions, however, do not explain the role of hydrodynamics for diffusion of rods in the isotropic or in the nematic phase. In simulations, an early attempt has been made to incorporate HI by transferring the hydrodynamically-caused diffusion anisotropy at infinite dilution (as derived in ref. 32,33) to dense rod systems by an anisotropic step size in Brownian-dynamics simulations. This, however, neglects HI with neighboring rods.[19] Recently, HI have been included through the explicit incorporation of the solvent on a coarse-grained level.[34–36] Thus, quantitative predictions based on a theory that includes both direct and hydrodynamic interactions are not available for the diffusion of rods in both the isotropic and nematic phases.

The goal of this paper is to assess the importance of HI in dense suspensions of colloidal rods, focusing on the nematic phase. Both experiments and simulations are performed. The relative importance of direct interactions and HI is varied in experiments by varying the range of electrostatic interactions and grafting the rods with a hydrodynamically impenetrable polymer brush. In the simulations, HI can be incorporated by embedding the rods in a particle-based mesoscopic solvent; in this approach, HI can be switched off by employing a collision rules corresponding to molecular chaos. We demonstrate that the dynamics in the isotropic phase is governed by steric interactions, and that HI cause a slowing down of the diffusion by at most 30%. In the nematic phase, HI are enhanced because they take place over the

---

[a] *Soft Condensed Matter Group, Institut für Festkörperforschung, Forschungszentrum Jülich, Jülich, Germany. E-mail: m.p.lettinga@fz-juelich.de*
[b] *Theoretical Soft-Matter and Biophysics Group, Institut für Festkörperforschung, Forschungszentrum Jülich, Jülich, Germany. E-mail: g.gompper@fz-juelich.de*

full length of the aligned rods, which is a situation not considered in ref. 34,36. As a result HI causes a slowing down of the diffusion by up to a factor of two.

2 Variation of hydrodynamic and direct interactions

The relative importance of hydrodynamic interactions (HI) and direct interactions can be tuned in the experiments by varying the range of direct interactions, either by variation of salt concentration that affects the range of electrostatic interactions between the charged rods, or by coating the rods with polymers. In order to quantify the variation of the interaction parameters, the effective diameter d_{eff} and the hydrodynamic diameter d_{hyd} are introduced. Here, the effective diameter d_{eff} characterizes the range of direct interactions, and is defined by the distance between parallel, repulsive rods at which the interaction potential equals k_BT. The hydrodynamic rod diameter d_{hyd} is the diameter of a virtual hard rod with no-slip boundary conditions, which shows the same hydrodynamic properties. For example, in the case of a particle with a dense polymer brush, the solvent is caught in the polymer mesh of the brush and does not contribute to hydrodynamic interactions, as described in ref. 38. Thus d_{hyd} is determined by the steric polymer-brush thickness.

In the case where $d_{eff} \gg d_{hyd}$, the average distance between rods is large as a result of the long-ranged repulsive interactions, so that hydrodynamic interactions are relatively weak. The maximum relative contribution of hydrodynamic interactions is realized for $d_{eff} = d_{hyd}$, which is the case for hard-core interactions.

In simulations it is a relatively simple matter to vary both radii independently. The hydrodynamic interactions can be switched on or off. Direct interactions are determined by the length parameter of a repulsive Lennard-Jones interaction. In fact, even the unphysical case $d_{eff} < d_{hyd}$ can be realized in simulations. We consider three cases that are depicted in Fig. 1a: rods without HI (*i.e.* no explicit solvent), rods with $d_{eff} = 2\ d_{hyd}$, and rods with $d_{eff} = d_{hyd}$. The importance of HI thus increases from top to bottom in Fig. 1a.

For experiments, a systematic variation of d_{eff} relative to d_{hyd} is less straightforward. We vary the salt concentration and coat the rods with polymer brushes to change both radii.[39] Variation of salt concentration affects the range of electrostatic interactions, but leaves the hydrodynamic radius essentially unchanged. Grafting the rod surface with a hydrodynamically impenetrable polymer brush affects both radii. A few typical choices are depicted in Fig. 1b. Without a polymer brush, d_{hyd} equals the hard core radius of the rod, while d_{eff} is large due to a low salt concentration. The case $d_{eff} = d_{hyd}$ can be achieved using a combination of salt and a polymer brush. We can thus tune two parameters independently: the effective aspect ratio of the rod $p_{eff} = L/d_{eff}$ (where L is the length of the rods), and the HI–size ratio

$$\alpha = \frac{d_{eff} - d_{hyd}}{d_{hyd}} \qquad (1)$$

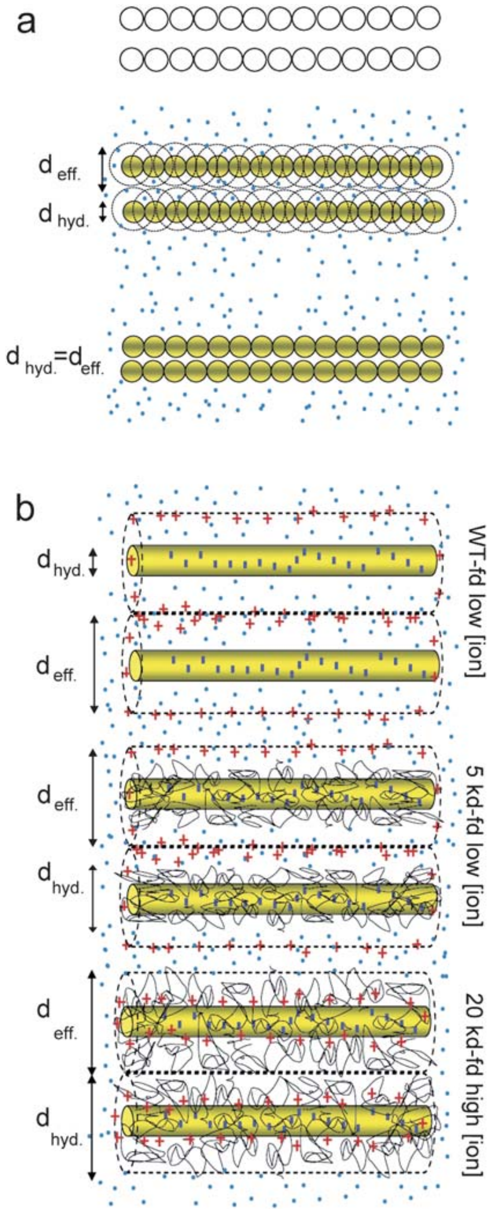

Fig. 1 Schematic representation of the tuning of hydrodynamic and direct interactions. (a) In simulations solvent particles are considered explicitly (middle and bottom) or left out (top). Long-range, repulsive direct interactions are mimicked by Lennard-Jones spheres with a diameter of $d_{eff} = 2d_{hyd}$, which are permeable for the solvent but not for other rods (middle). (b) Experimentally d_{eff} is determined by the ionic strength (top and middle) or the size of the coating polymers (bottom), while d_{hyd} is determined by the steric surface.

The effective aspect ratio affects the concentration where the isotropic–nematic phase transition occurs.[40] Rods with different lengths of coating polymers, see Fig. 1b, therefore have different orientational order parameters at the same effective volume fraction, which has to be taken into account when we want to assess the role of HI. The HI–size ratio characterizes the difference between d_{eff} and d_{hyd}. For large α, HI are relatively unimportant. Formally, no HI corresponds to an infinite value of α, since $d_{hyd} = 0$. The larger α is, the more solvent is contained within the region between two parallel rods at a distance where the direct-interaction energy equals k_BT.

The effect of HI is measured by the rate at which the rods diffuse. Translational diffusion coefficients can be determined from the slope of the mean square displacement (MSD) *versus* time. Since the interactions have a different influence on diffusion parallel and perpendicular to the long axis of the rods, we distinguish between displacements parallel, $\vec{r}_{\|}$, and perpendicular, $\vec{r}_{\perp}$, to the rod axis. The corresponding diffusion coefficients $D_{\|}$ and $D_{\perp}$ are defined as

$$\Delta\vec{r}_{\|}{}^{2}(t) = \langle|\vec{r}_{\|}(t) - \vec{r}_{\|}(0)|^2\rangle = 2D_{\|}\ t \tag{2}$$

$$\Delta\vec{r}_{\perp}{}^{2}(t) = \langle|\vec{r}_{\perp}(t) - \vec{r}_{\perp}(0)|^2\rangle = 4D_{\perp}\ t \tag{3}$$

where $\langle\ldots\rangle$ is an ensemble average over all rods. The total MSD, irrespective of orientation, defines the total diffusion coefficient D_{tot} as

$$\mathrm{MSD} = \langle|\vec{r}_{tot}(t) - \vec{r}_{tot}(0)|^2\rangle = \mathrm{D}_{tot}t = 2D_{\|}t + 4D_{\perp}t \tag{4}$$

The MSD is determined by fluorescence video microscopy, as will be discussed in more detail in Sec. 4 below. The above definitions of $D_{\|,\perp}$ can be used at infinite dilution to distinguish between diffusion parallel and perpendicular to the long axis of a rod. In the nematic phase, however, $D_{\|,\perp}$ are usually defined as the diffusion coefficient parallel and perpendicular to the nematic director, instead of the long axis of a rod. For the quite high degrees of alignment in the nematic phase, however, the difference between the two definitions of $D_{\|,\perp}$ is probably quite small.

3 Theoretical model and simulation technique

In the simulations, HI are implemented by employing a particle-based mesoscale simulation technique called multi-particle collision dynamics (MPC).[41] This method provides all hydrodynamic and thermodynamic properties of the fluid that are essential for rod dynamics.[42,43]

N_{rod} rods of length L and diameter d are modeled by a linear string of n monomer beads of mass M. The monomers are connected by a harmonic spring potential

$$U_{bond}(\mathbf{r}) = \frac{k}{2}(|\mathbf{r}| - l)^2 \tag{5}$$

with spring constant k, which controls the bond length l, so that $L = (n - 1)l$. A bending potential U_{bend}, with bending rigidity κ, ensures semi-flexibility of rods. The excluded-volume interaction between all monomers is modeled *via* a repulsive, shifted and truncated 6–12 Lennard-Jones potential, which is characterized by a diameter $\sigma = d$ and an energy scale ε. With these potentials, Newtonian equations of motion are solved by the velocity Verlet algorithm with a time step h_V.

The dynamics of the solvent particles of mass m of the MPC fluid proceeds in alternating streaming and collision steps, with time step h. In the streaming step, fluid particles move ballistically. For the collisions, particles are sorted into the cells of a cubic lattice with lattice constant a. All particles in a collision box exchange momentum by a rotation of their velocities relative to the center-of-mass velocity by an angle α. The coupling of the monomer beads with the fluid occurs in the collision steps of the MPC algorithm. To describe low-Reynolds-number fluids, the time step h has to be chosen small enough for the mean path $\ell = h\sqrt{k_BT/m}$ to be much smaller than the cell size a.[44] The parameters used in our simulations for the fluid are $h = 0.1\sqrt{ma^2/k_BT}$, $\alpha = 130°$, and number density $\rho = 10\ a^{-3}$. With these parameters, the fluid viscosity is obtained[45] to be $\eta = 8.21\sqrt{mk_BT}/a^2$. For the rods, we choose bond length $l = a$, $M = 10\,m$, and $h_V/h = 0.05$. Note that $h_V \ll h$ is typically required to resolve the motion of the monomers as determined by the strong direct interactions with the other monomers. For the stiffness of a rod we require that the end-to-end distance of a single rod in thermal equilibrium is 98% of its contour length. This determines the bending rigidity κ for a given aspect ratio L/d uniquely. In addition, we set $k = 4\kappa/l^2$.

The hydrodynamic diameter d_{hyd} of rods in a MPC fluid has been determined in ref. 46 by fixing a rod[47] at the center of the simulation box and exposing it to a constant flow, with streaming direction both perpendicular and parallel to the rod orientation. In the limit of a large box size, the friction coefficients $\xi_{\perp}$ and $\xi_{\|}$ were then fitted simultaneously to the theoretical expressions[32]

$$\xi_{\|} = 2\pi\eta L\left[\ln\frac{L}{d_{hyd}} - 0.207 + 0.980\ \frac{d_{hyd}}{L}\right]^{-1} \tag{6}$$

$$\xi_{\perp} = 4\pi\eta L\left[\ln\frac{L}{d_{hyd}} + 0.839 + 0.185\ \frac{d_{hyd}}{L}\right]^{-1} \tag{7}$$

which are very similar to the more precise calculations of Cichocki *et al.*,[33] by varying d_{hyd}. The hydrodynamic diameter was obtained to be $d_{hyd} \simeq 0.9a$.

The steric diameter d_{eff} of the rods is determined in the simulations by the parameter σ of the Lennard-Jones potential. We employ two values, $d_{eff} \equiv \sqrt[6]{2}\,\sigma = l$ (touching spheres) and $d_{eff} = 2l$ (overlapping spheres), see Fig. 1a. In addition, we choose $\varepsilon = 10k_BT$ to describe strong repulsion.

In order to demonstrate that HI is correctly captured by our simulation method, we simulated diffusion coefficients of single non-interacting rods with different aspect ratios. The diffusion coefficient of a single rod is sensitive to HI between "beads" within the rod. The leading order contribution to the friction coefficient in an expansion with respect to the aspect ratio, is in fact fully determined by HI. Simulated diffusion coefficients, orientationally averaged D_{iso} as well as parallel $D_{\|}$ and perpendicular $D_{\perp}$ to the long axis of the rod, are plotted in Fig. 2 as a function of the aspect ratio. The simulated values are compared to theoretical predictions

$$D_{\|} = \frac{k_BT}{\xi_{\|}};\ D_{\perp} = \frac{k_BT}{\xi_{\perp}} \tag{8}$$

with $\xi_{\|}$ and $\xi_{\perp}$ given by eqn (6) and (7), respectively. We find a very good correspondence between simulations and theory, with a hydrodynamic diameter $d_{hyd} \simeq a$. This is in good agreement with the calculation of friction coefficients in ref. 46 and of the total diffusion constants in ref. 48, and confirms that indeed HI are correctly accounted for in our simulations.

Hydrodynamic interactions can be switched off in the simulations by a small modification of the collision rule.[37,38] In this

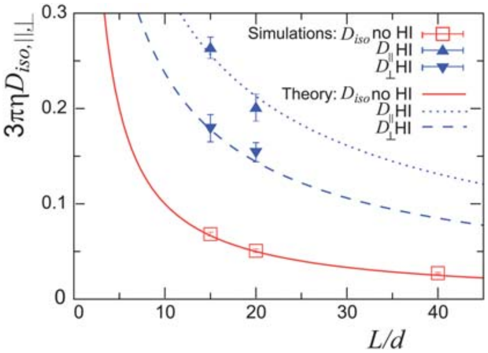

Fig. 2 Simulation data and theoretical values for diffusion constants of single rods with $d_{hyd} = a$. Dashed and dotted lines indicate theoretical predictions (8). The full line is given by $D_0 = k_BT/(3\pi\eta L)$. Simulation data are obtained from independent runs.

case, denoted Brownian-MPC, the momentum of all fluid particles in a collision box is selected from a Maxwell–Boltzmann distribution with temperature T;[38] this destroys all hydrodynamic correlations. However, thermodynamic properties as well as monomer friction coefficients are essentially the same as for the full MPC simulations.[38] The effect of hydrodynamic interactions on rod diffusion can thus be assessed by comparing simulation results for both solvents.

To generate an equilibrium initial configuration of the isotropic or nematic phase, we first prepare a system of straight rods with random positions (unless there is overlap), and random orientations for isotropic systems (*i.e.* $S \approx 0$) or unidirectional orientations for nematic systems (*i.e.* $S = 1$). In order to avoid finite-size effects, the linear dimensions of the simulation box in the isotropic phase is taken larger than twice the rod length. For nematic systems, we make use of the anisotropy and set the box lengths in the two dimensions perpendicular to the nematic director to just one rod length. Then we let the dynamics evolve using the Brownian-MPC solvent until the system reaches equilibrium as the potential energy and the nematic order parameter S approach stationary values. A configuration of the end of the equilibration run is used to initialize the simulation of rod diffusion. During the simulation, configurations are recorded periodically.

4 Experimental details

For the production of polymer-coated rods, we follow ref. 39 by using *fd* viruses[53] which are intrinsically mono-disperse, very thin ($L = 880$ nm, $d_{hyd} = 6.6$ nm) and stiff (persistence length $P = 3.0$ µm) rods. These wild-type viruses (WT-*fd*) are coated with the water soluble and neutral polymer poly-ethylene oxide (PEO) from Nektar with molecular masses of 5 and 20 kDa. These two systems of coated *fd*-viruses will be referred to as 5kd-*fd* and 20kd-*fd*, respectively. Dispersions are prepared at ionic strengths between 4 and 20 mM. The effective diameter of the rods is determined for the different systems from the lower spinodal concentration where the I–N transition takes place, which is according to Onsager[40] at $\varphi L/d_{eff} = 4$. We thus find that at an ionic strength of 20 mM $d_{eff} = 14$ nm for 5kd-*fd*, and $d_{eff} = 37$ nm for 20kd-*fd*. A cartoon of the systems with the different d_{eff} and d_{hyd} is shown in Fig. 1b. Fluorescence correlation spectroscopy experiments on the different virus derivatives in combination with eqn (6), (7) and (8) show that d_{hyd} to a good approximation is equal to the steric diameter of the virus[55].

To determine the self-diffusion coefficient, we rely on fluorescence video microscopy, as has been successfully used earlier.[15,49] To follow single rods in time, about one *fd* out of 10^4 has been labeled with the dye Alexa-488 (Invitrogen), with around 200 labeled particles in the field of view. Fluorescence microscopy was performed on a Axiovert Zeiss microscope using a Hamamatsu C9100 Electron Multiplying Charge Coupling Device operated by Metamorph software. We operated at frame rates of up to 50 frames per second taking 1000 frames per stack. Data were analyzed with an adapted version of free-ware particle tracking software,[54] allowing for the determination of the rod orientation.

5 Results

The mean square displacement (MSD) as a function of time just in the nematic region close to the I–N transition, are plotted in Fig. 3. The MSD along and perpendicular to the nematic director is considered.[15] In order to compare the experimental and simulated curves, the MSD is scaled by the rod length L, and the time is scaled by the time t_L it takes the rod to diffuse one rod length in the parallel direction. The first observation is the large

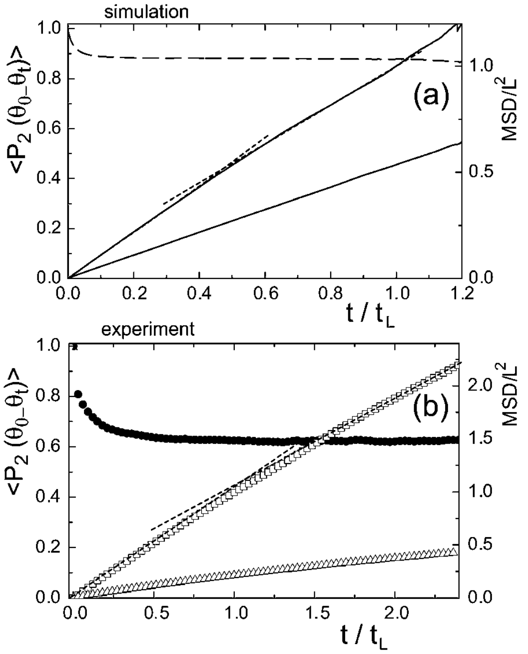

Fig. 3 The MSD scaled by the rod length and the time t_L where $MSD = L^2$ and $\langle P_2(\theta_0 - \theta_t)\rangle$ as a function of time. (a) Simulations, where the dashed line depicts the orientational diffusion. Also shown are the fits in two time windows of the parallel diffusion. (b) Experiments with diffusion parallel (□) and perpendicular (△) to the director. The solid symbols depict the measured rotational diffusion. The concentration was [5kd-*fd*] = 15 mg/ml and $t_L = 660$ ms.

ratio $D_{\|}/D_{\perp}$, which is consistent with earlier experimental results,[15] but is now also confirmed by simulations. We will come back to this point later.

Both experiment and simulations show that the slopes of the MSD *versus* time are not constant. Thus a distinction can be made between short- and long-time *translational* diffusion, similar to the dynamics of spherical colloids (see, *e.g.*, ref. 50). For spherical colloids, short-time diffusion relates to translational motion within a "static cage" formed by neighbouring spheres; for these small times, only hydrodynamic interactions play a role, direct interactions with the neighbouring spheres are not relevant. There is a transition to long-time diffusion when the tracer sphere diffused over distances comparable to the cage size. At this time scale, the dynamics of the tracer sphere is also affected by the direct interactions with the neighbouring spheres.

For rod-like colloids, a similar distinction can be made for both translational and rotational diffusion. As can be seen from Fig. 3, the transition from short- to long-time *translational* diffusion occurs when the tracer rod diffused over a distance of the order of its own length. A similar interpretation can be given for the short- and long-time *orientational* diffusion of rods. In the nematic phase, the "cage" consists of neighbouring rods that constrain the orientational motion of the tracer rod. The strength of the orientational constraint is characterized by the order parameter $\langle P_2 \rangle$, where $P_2 = ½(3\cos^2\theta - 1)$ is the second-order Legendre polynomial, and θ is the angle between the long axis of the rod and the director $\hat{n}$. For short times, a tracer rod displays an orientational diffusion within the cage, which is only affected by HI. For longer times, the tracer rod experiences direct interactions with the neighbouring rods that affects the orientational dynamics. In order to quantitatively distinguish short- and long-time dynamics, we introduce the orientational correlation function

$$<P_2(\Theta_0 - \Theta_t)> \\ = \int_0^{\pi} d\cos\Theta_0 \int_0^{\pi} d\cos\Theta P_2(\Theta_0 - \Theta)\; P(\Theta_0)\; P(\Theta, t|\Theta_0)\;, \tag{9}$$

where $P(\Theta_0)$ is the probability density function of the angle Θ_0 of the long axis of the tracer rod with the nematic director at time $t = 0$, and $P(\Theta, t \mid \Theta_0)$ is the conditional probability density function that the tracer rod has an angle Θ with the nematic director at time t, given that the angle was Θ_0 at $t = 0$. This correlation function is unity at $t = 0$, and relaxes in the long-time limit to $\langle P_2 \rangle^2$. As can be seen from Fig. 3, both the simulations and the experiments reveal that the rotational long-time limit is reached earlier than the translational long-time limit. The limited time-resolution of the experimental set up does not allow a detailed analysis of the effect of HI on the rotational diffusion, so that in the following we will focus on the long-time diffusion. In contrast to the short-time measurements, this regime is more easily accessible experimentally, but requires a substantial computational effort, especially for high aspect ratios.

The concentration dependence of both components of the translational long-time diffusion and the total long-time diffusion coefficients is shown in Fig. 4 for various aspect ratios p_{eff} and HI–size ratios α. The data are scaled by the orientationally averaged diffusion at infinite dilution, thus taking out the effect of HI on the single particle level. Fig. 4a,b shows results for $D_{\|,\perp}$ from simulations and experiments, respectively, while Fig. 4c shows simulation and experimental results for D_{iso}.

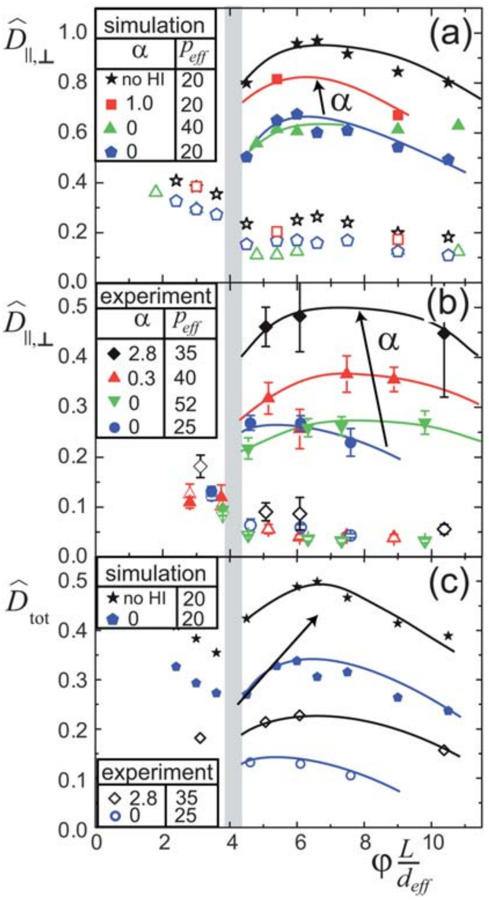

Fig. 4 Parallel (solid symbols) and perpendicular (open symbols) diffusion constants, scaled by the diffusion of the rods at infinite dilution, for (a) simulations and (b) experiments for various aspect ratios p_{eff} and HI ratios α, as indicated. (c) The total diffusion of a few selected experiments (open symbols) and simulations (solid symbols). The arrow here indicates the increase in the mobility of the rods. The gray bar indicates the phase transition concentration.

The vertical grey bars in Fig. 4a–c indicate the two-phase isotropic–nematic region. First, note that the diffusion coefficients in the isotropic phase just below the two-phase coexistence are larger than $D_{\perp}$ and smaller than $D_{\|}$ in the nematic phase just above the two-phase coexistence. This has been observed before,[15] and is also observed for diffusion of spherical colloids in a nematic liquid crystal.[7,51] The larger value of the total, orientationally averaged diffusion coefficient D_{iso} in Fig. 4c just inside the nematic phase as compared to the isotropic phase reflects the increase in free volume at the isotropic-to-nematic transition, in accordance with Onsager's theory.[40] Second, we find a maximum in $D_{\|}$ and D_{iso} as a function of concentration in the nematic phase. The non-monotonic concentration dependence within the nematic phase is found both with and without HI, and is in accordance with a similar observation in simulations by Löwen.[19]

The reason for the non-monotonic concentration dependence is that the orientational order parameter increases at low concentration rapidly, leading to an increase of diffusion coefficients, while at higher concentrations, where the order parameter is nearly constant, the increasing hindrance through direct interactions leads to a decrease of diffusion rates.[19] The increase of the diffusion rate in the nematic phase at low concentrations, and the larger total diffusion coefficient just inside the nematic phase as compared to the isotropic phase, reflects the increase of translational entropy due to an increase of the nematic ordering. The differences in the scaled diffusion rates between experiment and simulations can be related to the flexibility of the rods (see ref. 18, where it was found that the diffusion rate decreases significantly with increasing flexibility). This complies with the fact that the relative persistence length of the simulations rods were longer than the relative persistence length of the *fd* virus.

Both the simulation and experimental results in Fig. 4a,b show that the aspect ratio affects the absolute parallel diffusion rate only weakly; the curves for $\alpha = 0$ but different aspect ratios display almost the same diffusion rates. The diffusion coefficients do, however, strongly depend on α, which shows that interparticle HI has a considerable effect on the diffusive properties of the rods. The simulation results in Fig. 4a, where the diffusion of rods with and without HI is compared for aspect ratio $p_{eff} = 20$, show that the scaled parallel diffusion coefficient $\hat{D}_{\parallel}$ increases by almost a factor 2 when α increases from 0 to ∞ (no HI). The same trend is seen in the experimental results in Fig. 4b, where there is a considerable increase in $\hat{D}_{\parallel}$ with increasing HI–size ratio from $\alpha = 0.3$ to $\alpha = 2.8$ for a small difference in the effective aspect ratio ($p_{eff} = 35$ and $p_{eff} = 40$). The curve of $\hat{D}_{\parallel}$ with strong HI (small α) lies below the curve of $\hat{D}_{\parallel}$ with weak HI (large α). It is striking to see that without HI (Fig. 4a), the scaled parallel diffusion coefficient reaches unity in the nematic phase for $\varphi L/d_{eff} \simeq 6.5$. This implies that diffusion is almost free, and interactions with the neighboring particles have a very small effect.

Although the aspect ratio has a negligibly small effect on the value of the scaled parallel diffusion coefficient, it has a pronounced effect on the anisotropy of diffusion, as quantified by the ratio $D_{\parallel}/D_{\perp}$. The anisotropy in the diffusion increases with increasing p_{eff}, as shown in Fig. 5a for both experiments and simulations. In contrast to the absolute values of scaled diffusion coefficients, the diffusion anisotropy is only weakly affected by the HI ratio α: curves with the same (or similar) aspect ratios are close together for different values of α. The anisotropy in diffusion is thus essentially determined by direct interactions, and HI is unimportant. One effect of increasing the aspect ratio is that the orientational order increases. To assess the role of orientational order, we plot the diffusion anisotropy in Fig. 5b as a function of the orientational order parameter $< P_2 >$. If the concentration dependence of the orientational order parameter is at the origin of the differences observed in Fig. 5a for the different aspect ratios, then the data of Fig. 5a for different aspect ratios should fall on the same master curve when plotted as a function of the order parameter. Comparing, for example, the experimental curves in Fig. 5b for $\alpha = 0$ with $p_{eff} = 25$ and $p_{eff} = 52$, clearly shows that the diffusion anisotropy increases with increasing aspect ratio. Therefore, differences in order parameter alone do not explain the observed differences in the diffusion anisotropy.

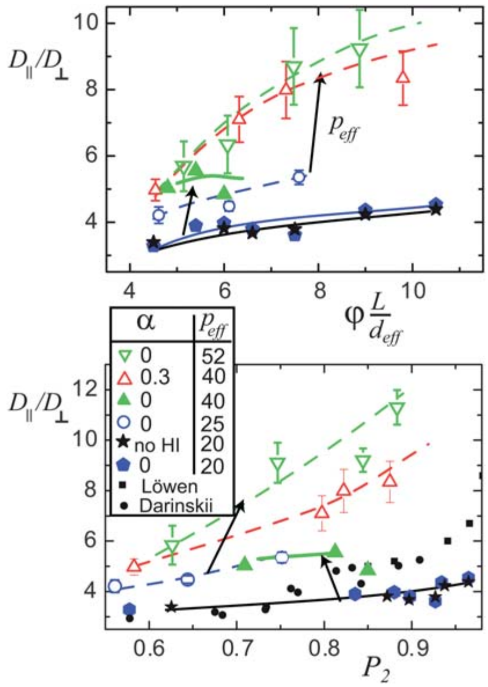

Fig. 5 The ratio of the diffusion coefficient parallel and perpendicular to the director as a function of (a) the dimensionless concentration and (b) the averaged orientational order parameter. The open and closed symbols indicate experimental and simulation results, respectively. In (b), the simulation results of Löwen[19] (■, $p_{eff} = 16$) and Darinskii *et al.*[18] (●, $p_{eff} = 8$) are also shown.

In Fig. 5b, we also include data from earlier simulations by Darinskii *et al.*[18] ($p_{eff} = 8$), where HI is neglected, and Löwen[19] ($p_{eff} = 16$), where HI within a rod are taken account of by imposing anisotropic diffusion constants for a single rod according to eqn (8), but HI between rods are neglected. These data lie somewhat above our simulation data without HI, even though their aspect ratio is smaller, which is probably due to the finite flexibility of the rods in our simulations. The fact that there is an overlay of simulation data with $p_{eff} = 40$ and experimental data for with $p_{eff} = 25$ reflects the fact that the orientational order parameter at the phase transition is higher for the simulation data due to the higher bending rigidity, as discussed in ref. 18. Thus flexibility is another important variable for the diffusion of rods. For an experimental study of flexibility, the stiff mutant fd-Y21M of the *fd* virus[52] could be used.

6 Conclusion

We have studied the effect of HI on the diffusion of rods in the nematic phase, both by simulations and experiments. We have determined the diffusion coefficient as a function of the aspect ratio p_{eff}, and the HI–size ratio α which measures the importance of direct interactions relative to HI: for $\alpha = \infty$, HI are unimportant, while for $\alpha = 0$ HI are maximally important. In the nematic phase, we could detect the transition from short-time to long-time translation and orientational diffusion. Long-time translational diffusion is reached when a rod diffuses over a distance comparable to its own length. On that time-scale, rotational correlations are completely relaxed.

To study the effect of hydrodynamic interactions in the nematic phase, we focused on long-time translational diffusion coefficients, where both diffusion parallel and perpendicular to the director is probed. In our experiments, we varied the HI–size ratio α by varying the hydrodynamic diameter d_{hyd} of the core of the rods and the effective diameter d_{eff} of direct interactions independently. In the simulations, the extreme case of no HI ($\alpha = \infty$) has also been explored. It is found that, in the nematic phase, the absolute values of diffusion coefficients (scaled with the diffusion coefficient at infinite dilution) depends only weakly on the aspect ratio, but is strongly affected by HI: scaled diffusion coefficients change significantly when α is varied. Inter-particle HI can give rise to a reduction of diffusion coefficients by a factor of 2. The ratio of the diffusion coefficient parallel and perpendicular to the nematic director, which characterizes the anisotropy of diffusion, on the other hand, depends only weakly on the HI–size ratio, but varies with the aspect ratio. The diffusion anisotropy is therefore only weakly affected by HI.

7 Acknowledgments

Sebastian Messlinger acknowledges a fellowship of the International Helmholtz Research School on Biophysics and Soft Matter (IHRS BioSoft). We thank Naveen Reddy Krishna for his assistance in some of the measurements. Financial support by the German Research Foundation (DFG) within SFB TR 6 “Colloids in external fields” is gratefully acknowledged.

References

1 A. J. Banchio, J. Gapinski, A. Patkowski, W. Häußler, A. Fluerasu, S. Saccana, P. Holmqvist, G. Meier, M. P. Lettinga and G. Nägele, *Phys. Rev. Lett.*, 2006, **96**, 138303.
2 S. Mangenot, S. Keller and J. Rädler, *Biophys. J.*, 2003, **85**, 1817–1825.
3 G. Koenderink, S. Sacanna, D. Aarts and A. Philipse, *Phys. Rev. E: Stat., Nonlinear, Soft Matter Phys.*, 2004, **69**, 021804.
4 J. Biegel, C. Hundegger, B. Nadig and R. Weber, *Eur. Phys. J. B*, 1999, **10**, 525–536.
5 K. Kang, J. Gapinski, M. P. Lettinga, J. Buitenhuis, G. Meier, M. Ratajczyk, J. Dhont and A. Patkowski, *J. Chem. Phys.*, 2005, **122**, 044905.
6 I. Y. Wong, M. L. Gardel, D. R. Reichman, E. R. Weeks, M. Valentine, A. R. Bausch and D. A. Weitz, *Phys. Rev. Lett.*, 2004, **92**, 178101.
7 K. Kang, A. Wilk, A. Patkowski and J. Dhont, *J. Chem. Phys.*, 2007, **126**, 214501.
8 A. A. Verhoeff, J. van Rijssel, V. W. A. de Villeneuve and H. N. W. Lekkerkerker, *Soft Matter*, 2008, **4**, 1602–1604.
9 A. Gennerich and D. Schild, *Biophys. J.*, 2002, **83**, 510–522.
10 J. Herzfeld, *Acc. Chem. Res.*, 1996, **29**, 31–37.
11 S. V. Dvinskikh and I. Furó, *J. Chem. Phys.*, 2001, **115**, 1946–1950.
12 M. J. Kim, K. Cardwell and A. K. Khitrina, *J. Chem. Phys.*, 2004, **120**, 11327–11329.
13 M. P. B. van Bruggen, *Langmuir*, 1998, **14**, 2245–2255.
14 P. S. Russo, M. Baylis, Z. Bu, W. Stryjewski, G. Doucet, E. Temyanko and D. Tipton, *J. Chem. Phys.*, 1999, **111**, 1746–1752.
15 M. P. Lettinga, E. Barry and Z. Dogic, *Europhys. Lett.*, 2005, **71**, 692–698.
16 P. W. Oakes, J. Viamontes and J. X. Tang, *Phys. Rev. E: Stat., Nonlinear, Soft Matter Phys.*, 2007, **75**, 061902.
17 M. P. Allen, *Phys. Rev. Lett.*, 1990, **65**, 2881–2884.
18 A. A. Darinskii, A. Zarembo, N. K. Balabaev, I. M. Neelovabd and F. Sundholm, *Phys. Chem. Chem. Phys.*, 2003, **5**, 2410–2416.
19 H. Löwen, *Phys. Rev. E: Stat. Phys., Plasmas, Fluids, Relat. Interdiscip. Top.*, 1999, **59**, 1989–1995.
20 M. Doi, *J. Phys.*, 1975, **36**, 607–611.
21 M. Doi and S. F. Edwards, *The Theory of Polymer Dynamics*, Oxford, 1986.
22 M. Fixman, *Phys. Rev. Lett.*, 1985, **55**, 2429–2432.
23 S. F. Edwards and K. E. Evans, *J. Chem. Soc., Faraday Trans. 2*, 1982, **78**, 113–121.
24 I. Teraoka and R. Hayakawa, *J. Chem. Phys.*, 1989, **91**, 2643–2648.
25 I. Teraoka and R. Hayakawa, *J. Chem. Phys.*, 1988, **89**, 6989–6995.
26 R. C. Cush and P. S. Russo, *Macromolecules*, 2002, **35**, 8659–8662.
27 I. Bitsanis, H. T. Davis and M. Tirrell, *Macromolecules*, 1990, **23**, 1157–1165.
28 Y.-G. Tao, J. K. G. Dhont and W. J. Briels, *J. Chem. Phys.*, 2006, **124**, 134906.
29 P. D. Cobb and J. E. Butler, *J. Chem. Phys.*, 2005, **123**, 054908.
30 M. Muthukumar and S. F. Edwards, *Macromolecules*, 1983, **16**, 1475–1478.
31 E. S. G. Shaqfeh and G. H. Fredrickson, *Phys. Fluids A*, 1990, **2**, 7–24.
32 M. Tirado, C. Martinez and J. G. Delatorre, *J. Chem. Phys.*, 1984, **81**, 2047–2052.
33 B. Cichocki, B. U. Felderhof, K. Hinsen, E. Wajntyb and J. Blawzdziewicz, *J. Chem. Phys.*, 1994, **100**, 3780–3790.
34 V. Pryamitsyn and V. Ganesan, *J. Chem. Phys.*, 2008, **128**, 134901.
35 M. Ripoll, P. Holmqvist, R. G. Winkler, G. Gompper, J. K. G. Dhont and M. P. Lettinga, *Phys. Rev. Lett.*, 2008, **101**, 168302.
36 J. T. Padding, *J. Chem. Phys.*, 2009, **130**, 144903.
37 N. Kikuchi, A. Gent and J. M. Yeomans, *Eur. Phys. J. E*, 2002, **9**, 63–66.
38 M. Ripoll, R. G. Winkler and G. Gompper, *Eur. Phys. J. E*, 2007, **23**, 349–354.
39 E. Grelet and S. Fraden, *Phys. Rev. Lett.*, 2003, **90**, 198302.
40 L. Onsager, *Ann. N. Y. Acad. Sci.*, 1949, **51**, 627–659.
41 A. Malevanets and R. Kapral, *J. Chem. Phys.*, 1999, **110**, 8605–8613.
42 R. Kapral, *Adv. Chem. Phys.*, 2008, **140**, 89–146.
43 G. Gompper, T. Ihle, D. M. Kroll and R. G. Winkler, *Adv. Polym. Sci.*, 2009, **221**, 1–87.
44 M. Ripoll, K. Mussawisade, R. G. Winkler and G. Gompper, *Europhys. Lett.*, 2004, **68**, 106–112.
45 N. Kikuchi, C. M. Pooley, J. F. Ryder and J. M. Yeomans, *J. Chem. Phys.*, 2003, **119**, 6388–6395.
46 J. Elgeti and G. Gompper, NIC Symposium 2008, *NIC Series*, 2008, **39**, 53–61(webpage: http://www.fz-juelich.de/nic-series/volume39/gompper.pdf).
47 The rods were modelled in ref. 46 by three parallel linear strings of monomers, with triangular cross-section and distance between strings equalling the bond length l, and $l = a/2$.
48 R. G. Winkler, K. Mussawisade, M. Ripoll and G. Gompper, *J. Phys.: Condens. Matter*, 2004, **16**, S3941–S3954.
49 M. P. Lettinga and E. Grelet, *Phys. Rev. Lett.*, 2007, **99**, 197802.
50 P. N. Segré and P. N. Pusey, *Phys. Rev. Lett.*, 1996, **77**, 771–774.
51 D. R. Spiegel, A. L. Thompson and W. C. Campbell, *J. Chem. Phys.*, 2001, **114**, 3842–3847.
52 E. Barry, D. Beller and Z. Dogic, *Soft Matter*, 2009, **5**, 2563–2570.
53 *fd* was grown using the XL1-Blue strain of *E. Coli* as the host bacteria and purified following standard biological protocols. To vary the ionic strength, viruses have been dialyzed against a 4 or 20 mM TRIS-HCl buffer at pH = 8.2 with an adjusted amount of NaCl.
54 Code used for tracking particles in available online at http://www.physics.emory.edu/weeks/idl/.
55 Private communication with R. G. Winkler and M. Ratajczyk.

Chapter 4

Self-diffusion of rod-like viruses through smectic layers

PRL **99,** 197802 (2007) PHYSICAL REVIEW LETTERS week ending 9 NOVEMBER 2007

Self-Diffusion of Rodlike Viruses through Smectic Layers

M. Paul Lettinga[1] and Eric Grelet[2]

[1]*IFF, Institut Weiche Materie, Forschungszentrum Jülich, D-52425 Jülich, Germany*
[2]*Centre de Recherche Paul Pascal, CNRS-Université Bordeaux 1, 115 Avenue Schweitzer, 33600 Pessac, France*

(Received 13 June 2007; published 8 November 2007)

We report the direct visualization at the scale of *single* particles of mass transport between smectic layers, also called permeation, in a suspension of rodlike viruses. Self-diffusion takes place preferentially in the direction normal to the smectic layers, and occurs by *quasiquantized* steps of one rod length. The diffusion rate corresponds with the rate calculated from the diffusion in the nematic state with a lamellar periodic ordering potential that is obtained experimentally.

DOI: 10.1103/PhysRevLett.99.197802 PACS numbers: 61.30.−v, 82.70.Dd, 87.15.Vv

Since the pioneering work of Onsager on the entropy driven phase transition to a liquid crystalline state [1], the structure and the phase behavior of complex fluids containing anisotropic particles with hard core interactions has been a subject of considerable interest, both theoretically [2] and experimentally [3]. Understanding of the particle mobility in the different liquid crystalline phases is more recent [4]. In experiments various methods have been applied to obtain the ensemble averaged self-diffusion coefficients in thermotropic [5] and amphiphilic [6] liquid crystals, block copolymer [7] and colloidal systems [8]. Only a few studies have been done where dynamical phenomena are probed at the scale of a *single* anisotropic particle: the Brownian motion of an isolated colloidal ellipsoid in confined geometry [9] and the self-diffusion in a nematic phase formed by rodlike viruses [10] represent two recent examples. In the latter case, the diffusion parallel ($D_{\parallel}$) and perpendicular ($D_{\perp}$) to the average rod orientation (the director) has been measured, showing an increase of the ratio $D_{\parallel}/D_{\perp}$ with particle concentration. Knowledge of the dynamics at the single-particle level is fundamental for understanding the physics of mesophases with spatial order like the smectic (lamellar) phase of rodlike particles. In this mesophase the particle density is periodic in one dimension parallel to the long axis of the rods, while the interparticle correlations perpendicular to this axis are short-ranged (fluidlike order). For parallel diffusion to take place, the rods need to jump between adjacent smectic layers, overcoming an energy barrier related to the smectic order parameter [11]. This process of interlayer diffusion, or *permeation*, was first predicted by Helfrich [12]. In this Letter, we use video fluorescence microscopy to monitor the dynamics of individual labeled colloidal rods in the background of a smectic mesophase formed by identical but unlabeled rods. In this way we directly observe *permeation* of single rods in adjacent layers. As in the nematic phase, self-diffusion in a smectic phase is anisotropic: the diffusion through the smectic layers is shown here to be much faster than the diffusion within each liquidlike layer, i.e., $D_{\parallel}/D_{\perp} \gg 1$, in contrast to thermotropic systems. Moreover, since the individual rod positions within the layer are monitored, the potential barrier for permeation is straightly determined for the first time. The permeation can then be described in terms of Brownian particles diffusing in a one-dimensional periodic symmetric potential.

The system of rods used in this work consists of filamentous bacteriophages *fd*, which are semirigid polyelectrolytes with a contour length of 0.88 μm, a diameter of 6.6 nm, and a persistence length of 2.2 μm [13]. Suspensions of *fd* rods in aqueous solution form several lyotropic liquid crystalline phases, in particular, the chiral nematic (cholesteric) phase and the smectic phase [14]. The existence of a smectic phase in suspensions of hard rods is an evidence of the high monodispersity and therefore of the model system character of such filamentous viruses [15,16]. The colloidal scale of the *fd* bacteriophage facilitates the imaging of individual rods by fluorescence microscopy, as well as smectic layers by differential interference contrast (DIC) microscopy [14]. Figure 1(a) shows a sequence of images of a single region [17] where both techniques are combined. A comparison of the images shows that some rods jump between two layers while others remain within a given layer. The trajectory of one of the rods is plotted in Fig. 1(b) in the direction parallel (z) and perpendicular (x) to the director. This figure summarizes the key observation of this Letter: the diffusion throughout the smectic layers takes place in *quasiquantized* steps of one rod length; i.e., the mass transport between the layers is a discontinuous process. Moreover, it shows that the diffusion within the smectic player is extremely slow [18].

The "hopping-type" diffusion is the consequence of the underlying ordering potential of the smectic phase and the vacancies available in adjacent layers. A phenomenological expression for permeation has been derived by coupling the displacement of a segment of a smectic layer u to the compressibility modulus $\tilde{B}$ via the permeation parameter λ_b [11]:

$$\frac{\partial u}{\partial t} = \lambda_b \tilde{B} \frac{\partial^2 u}{\partial z^2}. \tag{1}$$

On a single-particle level, the fundamental solution of this

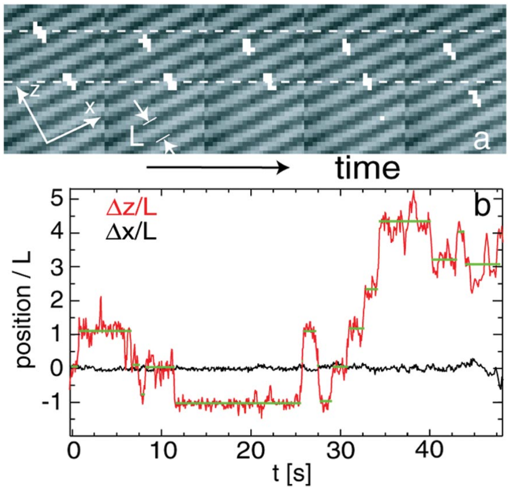

FIG. 1 (color). (a) Time sequence of an overlay of fluorescence and DIC images showing labeled particles jumping between adjacent smectic layers ($\Delta t = 0.071$ s is the time between two frames). The layer spacing is $L \simeq 0.9$ μm. (b) Displacement of a given particle in the direction parallel (red) and perpendicular (black) to the director. The green lines indicate the residence time, i.e., the time for which one particle stays in a given layer.

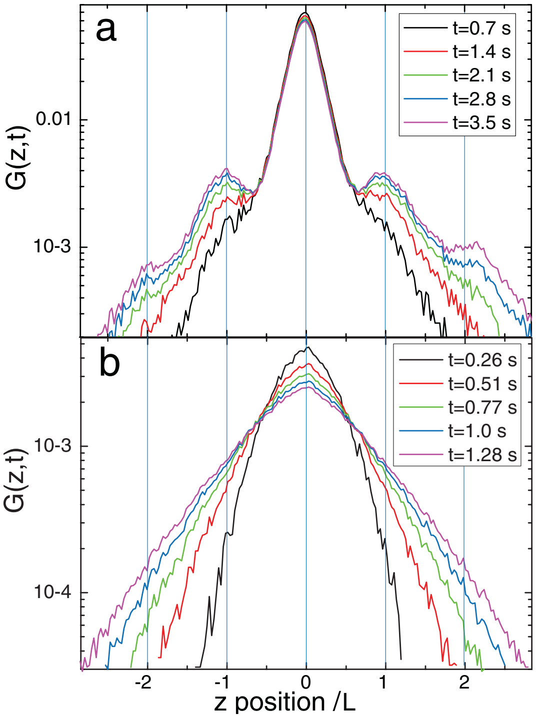

FIG. 2 (color). Probability density function in space at different times for two ionic strengths: 20 mM (a) and 110 mM (b). The functions are normalized to one, the z axis is scaled by the smectic layer thickness L.

diffusion equation is the self−van Hove function [19], which is the probability for a displacement z during a time t:

$$G(z, t) = \frac{1}{N} \sum_{i=1}^{N} \delta[z + z_i(0) - z_i(t)]. \qquad (2)$$

Since single particles are experimentally identified, the self−van Hove function can be directly obtained from the histogram of particle positions after a time t, as plotted in Fig. 2 for low ($I = 20$ mM) and high ionic ($I = 110$ mM) strengths. For a fluid made of Brownian particles, a smooth Gaussian distribution that smears out over time is expected for the self−van Hove function. However at low ionic strength, $G(z, t)$ shows distinct peaks exactly at integer multiples of the particle length [and therefore of the layer thickness, see Fig. 2(a)] as expected from visual observation (Fig. 1). At high ionic strength the curves are smoother [Fig. 2(b)], but in all cases the experimental self−van Hove function is not Gaussian at any time. This implies that the permeation parameter λ_b in Eq. (1) is a function of position z, due to the energy landscape imposed by the smectic layers.

The energy landscape can be determined experimentally from the distribution of particle positions with respect to the middle of a layer parallel to the director. To this end, time windows are selected where the particle remains for ten frames or more within the same layer. The distribution of particles within a single layer is then obtained by addition of all particle positions relative to the average position of particles for all selected time windows. The resulting distributions are plotted in Fig. 3(a) for the two ionic strengths. To obtain the total particle distribution for the full smectic phase, the distributions of particles in a single layer [Fig. 3(a)] is added periodically to itself at all integer numbers of layer spacing L [Fig. 1(a)]. The smectic ordering potential is then deduced from the Boltzmann factor $P(z) \sim e^{-U_{\text{layer}}(z)/k_BT}$ for the probability of finding a particle at position z, as shown in Fig. 3(b). Both potentials can be best fitted with a sinusoidal $U_{\text{layer}}(z) = U_0 \sin(2\pi z/L)$, giving an amplitude of $U_0 = 1.36 k_BT$ at low ionic strength and $U_0 = 0.66 k_BT$ at high ionic strength. The difference between the two amplitudes explains the fact that for $I = 20$ mM the self−van Hove function exhibits discrete peaks, while for $I = 110$ mM the potential barrier is small enough to exhibit a monotonic behavior of the probability density function. The reason for the more pronounced potential at low ionic strength might be that electrostatic interactions between rods are more long ranged; i.e., particles are more strongly correlated so that it is more difficult to create a void between them. The fact that the potential can be fitted by a sinusoidal is remarkable by itself. Indeed, the use of such a potential is very common due to its simplicity [20], but this ordering potential has never been directly observed until now. Moreover the height of the potential, i.e., the smectic order parameter, can be directly obtained.

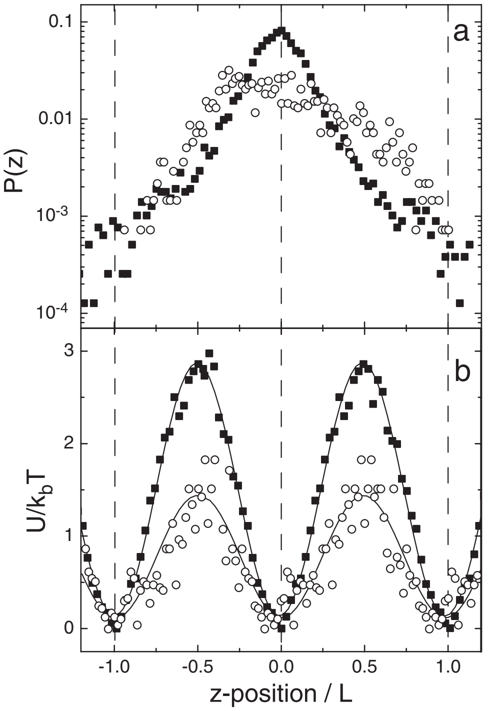

FIG. 3. (a) Histogram of time averaged particle positions parallel to the director *within* the smectic layer at 20 mM (■) and 110 mM (○). The histogram is normalized by the total number of positions. (b) Resulting effective mean ordering potential in the z direction obtained by applying the Boltzmann factor. The solid lines are a fit to a sinusoidal potential.

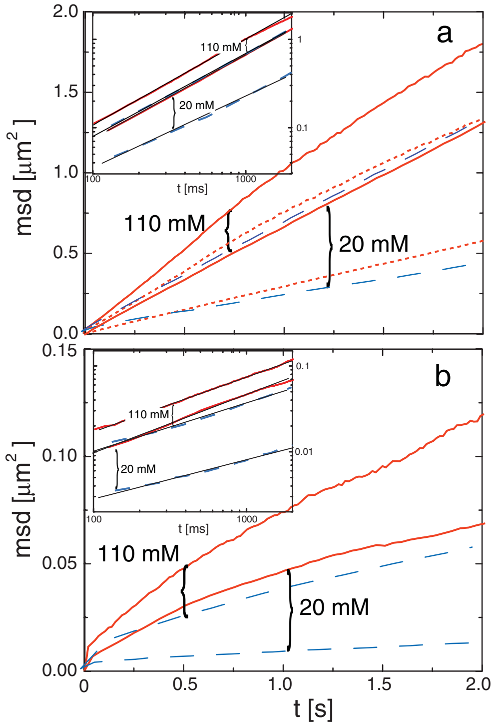

FIG. 4 (color). (a) Mean square displacement parallel to the director for the two indicated ionic strengths in the nematic phase (red line), in the smectic phase (blue dashed line), and in the nematic phase considering the oscillatory potential (red dotted line). (b) Mean square displacement perpendicular to the director (same convention as above). The insets show the same data in a log-log scale, yielding the degree of subdiffusion from the linear regression (black line).

The overall mean square displacement (MSD) of rods parallel and perpendicular to the director of the smectic and nematic phase is plotted in Fig. 4 for both ionic strengths. The time evolution of the MSD given by $\langle \Delta r^2(t) \rangle \sim t^\gamma$ provides the diffusion exponent γ: $\gamma < 1$ is characteristic of a *subdiffusive* behavior, while $\gamma > 1$ is referred to as *superdiffusion*. The parallel motion is close to be diffusive ($\gamma \simeq 1$) in both the nematic ($\gamma = 0.97$) and smectic ($\gamma = 0.94$) phases for $I = 110$ mM and in the nematic phase for $I = 20$ mM ($\gamma = 0.95$). Only the parallel motion in the smectic phase for low ionic strength, i.e., where the discrete peaks in the self–van Hove function are observed, is significantly subdiffusive: $\gamma = 0.81$. The perpendicular motion is in all cases strongly subdiffusive: for $I = 110$ mM, γ reduces from 0.63 before to 0.56 after the nematic-smectic (N-Sm) transition and for $I = 20$ mM it reduces from 0.68 to 0.46. Anomalous subdiffusive behavior has often been observed in systems where diffusion takes place by steps, e.g., in the case of release from a surrounding cage [21]. This "cage escape" might be at the origin of the observed subdiffusive behavior for both parallel and perpendicular diffusion. For parallel diffusion the cage is formed by the energy barrier imposed by the smectic layers, as shown by smaller γ for higher ordering potential. Perpendicular diffusion at high volume fractions is only possible through a reptationlike motion along the long axis to escape the local excluded volume, as observed for polymers for which typically $\gamma = 0.5$ [22]. This excluded volume is huge, even for rods at high orientational order, due to the large rod aspect ratio of ≈ 130. In addition, perpendicular diffusion in the smectic phase is hindered due to the ordering potential, which couples this diffusion to the permeation and which thus explains the decrease of γ from the nematic to the smectic phases. For subdiffusive systems, a non-Gaussian distribution of the probability density functions has been observed as in Fig. 2 [21], even though these two features are not *a priori* correlated. Note also that boundary effects might influence the probability density [23].

The anisotropy in the total diffusion, $D_\parallel/D_\perp$, which is about 20 in the nematic phase [10], increases in the smectic phase as a result of the pronounced subdiffusivity of the perpendicular motion (decrease of γ). These observations show an opposite trend as compared to thermotropic liquid crystals [4,5], where usually $D_\parallel/D_\perp$ evolves from being larger than 1 at temperatures close to the N-Sm transition temperature to being smaller than 1 at lower temperatures [24]. Therefore the diffusion in the smectic phase can be effectively considered as a one-dimensional diffusion of a Brownian particle in a periodic potential in the high friction limit. A general expression for such a diffusion process is given by [25]

$$D_{\parallel} = \frac{D_0}{\langle e^{-U_{\mathrm{layer}}(z)/k_B T}\rangle\langle e^{U_{\mathrm{layer}}(z)/k_B T}\rangle}. \qquad (3)$$

The brackets indicate averaging over one period of the ordering potential. The diffusion coefficient in the smectic phase can then be calculated taking D_0 as the diffusion coefficient in the nematic phase close to the N-Sm transition, and using U_{layer} as obtained from the fit of the potentials plotted in Fig. 3: the diffusion coefficient decreases by a factor 0.84 at $I = 110$ mM and by a factor 0.44 at $I = 20$ mM. Indeed the MSD in the smectic phase is obtained from the MSD in the nematic phase, using these factors for both ionic strengths (see Fig. 4), although at $I = 20$ mM some deviation appears due to the subdiffusivity in the MSD. Thus, we have shown how the mobility of rods decreases after the N-Sm transition, contrary to the isotropic-nematic transition where the global mobility increases due to entropic gain [1,10]. It seems therefore to indicate that *fd* virus suspensions do not behave as a system of rigid hard rods for high concentration in agreement with a recent work [16]. Moreover, the very slow diffusion within the layers suggests that the smectic phase of semiflexible colloidal rods consists of layers of glasslike, rather than fluidlike, particles.

In conclusion, we have for the first time visualized the process of permeation in the smectic phase at the scale of single particles for a system of charged rods. This allowed us to give a full and coherent description of the diffusion process without any assumptions on the system. The diffusion is strongly anisotropic in the direction normal to the smectic layers and quasidiscontinuous due to the presence of the layers. The parallel diffusion rate complies with the rate in the nematic phase, taking into account the ordering potential, which is obtained directly from our measurements.

We thank Jan Dhont for fruitful discussions. This project was supported by the European network of excellence SoftComp. MPL acknowledges also the SFB TR6 for financial support.

[1] L. Onsager, Ann. N.Y. Acad. Sci. **51**, 627 (1949).
[2] D. Frenkel *et al.*, Nature (London) **332**, 822 (1988); G. J. Vroege and H. N. W. Lekkerkerker, Rep. Prog. Phys. **55**, 1241 (1992).
[3] X. Wen *et al.*, Phys. Rev. Lett. **63**, 2760 (1989); H. Maeda and Y. Maeda, Phys. Rev. Lett. **90**, 018303 (2003); Z. Dogic and S. Fraden, Curr. Opin. Colloid Interface Sci. **11**, 47 (2006).
[4] S. Hess *et al.*, Mol. Phys. **74**, 765 (1991); H. Löwen, Phys. Rev. E **59**, 1989 (1999); R. L. B. Selinger, Phys. Rev. E **65**, 051702 (2002); M. A. Bates and G. R. Luckhurst, J. Chem. Phys. **120**, 394 (2004); M. Cifelli *et al.*, J. Chem. Phys. **125**, 164912 (2006).
[5] G. J. Krüger, Phys. Rep. **82**, 229 (1982); S. V. Dvinskikh *et al.*, Phys. Rev. E **65**, 061701 (2002); J. Xu *et al.*, Phys. Rev. E **72**, 051703 (2005).
[6] R. Blinc *et al.*, Phys. Rev. Lett. **25**, 1327 (1970); S. Gaemers and A. Bax, J. Am. Chem. Soc. **123**, 12343 (2001); P. L. Hubbard *et al.*, Langmuir **21**, 4340 (2005); Y. Gambin *et al.*, Phys. Rev. Lett. **94**, 110602 (2005).
[7] G. H. Fredrickson and F. S. Bates, Annu. Rev. Mater. Sci. **26**, 501 (1996).
[8] Z. Bu *et al.*, Macromolecules **27**, 6871 (1994); M. P. B. van Bruggen *et al.*, Phys. Rev. E **58**, 7668 (1998); R. Cush and P. S. Russo, Macromolecules **35**, 8659 (2002).
[9] Y. Han *et al.*, Science **314**, 626 (2006).
[10] M. P. Lettinga *et al.*, Europhys. Lett. **71**, 692 (2005).
[11] P. G. de Gennes and J. Prost, *The Physics of Liquid Crystals* (Clarendon, Oxford, 1993).
[12] W. Helfrich, Phys. Rev. Lett. **23**, 372 (1969).
[13] *fd* was grown using the XL1-Blue strain of *E. coli* as the host bacteria and purified following standard biological protocols [14]. To vary the ionic strength, viruses have been dialyzed against a 20 mM TRIS-HCl buffer at $p\mathrm{H} = 8.2$ with an adjusted amount of NaCl. About one *fd* out of 10^4 has been labeled with the dye Alexa-488 (Invitrogen).
[14] Z. Dogic and S. Fraden, in *Soft Matter*, edited by G. Gompper and M. Schick (Wiley-VCH, Weinheim, 2006), Vol. 2.
[15] M. A. Bates and D. Frenkel, J. Chem. Phys. **109**, 6193 (1998).
[16] K. R. Purdy and S. Fraden, Phys. Rev. E **76**, 011705 (2007).
[17] The time resolution of the used CCD camera (Hamamatsu C9100) was between 10 and 120 ms, depending on the region of interest.
[18] To quantify this hopping-type diffusion, the jumps have been identified with a home-written algorithm based on the criterion that the first N positions in time should deviate in one direction from the previous average, and that the distance between two jumps should be close to the particle length.
[19] J. P. Hansen and I. R. McDonald, *Theory of Simple Liquids* (Academic, London, 1986).
[20] B. Mulder, Phys. Rev. A **35**, 3095 (1987); A. Stroobants *et al.*, Phys. Rev. Lett. **57**, 1452 (1986).
[21] E. R. Weeks and D. A Weitz, Phys. Rev. Lett. **89**, 095704 (2002); Chem. Phys. **284**, 361 (2002).
[22] T. C. B. McLeish, Adv. Phys. **51**, 1379 (2002).
[23] Although data acquisitions were always taken in the middle of the sample which is rather thin (about 10 μm), the diffusion has been observed to slow down close to the cell walls.
[24] The interpretation of such behaviors is ambiguous due to the different temperature dependence of the viscosity parallel and perpendicular to the director.
[25] R. Festa and E. Galleani d'Agliano, Physica (Amsterdam) **90A**, 229 (1978).

Chapter 5

Dynamical and structural insights into the smectic phase of rod-like particles

IOP PUBLISHING JOURNAL OF PHYSICS: CONDENSED MATTER

J. Phys.: Condens. Matter **20** (2008) 494213 (6pp) doi:10.1088/0953-8984/20/49/494213

Dynamical and structural insights into the smectic phase of rod-like particles

Eric Grelet[1], **M Paul Lettinga**[2], **Markus Bier**[3],
René van Roij[3] **and Paul van der Schoot**[4]

[1] Centre de Recherche Paul Pascal, CNRS-Université Bordeaux 1, 115 Avenue Schweitzer,
33600 Pessac, France
[2] IFF, Institut Weiche Materie, Forschungszentrum Jülich, D-52425 Jülich, Germany
[3] Institute for Theoretical Physics, Utrecht University, Leuvenlaan 4, 3584 CE Utrecht,
The Netherlands
[4] Department of Applied Physics, Eindhoven University of Technology, PO Box 513,
5600 MB Eindhoven, The Netherlands

E-mail: grelet@crpp-bordeaux.cnrs.fr

Received 31 July 2008, in final form 15 August 2008
Published 12 November 2008
Online at stacks.iop.org/JPhysCM/20/494213

Abstract
Self-diffusion in a model system of rod-like particles is studied in the smectic (or lamellar) phase. The experimental system is formed by a colloidal suspension of filamentous *fd* virus particles, which allows the direct visualization at the scale of the *single* particle of mass transport between the smectic layers. Self-diffusion takes place preferentially in the direction normal to the smectic layers and occurs in steps of one rod length, reminiscent of a hopping-type of transport. The probability density function is obtained experimentally at different times and is found to be in qualitative agreement with theoretical predictions based on a dynamical density functional theory.

(Some figures in this article are in colour only in the electronic version)

1. Introduction

The self-organization into liquid crystalline states is a field of intensive research, both theoretically [1] and experimentally [2, 3]. Recently, the dynamics of such self-assembled anisotropic media has been investigated in particular by the determination of self-diffusion coefficients in different kinds of mesophases [4]. These measurements have been performed with experimental techniques probing the samples *collectively* (ensemble averaged), such as in nuclear magnetic resonance (NMR) for thermotropic [5] and amphiphilic [6] liquid crystals, and fluorescence recovery after photobleaching (FRAP) for lyotropic (colloidal) systems [7]. Only a few studies have been performed where dynamical phenomena are tracked at the scale of the *single* anisotropic particle [8, 9].

In this work, the model system of aqueous dispersion of filamentous virus *fd* particles, which exhibit a highly monodisperse length and width distribution and the ability to be visualized individually by fluorescence microscopy, has been used to explore the time-dependent phenomena in the smectic phase. In this lamellar mesophase, the particle density is quasi periodic in one dimension parallel to the long axis of the rods, while the interparticle correlations perpendicular to this axis are short-ranged (fluid-like order). In the smectic phase of *fd* virus suspensions, we investigate experimentally the process of interlayer diffusion or *permeation*, first predicted by Helfrich [10], corresponding to the jump along the long axes (or director) of *single* rod-like particles between adjacent smectic layers [9].

Here we first show that *fd* dispersions undergo a first order nematic–smectic and smectic–columnar phase transition, by using differential interference contrast microscopy. X-ray scattering is used to confirm that, within the smectic layers, rods show a Lorentzian radial distribution, typical for a liquid-like ordering, but also for a glass. Having established the structural characteristics of the smectic phase, fluorescence video microscopy is employed to study self-diffusion in this lamellar mesophase. Although particles can supposedly diffuse freely within each liquid-like layer (with diffusion coefficient $D_\perp$) but must overcome a free energy barrier to jump between adjacent layers (with diffusion coefficient $D_\parallel$), surprisingly,

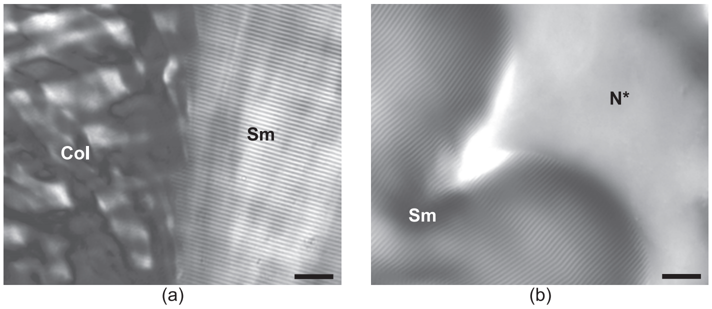

(a) (b)

Figure 1. Phase coexistence of the different mesophases observed in aqueous suspensions of *fd* rod-like viruses by differential interference contrast microscopy. Coexistence of the (a) columnar (left) and smectic (right) phases and of the (b) smectic (left) and chiral nematic (right) phases. The scale bars indicate 10 μm in both cases.

the diffusion through the smectic layers is shown here to be much faster than the diffusion within each liquid-like layer, i.e. $D_{\parallel}/D_{\perp} \gg 1$. This behaviour will be analysed in terms of a recently developed time-dependent density functional theory [11].

2. Experimental details

2.1. Materials and methods

The system of rods used in this work consists of filamentous bacteriophages *fd*, which are semi-rigid polyelectrolytes with a contour length $L = 0.88$ μm, a diameter $d = 66$ Å, a persistence length of 2.2 μm, and a molecular weight of $M_W = 1.64 \times 10^7$ g mol^{-1}. *fd* was grown using the XL1-Blue strain of *E. Coli* as the host bacteria and purified following standard biological protocols [3]. In this study, the ionic strength has been fixed at $I = 20$ mM by a dialysis of *fd* suspensions against a TRIS-HCl–NaCl buffer at pH = 8.2. At this pH, the *fd* charge density is about 10 e nm^{-1}. The virus concentrations were measured using spectrophotometry with an absorption coefficient of 3.84 cm^2 mg^{-1} at 269 nm. Video fluorescence microscopy has been used to monitor the dynamics of individual labelled colloidal rods in the background of a smectic mesophase formed by identical but unlabelled rods, where about one *fd* rod out of 10^4 has been labelled with the dye Alexa-488 (Invitrogen). The colloidal scale of the *fd* bacteriophage enables the imaging of individual rods by fluorescence microscopy, as well as smectic layers by differential interference contrast (DIC) microscopy [3].

2.2. Phase diagram and structural investigations

Suspensions of *fd* rods in aqueous solution form several lyotropic liquid crystalline phases with increasing particle concentration, ranging from the chiral nematic (N*) [12] via the smectic (Sm) [9, 13] to columnar (Col) and crystalline phases [14]. The existence of a smectic phase in suspensions of hard rods is an evidence of the high monodispersity in the particle length and therefore of the model system character of such filamentous viruses [15]. A conceptually appealing intuitive explanation for the appearance of the smectic phase was given by Wen and Meyer [16], and it goes as follows. In the uniaxial nematic phase, neighbouring rods overlap each other by random amounts along their principal direction. This creates volumes at the end of every rod, which are accessible only to that rod but not to any other rod. In the smectic phase, with rods distributed in layers, the random overlapping of rods along their length is avoided, so these excluded volumes disappear, thereby increasing the free volume of the system. Hence, though positional entropy is lost at the transition to the smectic phase, freely available volume is gained and therefore the overall configurational entropy increases.

At $I = 20$ mM, the typical virus concentration for the smectic phase to occur is 115 mg ml^{-1}, which corresponds to a volume fraction $\phi = 0.13$. The volume fraction has been calculated with the bare virus diameter, and not with an effective diameter taking into account the electrostatic interactions between rods. Figure 1 presents the phase coexistence of the smectic phase with the chiral nematic and columnar mesophases, respectively. Both Col–Sm and Sm–N* phase transitions are first order, and they are fully reversible by dilution or concentration of the sample. Note that a sufficiently pronounced particle length polydispersity has been shown to rule out the smectic phase [15] and that rod flexibility also destabilizes the smectic organization [17]. Another consequence of the virus flexibility is that the smectic layer spacing is very close to the particle length [18, 13].

In order to study the nature of the positional order *within* the smectic layers, small angle x-ray scattering (SAXS) has been performed at the ESRF-ID02 beamline (Grenoble, France). Figure 2(a) presents the average radial intensity in the wavevector range suitable for probing the interaxial organization of the rods. The position of the Bragg peak is $q_{100} = 0.0492$ Å^{-1}, which corresponds to a distance between rods of $d_{\text{inter}} = 4\pi/\sqrt{3}q_{100} = 147$ Å. In a conventional liquid the positional correlations decay exponentially with distance, giving a Lorentzian scattering profile of the Bragg reflections. A line shape analysis of the first order Bragg peak has been performed as shown in figure 2(b): a Lorentzian distribution almost perfectly fits the data. A positional correlation length of $\xi = 2\pi/\text{FWHM} = 540$ Å is found, which corresponds to an inter particle correlation extending up to about four neighbours.

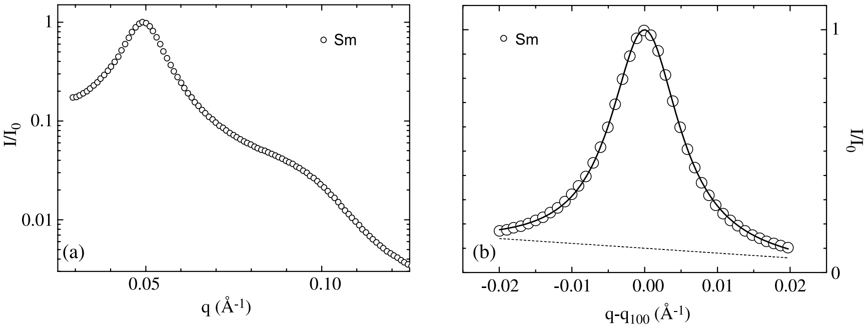

Figure 2. (a) Average radial intensity as a function of the scattering wavevector, probing the inter-rod structure within the smectic layer. (b) Lorentzian fit (solid line) of the first order Bragg reflection (open symbols) which are not resolution limited. The dashed line shows the subtracted linear background.

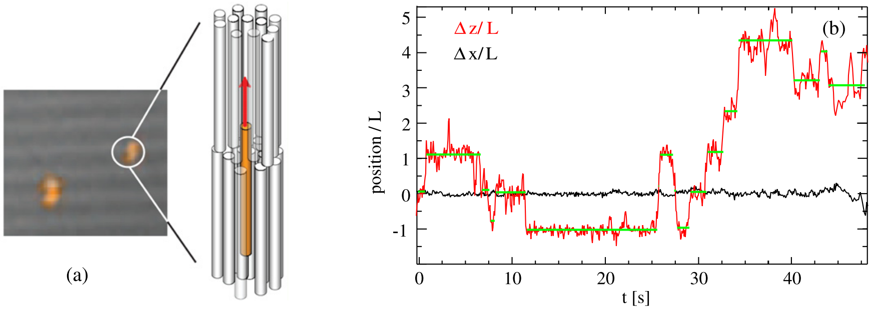

Figure 3. (a) Overlay of differential interference contrast and fluorescence images, showing the smectic layers and two fluorescently labelled particles, and the schematic representation of the jump of rod-like particles between adjacent smectic layers. The layer spacing is $L \simeq 0.9\ \mu$m. (b) Displacement of a given particle in the direction parallel (red line) and perpendicular (black line) to the normal of the smectic layers. The horizontal green lines indicate the residence time, i.e. the time for which one particle stays in a given layer.

This demonstrates that the structure of the order is liquid-like in the layers of the smectic phase.

2.3. *Self-diffusion of single particles*

Figure 3(a) shows an example of images of a single region where both DIC and fluorescence techniques are combined: some rods jump between two layers while others remain within a given layer. The trajectory of one of the rods is plotted in figure 3(b) in the direction parallel (z) and perpendicular (x) to the director. The main result of our measurements is the following: diffusion between the smectic layers takes place in *quasi-quantized steps* of one rod length, and the diffusion within the smectic layer is extremely slow.

The 'hopping-type' diffusion is the consequence of the underlying ordering potential of the smectic phase and the vacancies available in adjacent layers. It shows that the mass transport between the layers is a discontinuous process, as evidenced by the self-Van Hove function $G(z,t)$ in figure 4(a) [19], which is defined as the probability density for a displacement z during a time interval t:

$$G(z,t) = \frac{1}{N}\left\langle \sum_{i=1}^{N} \delta[z + z_i(0) - z_i(t)] \right\rangle. \qquad (1)$$

For an uniform fluid of Brownian particles, a smooth Gaussian distribution that smears out over time is expected for the self-Van Hove function. In the smectic phase, however, $G(z,t)$ shows distinct peaks exactly at integer multiples of the particle length (and therefore of the layer thickness), as also inferred from visual inspection of the rod trajectories (figure 3).

2.4. *Mean square displacement*

The overall mean square displacement (MSD) of rods parallel and perpendicular to the director of the smectic and nematic phases is plotted in figure 4(b). Here parallel MSD is scaled by the length of the rod L, while the time is scaled by the time it takes to diffuse one rod length in the nematic phase, i.e. $\tau_L = L^2/D_\parallel^{\mathrm{nem}}$. Similarly, the perpendicular MSD is scaled by the rod diameter d, while the time is scaled by the time it takes to diffuse one rod thickness in the nematic phase, i.e. $\tau_d = d^2/D_\perp^{\mathrm{nem}}$. The time evolution of the MSD given by $\langle \Delta r^2(t)\rangle \sim t^\gamma$ provides the diffusion exponent γ: $\gamma < 1$ is characteristic of a *sub* diffusive behaviour, while $\gamma > 1$ is referred to as *super* diffusion. The parallel motion is close to be diffusive in the (chiral) nematic phase ($\gamma = 0.95$) close to the N*–Sm phase transition over the whole studied time range, i.e. over several rod lengths. However, the parallel motion in

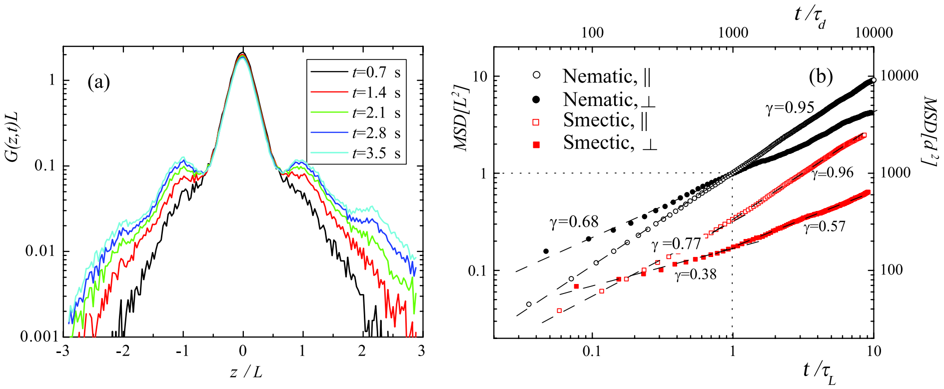

Figure 4. (a) Evolution of the self-Van Hove function at different times. The functions are normalized to one, the z-axis is scaled by the smectic layer thickness L. (b) Log–log representation of the scaled mean square displacement (MSD) parallel and perpendicular to the director in the nematic and smectic phases (see legend) versus the scaled time. The dotted lines indicate the time the rods diffuse one rod length. The dashed lines represent the numerical fits by a power law.

the smectic phase is significantly sub diffusive for $t < \tau_L$: $\gamma = 0.77$, while it is diffusive for $t > \tau_L$ ($\gamma = 0.96$). The perpendicular motion is, in both cases, strongly sub diffusive. In the nematic phase $\gamma = 0.68$, while in the smectic phase once again two regimes can be distinguished: $\gamma = 0.38$ for $t < 1000\tau_d$ and $\gamma = 0.57$ for $t > 1000\tau_d$.

3. Theoretical details

In order to theoretically study the diffusion in uniform and non-uniform complex fluids, a general method was put forward allowing for the straightforward calculation of Van Hove correlation functions within dynamical density functional theory [11]. Because the *fd* virus filaments can be considered as long, thin rods of high stiffness (see section 2.1) that are strongly aligned in the nematic and smectic phases, one can in a first approximation neglect the orientational degrees of freedom [20] and model a liquid crystalline *fd* virus dispersion as a fluid of aligned hard rods of an effective length and diameter. Within the dynamical density functional theory we next invoke the second virial approximation [21], which is not quite exact at the densities where the smectic phase is stable but contains the relevant physics, and numerically solve the relevant kinetic equations that link the self-diffusion of a test particle to the collective diffusion of all the other particles in the system.

In figure 5 we compare the self-Van Hove correlation function $G(z, t)$ obtained from our model calculations with the measurements displayed in figure 4. Here L denotes the smectic layer spacing and τ_L is the parallel diffusion time $\tau_L = L^2/D_{\|}^{\text{short}}$, where $D_{\|}^{\text{short}}$ is the short-time parallel diffusion. The model parameters for the smectic state in the calculation were chosen such that the smectic ordering potential barriers correspond to those determined in the experiment from a Boltzmann weighting of the density profiles [9].

Figure 5 shows that even a calculation at the level of the second virial approximation can account for the qualitative features of the non-trivial, hopping-type diffusive behaviour of rod-like particles along the director from one smectic layer to the next. The quantitative differences between the measurements and theory can be understood by realizing that the second virial approximation overestimates the compressibility of the fluid. Indeed, a rod in the model fluid can, compared to a real *fd* virus, more easily squeeze into a neighbouring layer, which increases the decay rate in the central region around $z = 0$ and the growth rate of the first side peaks around $z = \pm L$ in figure 5. The height of the peaks around $z = \pm 2L$ is associated with the cooperative movement of a rod from the central layer via a void in the first layer to the second layer, which is more pronounced in the experiment than in the calculation.

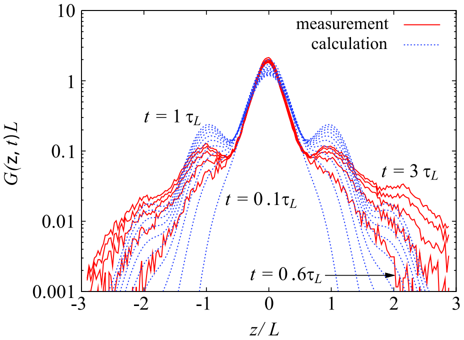

Figure 5. The self-Van Hove correlation function $G(z, t)$ obtained within the dynamical density functional calculation based on a highly idealized second virial model of perfectly aligned, perfectly rigid hard rods, indicated by the blue dotted lines, exhibits the qualitative features of the measurement (red solid lines). Here L is the smectic layer spacing and τ_L is a parallel diffusion time. The quantitative differences can be attributed to an overestimation of the compressibility and the neglect of the particle bending flexibility within the theoretical model.

4. Discussion

Anomalous sub diffusive behaviour has often been observed in systems where diffusion involves an initial waiting time, e.g. following the release of a test particle from a temporary cage caused by the presence of other particles [22]. It stands to reason that this 'cage escape' might be at the root of the observed sub diffusive behaviour for both parallel and perpendicular diffusion observed in the smectic phase. For parallel diffusion of rods the cage is actually formed by the free energy barrier imposed by the smectic layers, superimposed on which is the effective barrier from the enhanced number of particles that cage the central (test) particle [11]. Indeed in both the experiments and the calculations (see also figure 3(a) of [11]) the parallel behaviour is sub diffusive for $t < \tau_L$, related to the crossover between short-time and long-time diffusive behaviour.

The anisotropy in the diffusivities, $D_\parallel/D_\perp$, which is about 20 in the nematic phase [8], increases in the smectic phase within the measured time range as a result of the pronounced sub diffusivity of the perpendicular motion (as indicated by the decrease of γ). Since this sub diffusive behaviour lasts for the whole studied time range, i.e. thousands of rod diameters, it seems that the rods in the layers are glass-like rather then liquid-like. This observation is apparently opposite to the trend found for thermotropic liquid crystals, where usually $D_\parallel/D_\perp$ *decreases* due to an Arrhenius form of the diffusion constants [4, 5]. Also note that preliminary results by Dogic on the self-diffusion of *fd* virus particles in single lamellar membranes indicate that without neighbouring layers perpendicular diffusion is much faster [23].

The cause of the experimentally observed perpendicular sub diffusive behaviour is not clear *a priori*. The theoretical calculations show diffusive long-time behaviour in the perpendicular direction; it should be realized, however, that both flexibility and orientational degrees of freedom are not taken into account in the theory, both of which will result in significant excluded volume effects. Thus, the dominant mode of perpendicular diffusion could be a repetition-like parallel motion of the rod along the long axis to escape its locally excluded volume, similar in nature to what is observed for polymers in the dense melt, for which typically $\gamma = 0.5$ [24]. Including these effects could also help to explain the discrepancy between the envelope of the measured and calculated Van Hove functions plotted in figure 5, since the experimentally observed $\sim z^{-1}$ behaviour could be related to the relaxation of voids once a rod has jumped between two adjacent layers.

5. Summary

We have shown by means of real-space video fluorescence microscopy that the diffusive transport of particles between the layers of a smectic lyotropic colloidal liquid crystal is a discontinuous process that occurs in steps of one layer spacing. Our approach using the dynamical density functional theory, which is found to describe qualitatively the underlying dynamics, points out the importance of the existence of free energy barriers between the smectic layers. This gives rise to a kinetics where particles hop from one layer to the other with a time scale which is dictated by the height of the barriers. At shorter time scales, the particles remain trapped in the smectic layers and perform a diffusive 'bobbing' motion about the local minimum of the self-consistent molecular field.

Acknowledgments

We thank Marjolein Dijkstra for suggesting the application of DDFT to smectics of rods. This project was supported by the European Network of Excellence SoftComp and Transregio Sonderforschungsbereich TR6018 'Physics of Colloidal Dispersions in External Fields'. This work is part of the research programme of the 'Stichting voor Fundamenteel Onderzoek der Materie (FOM)', which is financially supported by the 'Nederlandse Organisatie voor Wetenschappelijk Onderzoek (NWO)'.

References

[1] Frenkel D, Lekkerkerker H N W and Stroobants A 1988 *Nature* **332** 822
Vroege G J and Lekkerkerker H N W 1992 *Rep. Prog. Phys.* **55** 1241
[2] Wen X, Meyer R B and Caspar D L D 1989 *Phys. Rev. Lett.* **63** 2760
Davidson P and Gabriel J C P 2005 *Curr. Opin. Colloid Interface Sci.* **9** 377
Dogic Z and Fraden S 2006 *Curr. Opin. Colloid Interface Sci.* **11** 47
[3] Dogic Z and Fraden S 2006 *Soft Matter* vol 2, ed G Gompper and M Schick (Weinheim: Wiley–VCH)
[4] Hess S, Frenkel D and Allen M P 1991 *Mol. Phys.* **74** 765
Löwen H 1999 *Phys. Rev.* E **59** 1989
Selinger R L B 2002 *Phys. Rev.* E **65** 051702
Bates M A and Luckhurst G R 2004 *J. Chem. Phys.* **120** 394
Cifelli M, Cinacchi G and De Gaetani L 2006 *J. Chem. Phys.* **125** 164912
[5] Krüger G J 1982 *Phys. Rep.* **82** 229
Dvinskikh S V, Furo I, Zimmermann H and Maliniak A 2002 *Phys. Rev.* E **65** 061701
[6] Blinc R, Easwaran K, Pirs J, Volfan M and Zupancic I 1970 *Phys. Rev. Lett.* **25** 1327
Gaemers S and Bax A 2001 *J. Am. Chem. Soc.* **123** 12343
Hubbard P L, McGrath K M and Callaghan P T 2005 *Langmuir* **21** 4340
[7] Bu Z, Russo P S, Tripton D L and Negulescu I I 1994 *Macromolecules* **27** 6871
van Bruggen M P B, Lekkerkerker H N W, Maret G and Dhont J K G 1998 *Phys. Rev.* E **58** 7668
Cush R C and Russo P S 2002 *Macromolecules* **35** 8659
[8] Lettinga M P, Barry E and Dogic Z 2005 *Europhys. Lett.* **71** 692
[9] Lettinga M P and Grelet E 2007 *Phys. Rev. Lett.* **99** 197802
[10] Helfrich W 1969 *Phys. Rev. Lett.* **23** 372
[11] Bier M, van Roij R, Dijkstra M and van der Schoot P 2008 arXiv:0807.4089
[12] Lapointe J and Marvin D A 1973 *Mol. Cryst. Liq. Cryst.* **19** 269
Dogic Z and Fraden S 2000 *Langmuir* **16** 7820
Grelet E and Fraden S 2003 *Phys. Rev. Lett.* **90** 198302
Tombolato F, Ferrarini A and Grelet E 2006 *Phys. Rev. Lett.* **96** 258302
[13] Dogic Z and Fraden S 1997 *Phys. Rev. Lett.* **78** 2417

[14] Grelet E 2008 *Phys. Rev. Lett.* **100** 168301
[15] Bates M A and Frenkel D 1998 *J. Chem. Phys.* **109** 6193
[16] Wen X and Meyer R B 1987 *Phys. Rev. Lett.* **59** 1325
[17] Hentschke R and Herzfeld J 1991 *Phys. Rev.* A **44** 1148
Selinger J V and Bruinsma R F 1991 *Phys. Rev.* A **43** 2922
van der Schoot P 1996 *J. Physique* II **6** 1557
[18] van der Schoot P 1997 *J. Physique* II **6** 1557
Tkachenko A V 1996 *Phys. Rev. Lett.* **77** 4218
[19] Hansen J P and McDonald I R 1986 *Theory of Simple Liquids* (London: Academic)
[20] Odijk T 1986 *Macromolecules* **19** 2313
[21] Mulder B 1987 *Phys. Rev.* A **35** 3095
[22] Weeks E R and Weitz D A 2002 *Phys. Rev. Lett.* **89** 095704
[23] Dogic Z 2008 private communication
[24] McLeish T C B 2002 *Adv. Phys.* **51** 1379

Part II

Isotropic-nematic Phase separation kinetics of rod dispersions

Chapter 6

Kinetic pathways of the nematic isotropic phase transition as studied by confocal microscopy on rod-like viruses

INSTITUTE OF PHYSICS PUBLISHING JOURNAL OF PHYSICS: CONDENSED MATTER

J. Phys.: Condens. Matter **17** (2005) S3609–S3618 doi:10.1088/0953-8984/17/45/055

Kinetic pathways of the nematic–isotropic phase transition as studied by confocal microscopy on rod-like viruses

M Paul Lettinga[1], **Kyongok Kang**[1], **Arnout Imhof**[2], **Didi Derks**[2] and **Jan K G Dhont**[1]

[1] IFF, Institut Weiche Materie, Forschungszentrum Jülich, D-52425 Jülich, Germany
[2] Soft Condensed Matter, Debye Institute, Utrecht University, Princetonplein 5, 3584 CC Utrecht, The Netherlands

E-mail: p.lettinga@fz-juelich.de

Received 28 September 2005
Published 28 October 2005
Online at stacks.iop.org/JPhysCM/17/S3609

Abstract

We investigate the kinetics of phase separation for a mixture of rod-like viruses (*fd*) and polymer (dextran), which effectively constitutes a system of attractive rods. This dispersion is quenched from a flow-induced fully nematic state into the region where the nematic and the isotropic phase coexist. We show experimental evidence that the kinetic pathway depends on the overall concentration. When the quench is made at high concentrations, the system is meta-stable and we observe typical nucleation-and-growth. For quenches at low concentration the system is unstable and the system undergoes a spinodal decomposition. At intermediate concentrations we see the transition between both demixing processes, where we locate the spinodal point.

(Some figures in this article are in colour only in the electronic version)

1. Introduction

Systems that are quenched into a state where at least one order parameter is unstable undergo spinodal phase separation. Here, the initially homogeneous system is unstable against fluctuations of arbitrary small amplitude, and phase separation sets in immediately after a quench. In the initial stage of phase separation an interconnected 'labyrinth structure' of regions with somewhat higher and lower values of the order parameter is observed. For quenches where the system becomes meta-stable, phase separation is initiated by fluctuations with a sufficiently large amplitude. Since such fluctuations have a small probability of occurring, phase separation sets in after a certain delay time, referred to as the induction time. Here, nuclei are formed throughout the volume which grow when they are sufficiently large. The

0953-8984/05/453609+10$30.00

two different mechanisms of phase separation (spinodal decomposition and nucleation-and-growth) can thus be distinguished during the initial stages of phase separation from (i) the difference in morphology (interconnected structures versus growth of isolated nuclei) and (ii) the delay time before phase separation sets in (no delay time for spinodal decomposition and a finite induction time for nucleation-and-growth). As Onsager showed in 1949 [1], the situation is different when the particles are not spherical in shape, i.e. disc-like or elongated particles. Here the system can become unstable or meta-stable with respect to fluctuations in *orientation*. These orientational fluctuations drive concentration differences, resulting in a phase with high concentration and orientational order, the *nematic* phase, and a phase with low concentration and no orientational order, the *isotropic* phase. For very long and thin rods with short-ranged repulsive interactions, the binodal concentrations, i.e. the concentrations of the isotropic and nematic phases in equilibrium after phase separation is completed, have been determined using different approximations in minimizing Onsager's functional for the free energy (see [2] and references therein), while for shorter rods computer simulations have been performed to obtain binodal concentrations [3, 4]. Also the spinodal concentration where the isotropic phase becomes unstable has been found [1, 5].

Binodal points are relatively easy to determine experimentally, since they are given by the concentrations of the bottom and top phase after phase separation. In contrast, it is not at all straightforward to obtain spinodal points, since one would ideally like to perform a concentration quench from low or high concentration into the two-phase region, where the initial state is isotropic or nematic, respectively. In a recent paper a 'quench' of this kind was performed by inducing polymerization of short actin chains [6], and tactoids and spinodal structures were observed. Signatures of spinodal decomposition have also been obtained for boehmite rods, by homogenizing a phase separated system and using sequential polarization microscopy and small angle light scattering measurements [7]. Alternatively, external fields like shear flow [8] and a magnetic field [9, 10] can be applied to prevent a system from phase separation and to stabilize the nematic phase. After cessation of such an external field the nematic phase will become unstable or meta-stable, depending on the constitution of the sample, and phase separation sets in. In this paper we induce a fully nematic phase with a well defined director by imposing shear flow to a dispersion of colloidal rods. We use *fd*-viruses as the system, since the equilibrium phase behaviour concerning the binodal points has been well understood on the basis of Onsager theory [11, 12]. Polymer is added to the dispersion in order to widen the region of isotropic–nematic phase coexistence, which facilitates the phase separation experiments [13]. We perform quenches of a flow aligned initial state to zero shear, which renders the system unstable or meta-stable to fluctuations in the orientation, depending on the concentration of rods. As a consequence phase separation sets in, which we observe by confocal scanning laser microscopy (CSLM). We perform this experiment for different concentrations, throughout the region of phase coexistence. Our results illustrate the difference between nucleation-and-growth and spinodal decomposition in the case of demixing elongated particles, and result in the determination of the nematic–isotropic spinodal point.

2. On the instability of initial states

A convenient way to analyse the stability of a homogeneous initial state is to derive an equation of motion for the order parameter tensor,

$$\mathbf{S}_0(t) = \oint \mathrm{d}\hat{\mathbf{u}}\, \hat{\mathbf{u}}\hat{\mathbf{u}} P_0(\hat{\mathbf{u}}, t). \tag{1}$$

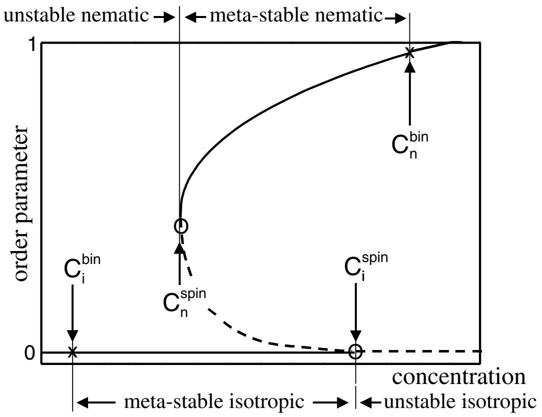

Figure 1. The bifurcation diagram, where the orientational order parameter P_2 is plotted against concentration. Indicated are the various meta- or unstable regions for the two different initial states of the homogeneous suspension. The points marked by X and O are spinodal and binodal points, respectively.

The largest eigenvalue P_2 of the tensor $\mathbf{Q}_0(t) = \frac{3}{2}[\mathbf{S}_0(t) - \frac{1}{3}\hat{\mathbf{I}}]$ (where $\hat{\mathbf{I}}$ is the identity) measures the degree of alignment. For the isotropic state $P_2 = 0$, while for a perfectly aligned state $P_2 = 1$. A stability analysis of stationary solutions of this equation of motion is most conveniently made on the basis of a bifurcation diagram [5], where P_2 for stationary solutions is plotted against the concentration. A schematic bifurcation diagram is given in figure 1. The two solid lines represent stable stationary solutions of the equation of motion, while the dotted lines represent unstable stationary solutions. The isotropic state ceases to be stable above the concentration indicated as C_i^{spin}, while the nematic state becomes unstable at concentrations lower than C_n^{spin}. Above C_i^{spin}, the isotropic state is still a stationary solution, but is now unstable. Below C_n^{spin}, in contrast, there is no unstable nematic state that is a stationary solution of the equation of motion. The two spinodal concentrations C_i^{spin} and C_n^{spin} are connected by a separatrix which separates the basins of attraction for the isotropic and nematic state. A homogeneous initial state above this separatrix develops a higher degree of alignment, while an initial state below the separatrix becomes more isotropic.

Note that the bifurcation diagram relates to homogeneous systems. In an experiment, starting from a homogeneous state, inhomogeneities develop simultaneously with the change of the order parameter of the otherwise homogeneous system. In equilibrium, after completion of phase separation, there is an isotropic phase with concentration C_i^{bin} in coexistence with a nematic phase with concentration C_n^{bin}. One can either start from a stationary state, in which case P_0 in equation (1) is independent of time, or from a non-stationary state, like a nematic state with a concentration lower than C_n, in which case the time dependence of the temporal evolution of alignment of the otherwise homogeneous system couples to the evolution of inhomogeneities through the time dependence of P_0.

In this paper we prepare an initial nematic state shearing a suspension at large enough shear rate such that the induced nematic phase is stable against phase separation (see [14] for a discussion of the bifurcation diagram for sheared systems), and then quench to zero shear rate. For this initial state it is expected that spinodal decomposition occurs at lower concentrations, while nucleation and growth is observed at higher concentrations. For an isotropic initial state this would be reversed: spinodal decomposition at high concentrations and nucleation

Table 1. Overview of the samples used.

Code	φ^5_{nem}	φ^4_{nem}	φ^3_{nem}	φ^2_{nem}	φ^1_{nem}
fd (mg ml^{-1})	29.5	28.1	25.8	23.6	19.3
φ_{nem}	0.96	0.85	0.68	0.52	0.18

and growth at lower concentrations. The observed phase separation kinetics thus depends crucially on the preparation of the initial state of the suspension.

3. Materials and methods

As model colloidal rods we use *fd*-virus particles which were grown as described elsewhere [13]. A homogeneous solution of 22.0 mg ml^{-1} *fd*-virus and 12.1 mg ml^{-1} of Dextran (507 kd, Sigma-Aldrich) in 20 mM tris buffer at pH 8.15 with 100 mM NaCl is allowed to macroscopically phase separate. This concentration of *fd*-virus is exactly in the biphasic region, which is very small when no polymer is added, namely between 21 and 23 mg ml^{-1}. Due to the added polymer, the binodal points shift to 17 and 30 mg ml^{-1}, respectively. New dispersions are prepared by mixing a known volume of the coexisting isotropic and nematic bulk phases. The relative volume of nematic phase in this new dispersion is denoted as φ_{nem}.

For the microscopic observations we used a home-built counter-rotating coneplate shear cell, placed on top of a Leica TCS-SP2 inverted confocal microscope. This cell has a plane of zero velocity in which objects remain stationary with respect to the microscope while shearing. For details of the setup we refer to [15]. For the measurements described here we used confocal reflection mode at a wavelength of 488 nm. Quench experiments were done as follows. Samples were first sheared at a high rate of 10 s^{-1} for several minutes. The shear was then suddenly stopped, after which images were recorded at regular time intervals. These images were parallel to the flow–vorticity plane. Table 1 gives an overview of the concentrations where quench experiments have been performed.

4. Results

In the top row of figure 2 we show micrographs of the initial stage of phase separation for five different concentrations taken after a shear rate quench from a high shear rate, where the nematic state is stable for each concentration, to zero shear. These images show the flow (vertical)–vorticity (horizontal) plane at a given time after the quench. Thus the director of the initial nematic phase lies in the vertical direction. Fourier transforms of the images are plotted in the second row of figure 2. The background is corrected for by subtracting the Fourier transform of the first frame. The third row plots the development of the total intensity of the images minus the intensity in the isotropic phase, as determined from an isolated isotropic region, normalized by the initial nematic intensity. Qualitatively the difference between the concentrations is obvious. In the first two images, i.e. the two highest concentrations, isolated dark ellipsoidal structures can be seen on a bright background. These are droplets of the isotropic phase referred to as tactoids. The number of tactoids increases when the concentration is decreased ((b) and (c)) until the structures become interconnected ((d) and (e)). This also follows from the Fourier transform of the pictures where a ring is detected for the lowest concentration and a constant increasing intensity towards $K = 0$ for the highest concentration. The timescale at which the inhomogeneities are formed also changes. As can be seen in the third row of figure 2, the high concentrations all show an induction time before the phase separation sets in, while

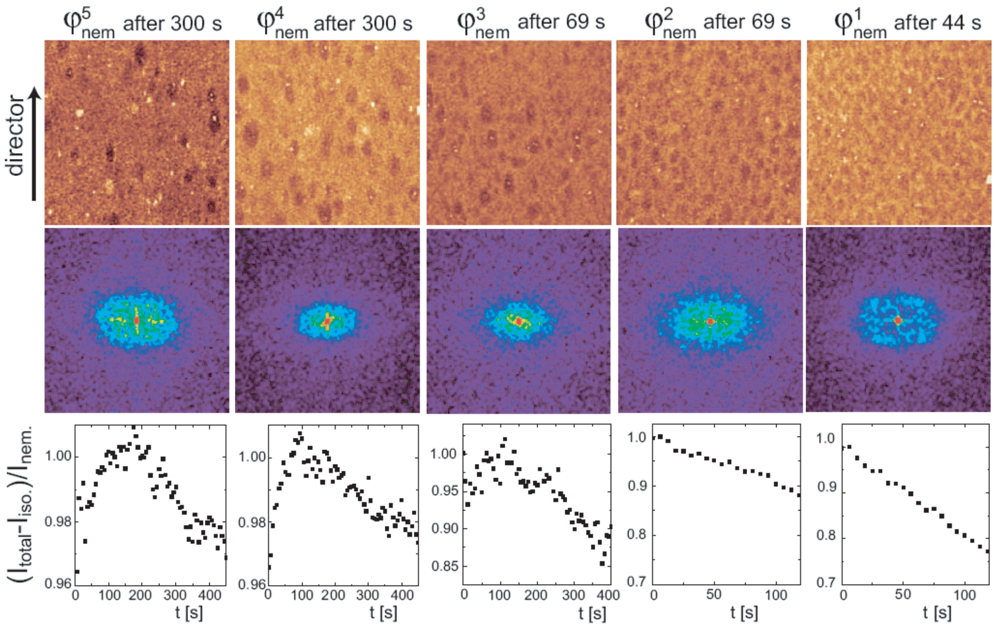

Figure 2. The initial stages of phase separation for five different concentrations after a quench from a flow aligned nematic phase to zero shear. The top row shows the micrographs taken by reflection confocal scanning laser microscopy (field of view = 110 μm); the middle row shows the Fourier transform of the micrographs; the bottom row plots the mean intensity of the micrographs minus the mean intensity for the isotropic phase, normalized by the initial intensity of the nematic phase.

for the low concentrations phase separation sets in immediately. Note also the times at which the images in figure 2 were taken. The isolated nuclei and the induction time are typical for nucleation-and-growth, while the interconnected structures and immediate phase separation are typical for spinodal decomposition.

We use the Fourier transform of the images as shown in figure 2 to quantify the phase separation processes. The interesting quantity for nucleation-and-growth is the width of the Fourier transform, Δk, which is a measure for the anisotropic form factor of the nuclei. Alternatively one could determine the average size of the features in real space, but due to the low contrast this is difficult. For spinodal decomposition the interesting quantity is the wavevector at which the Fourier transform reaches its maximum, k_{max}, quantifying the fastest growing concentration fluctuation. In both cases the fit of the Fourier transform should be performed in two dimensions, since the initial state is anisotropic. Therefore we took cross sections parallel and perpendicular to the director in the Fourier domain, i.e. the vertical and horizontal in figure 2 middle row, to determine k_{max}. Typical cross sections are shown in figure 3, where the wavevector k is scaled by the rod length L. To determine Δk, we performed a 2D Gaussian fit around the origin of the Fourier transforms. Results of a 2D Gaussian fit of the Fourier transform around the origin are shown for the higher concentrations in figures 4(a) and (b), plotting the width in the direction of the director and perpendicular to the director, respectively. k_{max} as found from fits of the cross sections parallel and perpendicular to the director are given in figures 4(c) and (d), respectively. Both fit procedures result in an anisotropic morphology as can be seen in figure 5, where we plotted $\Delta k_{\perp}L/\Delta k_{\parallel}L$ and $k_{\mathrm{max},\perp}L/k_{\mathrm{max},\parallel}L$.

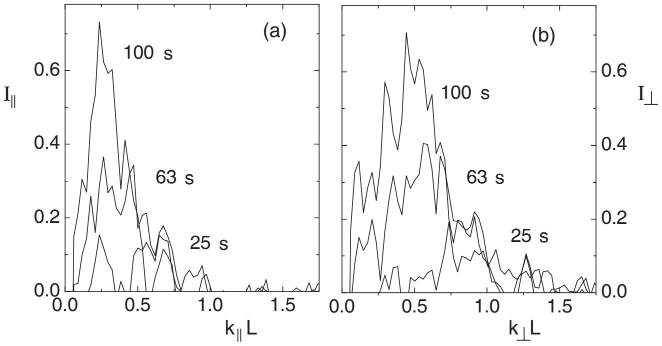

Figure 3. The cross section of the Fourier transform parallel (a) and perpendicular (b) to the director for φ^1_{nem}. The length is scaled by the rod length L.

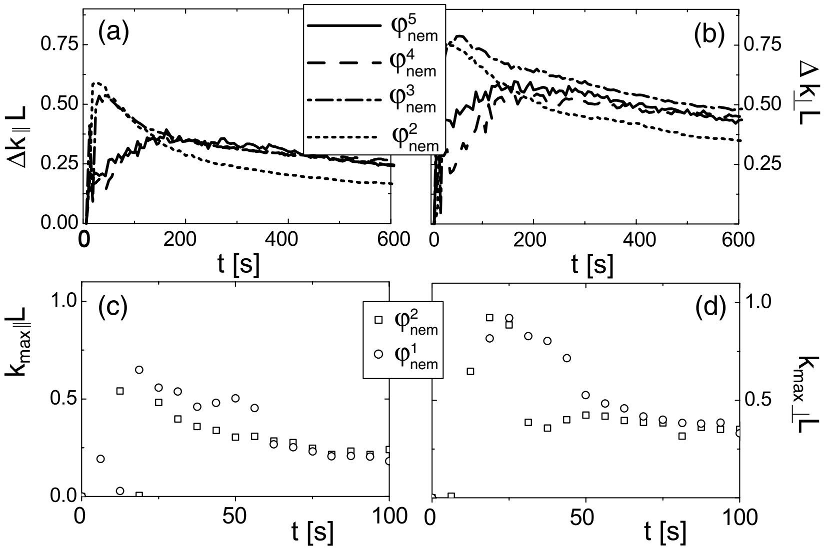

Figure 4. Width of the 2D Gaussian fit, ΔkL, of the Fourier transform parallel (a) and perpendicular (b) to the director for the higher concentrations. Wavevector $k_{\max}L$ where the intensity is maximum for the cross sections parallel (c) and perpendicular (b) to the director for the lower concentrations.

The late stages of the different phase separation processes also show some interesting phenomenology, as can be seen in figure 6. For spinodal decomposition we observe first a growing of the interconnected structures, which then break down into tactoids. Later on the tactoids coalesce, and they become more spherical with increasing size. Note that these tactoids contain the nematic phase and not the isotropic phase, as observed for the nucleation-and-growth process at higher concentrations. In the late stage of nucleation-and-growth, i.e. at high concentrations, we see that coalescence of tactoids containing the isotropic phase as shown in the bottom row of figure 6 is favorable when two tactoids meet somewhat from the middle. In this case the rod orientation near both features is similar and the barrier which has to be overcome for coalescence is low.

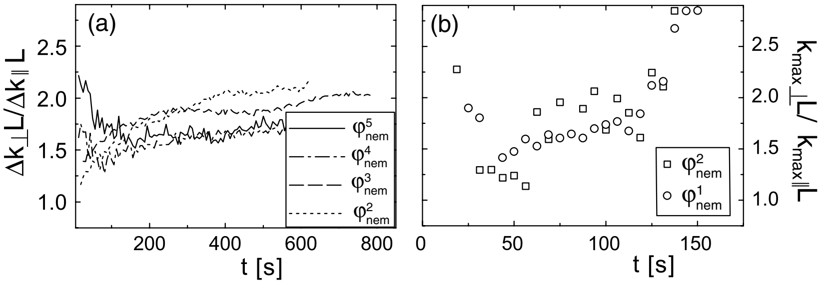

Figure 5. (a) The ratio $\Delta k_\perp L/\Delta k_\parallel L$ for the higher concentrations and (b) the ratio $k_{\max,\perp}L/k_{\max,\parallel}L$ for the lower concentrations.

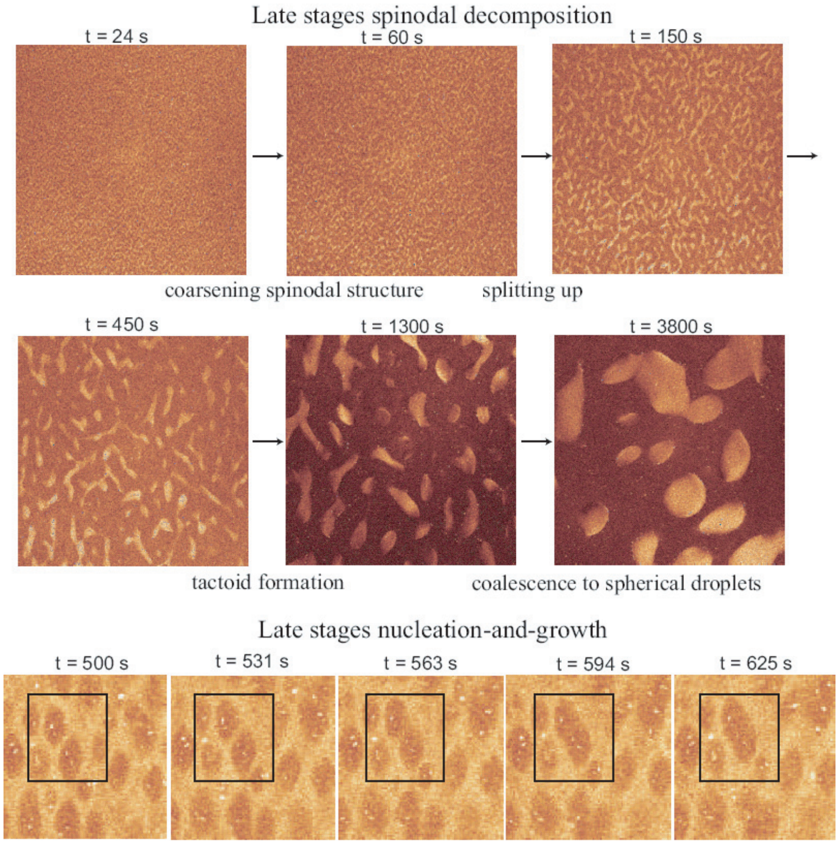

Figure 6. The late stages for spinodal decomposition in the top two rows (φ^1_{nem}, field of view = 375 μm), and coalescence of tactoids in the bottom row (φ^5_{nem}, field of view = 73 μm).

5. Discussion

On the basis of these observations we can now locate the metastable region, i.e. where the system has to overcome a free energy barrier, and the unstable region, where there is no such barrier. At the high concentrations (φ^5_{nem}, φ^4_{nem}) the system is meta-stable, which is reflected by the observed isolated structures formed (top row in figure 2) and the induction time (bottom row in figure 2). With decreasing concentration the system approaches the unstable region: the number of nuclei increases while the induction time decreases and finally vanishes. The lowest concentration φ^1_{nem} is clearly unstable after cessation of the flow. It shows all the features typical for spinodal decomposition: phase separation immediately sets in throughout the whole sample, with a typical length scale which is characterized by the scattering ring observed in the Fourier transform. It can be shown, in fact, that the observed phase separation process for the lowest concentration has features typical for the spinodal decomposition of rods, as derived recently from a microscopic theory by one of the authors [16]. This will be the subject of a following paper [17].

In the intermediate region it is difficult to judge from the morphology if nucleation-and-growth takes place or spinodal decomposition, since it is difficult to distinguish between a high number of tactoids and an interconnected structure. However, φ^3_{nem} shows a short induction time after the quench after which clearly separated tactoids are formed, while for φ^2_{nem} phase separation immediately sets in showing ellipsoidal structures which clearly 'influence' each other. Moreover, figure 4 shows that the size of the structures formed in φ^3_{nem} coincides after some time with the clearly nucleated structures of φ^4_{nem} and φ^5_{nem}, while the size of the structures formed in φ^2_{nem} coincides with samples which clearly show spinodal decomposition. Thus, we locate the transition from meta-stable to unstable, i.e. the spinodal point, between at 23.5 and 25.8 mg ml^{-1}. This is the first experimental observation of the spinodal point in a rod-like system. We should mention at this point that in fact our sample consists of a mixture of rods and polymer. Addition of the polymer causes a widening of the biphasic region [13], i.e. a shift of the binodal points. It is now interesting to see that the high concentration binodal shifts as much as from 23 to 30 mg ml^{-1}. In contrast, the high concentration binodal point, C_n^{bin}, shifts from a concentration between 21 and 23 mg ml^{-1} to somewhere between 23.5 and 25.8 mg ml^{-1}. This leads to the interesting conclusion that the shift of the high concentration binodal point, C_n^{bin}, due to the attraction between the rods, is considerable compared to the shift of the high concentration spinodal point, C_n^{spin}. In other words, making the rods attractive causes a widening of the meta-stable region, while the unstable region remains unaffected. Addition of more polymer will result in more complex kinetics as described in [18].

Interestingly, for all concentrations we observe that the morphology of the phase separating system is anisotropic. This is most clear for the highest concentrations, where the tactoids all point upwards, i.e. in the direction of the director of the surrounding nematic phase. Also the Fourier transforms for the lower concentrations show deformed intensity rings in Fourier space (rightmost FFT image in figure 2). Moreover, the kinetics of the phase separation is also fastest in the direction of the nematic director. This follows for instance from the ratio of $\mathbf{k}_{\text{max}}$ as plotted in figure 5(b), which increases in time. In other words, for all concentrations phase separation is anisotropic, due to residual alignment after the quench of the initially strongly sheared suspension, and not isotropic as is the case for spheres [19].

The length of the first observed tactoids just below C_n^{bin} is about 12 times the rod length, while just above C_n^{spin} it is seven times the rod length. The thickness is about two-thirds of the length in both cases. Typical length scales for the initial spinodal morphology are not more than six rod lengths. These sizes seem to be quite small, considering also the random orientation of the rods in the isotropic phase, but it is in accordance with the microscopic theory for spinodal decomposition of rods [16]. It does suggest that we really image the initial stage. The breaking up of the spinodal structure into nematic tactoids and the sequential growth in the late stage of spinodal decomposition seems surprising since for dispersions of spheres only coalescence and macroscopic phase separation would be observed. However, a similar order of events has been observed for polymer mixtures with thermotropic liquid crystals [20]. Simulations on such mixtures show that the breakdown is due to the effect of the flow-alignment coupling, and not primarily due to elastic effects [21]. An explanation along the same lines was given by Fukuda in a numerical treatment of time-dependent Ginzburg–Landau equations of liquid crystalline polymers [22]. The volume dependence of the morphology in the final stage can be explained by the competition between the interfacial tension and nematic elasticity of the tactoids [23].

6. Conclusion

We studied the kinetics of the nematic–isotropic phase transition of a dispersion of *fd*-virus particles with added polymer after shear quenches into the two-phase region. By varying the equilibrium rod concentration φ_{nem} we were able to detect a nucleation-and-growth mechanism for high φ_{nem}, spinodal decomposition for low φ_{nem}, and the transition between the two processes. In this way we were able to trace for the first time the nematic–isotropic spinodal point C_n^{spin}. Thus, we found that addition of polymer widens the meta-stable region greatly. Furthermore, we showed that the phase separation is strongly influenced by the director of the initial nematic state. The nematic phase also influences the late stages of spinodal decomposition, causing a splitting up of the interconnected structures.

Acknowledgment

This work was performed within the framework of the Transregio SFB TR6, 'Physics of colloidal dispersions in external fields'.

References

[1] Onsager L 1949 The effect of shape on the interaction of colloidal particles *Ann. New York Acad. Sci.* **51** 627–59
[2] Vroege G J and Lekkerkerker H N W 1992 Phase transitions in lyotropic colloidal and polymer liquid crystals *Rep. Prog. Phys.* **55** 1241–309
[3] Bolhuis P and Frenkel D 1997 Tracing the phase boundaries of hard spherocylinders *J. Chem. Phys.* **106** 666–87
[4] Graf H and Löwen H 1999 Phase diagram of tobacco mosaic virus solutions *Phys. Rev.* E **59** 1932–42
[5] Kayser R F Jr and Raveché H J 1978 Bifurcation in Onsager's model of the isotropic–nematic transition *Phys. Rev.* A **17** 2067–72
[6] Viamontes J and Tang J X 2005 Formation of nematic liquid crystalline phase of f-actin varies from continuous to biphasic transition http://arxiv.org/abs/cond-mat/0506813
[7] van Bruggen M P B, Dhont J K G and Lekkerkerker H N W 1999 Morphology and kinetics of the isotropic–nematic phase transition in dispersions of hard rods *Macromolecules* **32** 2256–64
[8] Lenstra T A J, Dogic Z and Dhont J K G 2001 Shear-induced displacement of isotropic–nematic spinodals *J. Chem. Phys.* **114** 10151–62
[9] Tang J and Fraden S 1993 Magnetic-field-induced phase transition in a colloidal suspension *Phys. Rev. Lett.* **71** 3509–12
[10] Lemaire B J, Davidson P, Ferré J, Jamet J-P, Petermann D, Panine P, Dozov I, Stoenescuc D and Jolivet J-P 2005 The complex phase behaviour of suspensions of goethite (α-FeOOH) nanorods in a magnetic field *Faraday Discuss.* **128** 271–83
[11] Fraden S 1995 *Observation, Prediction, and Simulation of Phase Transitions in Complex Fluids* (*NATO-ASI-Series* C, vol 460) ed M Baus, L F Rull and J P Ryckaert (Dordrecht: Kluwer–Academic) pp 113–64
[12] Chen Z Y 1993 Nematic ordering in semiflexible polymer chains *Macromolecules* **26** 3419–23
[13] Dogic Z, Purdy K R, Grelet E, Adams M and Fraden S 2004 Isotropic–nematic phase transition in suspensions of filamentous virus and dextran *Phys. Rev.* E **69** 051702
[14] Dhont J K G and Briels W J 2003 Viscoelasticity of suspensions of long, rigid rods *Colloids Surf.* A **213** 131–56
[15] Derks D, Wisman H, van Blaaderen A and Imhof A 2004 Confocal microscopy of colloidal dispersions in shear flow using a counter-rotating coneplate shear cell *J. Phys.: Condens. Matter* **16** S3917–27
[16] Dhont J K G and Briels W J 2005 Isotropic–nematic spinodal decomposition kinetics *Phys. Rev.* E at press

[17] Lettinga M P, Kang K, Holqvist P, Imhof A, Derks D and Dhont J K G 2005 Nematic–isotropic spinodal decomposition of rod-like viruses, submitted

[18] Dogic Z 2003 Surface freezing and a two-step pathway of the isotropic–smectic phase transition in colloidal rods *Phys. Rev. Lett.* **91** 165701

[19] Aarts D G A L and Lekkerkerker H N W 2004 Confocal scanning laser microscopy on fluid–fluid demixing colloid–polymer mixtures *J. Phys.: Condens. Matter* **16** S4231

[20] Nakai A, Shiwaku T, Wang W, Hasegawa H and Hashimoto T 1996 Process and mechanism of phase separation in polymer mixtures with a thermotropic liquid crystalline copolyester as one component *Macromolecules* **29** 5990–6001

[21] Araki T and Tanaka H 2004 Nematohydrodynamic effects on the phase separation of a symmetric mixture of an isotropic liquid and a liquid crystal *Phys. Rev. Lett.* **93** 015702

[22] Fukuda J 1999 Phase separation kinetics of liquid crystalline polymers: effect of orientational order *Phys. Rev.* E **59** 3275–88

[23] Prinsen P and van der Schoot P 2003 Shape and director-field transformation of tactoids *Phys. Rev.* E **68** 021701

Chapter 7

Nematic-isotropic spinodal decomposition kinetics of rod-like viruses

PHYSICAL REVIEW E **73**, 011412 (2006)

Nematic-isotropic spinodal decomposition kinetics of rodlike viruses

M. Paul Lettinga,[1] Kyongok Kang,[1] Peter Holmqvist,[1] Arnout Imhof,[1] Didi Derks,[2] and Jan K. G. Dhont[1]
[1]*Forschungs Zentrum Jülich, IFF, Weiche Materie, Jülich, D-52425 Jülich, Germany*
[2]*Soft Condensed Matter, Debye Institute, Utrecht University, Princetonplein 5, 3584 CC Utrecht, The Netherlands*

(Received 9 September 2005; published 27 January 2006)

We investigate spinodal decomposition kinetics of an initially nematic dispersion of rodlike viruses. Quench experiments are performed from a flow-stabilized homogeneous nematic state at a high shear rate into the two-phase isotropic-nematic coexistence region at a zero shear rate. We present experimental evidence that spinodal decomposition is driven by orientational diffusion, in accordance with a very recent theory.

DOI: 10.1103/PhysRevE.73.011412 PACS number(s): 82.70.Dd, 64.70.Md, 82.60.Lf, 83.80.Xz

I. INTRODUCTION

Systems that are quenched into a state where at least one order parameter is unstable, undergo spinodal phase separation. Here, the initially homogeneous system is unstable against fluctuations of an arbitrary small amplitude, and the phase separation sets in immediately after a quench. In the initial stage of the phase separation an interconnected "labyrinth structure" of regions with somewhat higher and lower values of the order parameter is observed. For systems containing spherical particles the relevant order parameter is the concentration. As Onsager showed in 1949 [1], the situation is different when the particles are not spherical in shape, i.e., disklike or elongated particles. Here the system can become unstable or metastable with respect to fluctuations in *orientation*. These orientational fluctuations drive concentrations differences, resulting in a phase with high concentration and orientational order, the *nematic* phase, and a phase with low concentration and no orientational order, the *isotropic* phase. For very long and thin rods with short-ranged repulsive interactions, the binodal concentrations, i.e., the concentrations of the isotropic and nematic phases in equilibrium after phase separation is completed, have been determined using different approximations in minimizing Onsager's functional for the free energy (see Ref. [2], and references therein), while for shorter rods computer simulations have been performed to obtain binodal concentrations [3,4]. The spinodal concentration, where the isotropic phase becomes unstable has been obtained [1,5].

Recently, a microscopic theory was developed by one of the authors, describing the initial stage of the *kinetics* of spinodal decomposition (SD) [6]. It is shown there that demixing is dominated by the rotational diffusion and not by the translational diffusion as suggested in earlier work [7,8]. This is in line with results based on the Ginzburg-Landau equations of motion, where the importance of the coupling between the concentration and orientation was studied [9,10] for rod-polymer mixtures.

Signatures of SD have been observed for suspensions of boehmite rods, by polarization microscopy and small angle light scattering (SALS) on a homogenized system [11]. For such experiments, however, there is always an experimental lapse time between homogenization and the first moment of observation. In these experiments the initial state is not well defined. Ideally one would like to perform a concentration quench from low or high concentration into the two-phase region, where the initial state is isotropic or nematic, respectively. In a recent paper such a kind of "quench" was performed by inducing polymerization of short actin chains [12]. Alternatively, external fields such as shear flow [13] or magnetic fields [14] can be used to achieve well-defined quenches. Switching on or turning off such an external field can take the initially homogeneous system into either an unstable or metastable state.

In this paper we induce a nematic phase with a well-defined director by imposing shear flow to a dispersion of colloidal rods. At a sufficiently high shear rate, the fully nematic, homogeneous state is stable. The shear flow is then suddenly switched off, after which the system becomes either unstable or metastable. As a system we use suspensions of *fd* viruses, which are monodisperse and very long and thin and are somewhat flexible particles. The equilibrium phase behavior for these semiflexible rods, as far as the binodal points are concerned, is well understood on the basis of an Onsager theory, extended to include charge and flexibility [15,16]. A polymer is added to the dispersion in order to widen the region of the isotropic-nematic phase coexistence, which renders phase separation experiments feasible [17]. In a previous study we obtained the spinodal point that separates the unstable and metastable region relevant for the initial state in the experiments described in the present paper [18]. In this paper, experiments are performed at concentrations such that the cessation of shear will render the system unstable. We interpret our data on the basis of the recent microscopic theory [6] mentioned above. Experimental evidence is given that phase separation is indeed driven by orientational ordering, which enslaves the concentration. We use confocal microscopy to confirm that demixing is indeed proceeding via spinodal decomposition, rather than nucleation and growth, through the observation of an initial interconnected structure of inhomogeneities. In addition we also use SALS experiments because these have a better time resolution and a better statistics. The present experiments are qualitative in the sense that only the specific wave vector dependence of the unstable eigenmode is discussed, without systematically varying the amount of added dextran which leads to attraction between the rods.

This paper is organized as follows. First we give a brief overview of the microscopic theory on SD of rod dispersions [6], leading to predictions that will be tested experimentally.

1539-3755/2006/73(1)/011412(7)/$23.00

After the section on materials and methods, experimental results are presented for both techniques. In the discussion we analyze our results using the predictions of the microscopic theory.

II. THEORY

The time evolution of the probability density function (pdf) of the orientations and positions of an assembly of N rods is described by the so-called Smoluchowski equation. From this microscopic equation of motion, an equation of motion for the number density $\rho(\mathbf{r},\hat{\mathbf{u}},t)$ of rods at $\mathbf{r}$ with orientation $\hat{\mathbf{u}}$ at time t can be derived by the integration [6]

$$\frac{\partial}{\partial t}\rho(\mathbf{r},\hat{\mathbf{u}},t) = \tfrac{3}{4}\bar{D}\boldsymbol{\nabla}\cdot\mathbf{D}(\hat{\mathbf{u}})\{\boldsymbol{\nabla}\rho(\mathbf{r},\hat{\mathbf{u}},t) - \beta\rho(\mathbf{r},\hat{\mathbf{u}},t)\overline{\mathbf{F}}(\mathbf{r},\hat{\mathbf{u}},t)\} + D_r\hat{\mathcal{R}}\cdot\{\hat{\mathcal{R}}\rho(\mathbf{r},\hat{\mathbf{u}},t) - \beta\rho(\mathbf{r},\hat{\mathbf{u}},t)\overline{\mathbf{T}}(\mathbf{r},\hat{\mathbf{u}},t)\}. \quad (1)$$

Here, $\bar{D}$ and D_r are the orientationaly averaged translational diffusion coefficient and rotational diffusion coefficient of a noninteracting rod, respectively. The orientational dependence of the translational diffusion coefficient of a noninteracting rod is described by the tensor $\mathbf{D}(\hat{\mathbf{u}})=[\hat{\mathbf{I}}+\hat{\mathbf{u}}\hat{\mathbf{u}}]$. Furthermore, $\hat{\mathcal{R}}_j(\cdots)=\hat{\mathbf{u}}_j\times\boldsymbol{\nabla}_{\hat{\mathbf{u}}_j}(\cdots)$ is the rotational operator with respect to $\hat{\mathbf{u}}_j$, where $\boldsymbol{\nabla}_{\hat{\mathbf{u}}_j}$ is the gradient operator with respect to the Cartesian coordinates of $\hat{\mathbf{u}}_j$. For very long and thin rods with hard-core interactions, the average force $\overline{\mathbf{F}}$ and torque $\overline{\mathbf{T}}$ on a rod with position $\mathbf{r}$ and orientation $\hat{\mathbf{u}}$ due to interactions with other rods are given by

$$\overline{\mathbf{F}}(\mathbf{r},\hat{\mathbf{u}},t) = -\nabla V^{\mathrm{eff}}(\mathbf{r},\hat{\mathbf{u}},t),$$

and

$$\overline{\mathbf{T}}(\mathbf{r},\hat{\mathbf{u}},t) = -\hat{\mathcal{R}}V^{\mathrm{eff}}(\mathbf{r},\hat{\mathbf{u}},t), \quad (2)$$

where the "effective potential,"

$$V^{\mathrm{eff}} = \tfrac{1}{2}DL^2\beta^{-1}\oint d\hat{\mathbf{u}}'|\hat{\mathbf{u}}\times\hat{\mathbf{u}}'|\int_{-1}^{1}dl\int_{-1}^{1}dl'\rho\left(\mathbf{r}+\tfrac{1}{2}Ll\hat{\mathbf{u}} + \tfrac{1}{2}Ll'\hat{\mathbf{u}}',\hat{\mathbf{u}}',t\right), \quad (3)$$

has been introduced earlier by Doi and Edwards [19].

In order to describe initial decomposition kinetics, the density $\rho(\mathbf{r},\hat{\mathbf{u}},t)$ is written as

$$\rho(\mathbf{r},\hat{\mathbf{u}},t) = \bar{\rho}P_0(\hat{\mathbf{u}},t) + \delta\rho(\mathbf{r},\hat{\mathbf{u}},t), \quad (4)$$

where $\delta\rho$ is the small deviation with respect to the initial probability density function $\bar{\rho}P_0(\hat{\mathbf{u}},t=0)$, with $\bar{\rho}=N/V$ the average number density of rods. Note that P_0 is generally a function of time, which reflects the temporal evolution of alignment of the otherwise homogeneous system. Although we treat in this paper a quench from the nematic state, we will now proceed by assuming that the initial state is isotropic. Nonisotropic initial states require numerical analysis, since an appropriate (nonlinear) equation of motion for P_0 should be solved simultaneously to the equation of motion for $\delta\rho$ [6]. The general features of demixing are probably not very different for the different initial states.

During the initial stage of demixing, $\delta\rho$ can be expanded up to second order in spherical harmonics as

$$\delta\rho(\mathbf{r},\hat{\mathbf{u}},t) = A_0(\mathbf{r},t) + \mathbf{A}_2(\mathbf{r},t):\hat{\mathbf{u}}\hat{\mathbf{u}}. \quad (5)$$

The scalar A_0 is proportional to the local number density of rods, while the tensor $\mathbf{A}_2$ describes the development of orientational order during demixing. As it turns out, the number density A_0 is enslaved by the orientational contribution $\mathbf{A}_2$.

Using these definitions in the equation of motion Eq. (1), the corresponding equations of motion for A_0 and $\mathbf{A}_2$ can be derived. These equations can be solved, leading to

$$A_0(\mathbf{k},t) = -\frac{\frac{1}{10}\bar{D}k^2\left\{1-\frac{1}{4}\frac{L}{D}\varphi\left[1+\frac{29}{84}(kL)^2\right]\right\}}{\bar{D}k^2\left\{1+2\frac{L}{D}\varphi\right\}-6D_r\left\{1-\frac{1}{4}\frac{L}{D}\varphi\left[1-\frac{499}{8064}(kL)^2\right]\right\}} \times\hat{\mathbf{k}}\hat{\mathbf{k}}:\mathbf{A}_2(\mathbf{k},t),$$

$$\hat{\mathbf{k}}\hat{\mathbf{k}}:\mathbf{A}_2(\mathbf{k},t) = \hat{\mathbf{k}}\hat{\mathbf{k}}:\mathbf{A}_2(\mathbf{k},t)(\mathbf{k},t=0)\exp\{-\lambda^{(-)}t\}, \quad (6)$$

where φ is the volume fraction of rods, and L and D are their length and thickness, respectively. Furthermore, $\hat{\mathbf{k}}$ is the unit vector along the wave vector k, and $\lambda^{(-)}$ is the eigenvalue related to the unstable mode, which is equal to

$$\lambda^{(-)} = 6D_r\left\{1-\frac{1}{4}\frac{L}{D\varphi}\left[1-\frac{499}{8064}(kL)^2\right]\right\} - \mathcal{O}(kL^4). \quad (7)$$

Note that for $L/D\varphi > 4$, this eigenvalue is negative for sufficiently small wave vectors, so that, according to Eq. (6), inhomogeneities with the corresponding wavelength $2\pi/k$ will grow in time without any time delay. This concentration marks the location of the isotropic-to-nematic spinodal and is in accordance with Onsager's prediction [1].

The proportionality of the density A_0 to the orientational contribution $\mathbf{A}_2$ in Eq. (6) reflects the enslavement of density to orientational order during demixing. That is, the transition is driven by orientational diffusion rather than translational diffusion.

Although Eq. (7) has been derived for an initial isotropic distribution, we think that the main conclusion, i.e., that orientational fluctuations dominate the phase separation, is also valid for phase separation starting from the nematic state.

In a scattering experiment the total scattered intensity is related to the quantities A_0 and $\hat{\mathbf{k}}\hat{\mathbf{k}}:\mathbf{A}_2$ as

$$I \sim \{A_0(\mathbf{k},t)[1-\tfrac{1}{72}(kL)^2] - \tfrac{1}{180}(kL)^2\hat{\mathbf{k}}\hat{\mathbf{k}}:\mathbf{A}_2(\mathbf{k},t)[1-\tfrac{3}{560}(kL)^2] + \mathcal{O}[(kL)^6]\}^2. \quad (8)$$

As for gas-liquid spinodal demixing suspensions of spheres, the scattered intensity during isotropic-nematic demixing suspensions of rods exhibits a ringlike pattern where a particular finite wave vector grows most rapidly. The occurrence of a maximum in the scattered intensity at finite wave vectors during demixing has a fundamentally different origin for demixing rods as compared to spheres. For gas-liquid demixing of suspensions of spheres, the eigenvalue (here referred to as $\lambda^{(-)}$) itself exhibits an extremum at a finite wave vector.

For spheres $\lambda^{(-)}$ is of the form $Dk^2[1-\alpha k^2]$, where D and α are wave vector-independent, positive coefficients [20,21]. The prefactor k^2 signifies the fact that the diffusion of spheres over long distances takes longer times, while αk^2 signifies the stabilization of large concentrations gradients. It is easily verified that an eigenvalue of this form exhibits an extremum at a finite wave vector. For gas-liquid demixing of suspensions of spheres this maximum in the growth rate results in the maximum in the scattering pattern. For the isotropic-nematic demixing of suspensions of *rods*, the eigenvalue is of the form $D[1-\alpha k^2]$ [see Eq. (7)], that is, the prefactor k^2 as compared to spheres is missing here. As a consequence $\lambda^{(-)}$ remains finite at zero wave vectors. This difference in the wave vector dependence of the eigenvalue $\lambda^{(-)}$ for gas-liquid and isotropic-nematic demixing is due to the fact that gas-liquid demixing is governed by translational diffusion while isotropic-nematic demixing is (predominantly) governed by rotational diffusion. The maximum in the scattering pattern is now due to the combination of the wave vector dependence of the eigenvalue *and* the wave vector-dependent prefactors to the time exponent. Note that according to Eq. (8), the prefactor of the time exponent is indeed $\sim k^2$, rendering *the scattered intensity equal to zero at a zero wave vector*, which expresses conservation of the number of rods. The k dependence of $\lambda^{(-)}$ can be tested experimentally using the fact that, according to Eqs. (6) and (8), the scattered intensity is $\sim \exp\{\lambda^{(-)}t\}$. Hence,

$$\frac{\partial}{\partial t}\ln\{I(k,t)\} = 2\lambda^{(-)} = 12D_r\{1 - \tfrac{1}{4}\tfrac{L}{D}\varphi[1 - \tfrac{499}{8064}(kL)^2]\}. \quad (9)$$

The slope of a plot of $\ln\{I(k,t)\}$ as a function of t for a given wave vector is thus equal to $\lambda^{(-)}$ for that particular wave vector. Repeating this for various wave vectors allows us to construct the wave vector dependence of $\lambda^{(-)}$.

In addition, the critical wave vector k_c above which the system becomes stable, that is, where $\lambda^{(-)}$ becomes positive, is equal to

$$k_cL = 2\sqrt{\frac{8064}{499}}\sqrt{\frac{1}{4}-\frac{1}{\frac{L}{D}\varphi}} \approx 8\sqrt{\frac{1}{4}-\frac{1}{\frac{L}{D}\varphi}}. \quad (10)$$

For shallow quenches, that is, for concentrations where the $L/D\varphi$ is close to 4, the critical wave vector is thus relatively small. That is, shallow quenches result in relatively large scale inhomogeneities while deeper quenches give rise to relatively small scale inhomogeneities.

In this paper we prepare an initial nematic state, by shearing a suspension at a large enough shear rate such that the induced nematic phase is stable against phase separation (see Ref. [22] for a discussion of the bifurcation diagram for sheared systems), and then quench to zero shear rate. Since the orientation of the rods dominates the phase separation, it is expected that *phase separation takes place anisotropically for an initial nematic state*. In the following we will test this assumption and also the predictions made above for the isotropic-nematic SD, which we believe to hold true also for the nematic-isotropic SD.

III. MATERIALS AND METHODS

As model colloidal rods we use *fd*-virus particles which were grown as described in Ref. [17]. The physical characteristics of the bacteriophage *fd* are length $L=880$ nm; diameter $D=6.6$ nm; persistence length 2.2 μm. A homogeneous solution of 22.0 mg/mL *fd*-virus and 10.6 mg/mL of dextran (507 kd, Sigma-Aldrich, radius of gyration of 18 nm) in 20 mM tris buffer at pH 8.15 with 100 mM NaCl is allowed to macroscopically phase separate. Without dextran the binodal concentrations are 21 and 23 mg/mL for the isotropic and nematic phase, respectively. Due to the added dextran, the binodal points shift to 17 and 31 mg/mL, respectively. The lower spinodal point C^{spin} for this sample was found to be equal to 24.7 ± 1.1 mg/mL, as determined in a previous paper [18]. We prepared three dispersions by mixing a known volume of coexisting isotropic and nematic bulk phases of the quiescent dispersion. In this way, the osmotic pressure is independent of the varying ratio of dextran to the *fd*-virus concentration. The mixing ratios of isotropic and nematic phases are chosen such that a quench from the nematic phase under the flow will always render the aligned system unstable without flow, that is, the *fd* concentration is larger than the lower binodal concentration $C^{bin}=17$ mg/mL and smaller than the lower spinodal concentration $C^{spin}=24.7\pm1.1$ mg/mL [18]. The *fd* concentrations are denoted hereafter as ϕ_f, where $f=(C-C^{bin})/(C^{spin}-C^{bin})$ relates to the fraction of the concentration between the lower binodal and spinodal. The concentrations used in the present study are as follows: $\phi_{0.52}=19.3$ mg/mL, $\phi_{0.55}=19.9$ mg/mL, and $\phi_{0.84}=23.6$ mg/mL. For the SALS measurements the concentration of *fd* and dextran were 21.0 mg/mL and 12.1 mg/mL, respectively. Due to the fact that we used different concentrations of dextran for the different experiments, we cannot directly compare the SALS data to the microscopy data.

For the microscopy experiments we used a home-built counter rotating cone-plate shear cell, placed on top of a Leica TCS-SP2 inverted confocal microscope. This cell has a plane of zero velocity in which objects remain stationary with respect to the microscope while shearing. For details of the setup we refer to Ref. [23]. For the measurements described here we used a confocal reflection mode at a wavelength of 488 nm. Quench experiments were done as follows. Samples were first sheared at a high rate of 10 s^{-1} for several minutes. The shear was then suddenly stopped, after which images were recorded at regular time intervals. For the SALS measurements we used a home made cylindrical optical shear cell. The rotating hollow inner cylinder has a radius of 21.5 mm, the gap width is 2.47 mm. The shear cell is placed in a cylindrical toluene bath with the second gap of the cell exactly in the middle of the bath. A 5 mW He-Ne laser (Melles-Griott) with a wavelength of 632.8 nm was used as a light source. The laser beam is directed along the gradient direction through one single gap using a periscope system, which is inserted into a silicon oil filled inner cylinder at a fixed position. In this way the flow-vorticity plane is probed. Scattered intensities are projected on a white screen, with a beam stop in the middle. The size of the beam stop corresponds to a scattering angle of 1.4° and a wave vector

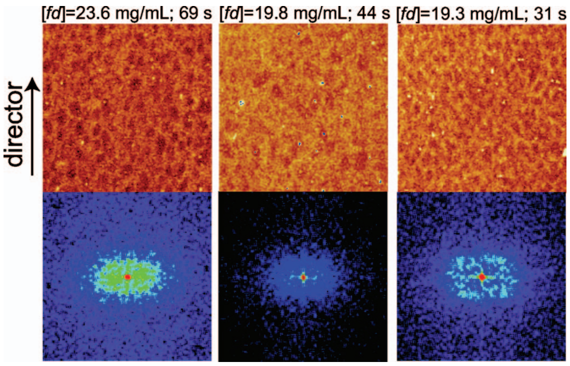

FIG. 1. (Color) The initial stages of SD for three different concentrations, as indicated in the figure. The top row shows the micrographs taken by the reflection confocal scanning laser microscopy (field of view =110 μm); the bottom row shows the Fourier transform of the micrographs.

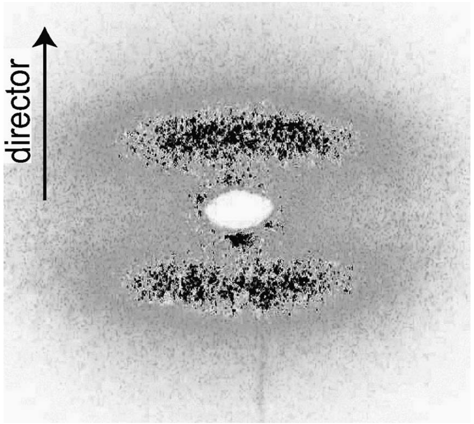

FIG. 2. The scattering pattern for a sample with $[fd]=21.0$ mg/mL and $[\text{dextran}]=12.1$ mg/mL taken 23 s after the cessation of flow.

of 2.4×10^5 m^{-1}. Images were taken in transmission with a peltier cooled 12 bit CCD camera, with 582×782 pixels (Princeton Instruments, microMAX). The maximum scattering angle was 5.1°, which corresponds to a wave vector of 1.0×10^6 m^{-1}.

IV. EXPERIMENTAL RESULTS

Confocal images of the morphology during spinodal decomposition in the early stage after a shear rate quench for different concentrations are given in the top row of Fig. 1 while in the bottom the corresponding Fourier transforms are plotted. The observed ringlike scattering patterns, typical for spinodal decomposition, are anisotropic with symmetry around the nematic director which is along the flow direction. The same anisotropy is observed in the SALS measurements, where such Fourier space images are directly probed (see Fig. 2).

Cross sections of the Fourier transforms and scattering patterns parallel and perpendicular to the director are given in Figs. 3(a) and 3(b), respectively. From these profiles we obtain the wave vector at which the Fourier transform exhibits its maximum, $k_{max}L$, quantifying the wavelength of the fastest growing Fourier component of the inhomogeneous morphology. The values for $k_{max}L$ for directions parallel and perpendicular to the director as obtained from such cross sections of the Fourier transform of the confocal images and the SALS patterns are plotted as a function of time in Figs. 4(a) and 4(b), respectively. The ratio $k_{max,\perp}/k_{max,\parallel}$ of k_{max} perpendicular and parallel to the director is plotted in Fig. 4(c). This figure thus characterizes the anisotropy in the morphology. Since this ratio is larger than 1, the typical size of inhomogeneities perpendicular to the director is smaller than the size of inhomogeneities in the direction parallel to the director.

Comparing the profiles obtained from microscopy and from SALS, it is obvious that the SALS signal is less noisy. This is due to the fact that the volume that is being probed by microscopy is much smaller than the volume probed by SALS. On the other hand, due to the beam stop the profile starts at higher k values than the profiles obtained from microscopy. The large difference in the scattered intensity parallel and perpendicular to the flow direction is also observed under identical conditions for isotropic systems, and is caused by the experimental setup [24].

V. DISCUSSION

The main result of the theoretical treatment in Sec. II for SD of a dispersion of rods is expressed by Eq. (6). This

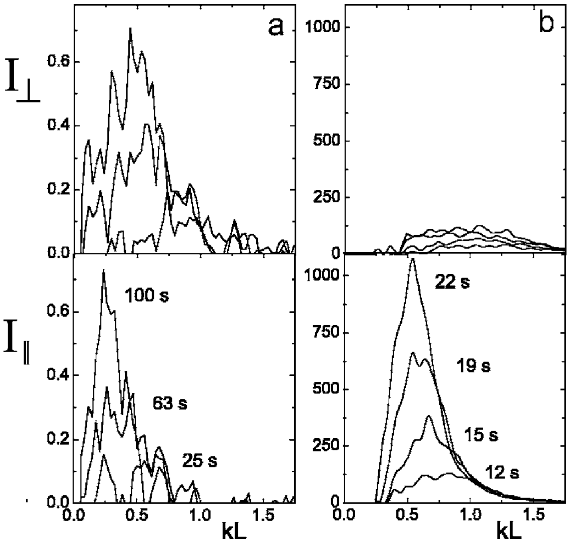

FIG. 3. Cross sections of the Fourier transform of the confocal images parallel and perpendicular to the director for a *fd* concentration of $\phi_{0.52}$ (a), and the parallel and perpendicular cross sections of the scattered intensity as found from SALS (b). The wave vector is scaled by the length L of the *fd* virus and the intensities are given in arbitrary units.

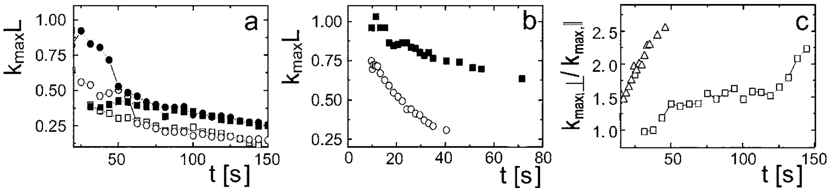

FIG. 4. The wavelength of the fastest growing Fourier component $k_{max}L$ as found from the cross sections parallel to the director (open symbols) and perpendicular to the director (filled symbols) of (a) the Fourier transforms of confocal images with a *fd* concentration of $\phi_{0.84}$ (squares) and $\phi_{0.52}$ (circles), and (b) the SALS pattern. (c) The anisotropy of the spinodal structure given by the ratio $k_{max,\perp}L/k_{max,\parallel}L$ for $\phi_{0.84}$ (squares) and the SALS measurement (triangles).

equation shows that changes in the concentration of rods are enslaved by changes in the orientation of the rods. Although the treatment was done for an initially isotropic state we believe that this result is valid independent of the initial condition. This relation between concentration and orientation has a few consequences, which can be tested experimentally: (1) as for spheres there is no demixing for $k \rightarrow 0$; (2) but the driving force of phase separation given by $\lambda^{(-)}$ goes to a constant value for $k \rightarrow 0$ and not to zero as would have been the case when the translational diffusion dominates phase separation kinetics [see the exponent in Eq. (6)]. As a result k_{max} shifts in time also in the initial stage of demixing; (3) shallow quenches result in relatively large scale inhomogeneities while deeper quenches give rise to relatively small scale inhomogeneities, see Eq. (10).

All micrographs in images Fig. 1 show interconnected structures typical for spinodal decomposition. The resulting Fourier transforms in Fig. 1 as well as the SALS pattern in Fig. 2 are slightly elongated in the direction of the director. The observation of a ring structure confirms the prediction that the scattered intensity is zero for $k \rightarrow 0$, i.e., that there is no demixing for $k \rightarrow 0$ (see also the cross sections in Fig. 3). As pointed out in the theory section this is a general feature of SD, and it is a consequence of the conservation of the number of rods. The anisotropy in the morphology as well as in the growth rates, see Fig. 4(c), shows that the formation of inhomogeneities is affected by the initial orientation of the rods. The anisotropy in the phase separation is also seen in the case of nucleation and growth, where we observed that the nucleating tactoids of isotropic phase are oriented along the director of the nematic background phase [18]. This anisotropy is due to the residual alignment after the quench of the initially strongly sheared suspension.

When plotting the wave vector where the intensity ring exhibits its maximum, i.e., k_{max}, as a function of time, it is readily seen that this maximum shifts to smaller values also during the initial stage of demixing right after the quench (see Fig. 4). That the initial stage of demixing is probed follows from Fig. 5, where the logarithm of the intensity is plotted versus time. In the initial stage this relation should be linear [see Eq. (9)], which is indeed seen to be the case for all values of *kL*. The initial stage of the SD ends where this curve starts to deviate from linearity. For more shallow quenches closer to the spinodal, at higher concentrations, the initial stage extends up to 100 sec.

More importantly, for each value of *kL* we obtain the phase separation rate $\lambda^{(-)}$ from the slope of the curve [see Eq. (9)]. The resulting curves of $\lambda^{(-)}$ vs *kL* are plotted in Fig. 6 for two different confocal microscopy samples (a) and the SALS sample (b). Clearly, $\lambda^{(-)}$ approaches a finite value for $k \rightarrow 0$, as was predicted by theory, see Fig. 6(c). This shows that the demixing kinetics is dominated by rotational diffusion. The absolute value for $\lambda^{(-)}$ is about a factor of 10 higher for the SALS experiment than for the microscopy experiments, which is probably due to the lower dextran concentration that has been used in the microscopy experiment as compared to the SALS experiment. The analysis we used for our data could, in principle, also be applied to the measurements of van Bruggen *et al.* [11], where a similar behavior of the SALS patterns is observed.

Figure 4(a) also confirms the theoretical prediction in Eq. (10) that the initial inhomogeneities are larger for shallow quenches than for deep quenches. The length scale of the initially formed structures for the deep quench (circles,$\phi_{0.84}$) is 11 times the rod length in the direction parallel to the initial director and 7.1 times the rod length in the direction perpendicular to the initial director. For the shallow quench (squares, $\phi_{0.52}$) the initial structure is barely anisotropic and has a typical size of 17 times the rod length. After about 1 m the typical sizes for both concentrations start to overlap.

Finally we would like to remind our readers that the theory presented in Sec. II is valid for repulsive rods. In our experimental system, however, depletion attractions between rods are induced by adding dextran. On adding more dextran, translational diffusion could play a more important role during phase separation. Rod-polymer mixtures has been treated on the basis of Ginzburg-Landau equations of motion with a

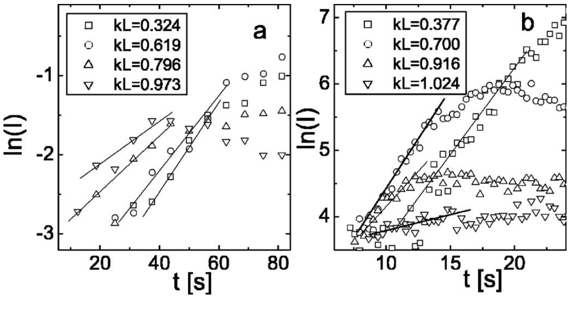

FIG. 5. The logarithm of the Fourier component of confocal images for sample $\phi_{0.52}$ (a) and the scattered intensity from SALS experiments (b) as a function of time for various values of *kL*. The eigenvalue $\lambda^{(-)}$ is obtained from the initial slope of this plot.

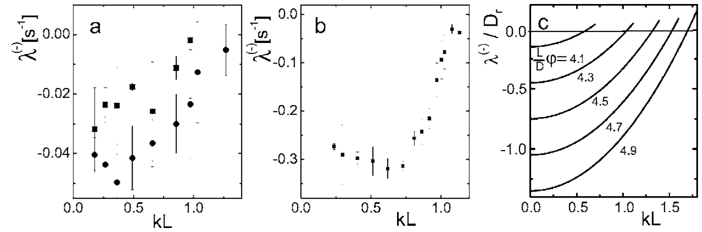

FIG. 6. The *kL* dependence of the eigenvalue $\lambda^{(-)}$ as obtained from confocal microscopy for $\phi_{0.52}$ (bullets) and $\phi_{0.54}$ (squares) (a), as obtained from SALS (b), and as obtained from the theory for the isotropic-nematic transition for different dimensionless concentrations $L/D\phi$(c). Here *L* and *D* are the rod length and thickness, respectively, ϕ is the volume fraction of the rods, and D_r is its rotational diffusion at infinite dilution.

thermodynamics input, amongst others, by Liu and Fredrickson [9], Matsuyama *et al.* [10], and by Fukuda [25]. In these papers it is shown that translational diffusion indeed becomes more important on increasing the polymer concentrations. This results in a minimum in $\lambda^{(-)}$ as a function of the wave vector at sufficiently high polymer concentrations. We therefore believe that the pronounced minimum that is observed for the SALS measurement, see Fig. 6(b), is related to attractions between the rods as induced by the added dextran. The two microscopy measurements depicted in Fig. 6(a) are done at a lower overall dextran concentration. The sample with the somewhat lower *fd* concentration, i.e., higher polymer concentration, shows a less pronounced minimum as compared to the SALS sample, while for the sample with the lowest polymer concentration no minimum is present. These observations confirm the theoretical prediction on the polymer dependence of the phase separation kinetics. In future studies we will systematically vary the polymer concentration for a fixed concentration of *fd*.

VI. CONCLUSION

We studied the nematic-isotropic SD of dispersions of *fd*-virus particles with added polymer after shear quenches into the two-phase region for varying concentrations. We exemplified the fundamental difference between spinodal decomposition of dispersions of rods and spheres using a recently developed theory. The main difference is that in the case of rods the phase separation is dominated by rotational diffusion. As a result the eigenvalue $\lambda^{(-)}$, which quantifies the rate of the phase separation, approaches a nonzero constant value for $k \to 0$, contrary to gas-liquid demixing of spheres where the corresponding eigenvalue becomes zero for $k \to 0$. This is due to the fact that for rods a local reorientation is sufficient to start the phase separation, whereas for spheres translational diffusion over finite distances is needed. We found experimentally the same *k* dependence of $\lambda^{(-)}$ as predicted by theory [6,9,10]. Our experiments thus confirm that demixing is dominated by rotational diffusion and not by translational diffusion as suggested in earlier work [7,8]. In addition, we found a possible effect of translational diffusion through the minimum of the wave-vector dependence of the unstable eigenmode, due to attractions between the rods as induced by the added dextran Refs. [9,10]. This will be subject of further investigations.

ACKNOWLEDGMENTS

This work was performed within the framework of the Transregio SFB TR6 ”Physics of colloidal dispersions in external fields” and the European Network of Excellence Soft Matter Composites (SoftComp).

---

[1] L. Onsager, Ann. N.Y. Acad. Sci. **51**, 62 (1949).
[2] G. J. Vroege and H. N. W. Lekkerkerker, Rep. Prog. Phys. **55**, 1241 (1992).
[3] P. Bolhuis and D. Frenkel, J. Chem. Phys. **106**, 666 (1997).
[4] H. Graf and H. Löwen, Phys. Rev. E **59**, 1932 (1999).
[5] R. F. Kayser Jr. and H. J. Raveché, Phys. Rev. A **17**, 2067 (1978).
[6] J. K. G. Dhont and W. J. Briels, Phys. Rev. E **72**, 031404 (2005).
[7] J. W. Winters, Th. Odijk, and P. van der Schoot, Phys. Rev. E **63**, 011501 (2000).
[8] T. Maeda, Macromolecules **22**, 1881 (1998).
[9] A. J. Liu and G. H. Fredrickson, Macromolecules **29**, 8000 (1996).
[10] A. Matsuyama, R. M. L. Evans, and M. E. Cates, Phys. Rev. E **61**, 2977 (2000).
[11] M. P. B. van Bruggen, J. K. G. Dhont, and H. N. W. Lekkerkerker, Macromolecules **32**, 2256 (1999).
[12] J. Viamontes and J. X. Tang, http://arxiv.org/abs/; cond-mat/0506813 (unpublished).
[13] T. A. J. Lenstra, Z. Dogic, and J. K. G. Dhont, J. Chem. Phys. **114**, 10151 (2001).
[14] J. Tang and S. Fraden, Phys. Rev. Lett. **71**, 3509 (1993).
[15] J. Tang and S. Fraden, Liq. Cryst. **19**, 459 (1995).
[16] Z. Y. Chen, Macromolecules **26**, 3419 (1993).
[17] Z. Dogic, K. R. Purdy, E. Grelet, M. Adams, and S. Fraden, Phys. Rev. E **69**, 051702 (2004).
[18] M. P. Lettinga, K. Kang, A. Imhof, D. Derks, and J. K. G. Dhont, J. Phys.: Condens. Matter **17**, S3609 (2005); The dextran concentration given in this paper was for hydrated dext-

ran. Dehydrated dextran had a concentration of 10.6 mg/mL.
[19] M. Doi and S. F. Edwards, *The Theory of Polymer Dynamics* (Oxford, London, 1986).
[20] J. W. Cahn, J. Chem. Phys. **42**, 93 (1965).
[21] J. Kojima, M. Takenaka, Y. Nakayama, and T. Hashimoto, Macromolecules **32**, 809 (1999).
[22] J. K. G. Dhont and W. J. Briels, Colloids Surf., A **213**, 131 (2003).
[23] D. Derks, H. Wisman, A. van Blaaderen, and A. Imhof, J. Phys.: Condens. Matter **16**, S3917 (2004).
[24] P. Holmqvist, M. P. Lettinga, J. Buitenhuis, and J. K. G. Dhont, Langmuir **21**, 10976 (2005).
[25] J. Fukuda, Phys. Rev. E **59**, 3275 (1999).

Chapter 8

Supersaturated dispersions of rod-like viruses with added attraction

PHYSICAL REVIEW E **80**, 031402 (2009)

Supersaturated dispersions of rodlike viruses with added attraction

P. Holmqvist,[1] M. Ratajczyk,[1,2] G. Meier,[1] H. H. Wensink,[3] and M. P. Lettinga[1]
[1]*Institut für Festkörperforschung, Forschungszentrum Jülich, D-52425 Jülich, Germany*
[2]*Institute of Physics, A. Mickiewicz University, Umultowska 85, 61-614 Poznan, Poland*
[3]*Department of Chemical Engineering, Imperial College London, South Kensington Campus, London SW7 2AZ, United Kingdom*
(Received 14 May 2009; published 21 September 2009)

The kinetics of isotropic-nematic (I-N) and nematic-isotropic (N-I) phase transitions in dispersions of rodlike fd viruses are studied. Concentration quenches were applied using pressure jumps in combination with polarization microscopy, birefringence, and turbidity measurements. The full biphasic region could be accessed, resulting in the construction of an experimental analog of the bifurcation diagram. The N-I spinodal points for dispersions of rods with varying concentrations of depletion agent (dextran) were obtained from orientation quenches using cessation of shear flow in combination with small-angle light scattering. We found that the location of the N-I spinodal point is independent of the attraction, which was confirmed by theory. Surprisingly, the experiments showed that also the absolute induction time, the critical nucleus, and the growth rate are insensitive of the attraction if the concentration is scaled to the distance to the phase boundaries.

DOI: 10.1103/PhysRevE.80.031402 PACS number(s): 82.70.Dd, 64.70.−p, 82.60.Lf, 83.80.Xz

I. INTRODUCTION

A long-standing issue in the physics of fluids is the behavior of the homogeneous fluid close to the point where it becomes unstable and phase separates, i.e., the *spinodal* point φ_s [1]. Before the spinodal point the fluid will be metastable or supersaturated, which means that the fluid will only undergo a phase transition if fluctuations in the concentration are sufficiently high to overcome a certain nucleation barrier. Thus the metastable region is characterized by the induction time τ_{ind} for phase separation to set in. τ_{ind} goes to infinity entering the metastable region from the stable region at the *binodal* point φ_b, i.e., $1/\tau_{\text{ind}} \to 0$ at φ_b, while $\tau_{\text{ind}} \to 0$ approaching φ_s. For molecular fluids it is very difficult to determine the spinodal point because the tiniest impurity will lower the nucleation barrier and the phase separation is very fast. The binodal point is easier to access since it is given by the final phase-separated state. Colloidal systems have proven to be very suitable for this type of fundamental studies. The main reason is that the interactions between the colloids can be tailored, while the size of the colloids slows down the kinetics as compared to fluids permitting direct visualization [2]. One way of tailoring the interaction between colloids is to add nonadsorbing polymers to the system. Polymers induce attractive interaction between the colloids due to the depletion of the polymer between the colloids [3]. The range and the strength of the attractive potential is controlled by the polymer size and concentration, respectively. Due to attractions colloid-polymer mixtures typically show a gas-liquid-like phase transition [4]. Despite of the advantages of colloids, it is also for this class of systems difficult to access the metastable and unstable region in a controlled way. First, the spinodal and binodal line are located very close to each other, while the energy barrier for phase separation to take place is low. Second, systems might be arrested in the metastable state [5]. The challenge is to bring the system in a metastable state while maintaining the system homogeneous.

While the concentration is the only order parameter of interest for gas-liquid phase separating colloidal spheres, dispersions of colloidal rods have two order parameters that characterize the phase behavior which are strongly coupled: particle concentration and orientational order. These systems exhibit an isotropic-nematic (I-N) phase transition, where the system gains positional entropy at the cost of the orientational entropy. The location of the transition can be derived from Onsager theory for slender hard rods [6]. The phase behavior around the I-N transition is characterized by two branches [7]: an isotropic branch with zero orientational order and a nematic branch with a finite orientational order, as depicted in Fig. 1. The I-N binodal point $\varphi_b^{(I)}$ will be first encountered when following the isotropic branch by increasing the concentration. For $\varphi > \varphi_b^{(I)}$ the system will be metastable or supercooled with respect to fluctuations in the orientation toward an aligned state. After some typical induction time τ_{ind} fluctuations will be sufficient to overcome the nucleation barrier and isolated nematic droplets (tactoids) will grow in an isotropic background. For even higher con-

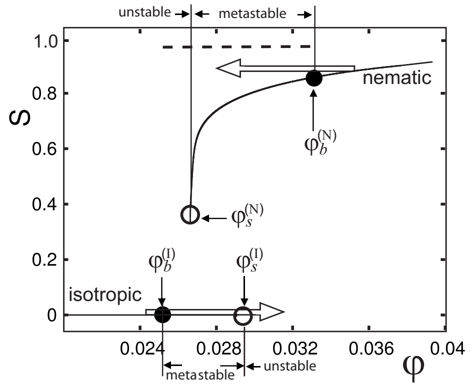

FIG. 1. Bifurcation diagram of the nematic order parameter S for hard rods ($\varphi_p^R=0$) with $L/D=133$ corresponding to the free energy Eq. (1). Open circles indicate spinodal points, while the filled circles indicate binodal points. The arrows indicate concentration quenches that are made to render the system in a supersaturated state. The dashed line indicates possible locations of the system when inducing a full nematic phase applying an external field.

centrations, i.e., for $\varphi > \varphi_s^{(I)}$ the system becomes unstable to fluctuations, such that each fluctuation in the orientation of the rods will result in a continuous growth of the nematic phase out of the isotropic phase. Likewise, the system will have a nematic-isotropic (N-I) binodal $\varphi_b^{(N)}$ and spinodal $\varphi_s^{(N)}$ point when following the nematic branch by decreasing the concentration. In this case the system is superheated because fluctuations toward a lower ordering drive the phase separation. Beyond the binodal point, i.e., for $\varphi < \varphi_b^{(N)}$ isotropic nuclei (atactoids) will form after some induction time τ_{ind}, while beyond the spinodal point, i.e., for $\varphi < \varphi_s^{(N)}$, each fluctuation in the orientation of the rods initiates spinodal phase separation and an isotropic phase of disordered rods continuously grows out of the nematic phase.

The difference in concentration between the I-N and N-I binodal points of a hard rod liquid is only about 10% [8]. Hence the spinodal and binodal points are located very close to each other. The density difference between the binodal points increases when the rods are made attractive: the I-N binodal shifts to lower concentrations while the N-I binodal shifts to higher concentrations. This has been shown experimentally for various rod-polymer mixtures [9–12]. It is, however, not obvious that the location of the spinodal points are equally affected by adding polymer. As a consequence it is not known to what extend the metastable and unstable regions are affected by the addition of polymer. Even for hard rods the location of the spinodal points, i.e., the open symbols in Fig. 1, has never been experimentally confirmed. The goal of this paper is to locate the spinodal points with respect to the binodal points over a range of attractions by probing the kinetics of the phase-separation process. This goal requires a well defined time $t=0$ at which the system is quenched from an initially stable state into a metastable or unstable state, in order to determine the induction time τ_{ind}. Taking advantage of the two order parameters that characterize rod dispersions also two types of quenches can be made: a quench in the orientation and in concentration.

An orientation quench can be performed by first applying an external field to a phase-separated system somewhere in the biphasic region, thus preparing a full nematic phase, as indicated by the dashed line in Fig. 1. The system is quenched when at $t=0$ the external field is switched off, which renders the system either unstable or metastable depending on the concentration. Tang and Fraden used the diamagnetic anisotropy of fd virus to induce I-N phase transitions with a high magnetic field [13] and demonstrated nicely the existence of an unstable region. Here they quenched, however, always to some finite field strength. Similarly, we used in an earlier paper shear flow to prepare a stable nematic phase [14]. Cessation of flow at $t=0$ renders the nematic phase metastable or unstable depending on the concentration, see Fig. 1. Small-angle light scattering (SALS) was then used to probe the formed biphasic structures and determine the spinodal as the concentration where structure formation sets in immediately after the quench. In this paper we again rely on this technique on mixtures of fd and dextran but as compared to the earlier experiments the sensitivity is improved such that measurements could be performed also when density differences between the phases were small as is the case at low polymer concentrations.

The disadvantage of the orientation quench is that only the nematic-isotropic transition is probed. In order to access also the I-N transition one needs to make a concentration quench. Such a quench can be made by rigorous stirring a phase-separated system and probe it immediately after stirring as was done for dispersions of boehmite rods [15].

Apart from the practical problems this imposes on the experiment, the results could also be biased by residual alignment in the sample after mixing [16]. Quenches were also initiated by polymerizing short actin filaments [17]. Both methods could evidence the distinction between nucleation-and-growth and spinodal decomposition by the morphology of the phase-separated structures without pinpointing the actual location of the spinodal points. Nucleation-growth mechanisms and spinodal structures have also been observed in computer simulations [18–21]. In this paper we perform pressure quenches from 1 bar up to 1000 bar and vice versa. Given the compressibility of water, this corresponds with instantaneous concentration quenches of up to 5% [22] as indicated by the solid arrows in Fig. 1. We probe changes using polarization microscopy, birefringence, and turbidity measurements. We could determine both the I-N and N-I spinodal since a full nematic phase could be induced, starting with a full isotropic phase. Thus we construct an experimental analog of the bifurcation diagram plotted in Fig. 1. Since with pressure quenches only a small concentration range can be accessed, we relied on cessation of shear flow to study the attractive rods with added dextran.

To supplement the experiments we have used scaled particle theory (SPT) approach to predict the phase behavior of colloidal rods for a range of polymer concentrations, including the I-N and I-N spinodal lines. The experimental data are qualitatively compared with this theory. In Sec. II we introduce the SPT and present its results in the form of two phase diagrams. In Sec. III we introduce our experimental techniques and sample preparation. The effect of the pressure and orientation quenches are given in Secs. III B and III C, respectively, resulting in the determination of the spinodal and binodal points in Sec. IV C and growth rates in Sec. IV D.

II. THEORY

The phase diagram of a rod-polymer mixture can be predicted from free-volume theory, as elaborated in detail in Refs. [23,24]. The free energy per particle of a system of N hard spherocylindrical rods with length L and diameter D in a volume V in osmotic equilibrium with a reservoir of ideal nonadsorbing polymer with a volume fraction φ_p^R takes the following form:

$$\frac{\beta F}{N} \sim \log y + \sigma[f] + P[f]y + \frac{1}{2}Q[f]y^2 - \frac{(3\gamma-1)\varphi_p^R}{2q^3}\frac{\alpha([f],\varphi)}{\varphi} \tag{1}$$

in terms of the thermal energy $\beta^{-1}=k_BT$, rod aspect ratio $L/D=\gamma \gg 1$, and polymer-colloid size ratio $q=2R_g/D$ (with R_g the polymer radius of gyration). The density variable $y=\varphi/(1-\varphi)$ is related to the rod packing fraction $\varphi=(\pi/4)LD^2N/V$. The reference part $\varphi_p^R=0$ corresponds to a system of hard rods and stems from SPT. The orientational entropic contribution in Eq. (1) is defined as

$$\sigma[f] = \int d\hat{\mathbf{u}} f(\hat{\mathbf{u}}) \ln[4\pi f(\hat{\mathbf{u}})], \tag{2}$$

where the unspecified distribution $f(\hat{\mathbf{u}})$ describes the probability of rods with orientational unit vector $\hat{\mathbf{u}}$ normalized over all possible orientations via $\int d\hat{\mathbf{u}} f(\hat{\mathbf{u}})=1$. The coefficients P and Q pertain to the shape (i.e., aspect ratio) of the rods:

$$P[f] = 3 + \frac{3(\gamma-1)^2}{3\gamma-1}\tau[f],$$

$$Q[f] = \frac{12\gamma(2\gamma-1)}{(3\gamma-1)^2} + \frac{12\gamma(\gamma-1)^2}{(3\gamma-1)^2}\tau[f]. \tag{3}$$

The quantity $\tau[f]$ represents the following double orientational average:

$$\tau[f] = \frac{4}{\pi}\int\int d\hat{\mathbf{u}} d\hat{\mathbf{u}}' f(\hat{\mathbf{u}}) f(\hat{\mathbf{u}}') |\hat{\mathbf{u}} \times \hat{\mathbf{u}}'|. \tag{4}$$

The last term in Eq. (1) accounts for the depletion contribution. It depends on the *free-volume fraction* α, expressing the average fraction of the system volume available to the polymer at a given rod packing fraction φ. An explicit expression follows from SPT:

$$\alpha([f],\varphi) = (1-\varphi)\exp(-Ay - B[f]y^2 - C[f]y^3), \tag{5}$$

with coefficients A,B,C given explicitly in [24]. Since the reservoir polymer concentration φ_p^R is proportional to the depth of the minimum of the attractive *depletion potential*, it serves as a measure for the strength of attraction between the rods. As the polymers are treated as an ideal gas, the polymer volume fraction φ_{poly} in the *system* simply follows from multiplying the reservoir value φ_p^R with the fraction of available free volume $\alpha([f],\varphi)$.

The SPT coefficients P, Q and free-volume fraction depend implicitly on the unspecified orientational distribution $f(\hat{\mathbf{u}})$. In the isotropic state, all orientations are equally probable so that $f=1/4\pi$, $\sigma\equiv 0$, and $\tau\equiv 1$. In the nematic state, it will be a nonuniform distribution peaked along some nematic director $\hat{\mathbf{n}}$. An accurate variational form for f has been proposed by Onsager [6] which takes the following form:

$$f(\theta) = \frac{\kappa \cosh(\kappa \cos\theta)}{4\pi \sinh \kappa}, \tag{6}$$

with $0 \le \theta \le \pi$ the polar angle between $\hat{\mathbf{u}}$ and the nematic director $\hat{\mathbf{n}}$ ($\cos\theta = \hat{\mathbf{u}} \cdot \hat{\mathbf{n}}$) and $\kappa \ge 0$ a variational order parameter (note that $\kappa=0$ leads back to the isotropic constant $f = 1/4\pi$). With the use of an explicit trial function, the orientational averages associated with Eqs. (2) and (4) become analytically tractable [6,25]. The results for the orientational averages are

$$\sigma(\kappa) = \ln(\kappa \coth \kappa) - 1 + \frac{\arctan(\sinh \kappa)}{\sinh \kappa} \ge 0 \tag{7}$$

and

$$\tau(\kappa) = \frac{2 I_2(2\kappa)}{2 \sinh^2 \kappa} \le 1, \tag{8}$$

with $I_2(x)$ a modified Bessel function.

The equilibrium value for κ is found by a minimization of the total free energy which leads to the stationarity condition

$$\frac{\partial F}{\partial \kappa} \equiv 0 \tag{9}$$

for a given rod packing fraction and attraction strength φ_p^R. The nematic order parameter associated with the equilibrium value for κ is found from

$$S = \int d\hat{\mathbf{u}} \mathcal{P}_2(\hat{\mathbf{u}} \cdot \hat{\mathbf{n}}) f(\hat{\mathbf{u}}) = 1 - \frac{3 \coth \kappa}{\kappa} + \frac{3}{\kappa^2}, \tag{10}$$

where $S \equiv 0$ in the isotropic and $0 < S < 1$ in the nematic phase. The solution of Eq. (9) for hard rods ($\varphi_p^R = 0$) is given in Fig. 1, showing two branches where the stationary solutions correspond to a local minimum of the free energy [7]. The spinodal point marks the transition between a stable and an unstable solution of Eq. (9).

However, this (second-order) transition is pre-empted by a first-order phase transition. Thus a discontinuity both in concentration and in the ordering of the system will occur. The coexistence of two phases requires that the osmotic pressure Π and chemical potential μ of the isotropic phase, with volume fraction $\varphi_b^{(I)}$, and the nematic phase, with volume fraction $\varphi_b^{(N)}$, are equal:

$$\Pi(\varphi_b^{(I)}) = \Pi(\varphi_b^{(N)}), \tag{11}$$

$$\mu(\varphi_b^{(I)}) = \mu(\varphi_b^{(N)}). \tag{12}$$

The binodal points can thus be found using the thermodynamic relations $\mu = \frac{\partial F}{\partial N_{V,T}}$ and $\Pi = -\frac{\partial F}{\partial V_{N,T}}$ in combination with Eq. (1).

The phase diagram for a rod-polymer mixture is given in Fig. 2(a) and shows the characteristic widening of the biphasic gap as the amount of polymer is increased. The location of the spinodal points, however, appears much less affected by the depletion attraction. This is reflected more clearly if we plot the spinodal curves in terms of the fraction $0 \le \varphi_{\mathrm{nem}} \le 1$ of nematic phase formed rather than the overall rod packing fraction φ. Applying the lever rule, we may relate φ_{nem} to φ via

$$\varphi_{\mathrm{nem}} = \frac{\varphi - \varphi_b^{(I)}}{\varphi_b^{(N)} - \varphi_b^{(I)}}, \tag{13}$$

with $\varphi_b^{(I/N)}$ as the binodal rod packing fractions corresponding to the coexisting isotropic and nematic phases. Figure 2(b) shows that the N-I spinodal instability occurs if the overall rod concentration corresponds to the nematic phase occupying about 20% of the system volume. This result is virtually independent of the strength of the depletion attraction as long as the amount of added polymer is not too large.

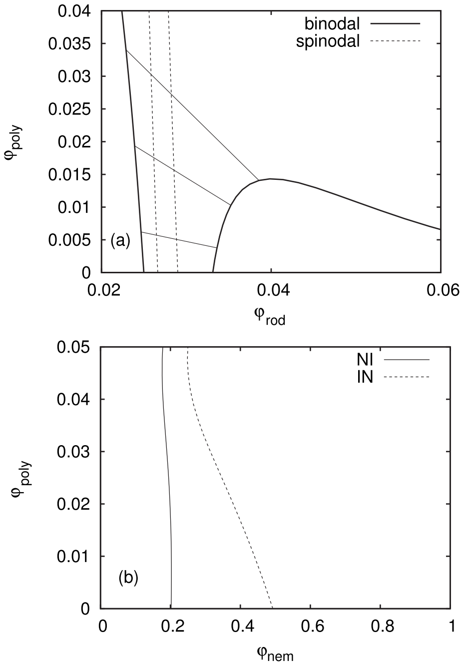

FIG. 2. (a) Phase diagram for a rod-polymer mixture with $L/D=133$ and colloid-polymer size ratio $q=2R_g/D=5.4$. Plotted in terms of the rod packing fraction $\varphi_{\rm rod}$ and polymer volume fraction $\varphi_{\rm poly}$ in the system. Coexisting isotropic and nematic phases are connected by tie lines, with the nematic phase having a higher $\varphi_{\rm rod}$. (b) Location of the isotropic-nematic spinodals in terms of the fraction of nematic phase $\varphi_{\rm nem}$ [Eq. (13)] plotted versus the system polymer concentration $\varphi_{\rm poly}$ on the vertical axis.

III. EXPERIMENT

A. Sample

Fd-virus suspensions were used in a 20 mM Tris buffer with 100 mM NaCl at a *p*H of 8.2. The virus is a long and thin rodlike particle (length of 880 nm long, width of 6.6 nm, persistence length 2.2 μm). Attractions between the rods are varied through depletion by addition of dextran (480 kd, Pharmacosmos). A small amount of fluoresceinisothiocyanat (FITC)-labeled dextran was added to be able to determine the dextran concentration spectroscopically. See Ref. [26] for the labeling procedure of dextran. The samples were prepared as follows: first, a homogeneous fd-virus suspension of 21.1 mg/ml fd virus with dextran is allowed to macroscopically phase separate into an isotropic and nematic phase. The two phases were then separated into two different vials and the dextran and fd-virus concentrations were determined spectroscopically. Three different dextran concentration were used in this study given an initial virus concentration of 21.1 mg/ml: 6 mg/ml (low), 13 mg/ml (middle) and 20 mg/ml (high). The resulting phase diagram is shown in Fig. 3. This phase behavior differs somewhat from previous published results for the same system [9,14]. The deviation might be due to different polydispersity of the dextran which can drastically change the interaction [27] and thus the phase behavior [28]. By combining different volumes of the isotropic, $\varphi_b^{(I)}$, and the nematic, $\varphi_b^{(N)}$, phase from the initially phase-separated sample we can prepare any concentration along one tie line, with a concentration $\varphi_{\rm nem}$ relative to the phase boundaries as expressed in Eq. (13). The concentration of dextran and fd virus for each sample was checked after every new mixing. For pressure experiments a sample very close to the isotropic-nematic spinodal has been prepared at the same ionic strength but without dextran.

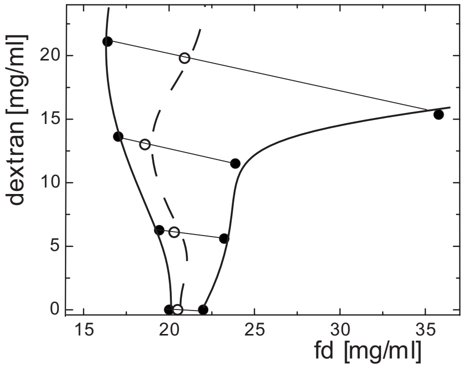

FIG. 3. Phase diagram of the I-N transition of (dextran) vs (fd) at an ionic strength of 110 mM. The solid symbols are the binodal points as determined spectroscopically after phase separation. The open symbols are the spinodal points as determined after shear rate quenches, see below. The thin lines connecting the binodal points are the tie lines.

B. Microscopy, birefringence, and turbidity at high pressure

For all pressure experiments we used a small container sealed by a vitron ring, which contains the sample while it allows for pressurizing via holes in the brass support ring. For microscopy and birefringence measurements the container was placed in the polarization microscopy cell, where the polarization was maintained. The cell was mounted in a specially designed cell holders for microscopy or birefringence. For turbidity measurements a small angle neutron scattering (SANS) cell was used, which has longer optical pathway, to increase the sensitivity of the experiments, but which has windows that scramble the polarization. The detailed description of the cell and the preparation procedure can be found in Ref. [29].

Polarization microscopy was performed on a Zeiss Axioplan microscope with a 10x/0.30 Plan, NEOFLUAR objective. The cell was placed between crossed polarizers in order to detect birefringence corresponding to the change in the order parameter. Starting at 1 bar we applied different pressures up to 1000 bar with steps of 200 bar steps. Pressurizing was performed with a rate of 100 bar/s. Pressure releases were performed from a sample in the nematic phase that had been equilibrated at a pressure of 1000 bar for about 1 h. Consequently, we decreased the pressure starting from this equilibrated sample inducing the nematic-isotropic phase transitions. After changing the pressure, sequences of images were taken using a Carl Zeiss Axiocam charge coupled device (CCD) color camera and Zeiss acquisition software. The sequences of images were taken with different time resolution: in the beginning every 5 s and in the end every minute over a total time of 3 h. Optical birefringence measurements were performed on a home made setup consisting of a argon ion laser line at 514.5 nm, a beam expander, two polarizers and a coherent fieldmaster-GS power and energy meter. The detector was operated by a self written LABVIEW application. The pressure quenches were applied with the same protocol as described above, starting always at 1 bar. The detector registered the intensity of the through-going beam with a time resolution of 0.4 s over a total time of 1 h. To acquire more information about kinetics of the nematic-isotropic transition, measurements of the forward transmission were performed. When a phase transition takes place, the sample becomes turbid which is indicated by a decrease in the transmission. Turbidity was probed with a He-Ne laser and a coherent fieldmaster-GS power and energy meter. Pressure releases were performed as described above. The transmission was detected and registered as in the birefringence measurements with the help of the LABVIEW software.

C. SALS under shear

A homebuild optical couette shear cell combined with a SALS setup was used [30]. The shear cell consisted of a rotating inner cylinder with a diameter of 43 mm and a static outer cylinder with a diameter of 47 mm resulting in a gap width of 2 mm. The inner and outer cylinders were both made of optical grade glass. A 15 mW HeNe laser (Melles Griot) operating at a wavelength of 632.8 nm was used. To ensure that the laser beam went through only one gap, it was directed through the center of the rotational axis of the inner cylinder. In the rotating cylinder, the beam was directed along the radial direction with a prism. Scattered intensities were projected with a lens directly on to the chip of a Peltier cooled 12-bit CCD camera with 582×782 pixels (Princeton Instruments, microMAX). The scattering angles on the chip were calibrated by placing a known grid (PAT 13 Heptagon) in the scattering volume.

The fd-virus solution was always presheared at 100 s^{-1} and quenched to zero shear rate at $t=0$, at which time the registration of the SALS patterns started with a rate of about 2 frames/s. Immediately after cessation of flow the rods will on average be oriented along the flow direction. Thus initially the system will be in a homogenous flow-induced nematic state with a well defined "director" $\hat{n}$. The effect of the preshearing was checked for a number of samples by reducing the preshearing to 50 s^{-1}. No difference on the result could be found, and we therefore kept the protocol of a preshearing rate of 100 s^{-1}.

IV. RESULTS

A. Concentration quenches using pressure

Sequences of micrographs taken after pressure quenches for different time delays are gathered in Figs. 4 and 5. The starting pressure for Fig. 4 was 1 bar so that initially the system was in the isotropic phase. The varied depth of the quenches allowed for exploration of different regions on the phase diagram. For the 200 bar pressure quench the images stay dark throughout the whole experiment (data not shown). For a quench to 400 bar the total intensity only starts to increase after about 5 min. At longer times brighter regions, indicative of a finite order parameter, are visible due to nucleation and growth. The possible presence of tactoids could not be observed, because a 10× objective was used. An induction time τ_{ind} for phase separation to set in is characteristic for the metastable states. For a quench to 800 bar an almost instant change in the intensity is observed along with homogeneous structure formation. This observation suggests that the I-N spinodal is located in the immediate vicinity of this applied pressure. In the last sequence corresponding to the deepest quench of 1000 bar one can see the full transition from isotropic to nematic phase through spinodal decomposition. First, the increase in intensity started immediately after the quench, i.e., $\tau_{\text{ind}}=0$. Second, the initial early stages of the transition exhibited morphology characteristic for spinodal decomposition-interconnected labyrinth-like structures spanning through the whole sample. Figure 6

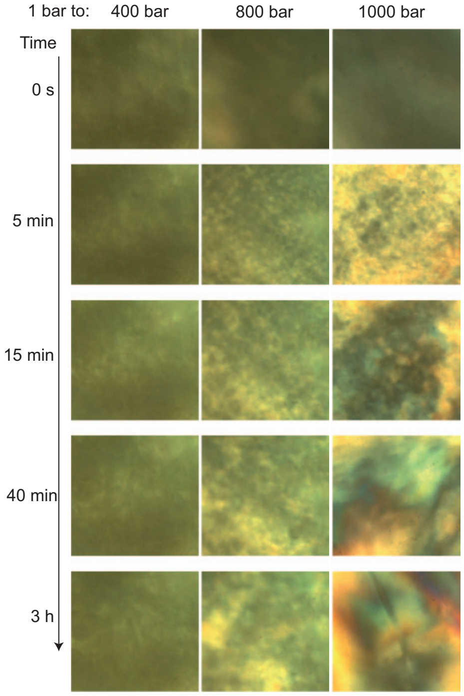

FIG. 4. (Color) Sequence of polarization microscopy image after an increase in pressure, starting at 1 bar. The final pressure is a measure of the concentration. Bright regions with a higher orientational order parameter appear at about 15 min after a quench to 400 bar indicative of a nucleation-growth mechanism (middle left). For a final pressure of 1000 bar phase-separation sets in immediately (top right), indicative of spinodal decomposition, while after 40 min a full nematic phase is formed (bottom right).

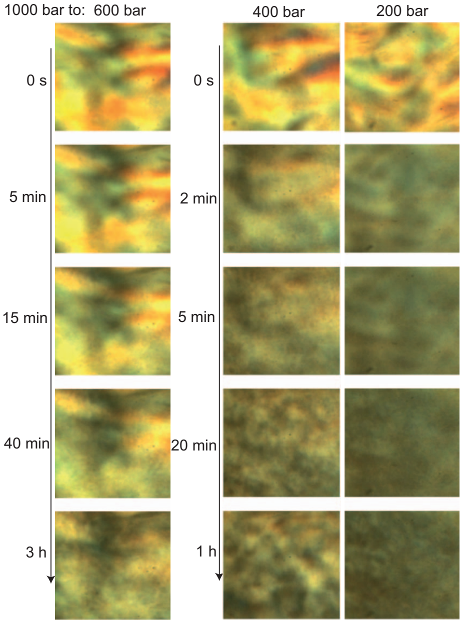

FIG. 5. (Color) As Fig. 4 but now starting at 1000 bar. Nucleation-and-growth events can be seen for a final pressure of 600 bar after 15 min (middle left). For a final pressure of 200 bar phase-separation sets in immediately (top right), indicative of spinodal decomposition, but also the total intensity is much reduced, indicative of a lower ordering. After 1 h a full isotropic phase is formed (bottom right).

shows a thresholded picture taken at 50 s after this quench. Typical spinodal decomposition morphology is evident. The last two micrographs of the 1000 bar quench show that the system develops into a fully nematic phase indicated by large homogenous regions of the same color that only reorient with time. Thus the I-N spinodal $\varphi_s^{(I)}$ is located in the very proximity of the N-I binodal $\varphi_b^{(N)}$.

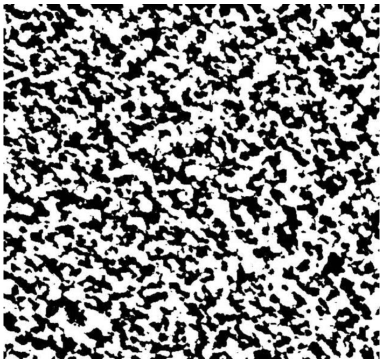

FIG. 6. Filtered and binarized micrographs of fd virus after the pressure jump from 0 to 1000 bar taken at 50 s after the quench. Growing interconnected structures are a clear proof of spinodal decomposition taking place.

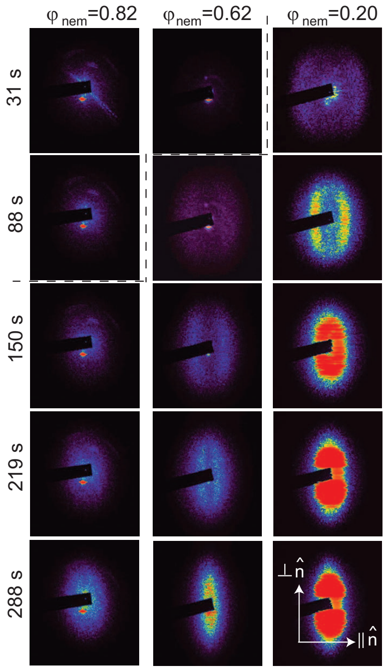

FIG. 7. (Color) Development of the scattering pattern for φ_{nem} =0.20, 0.62, and 0.82, after a shear rate quench from 100 to 0 s^{-1} for the high dextran concentration. For $\varphi_{\mathrm{nem}}=0.20$ spinodal decomposition immediately sets in as can be concluded from the faint ring at 31 s (upper right), while for $\varphi_{\mathrm{nem}}=0.82$ nucleation of structure can only be observed after about 150 s (middle left). The induction time for structure formation is indicated by the dashed line.

Figure 5 depicts the nematic-isotropic phase transition after the pressure quenches from 1000 bar to the indicated pressures. The difference in the morphology for the shallowest quench from 1000 to 800 bar are subtle and changes are only visible 3 h after quenching (data not shown). For the quench from 1000 to 600 bar the changes are more pronounced. After about 20 min grainy structures are formed, characteristic for a phase separation via nucleation and growth. Such structures can still be seen in the last image of the sequence though the overall intensity decreased substantially. The image taken two minutes after the quench from 1000 to 400 bar shows that the overall intensity has decreased, indicative of a lower ordering, while already some biphasic dark and white structures seem to be visible. The first image after the deepest quench, from 1000 to 200 bar, shows that phase-separation sets in immediately (top right), indicative of spinodal decomposition, while the total intensity is much reduced. After 1 h a full isotropic phase is formed (bottom right) showing that a full phase transition took place. A more conclusive location of the spinodal and binodal points can be obtained with turbidity and birefringence measurements as presented in Sec. IV C.

Since with 1000 bar we approach the limit of the maximum applicable pressure, we cannot use this technique to study dispersions of rod-polymers mixtures. For such disper-

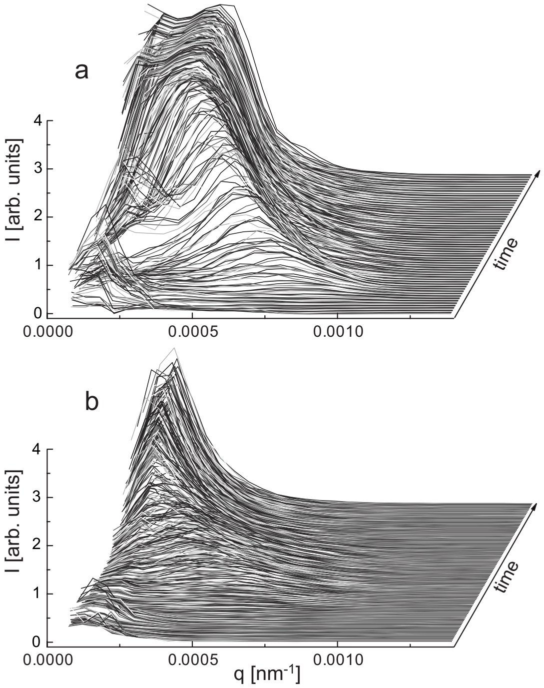

FIG. 8. Development of the scattering along the flow direction for (a) $\varphi_{\text{nem}}=0.20$ and (b) $\varphi_{\text{nem}}=0.62$ as deduced from the scattering patterns in Fig. 7. The total time is three and a half minutes in (a) and six minutes in (b).

sions the width of the biphasic region (see Fig. 3) cannot anymore be bridged. For this reason we use shear flow to induce a flow-stabilized nematic phase followed by cessation of shear flow.

B. Orientation quenches using cessation of shear flow

The development of the scattering pattern after a quench in the shear rate can be seen in Fig. 7 for three different φ_{nem}: 0.20, 0.62, and 0.82. The time at which the first detectable scattering structure appears increases with increasing φ_{nem} as indicated by the dashed line in Fig. 7. For the highest concentration this is the case only after about 150 s. For this concentration it is difficult to identify specific features. For the lower two concentrations the scattering pattern occurs as two slightly bend lines perpendicular to the director ($\hat{x}$). In the early stage these lines scatter weakly but with time the intensity increases, the peak sharpens and the position moves to smaller wave vectors. The scattering patterns are isotropic in the initial stage but become increasingly more asymmetric with time. This indicates that the formed objects are increasingly more elongated and oriented along the director. To quantify the development of the formed biphasic structure we extract intensity profiles along and perpendicular to the director. The time development of the scattering along the director is shown in Fig. 8. Here the formation of the structure peak and both the movement to lower q values and the intensity increase in this peak are clearly seen for the two lowest concentrations, φ_{nem}, where it should be mentioned that for the lowest φ_{nem} the peak develops immediately after cessation of flow, indicative of spinodal decomposition. At the highest concentration the structure peak can only be distinguished at longer times, characteristic for nucleation and growth. Figure 8 and similar plots taken for other concentrations will be used in the following sections as a base to deduce the induction time for structure formation.

C. Spinodal and binodal points

Figures 4, 5, and 7 all show that after the quench phase-separation sets in immediately or after some induction time τ_{ind}, depending on the depth of the quench. As explained in the introduction, in order to locate the spinodal and binodal points we have to find at what concentration τ_{ind} for the formation of nematic (for the I-N transition) or isotropic structures (for the N-I transition) goes either to zero or to infinity.

To determine τ_{ind} for quenches in the orientation we plot the intensity of the peak in the scattering pattern, see Fig. 8, as a function of time. Figure 9(a) shows this time development for three different φ_{nem}. The induction τ_{ind} is now obtained by extrapolating the linear intensity increase to zero intensity. This procedure was repeated for different attraction strength, i.e., different dextran concentrations. The result is shown in Fig. 10(a), where, respectively, τ_{ind} and $1/\tau_{\text{ind}}$ are plotted vs φ_{nem} for the three attractions. The N-I spinodal $\varphi_s^{(N)}$ and binodal $\varphi_b^{(N)}$ points are determined by extrapolating τ_{ind} and $1/\tau_{\text{ind}}$ to zero, respectively. Interestingly, the curves of τ_{ind} and $1/\tau_{\text{ind}}$ for the different attractions overlap if we scale the concentration relative to the phase boundaries. As a consequence the location of $\varphi_s^{(N)}$ is independent of the attraction and is found to be $\varphi_{\text{nem}}=0.25$. More striking even is the observation that also the absolute induction times are only effected by the relative distance from the phase boundary φ_{nem} and not the absolute fd concentration or the attraction, i.e., the dextran concentration. Of course the phase boundaries can also be determined by measuring the concentration of the two separated phases or visual observation, considering that no scattering pattern should occur for the homogeneous phases. The deviation between the different methods is less than 5%. This means that the high-concentration phase boundaries can be determined in three different ways and the low-concentration phase boundary in two ways.

The spinodal decomposition is characterized not only by the fact that it immediately sets in but also by the morphology of the formed structure, which should be bicontinuous. It has been shown that the transition in the morphology is quite smooth [14,15]. This is also exemplified by Figs. 7 and 8(b) for $\varphi_{\text{nem}}=0.62$. A clear ring structure is observed, exemplary for spinodal structures, but also for this concentration an induction time is observed. Thus the phase separation has already spinodal characteristics, but clearly the system is still in the metastable region. Therefore the only reliable way to determine the spinodal point is by using the induction time.

The kinetics of the phase separation for samples without polymer was studied using the pressure quench. The reason

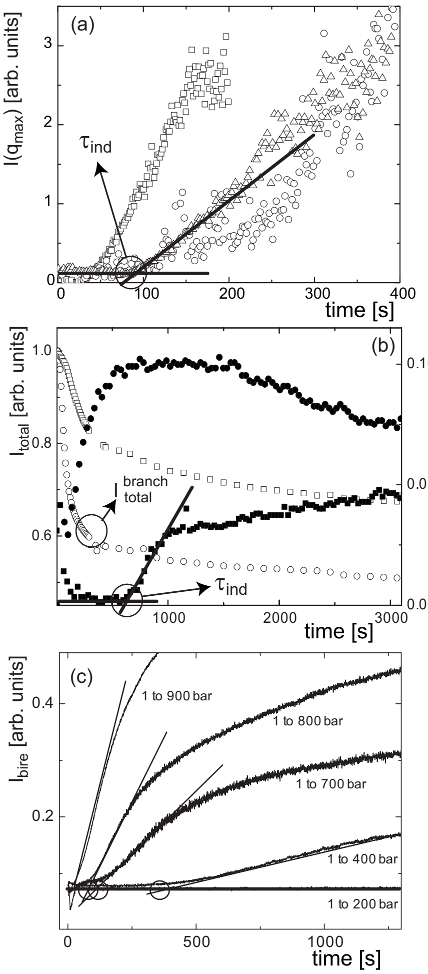

FIG. 9. (a) The intensity at the peak of the scattering pattern, $I(q_{\max})$, after cessation of shear flow for $\varphi_{\text{nem}}=0.30$ (□), $\varphi_{\text{nem}}=0.62$ (○), and $\varphi_{\text{nem}}=0.82$ (△) at the high dextran concentration to study the N-I transition. (b) Turbidity (solid symbols) and total intensity of the polarization micrographs (open symbols) after a pressure drop (cubes: 400 bar, bullets: 200 bar) to study the N-I transition. The total intensity of the polarization micrographs after the initial decay, $I_{\text{total}}^{\text{branch}}$, is also indicated. (c) Birefringence intensity after an increase in pressure to study the I-N transition. The lines in the plots indicate the extrapolation to determine the induction time after a shear rate or pressure quench.

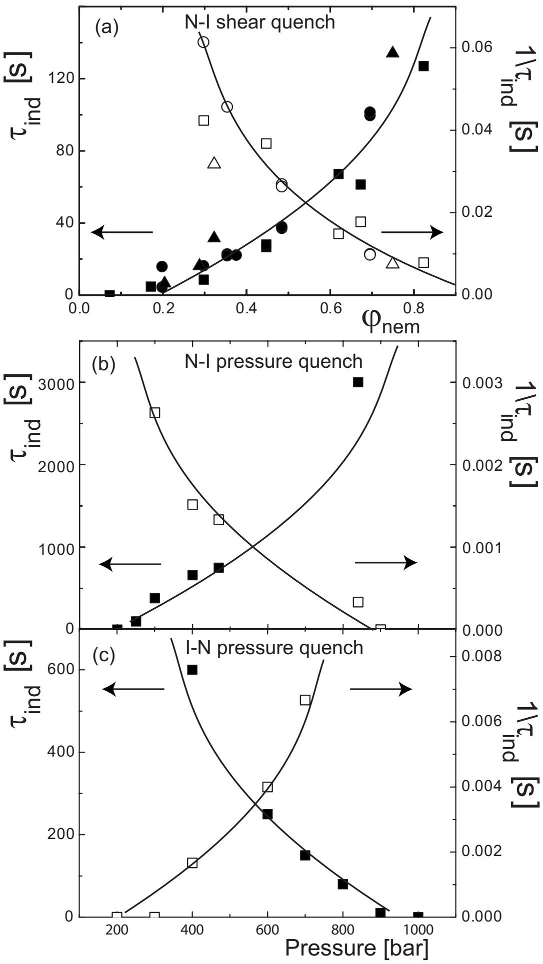

FIG. 10. Induction times (filled symbols) and inverse induction times (open symbols) starting [(a) and (b)] with an initial nematic phase to determine $\varphi_b^{(N)}$ and $\varphi_s^{(N)}$ and (c) with an initial isotropic phase to determine $\varphi_b^{(I)}$ and $\varphi_s^{(I)}$; (a) as a function of φ_{nem} for three dextran concentrations [high (□), middle (○), and low (△)] after preshearing; [(b) and (c)] as a function of the final pressure after an initial pressure of 1000 and 1 bar, respectively. The lines are guide to the eyes.

is that with this technique we access both the N-I and the I-N transitions. As described in Sec. III B the location of these points could be estimated from microscopy experiments. The interpretation of the micrographs is, however, not straightforward. Quenches starting from an initial nematic phase at 1000 bar show that the overall intensity decreases as well as that structures are formed. To separate the two effects we additionally performed turbidity measurements since turbidity is a measure of the biphasic structure that is created in the sample during phase separation. In Fig. 9(b) the responses of the turbidity and the total integrated intensity I_{total} of the polarization micrographs are plotted for quenches to 400 and 200 bar. For the quench to 400 bar clearly an induction time is observed in the turbidity, while the birefringence, which dominates the intensity of the polarization microscopy, shows a fast and a slow decay. Since the flow induced nematic phase has a higher-order parameter than the metastable nematic branch (see Fig. 1) the nematic phase will first relax to this branch, which explains the initial fast decay of the birefringence to $I_{\text{total}}^{\text{branch}}$. Turbidity is not sensitive for this process because structure formation is not involved in this process. Hence we can conclude that phase-separation sets in only after an induction time of about 650 s. For the quench to

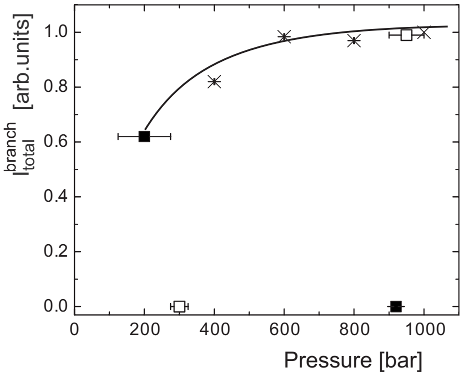

FIG. 11. The experimental equivalent of the bifurcation diagram. The pressures corresponding to $\varphi_s^{(N)}$ and $\varphi_s^{(I)}$ are determined from Figs. 9(b) and 9(c) as the pressures where $\tau_{\text{ind}} \rightarrow 0$ (solid symbols). The pressures corresponding to $\varphi_b^{(N)}$ and $\varphi_b^{(I)}$ are given by the pressures where $1/\tau_{\text{ind}} \rightarrow 0$ (open symbols). The total intensity of the polarization micrographs after the initial decay, $I_{\text{total}}^{\text{branch}}$, [see Fig. 9(b)] is taken as a measure of the orientational order parameter (stars). The line is guide to the eyes.

200 bar changes in birefringence and turbidity set in immediately so $\tau_{\text{ind}}=0$. Since we know from microscopy that the final stage for 200 bar is fully isotropic, the down turn in the turbidity after half an hour can be interpreted as the disappearance of biphasic structure. Before reaching the fully isotropic phase (low turbidity) the system undergoes a phase transition (high turbidity). When pressurizing an initially isotropic sample then the increase in birefringence can only be caused by the formation of the nematic phase. Thus the induction times for the formation of the nematic phase can be obtained from the birefringence responses as plotted in Fig. 9(c).

The induction times and the reverse induction times are plotted in Figs. 10(b) and 10(c) for the turbidity and birefringence, respectively. The pressures corresponding to $\varphi_s^{(N)}$ and $\varphi_s^{(I)}$ are determined from these two figures as the pressures where $\tau_{\text{ind}} \rightarrow 0$, while the pressures corresponding to $\varphi_b^{(N)}$ and $\varphi_b^{(I)}$ are given by the pressures where $1/\tau_{\text{ind}} \rightarrow 0$. We can now construct the experimental equivalent (Fig. 11) of the theoretical bifurcation diagram (Fig. 1) using pressure as a measure of concentration and the total intensity of the micrographs after the initial decay as a measure of the orientational order parameter [Fig. 9(b)]. Note that the error bar in the pressure is determined from the uncertainty in the extrapolation to $\tau_{\text{ind}} \rightarrow 0$ and $1/\tau_{\text{ind}} \rightarrow 0$. Another source of error could also be the exact concentration of the rods since the data were taken on different batches. This error would show up as a shift of the entire curve that is obtained from the used batch. This could explain why $\varphi_s^{(N)}$ is somewhat smaller than $\varphi_b^{(I)}$, which is in principle not possible.

D. Growth rates

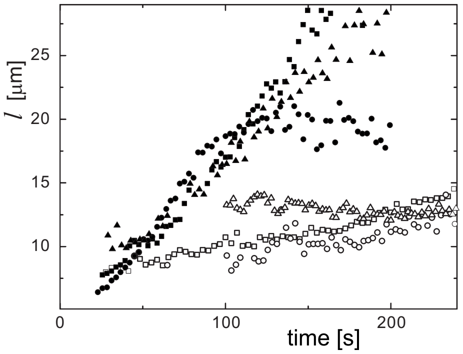

FIG. 12. Time development of the structure size parallel (solid symbols) and perpendicular (open symbols) to the director for three dextran concentrations at a scaled volume fraction of $\varphi_{\text{nem}}=0.30$. Symbols as in Fig. 10(a).

The average size of the structures that are formed during the phase separation can be deduced from the location of the peak of the scattered intensity. The resulting size parallel and perpendicular to the director are plotted in Fig. 12 as a function of time. Surprisingly the size of the formed structures as well as the rate with which they grow do not depend on the attraction. The structure formed in the early stage is isotropic, while the structure growth is anisotropic: the structures are growing faster along the director so that the structure becomes anisotropic with time but the anisotropy in the structure does not seem to increase beyond an aspect ratio of 2. This can also be appreciated from Fig. 13, where the extracted growth rates are plotted against φ_{nem} for all attractions in. The only factor that affects the growth rate is the distance from the phase boundaries. As expected the growth rates go to zero at $\varphi_b^{(N)}$ while the growth rate seems to go to a plateau value around $\varphi_{\text{nem}}=0.25$, which is, as we have seen in the last paragraph, the spinodal point $\varphi_s^{(N)}$.

To access the very early changes, below 25 s, we look at the logarithm of the intensity $\ln(I)$ with time, at different wave vectors q. In this way we probe the length scale of the density fluctuations which has initially the highest probability to grow. This investigation is only done along the director since for the neutral direction the signal-to-noise ratio is too

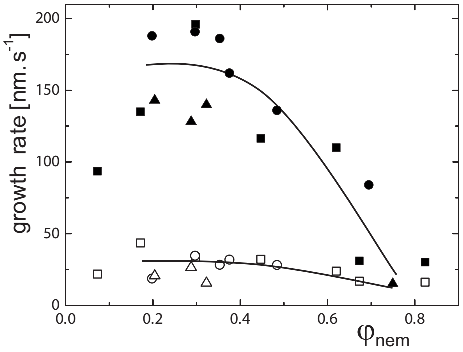

FIG. 13. The growth rate vs φ_{nem} parallel (open symbols) and perpendicular (solid symbols) to the director for three dextran concentrations. Symbols as in Fig. 10(a).

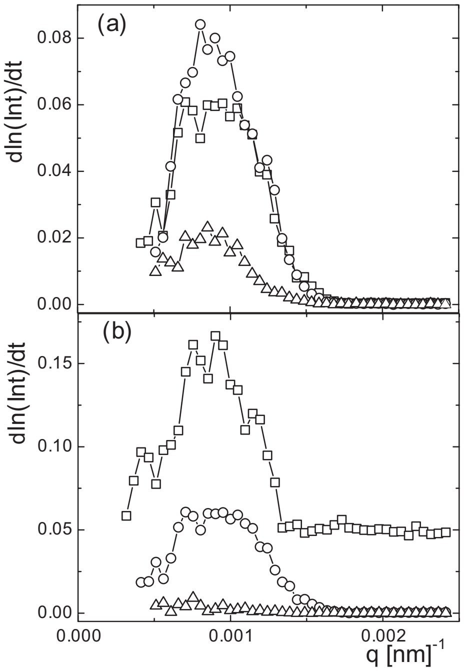

FIG. 14. ln(Int)/dt vs q for (a) three different φ_{nem}: $\varphi_{\text{nem}}=0.20$ (□), $\varphi_{\text{nem}}=0.30$ (○), and $\varphi_{\text{nem}}=0.70$ (△) for the middle dextran concentration and (b) three dextran concentrations at $\varphi_{\text{nem}}=0.2$. Symbols as in Fig. 10(a).

low. In Fig. 14(a) $d\ \ln(I)/dt$ is plotted as a function of q for three different φ_{nem} for sample B. $d\ \ln(I)/dt$ peaks at the same q vector for all φ_{nem}, i.e., independent if it is in the unstable region or far in the metastable region. The length scale over which the system grows fastest turns out to be of the same size as the objects which have just formed at the induction time, i.e., the critical nuclei. For the nucleation-growth regime this means that in the first time window new nuclei are formed continuously with a well defined size, which start growing at the induction time. In Fig. 14(b) $d\ \ln(I)/dt$ vs q is plotted for the three different attractions at a volume fraction of $\varphi_{\text{nem}}=0.2$, i.e., for a spinodal decomposing sample. Again the maximum q of the growth is the same for all attractions, as was found for the induction time. On the other hand the amplitudes are different. This amplitude difference is due to the change in contrast difference between the isotropic and nematic. With increasing dextran concentration the width of the biphasic region increases and thus the density and contrast between the two phases. If we now combine this observation with the observation that both the growth rate of the objects and the induction time do not change with added attraction it is evident that what by eye seems to be a faster phase separation with more dextran added only is an optical effect due to the increase in contrast.

V. DISCUSSION

The main goal of our investigations was to study the extent of the supercooled or superheated regime for dispersions of attractive rods and how it depends on the strength of the attraction. This dependence is given in Fig. 3. The location of the N-I spinodal point almost does not change in the range of attractions studied here. This holds both for the absolute concentration of fd virus (Fig. 3) as well as the fraction of the coexisting nematic phase φ_{nem} [Fig. 10(a)], at least within the experimental error. These observations are confirmed by theory, where it is found that both spinodal lines as a function of the absolute rod concentration are insensitive of the attraction [Fig. 2(a)]. The N-I spinodal line has a weak dependence on the attraction when plotted as a function of φ_{nem} [Fig. 2(b)].

Using φ_{nem} as the scaled concentration we observed that not only the location of the spinodal is insensitive for the attraction, but also the size of the critical nuclei that are formed in the metastable region (Fig. 12) the induction after which they start to grow [Fig. 10(a)] and the rate with which they grow (Fig. 12). This is surprising since in classical nucleation theory these parameters depend on the difference in the chemical potential between the homogeneous and demixed state and the interfacial tension between the two formed phases [1]. These thermodynamic parameters are expected to be quite different, considering that the width of the biphasic region for the highest used dextran concentration has increased with an order of magnitude, see Fig. 3. Given the fact, however, that the relative location between $\varphi_b^{(N)}$ and $\varphi_s^{(N)}$ set the length and time scales, there must be another parameter that determines the nucleation barrier. To gain theoretical understanding of this problem would require a full dynamical density-functional approach, including spatial inhomogeneities [31], to access the evolution of the microstructure over time. Using Monte Carlo simulations Schilling *et al.* [32] did not find an increased orientation correlation for polymer volume fraction comparable to those used in the experiments. If the initial stage of phase separation is dominated by collective rotational diffusion, then both experiments and the simulation [32] hint that depletion interactions do not lead to a stronger preference of rods to align. Simulations by Cuetos *et al.* [19] confirm that the aspect ratio of critical nucleus is less than two independent of supersaturation. The size of the critical nuclei is, however, in the order of 1 rod length, whereas our measurements indicate that the critical nucleus is about 7 rod lengths long independent of the depth of the quench or the attraction strength. This is most clearly shown in Fig. 14 because this figure plots at what density wavelength the intensity growths fastest. Combination of simulations and theory does show that the anisotropy in the surface tension due to the planar anchoring of rods at the interface plays an important role in the formation of a critical nucleus [20]. If this effect dominates the kinetics, it is understandable that attraction between the rods is less important than for example the aspect ratio of the rod. Comparing experiments and simulations one should realize that not only the aspect ratio of the viruses is an order of magnitude bigger than those used in simulations but also that we consider in Fig. 14 the N-I and not the I-N transition.

The only parameter that is influenced by the attraction is the rate at which the gradient in the density grows, as plotted in Fig. 14(b), which is due to the increasing width of the biphasic region. All samples in this plot are quenched into the unstable region, and therefore undergo spinodal decomposition. The curve for the highest attraction, i.e., the highest polymer concentration, shows a clear peak. This is typical for spinodal decomposition that is dominated by translational diffusion [33,34]. At the middle concentration there is still a clear peak, but it is not obvious whether the demixing rate goes to zero for $q \rightarrow 0$ or not. For the lowest concentration of dextran the data are too noisy to draw any conclusions. Our results are somewhat different from earlier experiments performed at 13 mg/ml of dextran, which hinted that the growth rate does not go to zero for $q \rightarrow 0$ [14]. Also the binodal lines found in this paper have sharper features as compared to those published in Ref. [9]. Differences in the polydispersity of the dextran that is used could explain these discrepancies. In the latter paper also a significantly large part of the phase diagram was covered. The reason for the somewhat limited range of attraction studied here is that higher concentrations of dextran would lead to a too high turbidity of the sample and multiple scattering, corrupting the reliability of the measurements. This effect could explain the fact that for the high polymer concentrations in Fig. 14(b) a finite growth rate is found at high q values. Concerning the time dependence of the structure growth we found within experimental error a power law of around one, see the linear dependence in Fig. 12(a), whereas theory predicts a lower power dependence [31]. Possibly we are restricted to the very initial stage of the phase-separation process. The sizes of the coalescing structure formed at later times are too big so that the scattered light hits the beam stop. This problem does not occur when using microscopy as in Refs. [17,35].

With the pressure quench we accessed both the N-I and the I-N transition. As for the N-I transition we observed that also $\varphi_s^{(I)}$ is located in the proximity of $\varphi_b^{(N)}$. With this we confirm the theoretical prediction done in Ref. [7]. What these experiments also show is that for the deepest quenches the initially homogeneous single phase (I or N) undergoes a local phase separation before it completely turns into the new single phase. This mechanism confirms similar observations in computer simulations [20] on initially isotropic hard spherocylinder-polymer mixtures. The fact that we can reach the full nematic state from the isotropic state with the pressure quench is striking since it is known that the concentration difference between the two binodal points is 10%, whereas with a pressure quench to 1000 bar the water is compressed only 5%. Here it is important to note that we are comparing the isotropic phase at 1 bar with the nematic phase at 1000 bar. Assuming that the width of the biphasic region does not change with pressure, it would mean that at high pressure the I-N transition sets in at lower concentrations. It is known that the location of the I-N transition is temperature dependent. This dependency could be linked to the temperature dependence of the flexibility of the fd virus [36]. Similarly, the features of fd virus could changes at high pressures. This change cannot be an irreversible process such as denaturation since the phase transitions are completely reversible. Further experiments are needed to show if is a specific feature like the flexibility of rodlike viruses that changes with pressure. Alternatively, more general features such as the Debye screening length of charged colloids could be pressure dependent.

VI. CONCLUSIONS

We have studied the behavior of supersaturated dispersions of rodlike viruses. Superheated nematic dispersions were prepared by first applying a strong shear flow. Cessation of the shear flow at $t=0$ renders the nematic phase metastable or unstable depending on the concentration, see Fig. 1. We probed the structure formation using small-angle light scattering. With the analysis of the scattering patterns we could access the induction time for structure formation τ_{ind}, the size of the critical nucleus and the growth rate. These parameters were measured over a broad range of attractions as induced by the addition of dextran as a depletion agent. We found that the N-I spinodal point, i.e., the concentration where $\tau_{\mathrm{ind}} \rightarrow 0$, is independent of the attraction, which was confirmed by theoretical calculations. Interestingly, also the absolute induction time, the critical nucleus and the growth rate are found to be insensitive of the attraction if the results are plotted in terms of the fraction occupied by the nematic phase. This observation suggests that concepts of classical nucleation theory are insufficient to understand nucleation processes in anisotropic fluids. We also applied pressure quenches on dispersions of rods without added polymer, thus supercooling or superheating the system. The pressure quenches were deep enough to induce a complete phase transition from the isotropic to the nematic phase and vice versa, which takes place initially via phase separation. As a consequence both the N-I and I-N spinodal could be accessed. By a combination of polarization microscopy, birefringence, and turbidity measurements we were able to construct an experimental analog of the bifurcation diagram of Kayser and Raveché [7].

ACKNOWLEDGMENTS

This work was performed within the framework of the Transregio SFB TR6 “Physics of Colloidal Dispersions in External Fields.” The authors thank R. Tuinier, A. Patkowski, and J. Dhont for stimulating discussions. D. Kleshchanok is thanked for critical reading of the paper. R. Vavrin is thanked for technical assistance with the turbidity measurements. HHW acknowledges the Ramsay Memorial Foundation Trust for financial support.

[1] P. G. Debenedetti, *Metastable Liquids*, 2nd ed. (Princeton university Press, Princeton, 1996).
[2] V. J. Anderson and H. N. W. Lekkerkerker, Nature (London) **416**, 811 (2002).
[3] S. Asakura and F. Oosawa, J. Chem. Phys. **22**, 1255 (1954).
[4] H. N. W. Lekkerkerker, W. C.-K. Poon, P. N. Pusey, A. Stroobants, and P. B. Warren, Europhys. Lett. **20**, 559 (1992).
[5] H. Verduin and J. K. G. Dhont, J. Colloid Interface Sci. **172**, 425 (1995).
[6] L. Onsager, Ann. N.Y. Acad. Sci. **51**, 627 (1949).
[7] R. F. Kayser and H. J. Raveché, Phys. Rev. A **17**, 2067 (1978).
[8] G. J. Vroege and H. N. W. Lekkerkerker, Rep. Prog. Phys. **55**, 1241 (1992).
[9] Z. Dogic, K. R. Purdy, E. Grelet, M. Adams, and S. Fraden, Phys. Rev. E **69**, 051702 (2004).
[10] M. P. B. van Bruggen and H. N. W. Lekkerkerker, Macromolecules **33**, 5532 (2000).
[11] J. Buitenhuis, L. N. Donselaar, P. A. Buining, A. Stroobants, and H. N. W. Lekkerkerker, J. Colloid Interface Sci. **175**, 46 (1995).
[12] C. D. Edgar and D. G. Gray, Macromolecules **35**, 7400 (2002).
[13] J. Tang and S. Fraden, Phys. Rev. Lett. **71**, 3509 (1993).
[14] M. P. Lettinga, K. Kang, A. Imhof, D. Derks, and J. K. G. Dhont, J. Phys.: Condens. Matter **17**, S3609 (2005).
[15] M. P. B. van Bruggen, J. K. G. Dhont, and H. N. W. Lekkerkerker, Macromolecules **32**, 2256 (1999).
[16] M. Ripoll, P. Holmqvist, R. G. Winkler, G. Gompper, J. K. G. Dhont, and M. P. Lettinga, Phys. Rev. Lett. **101**, 168302 (2008).
[17] P. W. Oakes, J. Viamontes, and J. X. Tang, Phys. Rev. E **75**, 061902 (2007).
[18] T. Schilling and D. Frenkel, Phys. Rev. Lett. **92**, 085505 (2004).
[19] A. Cuetos and M. Dijkstra, Phys. Rev. Lett. **98**, 095701 (2007).
[20] A. Cuetos, R. van Roij, and M. Dijkstra, Soft Matter **4**, 757 (2008).
[21] R. Berardi, A. Costantini, L. Muccioli, S. Orlandi, and C. Zannoni, J. Chem. Phys. **126**, 044905 (2007).
[22] R. A. Fine and F. J. Millero, J. Chem. Phys. (1973).
[23] H. N. W. Lekkerkerker and A. Stroobants, Nuovo Cimento **16**, 949 (1994).
[24] R. Tuinier, T. Taniguchi, and H. H. Wensink, Eur. Phys. J. E **23**, 355 (2007).
[25] M. Franco-Melgar, A. J. Haslam, and G. Jackson, Mol. Phys. **106**, 649 (2008).
[26] R. H. Tromp, F. van de Velde, J. van Riel, and M. Paques, Food Res. Int. **34**, 931 (2001).
[27] D. Kleshchanok, R. Tuinier, and P. R. Lang, Langmuir **22**, 9121 (2006).
[28] R. Tuinier, J. Rieger, and C. G. de Kruif, Adv. Colloid Interface Sci. **103**, 1 (2003).
[29] J. Kohlbrecher, A. Bollhalder, R. Vavrin, and G. Meier, Rev. Sci. Instrum. **78**, 125101 (2007).
[30] P. Holmqvist, M. P. Lettinga, J. Buitenhuis, and J. K. G. Dhont, Langmuir **21**, 10976 (2005).
[31] J. K. G. Dhont and W. J. Briels, Phys. Rev. E **72**, 031404 (2005).
[32] T. Schilling, S. Jungblut, and M. A. Miller, Phys. Rev. Lett. **98**, 108303 (2007).
[33] A. Matsuyama, R. M. L. Evans, and M. E. Cates, Phys. Rev. E **61**, 2977 (2000).
[34] J. W. Winters, T. Odijk, and P. van der Schoot, Phys. Rev. E **63**, 011501 (2000).
[35] A. H. Chowdhury and P. S. Russo, J. Chem. Phys. **92**, 5744 (1990).
[36] J. Tang and S. Fraden, Biopolymers **39**, 13 (1996).

Part III

Dispersions of rod-like particles under shear flow

Chapter 9

Non-equilibrium phase behaviour of rod-like viruses under shear flow

INSTITUTE OF PHYSICS PUBLISHING JOURNAL OF PHYSICS: CONDENSED MATTER

J. Phys.: Condens. Matter **16** (2004) S3929–S3939 PII: S0953-8984(04)79970-1

Non-equilibrium phase behaviour of rod-like viruses under shear flow

M P Lettinga and J K G Dhont

IFF, Institut Weiche Materie, Forschungszentrum Jülich, D-52425 Jülich, Germany

E-mail: p.lettinga@fz-juelich.de

Received 27 April 2004
Published 10 September 2004
Online at stacks.iop.org/JPhysCM/16/S3929
doi:10.1088/0953-8984/16/38/011

Abstract

We present the non-equilibrium phase diagram of rod-like colloids (*fd*-viruses) under shear flow. The shear-induced displacement of the isotropic–nematic binodal is obtained from time resolved rheology measurements. Vorticity banding is observed within the biphasic region, as bounded by the binodal. Here, in the stationary state, regular, millimetre sized bands with mutually differing orientational order are stacked along the vorticity direction. For the fully nematic phase we determine the location of transition lines from tumbling to either wagging or flow aligning, depending on the concentration. The location of these dynamical transition lines agree with theory for hard rods, when scaling to the orientational order parameter in equilibrium.

1. Introduction

Dispersions of rods are sensitive to external fields such as shear flow or a magnetic field, since they can undergo transitions in orientational order. On increasing the concentration, a first-order transition occurs, from an disordered isotropic state to an orientationally ordered nematic state. The binodal concentrations for this isotropic–nematic phase transition are fully determined by the balance between orientational and translational entropy when only excluded volume interactions are involved. When rods are subjected to shear flow, the rod orientation will be affected, so the concentration at which the transition occurs will be shear rate dependent. In other words, the location of the binodal will change on applying shear flow. The transition will cease to occur at sufficiently high shear rates where shear aligning forces dominate over inter-rod forces. The binodal thus closes on itself in the shear rate versus concentration plane.

At finite shear rates, banded structures of macroscopic size can be formed. There are two such structures to be distinguished: vorticity banded and gradient banded structures. In the former case, a regular alternating banded structure extends along the vorticity direction, where the orientational order in the two kinds of bands is different. The latter type of banding consists of coexisting regions (the bands) with different shear rates extending along the gradient direction [1–3]. For rigid hard rods, gradient banding is predicted to occur in a very limited region close to the non-equilibrium critical point in the shear rate versus concentration plane [1, 4].

In addition, in the fully nematic state, stationary shear flow can induce oscillatory motion of the nematic director. That is, the shear aligned state becomes unstable in some regions in the shear rate versus concentration diagram. The trajectory which is described by the tip of the director is very sensitive to the applied shear rate and the rod concentration. At low shear rates the director undergoes a continuous tumbling motion in the plane defined by the flow and the gradient of the flow, while at high shear rates the rods align with the flow [5, 6]. At intermediate shear rates multiple solutions to the Doi–Edwards equation are obtained, which are sensitive to the initial orientation of the director [7, 8]. In a small region of the phase diagram even chaotic behaviour of the stress is found. A full theoretical phase diagram of this dynamic behaviour is presented in the contribution of Hess and Kröger in this Special Issue [9].

Experimental indications of the instabilities mentioned above have been found in various kinds of systems. Wormlike micelles at low concentrations show shear-induced phase transitions and structure formation [3, 2, 10], whereas at higher concentrations tumbling behaviour was found [11]. Also hydroxypropylcellulose, which is a liquid crystalline polymer, undergoes shear-induced phase transitions [12] at low concentrations and shows a tumbling behaviour at high concentrations [13]. Evidence for the transition from tumbling to wagging has been found by Mewis *et al* [14] and Grosso *et al* [15], using nematic solutions of polybenzyl glutamate, another liquid crystalline polymer. Direct comparison of these experiments with theory for hard rod suspensions, however, is not straightforward. In the case of polymeric liquid crystals the analysis is hampered by the fact that the inter-domain stress dominates the response at higher concentrations [16]. For wormlike micelles comparison between theory and experiment is complicated by shear-dependent scission–association kinetics [17]. To gain fundamental understanding of the above-mentioned phenomena, the ideal system would be a system of monodisperse hard rods with a very large aspect ratio (say $L/D > 100$, where L is the length and D is the thickness of the rod). For such rods, Onsager showed that in the absence of shear flow the isotropic–nematic transition concentrations can be calculated exactly on the basis of a second-virial-coefficient approach [18]. One of the few systems available that comes close to the ideal system is that of *fd*-virus suspensions. The *fd*-virus is a rodlike virus, inherently monodisperse, very thin and relatively stiff. Its equilibrium behaviour can be quantitatively predicted, taking into account the semi-flexible nature of the rods and their charge [19]. Furthermore, as will become clear in the present paper, contributions to the stress from domain boundaries are relatively small, so theoretical predictions that apply for homogeneous dispersions of rods can be employed. Moreover, we already successfully used this system to determine the average isotropic–nematic spinodal [20].

In this paper we will therefore use *fd*-virus dispersions in shear flow to access the above-mentioned shear-induced instabilities. The goal is then to determine the full non-equilibrium phase diagram (in the shear rate versus concentration plane) and show the connection between the different regions. For the director instability diagram we will discuss a direct comparison with the theory of hard rods. For the determination of the non-equilibrium binodal and the shear banding regime we added polymer to the dispersion in order to induce some attraction between the rods. This causes the biphasic region to widen, such that it is easier to access the concentration dependence of the binodal and to enhance the phase separation kinetics. We use rheology to determine the location of the paranematic–nematic binodal of sheared suspensions. We perform *in situ* macroscopic and microscopic birefringence measurements to study vorticity shear band formation. Rheology and *in situ* microscopy are used to study the director instabilities in the fully nematic phase. In the discussion we summarize the results and suggest a connection between the different phenomena.

2. Experimental details

The viscosity and stress response was measured using an ARES strain controlled rheometer (Rheometric Scientific, Piscataway, NJ). A double-Couette geometry was used because of the fairly low viscosity of the samples under study. Microscopy under shear has been carried out using a Linkam plate–plate shear cell and a standard polarizing microscope. We used a home-built shear cell with a Couette geometry of optical glass in order to monitor the birefringence of the sheared sample. The inner cylinder has a radius of 21.5 mm; the gap width is 2.47 mm. A periscope was inserted into the inner cylinder which guides polarized light through one gap only. Transmitted light was detected through a second polarizer which is used as an analyser.

The physical characteristics of the bacteriophage *fd* are: length $L = 880$ nm; diameter $D = 6.6$ nm; persistence length 2.2 μm; and the number of elementary charges per unit length is around 10 e^- nm^{-1} at pH 8.2 [21]. Also, *fd* exhibits isotropic, cholesteric and smectic phases with increasing concentration [22, 23]. The *fd* virus was prepared according to standard biological protocols found in [24], using the XL1 blue strain of *E. coli* as the host bacterium. The standard yield is ≈50 mg of *fd* per litre of infected bacteria, and virus is typically grown in 6 l batches. The virus was purified by repetitive centrifugation (108 000 g for 5 h) and finally re-dispersed in a buffer. A buffer of 20 mM tris-HCl at pH 8.2 was used for the measurements in the fully nematic phase (isotropic to nematic phase separation occurs at 11 mg ml^{-1}). The same buffer with an extra 100 mM NaCl was used for the measurements in the biphasic region, and 12 mg ml^{-1} of dextran (507 kd, Sigma-Aldrich) was added in order to widen the biphasic region [25].

3. Theory

For spatially homogeneous dispersions of rigid rods, the *orientational* probability density function, or orientational distribution function (P), is sufficient to describe the state of the system. The temporal evolution of the orientational distribution function in shear flow can be found by solving the equation of motion of the orientational distribution function, given by the N-particle Smoluchowski equation [1, 5, 26]

$$\frac{\partial P(\hat{\mathbf{u}},t)}{\partial t} = D_{\mathrm{r}}\hat{\mathcal{R}}\cdot\left\{\hat{\mathcal{R}}P(\hat{\mathbf{u}},t) + DL^2\bar{\rho}P(\hat{\mathbf{u}},t)\hat{\mathcal{R}}\oint \mathrm{d}\hat{\mathbf{u}}'\, P(\hat{\mathbf{u}}',t)|\hat{\mathbf{u}}'\times\mathbf{u}|\right\} - \hat{\mathcal{R}}\cdot P(\hat{\mathbf{u}},t)\hat{\mathbf{u}}\times(\mathbf{\Gamma}\cdot\hat{\mathbf{u}}). \qquad (1)$$

Here $\mathcal{R}(\cdots) = \hat{\mathbf{u}}\times\nabla_{\hat{\mathbf{u}}}(\cdots)$ is the rotation operator with respect to the orientation $\hat{\mathbf{u}}$ of a uniaxial rod, $\bar{\rho}$ is the number density of rods, D is the thickness and L is the length of the rods. Furthermore, $\mathbf{\Gamma} = \dot{\gamma}\hat{\mathbf{\Gamma}}$ is the velocity gradient tensor and $\dot{\gamma}$ the shear rate:

$$\hat{\mathbf{\Gamma}} = \begin{pmatrix} 0 & 1 & 0 \\ 0 & 0 & 0 \\ 0 & 0 & 0 \end{pmatrix}, \qquad (2)$$

complying with a flow in the x-direction with its gradient in the y-direction.

In the absence of flow, equation (1) reproduces Onsager's thermodynamic approach for very long and thin hard rods. In the presence of shear flow, new phenomena are predicted by equation (1) in addition to the paranematic–nematic phase transition. Marrucci and Maffettone [5] were the first to solve the equation of motion for the orientational distribution

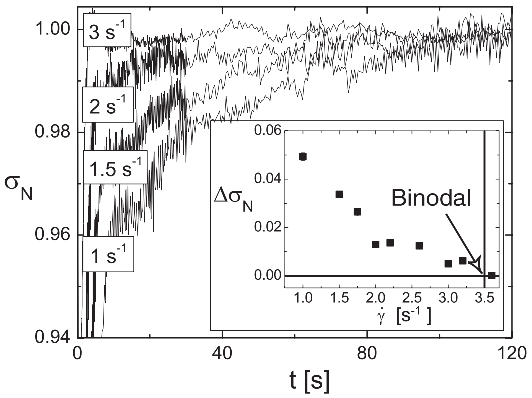

Figure 1. Determination of the binodal for [*fd*] = 20 mg ml^{-1} and [*dextran*] = 12.5 mg ml^{-1}, using shear rate quenches from the fully nematic state to the biphasic region and measuring the normalized stress $\sigma_N(t) = \sigma(t)/\sigma(t \to \infty)$. The initial shear rate was $\dot{\gamma} = 7\ \mathrm{s}^{-1}$ and the low shear rates were varied between $\dot{\gamma} = 1.0\ \mathrm{s}^{-1}$ (bottom) and $\dot{\gamma} = 3\ \mathrm{s}^{-1}$ (top). The inset shows the magnitude of the stress response $\Delta\sigma_N$, obtained from the fit to $\sigma_N = 1 - \Delta\sigma_N e^{-t/\tau}$, as a function of the shear rate.

function numerically, restricting consideration to two dimensions in order to reduce the computational effort. They found that the director undergoes a tumbling motion with respect to the flow direction, resulting in a negative normal stress N_1. Larson used a more general solution, relying on an approximation for the excluded volume interaction term (the last term in equation (1)), in the form of a closure relation, in order to derive from equation (1) a closed equation of motion for the orientational order parameter tensor. He predicted a transition from tumbling to wagging, where the director oscillates between two small angles at somewhat higher shear rates, and finally to flow aligning at high shear rates. The use of approximation for the interaction contribution, however, can greatly bias the results, as has been discussed by Feng *et al* [27]. The location of the transitions in the shear rate versus concentration diagram is especially sensitive to the approximation, and in fact no satisfactory approximation has been found previously. In this paper we will use a finite element method to numerically solve the full equation of motion (1) for the orientational distribution function, without any approximation.

4. The non-equilibrium binodal

During the isotropic–nematic phase separation, ellipsoidal droplets (tactoids) of one phase dispersed in a background of the other phase exist. When shear is applied to the system, the tactoids will be distorted and long stripes along the flow will be formed (see the left micrograph in figure 2) and the rods in the paranematic phase will gain some ordering due to flow alignment. When approaching the binodal we observed that the contrast between the elongated tactoids and the background phase disappears, with the result that light scattering and microscopy are not useful tools for obtaining the position of the binodal. The viscosity of a rod dispersion, on the other hand, is very sensitive to ordering in the system, which makes rheology a more suitable tool for obtaining the binodal point: an increase in the viscosity is expected when a system which is forced into the fully nematic phase by applying a high shear rate is quenched into the biphasic region through a sufficient reduction of the shear rate. In figure 1 we show an example of such an experiment, where we plot the normalized stress $\sigma_N(t) = \sigma(t)/\sigma(t \to \infty)$ as a function of time after the shear rate is quenched. The initial shear rate was 7 s^{-1}, while the

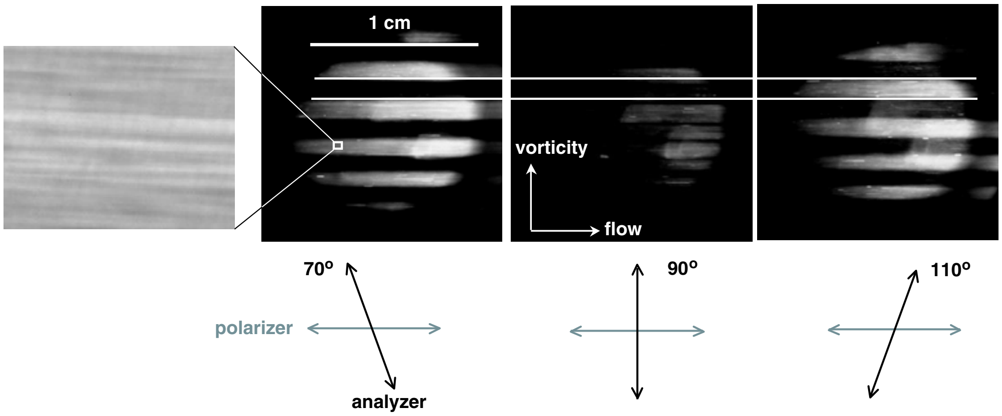

Figure 2. Three images of shear bands stacked in the vorticity direction. The images are taken by using a 1 cm radius polarized light source placed in the centre of the Couette shear cell. The analyser is placed at the other side of the gap under 70°, 90° and 110° respectively. Also shown is a close-up taken with a home-made polarization microscope within the bands, showing typical elongated regions of nematic and paranematic phases as discussed above. The shear bands are about 1 mm in height. The typical height of the elongated regions within the bands is about 10–20 μm.

(This figure is in colour only in the electronic version)

final shear rate is varied between 1.5 and 3 s^{-1}. We fitted the response to a single exponential ($\sigma_N = 1 - \Delta\sigma_N e^{-t/\tau}$), disregarding the initial fast response, which is probably due to relaxation of the pure nematic phase. The viscosity increases with a typical exponential time constant of around $\tau = 15$ s. The magnitude of the exponent $\Delta\sigma_N$ is set by the amount that the ordering in the nucleated paranematic tactoids deviates from the ordering in the nematic phase. Since the ordering in the paranematic phase increases with shear rate, it will approach the ordering of the nematic phase at the binodal. Thus $\Delta\sigma_N$ will vanish at the binodal, as can be seen in the inset in figure 1. The full binodal is found from such experiments for various concentrations obtained by mixing coexisting equilibrium isotropic and nematic phases at different ratios. The binodal is plotted in figure 3. Note that the position of the binodal very much depends on the amount of polymer added to the system. Preliminary investigations show that position of the binodal shifts to higher shear rates with increasing polymer content.

5. Vorticity shear banding within the biphasic region

In order to study the birefringence of the sheared biphasic system, we arranged a polarizer and analyser in such a way that the birefringence throughout a single gap was detected. Doing so, we observed, in addition to the formation of tactoids after a shear rate quench, the formation of macroscopic bands. The bands are stacked in the vorticity direction, indicative of an instability in that direction. The bands are up to a millimetre in height (see figure 2) and form in about 12 h. Both the size of the bands and the timescale on which they are formed are orders of magnitude larger than those for the microscopic phase separation—that is, the formation of tactoids.

Interestingly, as can be seen in figure 2, the typical biphasic structure is maintained inside the bands, and also no concentration differences are observed between the bands (data not shown). The contrast between the bands is fully determined by the differences in the orientational order. Keeping the polarizer fixed along the flow direction, the intensity of the bands can be inverted by changing the orientation of the analyser. When the angle is less than

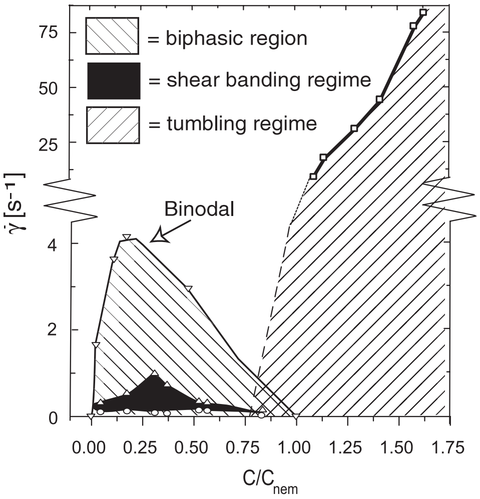

Figure 3. The experimental phase diagram of the *fd*-virus under shear. The negative hatched region indicates the biphasic region. Here the sample also contains polymer (dextran), in order to widen the concentration difference of the two coexisting phases. The black region indicates the region where the sample exhibits shear banding, which is completely contained within the two-phase region. The positive hatched region is the region where the director of the nematic phase tumbles with respect to the shear flow. The boundary given by the solid line is the experimental points in the fully nematic phase; the dashed line indicates that in the biphasic region tumbling already takes place.

90°, one band will light up; when it is more than 90°, the other band will light up. Changing the orientation of both the polarizer and analyser with respect to the shear flow while keeping them crossed does not cause a change of the relative intensity of the bands. The intensity will just increase to reach a maximum at 45° with the shear flow. Combining the two observations, it can be concluded that the polarized light is not retarded within the bands, but rotated. This means that the average orientation of the rods is tilting towards or from the vorticity direction depending on the band. This is similar to what is happening in the cholesteric phase; however, in this case the tilt is occurring in the presence of the biphasic structure.

The region in the phase diagram where the bands are formed (the black region in figure 3) is limited to the biphasic region. On the low concentration side, banding abruptly ceases to occur on crossing the binodal. On the high concentration side, banding ceases to occur at a concentration where the sample contains about 70% of nematic phase. Interestingly, at these concentrations oscillations in the viscosity after a step down of the shear rate are also observed (data not shown). As will be discussed later, these oscillations are reminiscent of instabilities in the nematic director. The concentration at which the highest shear rate is reached for which bands are still observed is somewhat higher than the concentration where the binodal peaks. The bands start to form at low but non-zero shear rates. The shear band region is fully contained within the biphasic region, defined as the region that is bounded by the binodal.

The fact that banding occurs only in the biphasic region suggests that inhomogeneities that are intrinsically present in this region are responsible for the vorticity banding instability.

6. Director dynamics in the fully nematic phase

Contrary to observations on the otherwise isotropic phase, the viscosity in the nematic phase does not monotonically shear thin, as can be seen in figure 4(a). There are two regions of shear

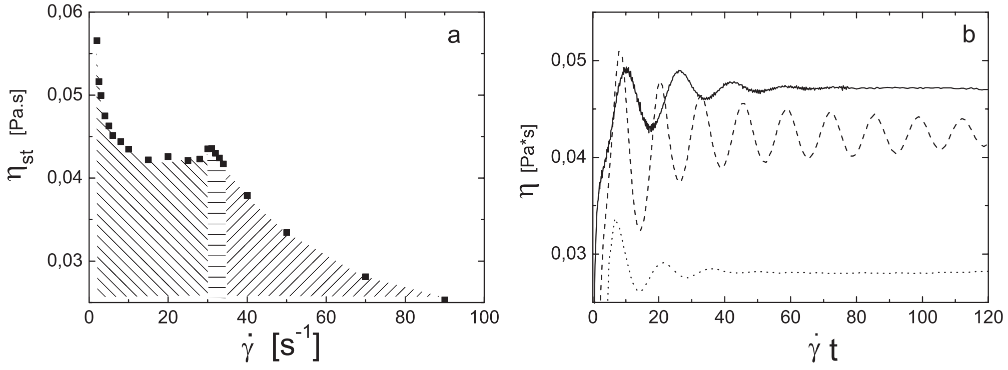

Figure 4. (a) The stationary viscosity as a function of the shear rate at an *fd*-virus concentration of 19 mg ml^{-1} or $C/C_{\mathrm{nem}} = 1.3$. (b) The response of the viscosity to a flow reversal as a function of the strain for three different shear rates (solid curve: $\dot{\gamma} = 4\ \mathrm{s}^{-1}$; dashed curve: $\dot{\gamma} = 33\ \mathrm{s}^{-1}$; dotted curve: $\dot{\gamma} = 70\ \mathrm{s}^{-1}$). The negatively hatched region in (a) corresponds to a phase where oscillations are strongly damped (solid curve in (b)); the horizontally hatched region in (a) corresponds to a phase where the oscillations are weakly damped (dashed curve in (b)); the positively hatched region in (a) corresponds to a phase of very strongly damped oscillations (dotted curve in (b)).

thinning separated by a small local maximum in the viscosity. This local maximum indicates that at this shear rate the ordering in the system is partly lost, contrary to what is expected when the degree of alignment increases with the shear rate.

In order to understand the local maximum in viscosity and to detect possible oscillatory viscoelastic responses, one needs to access the dynamic behaviour by means of transient experiments such as step down and flow reversal experiments. As mentioned in the last paragraph, the response of a pure nematic phase to a step down of the shear rate will lead to an oscillatory response of the viscosity. Likewise, an oscillatory response is seen when performing flow reversal, where the direction of the flow is suddenly reversed without changing the absolute value of the shear rate [14]. In figure 4(b) we show typical responses of the viscosity after a flow reversal for shear rates in three characteristic regions: a region where the response shows strongly damped oscillations, a region where the response is weakly damped and a region where the response is very strongly damped. Interestingly, the region of the weakly damped oscillations starts at the point where the viscosity reaches its local maximum.

This type of behaviour has been predicted by Larson, who solved the equation of motion for the orientational distribution function in an approximated way [6]. Larson argued that the nematic phase will tumble due to the torque that is exerted on those rods which have an orientation in the wings of the orientation distribution. This torque is then transmitted to the rest of the distribution due to strong excluded volume interactions between the rods. However, during the tumbling process the distribution passes the angle corresponding to the extensional direction of the velocity gradient tensor in shearing flow. At this point the distribution of the rods will be distorted with the result that the ordering will be partly lost. With increasing shear rate this effect becomes stronger and as a consequence the experimentally observed viscosity will increase. At a critical shear rate this effect is so strong that the ordering is completely lost. Since isotropically distributed rods flow align, the director will not pass the angle of extensional flow and return to the flow direction. This is the point where the so-called wagging regime is entered and where the viscosity will reach its maximum.

The damping of oscillations in the tumbling regime is probably caused by interaction between different nematic domains [28]. The explanation of the transition from strongly damped to weakly damped is then that in the wagging state the director oscillates around the

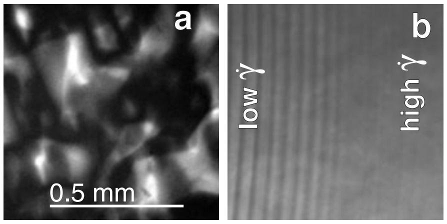

Figure 5. The structure in the nematic phase at rest (a) and at a shear rate of 250 s^{-1} (b) at a concentration of 25 mg ml^{-1}, as observed by using a shear cell with a plate–plate geometry under the polarizing microscope. Note that the shear rate increases somewhat when going from the left to the right of this picture, since a plate–plate geometry is used.

flow direction. Compared to the tumbling state, the wagging state corresponds to a more ordered state where the polydomain structure will have disappeared. This disappearance of polydomain structure at the shear rate where the viscosity reaches its maximum is demonstrated in figure 5. Here we use polarization microscopy in combination with an optical shear cell to monitor the structure. It can be clearly seen that structure disappears at a very well defined shear rate, since for a plate–plate geometry the shear rate is increasing with increasing distance from the centre. Another interesting feature shown in this image is that at this shear rate and concentration shear bands are formed. The origin of these bands, which are only formed at higher concentrations, is not clear yet and further experiments are needed. The presence of the bands does however facilitate the identification of the point where the domain structure disappears. At lower concentrations no bands are observed. Since it takes a force of 108 000 g over 5 h to sediment *fd*-virus particles over a distance of a few centimetres, which is orders of magnitude larger than the forces resulting from gradients in the shear rate, inhomogeneities as a result of shear rate gradients are negligibly small.

We can now identify the shear rate where the maximum viscosity is reached with the shear rate where the tumbling region ends and wagging sets in. Making this identification for concentrations between $C = 1.1 * C_{\mathrm{nem}}$ and $2.5 * C_{\mathrm{nem}}$ (where C_{nem} is the binodal concentration beyond which the pure nematic state is stable), we can produce a phase diagram plotting the transition shear rate as a function of concentration (■ in figure 3). In order to compare experiments with theory the shear rate and the concentration need to be expressed in dimensionless units. According to the Smoluchowski equation (1), the dimensionless shear rate, the Peclet number *Pe*, is the shear rate divided by the rotational diffusion of the rods at infinite dilution. The latter can be measured by means of electric birefringence measurements [29]. When scaling the concentration, one should consider the particles which are used not to be ideal rods, since they are somewhat flexible and charged. Therefore, the dynamic phase behaviour for ideal rods is probably *not* recovered when an experimental binodal concentration is simply scaled to Onsager's theoretical binodal concentration. It is more reasonable to compare the dependence of the transition shear rate on the orientational order parameter $P_2 = \langle \frac{1}{2}(3\cos^2(\theta) - 1)\rangle$ describing the average ordering of the rods, where θ refers to the angle between the rod and the director of the nematic phase. Since the ordering of the rods directly reflects the interaction between the rods, it is a more reliable parameter than the concentration. For *fd*-virus it was shown that order parameter was well predicted by theory, when taking the flexibility and charge of the particles into account [19]. In figure 6 we plot both comparisons of experiment and theory, rescaling the concentration to the higher binodal concentration (a) and to the order parameter in equilibrium (b). The theoretical points in figure 6 are obtained by tracking the angle between the director and the flow direction in

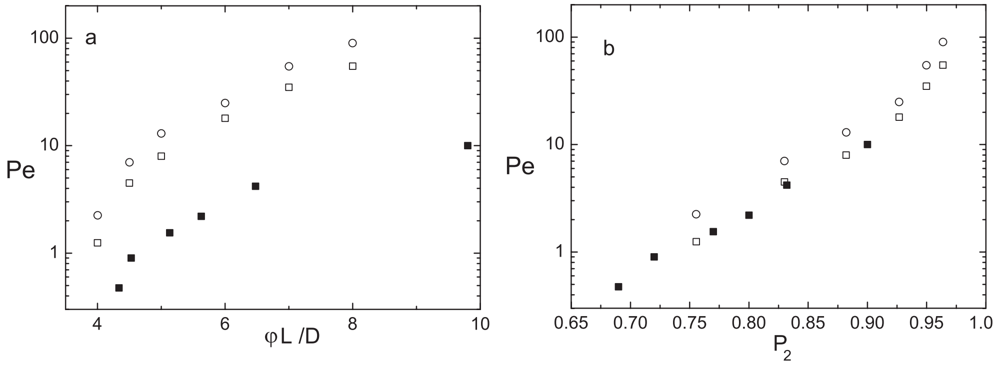

Figure 6. Comparison between the experimental and theoretical dimensionless transition shear rates *Pe* as a function of the concentration scaled to the concentration at the isotropic–nematic transition (a) and as a function of the equilibrium order parameter $P_2 = \langle \frac{1}{2}(3\cos^2(\theta) - 1)\rangle$, obtained using experimental data of Purdy *et al* [19] and equation (1) for zero shear. Here θ refers to the angle of the rod with respect to the director of the nematic phase. For experiments, the tumbling–wagging transition is identified via the shear rate where the viscosity shows a local maximum (■). For theory, the tumbling–wagging transition (□) and wagging–flow aligning transition (○) are found by solving the equation of motion (1) for the orientational distribution function. The experimental shear rate is in both figures scaled to the Peclet number with the rotational diffusion at infinite dilution (21 s^{-1} [29]).

time, solving equation (1) numerically. The time dependence of this angle defines whether the system is in the tumbling, wagging or flow aligning regime.

Clearly, the scaling with respect to the order parameter gives the best comparison between experiment and theory; note that *no* adjustable parameters were used in the theory. Apparently the above-mentioned non-ideal features of the *fd*-virus are accounted for when scaling results to the same orientational order parameter. In addition, the polydomain structure of the sample, which is not included in the theory, does not seem to hamper the comparison. This is probably due to two factors. First, the viscosity of the dispersion is relatively low. It is for example about three orders of magnitude lower than that of typical polymeric liquid crystals such as PBG [16]. Second, at the transition, polydomain structure has disappeared and is therefore not important any longer. Thus, we believe that in principle all the physics is contained in the equation of motion given by equation (1). To describe vorticity banding, however, equations of motion that include spatial inhomogeneities must be derived (see [30, 31] for the derivation of such an equation).

7. Discussion and conclusion

The aim of this paper is to give an experimental overview of the phase behaviour under shear flow and the flow behaviour of rod dispersions, ranging from concentrations where the isotropic–nematic phase transition occurs up to concentrations deep into the nematic phase. A summary of the phase and flow behaviour is given in the preliminary non-equilibrium phase diagram in figure 3. As far as we know, this is the first attempt to experimentally determine a complete phase diagram under shear flow of stiff rods, ranging from low concentrations, through the biphasic region, far into the nematic region.

Measurements in the biphasic region have been performed on rod–polymer mixtures at high ionic strength, while for the pure nematic phase measurements have been performed without polymer and at low ionic strength. Comparing values for the shear rates for these two regions as given in our phase diagram should therefore be done with caution. For example, the shear rates at which the non-equilibrium binodal is found will decrease with decreasing polymer concentration. Still missing in the experimental phase diagram is the location of spinodals for a system of attractive rods and in particular the location of the critical point. Systematic measurements to determine the full phase diagram for several polymer concentrations are in progress.

Vorticity banding is found to occur only within the two-phase region as bounded by the non-equilibrium binodal. Vorticity banding is therefore most probably the result of a normal stress related instability induced by inhomogeneities that are formed after quenching into the two-phase region. Theoretically, the challenge is to incorporate stresses that are generated by spatial inhomogeneities in orientational order (and possibly concentration) in the Navier–Stokes equation. A first attempt to derive appropriate equations of motion for stiff, long and thin rods on a microscopic level can be found in [30, 31]. Gradient banding is expected to occur close to the critical point due to critical slowing down of rotational diffusion. However, theory predicts gradient banding to occur only in a very small concentration interval near the critical point. Furthermore, theory predicts a very small difference between the shear rates in the two bands. Gradient banding of stiff rods is therefore probably very difficult to detect.

The measurements for the fully nematic phase show that the Smoluchowski theory for homogeneous rod suspensions quantitatively describes tumbling and wagging in *fd*-virus suspensions as long as the concentrations at which the transitions occur are scaled to the order parameter of the dispersion. Stresses arising from polydomains are of minor importance for these kinds of dispersions. The combination of *fd*-virus suspensions with the extension of the theory towards inhomogeneous systems is therefore promising for the full understanding of rods under shear.

Acknowledgments

We thank Zvonimir Dogic for initiating this project and for many discussions. We thank Hao Wang for the theoretical calculations. We thank Jan Vermant for the use of the rheometer and the many discussions.

References

[1] Dhont J K G 1999 A constitutive relation describing the shear-banding transition *Phys. Rev.* E **60** 4534–44

[2] Boltenhagen P, Hu Y, Matthys E F and Pine D J 1997 Observation of bulk phase separation and coexistence in a sheared micellar solution *Phys. Rev. Lett.* **79** 2359–62

[3] Lerouge S, Decruppe J P and Humbert C 1998 Shear banding in a micellar solution under transient flow *Phys. Rev. Lett.* **81** 5457–60

[4] Olmsted P D and Lu C-Y D 1999 Phase separation of rigid-rod suspensions in shear flow *Phys. Rev.* E **60** 4397–415

[5] Marrucci G and Maffettone P L 1989 Description of the liquid-crystalline phase at high shear rates *Macromolecules* **22** 4076

[6] Larson R G 1990 Arrested tumbling in shearing flows of liquid crystal polymers *Macromolecules* **23** 3983–92

[7] Faraoni V, Grosso M, Crescitelli S and Maffettone P L 1999 The rigid-rod model for nematic polymers: an analysis of the shear flow problem *J. Rheol.* **43** 829

[8] Forest M G and Wang Q 2003 Monodomain response of finite-aspect-ratio macromolecules in shear and related linear flows *Rheol. Acta* **42** 20–46

[9] Hess S and Kröger M 2004 Regular and chaotic orientational and rheological behavior of liquid crystals *J. Phys.: Condens. Matter* **16** S3835–59

[10] Britton M M and Callaghan P T 1997 Two-phase shear band structures at uniform stress *Phys. Rev. Lett.* **78** 4930–3

[11] Caputo F E, Ugaz V M, Burghardt W R and Berret J-F 2002 Transient 12 plane small-angle x-ray scattering measurements of micellar orientation in aligning and tumbling nematic surfactant solutions *J. Rheol.* **46** 927–46

[12] Grizzuti N and Maffettone P L 2003 Quiescent and flow-induced transitional behavior of hydroxypropylcellulose solutions *J. Chem. Phys.* **118** 5195–200

[13] Hongladarom K, Secakusuma V and Burghardt W R 1994 Relation between molecular orientation and rheology in lyotropic hydroxypropylcellulose solutions *J. Rheol.* **38** 1505–23

[14] Mewis J, Mortier M, Vermant J and Moldenaers P 1997 Experimental evidence for the existence of a wagging regime in polymeric liquid crystals *Macromolecules* **30** 1323–8

[15] Grosso M, Crescitelli S, Somma E, Vermant J, Moldeaers P and Maffettone P L 2003 Prediction and observation of sustained in a shear liquid crystalline polymer *Phys. Rev. Lett.* **90** 098304

[16] Walker L M, Mortier M and Moldenaers P 1996 Concentration effects on the rheology and texture of pbg/m-cresol solutions *J. Rheol.* **40** 967–81

[17] Cates M E 1987 Reptation of living polymers: dynamics of entangled polymers in the presence of reversible chain–scission reactions *Macromolecules* **20** 2289–96

[18] Onsager L 1949 The effect of shape on the interaction of colloidal particles *Ann. New York Acad. Sci.* **51** 627–59

[19] Purdy K R, Dogic Z, Fraden S, Rühm A, Lurio L and Mochrie S G J 2003 Measuring the nematic order of suspensions of colloidal fd virus by x-ray diffraction and optical birefringence *Phys. Rev.* E **67** 031708

[20] Lenstra T A J, Dogic Z and Dhont J K G 2001 Shear-induced displacement of isotropic–nematic spinodals *J. Chem. Phys.* **114** 10151–62

[21] Fraden S 1995 *Observation, Prediction, and Simulation of Phase Transitions in Complex Fluids* (*NATO-ASI Series C* vol 460) ed M Baus, L F Rull and J P Ryckaert (Dordrecht: Kluwer–Academic) pp 113–64

[22] Dogic Z and Fraden S 2000 Cholesteric phase in virus suspensions *Langmuir* **16** 7820

[23] Dogic Z and Fraden S 1997 Smectic phase in a colloidal suspension of semiflexible virus particles *Phys. Rev. Lett.* **78** 2417

[24] Sambrook J, Fritsch E F and Maniatis T 1989 *Molecular Cloning: A Laboratory Manual* 2nd edn (Cold Spring Harbor, NY: Cold Spring Harbor Laboratory Press) chapter 4

[25] Dogic Z and Fraden S 2001 Development of model colloidal liquid crystals and the kinetics of the isotropic–smectic transition *Phil. Trans. R. Soc.* A **359** 997

[26] Doi M and Edwards S F 1986 *The Theory of Polymer Dynamics* (Oxford: Oxford University Press)

[27] Feng J, Chaubal C V and Leal L G 1998 Closure approximations for the Doi theory: which to use in simulating complex flows of liquid-crystalline polymers? *J. Rheol.* **42** 1095–119

[28] Larson R G and Doi M 1991 Mesoscopic domain theory for textured liquid crystalline polymers *J. Rheol.* **35** 539–63

[29] Kramer H, Deggelmann M, Graf C, Hagenbtichle M, Johner C and Weber R 1992 Electric birefringence measurements in aqueous fd virus solutions *Macromolecules* **25** 4325–8

[30] Dhont J K G and Briels W J 2002 Stresses in inhomogeneous suspensions *J. Chem. Phys.* **117** 3992–9

[31] Dhont J K G and Briels W J 2003 Inhomogeneous suspensions of rigid rods in flow *J. Chem. Phys.* **118** 1466–78

Chapter 10

Flow behavior of colloidal rod-like viruses in the nematic phase

Flow Behavior of Colloidal Rodlike Viruses in the Nematic Phase

M. Paul Lettinga*

IFF, Institut Weiche Materie, Forschungszentrum Jülich, D-52425 Jülich, Germany

Zvonimir Dogic

Rowland Institute at Harvard, Harvard University, Cambridge Massachusetts 02142

Hao Wang

Department of Physics, North Dakota State University, Fargo, North Dakota 58105

Jan Vermant

Department of Chemical Engineering, Katholieke Universiteit Leuven,
de Croylaan 46, B-3001 Leuven, Belgium

Received January 14, 2005. In Final Form: May 24, 2005

The behavior of a colloidal suspension of rodlike *fd* viruses in the nematic phase, subjected to steady state and transient shear flows, is studied. The monodisperse nature of these rods combined with relatively small textural contribution to the overall stress make this a suitable model system to investigate the effects of flow on the nonequilibrium phase diagram. Transient rheological experiments are used to determine the critical shear rates at which director tumbling, wagging, and flow-aligning occurs. The present model system enables us to study the effect of rod concentration on these transitions. The results are in quantitatively agreement with the Doi−Edwards−Hess model. Moreover, we observe that there is a strong connection between the dynamic transitions and structure formation, which is not incorporated in theory.

I. Introduction

When subjected to shear flow, liquid crystals can exhibit a variety of surprising phenomena, which arise because of the anisotropic shape of the constituent rods. Theoretically, the behavior of a suspension of hard rods during shear flow can be described by the equation that governs the time development of their probability distribution function, as derived by Hess[1] and by Doi and Edwards.[2] In the absence of a flow, the Doi−Edwards−Hess (DEH) theory reduces to the Onsager description of equilibrium nematic liquid crystals and can be used to describe the isotropic−nematic (I−N) phase transition of a hard rod suspension.[3] The rheological properties are predicted to be highly nonlinear functions of the Péclet number (*Pe*), which is the ratio of shear rate $\dot{\gamma}$ over rotational diffusion constant D_r. This is not surprising as the *Pe* number can be much larger than unity when the rodlike molecules have large aspect ratios.

The nonlinear response of the rheological properties indicates that the shear flow distorts the equilibrium distribution of macromolecules or rods. The spatiotemporal microstructural changes during flow are even more complex. At low shear rates, the DEH theory predicts that the pseudo vector describing the average alignment of the rods, i.e., the "director", undergoes a continuous "tumbling" motion in the plane defined by the velocity and the velocity gradient vectors. At high shear rates the director is predicted to align with the flow.[4,5] At intermediate shear rates, it is possible to obtain multiple solutions to the Doi−Edwards-Hess equation, which are dependent on the initial orientation of the director.[6,7] For one stable solution called "wagging" the nematic director oscillates between two angles in the plane defined by the flow and the gradient of the flow. Other solutions such as kayaking and log-rolling are also possible, in which the director oscillates out of the flow-gradient plane at these intermediate shear rates.[8]

Experiments on polymeric liquid crystals have confirmed several predictions of the Doi−Edwards equation. Using a combination of rheological and rheo-optical measurements, it was shown that nematic solutions of poly(benzyl-glutamate) (PBG) tumble at low shear rate and become flow aligning at high shear rates.[9] The existence of a wagging regime and a potential coexistence of wagging and log-rolling regimes at intermediate flow rates have also been revealed in experiments.[8,10] However, there remain significant difficulties when comparing experiments on polymeric liquid crystals (PLC) to theoretical predictions. One problem is that different levels of

---

* To whom correspondence should be addressed.

[1] Hess, S. Fokker-planck-equation approach to flow alignment in liquid crystals. *Z. Naturforsch.* **1976**, *31* (a), 1034−1037.

[2] Doi, M.; Edwards, S. F. *The Theory of Polymer Dynamics*; Clarendon Press: Oxford, U.K., 1986.

[3] Onsager, L. The effect of shape on the interaction of colloidal particles. *Ann. N.Y. Acad. Sci.* **1949**, *51*, 62−659.

[4] Marrucci, G.; Maffettone, P. L. Description of the liquid-crystallin phase at high shear rates. *Macromolecules* **1989**, *22*, 4076.

[5] Larson, R. G. Arrested tumbling in shearing flows of liquid crystal polymers. *Macromolecules* **1990**, *23*, 3983−3992.

[6] Faraoni, V. Grosso, M.; Crescitelli, S.; Maffettone, P. L. The rigid-rod model for nematic polymers: An anaysis of the shear flow problem. *J. Rheol.* **1999**, *43*, 829.

[7] Forest, M. G.; Wang, Q. Monodomain response of finit-aspect-ratio macromolecules in shear and realted linear flows. *Rheol. Acta* **2003**, *42*, 20−46.

[8] Grosso, M.; Crescitelli, S.; Somma, E.; Vermant, J.; Moldeaers, P.; Maffettone, P. L. Prediction and observation of sustained in a shear liquid crystalline polymer. *Phys. Rev. Lett.* **2003**, *90*, 098304.

[9] Burghardt, W. R.; Fuller, G. G. Role of director tumbling in the rheology of polymer liquid crystal solutions. *Macromolecules* **1991**, *24*, 2546.

[10] Mewis, J.; Mortier, M.; Vermant, J.; Moldenaers, P. Experimental evidence for the existence of a wagging regime in polymeric liquid crystals. *Macromolecules* **1997**, *30* (5), 1323−1328.

10.1021/la050116e CCC: $30.25

the microstructure may lead to different contributions to the stress tensor.[11] In addition to the molecular contribution to the stress tensor, textural aspects contribute. The latter include Frank elasticity contributions due to the presence of spatial distortions of nematic director and viscous interactions between "domains". In addition, there is an indirect effect to the stress tensor as the defects disturb the orientation distribution function. These textural contributions to the total stress dominate the behavior at high concentrations and low shear rates,[12] making it difficult to accurately extract information about the concentration dependence of different flow transitions. The textural portion of the stress typically displays scaling of the transient rheological response with strain rather than with *Pe* number.[13] The strain scaling is a typical feature of materials where the time response is determined by an inherent length scale which in the case of PLCs is set by the size of the large non-Brownian nematic domains.[14]

The DEH theory describes the flow behavior of a homogeneous ensemble of rods but does not consider any polydomain effects. Therefore, an ideal system for testing DEH theory should have small textural contributions. In this paper, we use rodlike *fd* virus suspensions to access the concentration dependence of the transition of tumbling to wagging and wagging to flow aligning. We show that the contribution of textural stress is very low, although the spatial distribution of directors still has to be accounted for. The main motive for using *fd* virus is the thorough understanding of its equilibrium behavior, which has been quantitatively described using the Onsager theory extended to take into account the semiflexible nature of *fd* as well as its surface charge.[15] Moreover, *fd* has already successfully been used for (micro)rheology experiments in the isotropic phase.[16,17] The aim of the present paper is to make a comparison between the *dynamic* flow behavior of *fd* suspensions and the available *microscopic* theoretical predictions of the DEH theory for a homogeneous system of colloidal rods under shear.

The paper is organized as follows. In section II, we discuss the equation of motion of the orientational distribution function and the numerical method we use to solve it. The experimental details about sample preparation and measurements are given in section III. The results are discussed in five parts: the stationary viscosity of *fd* suspensions, the concentration and shear rate dependence of the oscillatory response to a flow reversal, the relaxation after cessation of flow at high concentration, and in situ microscopy under shear. In section IV, the textural contribution to the stress tensor is investigated in more detail. Finally, we present a nonequilibrium phase diagram of shear and concentration dependence of different flow transitions.

II. Theory

The distribution of an ensemble of rods can be described by the probability density function $P(\hat{\mathbf{u}}_1,.., \hat{\mathbf{u}}_N, \mathbf{r}_1,.., \mathbf{r}_n)$ of the positions $\{\vec{\mathbf{r}}_i\}$ and orientations $\{\hat{\mathbf{u}}_i\}$ of the rods. Ignoring any spatial correlations, i.e., restricting to a monodomain, we have $P(\hat{\mathbf{u}}_1,.., \hat{\mathbf{u}}_N, \mathbf{r}_1,.., \mathbf{r}_n) = \bar{\rho}P(\hat{\mathbf{u}}_1,.., \hat{\mathbf{u}}_N)$, where $\bar{\rho} = N/V$ is the particle density. Therefore, the *orientational* probability density function, or orientational distribution function (ODF), fully characterizes the system. The time evolution of the ODF for a suspension of rods during flow is obtained by solving the equation of motion for the ODF, given by the *N*-particle Smoluchowski equation

$$\frac{\partial P(\hat{\mathbf{u}}, t)}{\partial t} = D_r \mathscr{R}\cdot\{\mathscr{R}P(\hat{\mathbf{u}}, t) + DL^2\bar{\rho}P(\hat{\boldsymbol{u}}, t)\hat{\mathscr{R}}\oint d\hat{\mathbf{u}}'P(\hat{\mathbf{u}}', t)|\hat{\mathbf{u}}' \times \hat{\mathbf{u}}|\} - \hat{\mathscr{R}}\cdot P(\hat{\mathbf{u}}, t)\hat{\mathbf{u}} \times (\Gamma\cdot\hat{\mathbf{u}}) \quad (1)$$

where $\mathscr{R}(...) = \hat{\mathbf{u}} \times \nabla_{\hat{\mathbf{u}}}(...)$ is the rotation operator with respect to the orientation $\hat{\mathbf{u}}$ of a rod. D_{r} is the rotational diffusion of a rod at infinite dilution. Furthermore, D is the thickness of the rods and L is their length. $\Gamma = \dot{\gamma}\,\hat{\Gamma}$ is the velocity-gradient tensor with $\dot{\gamma}$ the shear rate. Here we choose

$$\hat{\Gamma} = \begin{pmatrix} 0 & 1 & 0 \\ 0 & 0 & 0 \\ 0 & 0 & 0 \end{pmatrix} \quad (2)$$

which corresponds to a flow $\mathbf{v}$ in the x-direction and its gradient $\nabla\mathbf{v}$ in the y direction.

The concentration where the isotropic phase becomes unstable *in the absence of shear flow* can be calculated by solving the Smoluchowski equation at zero shear rate. This equation agrees with Onsagers approach to the I−N transition. Often the Maier-Saupe potential is used instead of the exact potential, which in fact corresponds to the first term of the Ginzburg-Landau expansion of the outer product in the exact potential given between the brackets in eq 1.[18] Under *flow conditions*, a rich dynamics phase behavior is found as a function of shear rate and rod concentration. Marrucci and Maffettone were the first to solve the equation of motion of the ODF numerically, restricting themselves to two dimensions in order to reduce the computational effort.[4] They found that the director undergoes a tumbling motion with respect to the flow direction, resulting in a negative normal stress N_1. Larson expanded the ODF in three dimensions using spherical harmonics and truncated the expansion after checking for convergence.[5] This treatment predicts a transition from tumbling to "wagging" and finally to flow aligning state with increasing shear rates. A closure relation is frequently used for the interaction term on the right side of eq 1. This can greatly bias the results, see e.g., Feng et al.[19] The location of the flow transitions in the flow-concentration diagram is very sensitive to the choice of the closure, and no satisfactory closure has been found up till now.

In this paper, we use a finite element method to numerically solve the equation of motion for the ODF, thus avoiding the use of any specific closure relation. As a typical diffusion−convection equation, eq 1 describes the diffusive−convective transport dynamics of an ori-

---

(11) Larson, R. G. On the relative magnitudes of viscous, elastic and texture stresses in liquid crystalline PBG solutions. *Rheol. Acta* **1996**, *35* (2), 150−159.

(12) Walker, L. M.; Mortier, M.; Moldenaers, P. Concentration effects on the rheology and texture of pbg/*m*-cresol solutions. *J. Rheol.* **1996**, *40* (5), 967−981.

(13) Moldenaers, P.; Mewis, J. Transient behavior of liquid crystalline solutions of poly(benzylglutamate). *J. Rheol.* **1986**, *30* (1), 567−584.

(14) Larson, R. G.; Doi, M. Mesoscopic domain theory for textured liquid crystalline polymers. *J. Rheol.* **1991**, *35* (4), 539−563.

(15) Purdy, K. R. Dogic, Z.; Fraden, S.; Rühm, A.; Lurio, L.; Mochrie, S. G. J. Measuring the nematic order of suspensions of colloidal fd virus by X-ray diffraction and optical birefringence. *Phys. Rev. E.* **2003**, *67*, 031708.

(16) Graf, C. Kramer, H.; Deggelmann, M.; Hagenbüchle, M.; Johner, Ch.; Martin, Ch.; Weber, R. Rheological properties of suspensions of interacting rodlike fd-virus particles. *J. Chem. Phys.* **1993**, *98* (6), 4921−4928.

(17) Schmidt, F. G.; Hinner, B.; Sackmann, E.; Tang, J. X. Viscoelastic properties of semiflexible filamentous bacteriophage *fd*. *Phys. Rev. E* **2000**, *62* (4), 5509−5517.

(18) Dhont, J. K. G.; Briels, W. J. Viscoelasticity of suspensions of long, rigid rods. *Colloid Surf. A* **2003**, *213* (2−3), 131−156.

(19) Feng, J.; Chaubal, C. V.; Leal, L. G. Closure approximations for the doi theory: Which to use in simulating complex flows of liquid-crystalline polymers? *J. Rheol.* **1998**, *42* (5), 1095−1119.

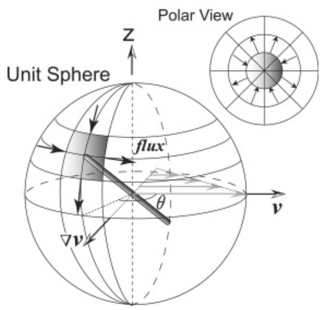

Figure 1. Flux conservation method used in discritizing eq 1. The rod indicates the orientation of the director with respect to the shear flow. The probability of finding a tip of one rod in the shaded area of the unit sphere is determined by the flux of the probabilities through the boundary of that area.

entation of a homogeneous ensemble of thin rigid rods. A surface of a sphere is constructed on which a tip of the rod moves with respect to its center of mass. The equation for the probability of finding the tip of a rod in an area is determined by the transport fluxes on its boundaries due to (1) the Brownian diffusion (the first term in the brace brackets of eq 1), (2) the convection induced by the interparticle forces (the second term in the brace brackets of eq 1), and (3) the convection due to the imposed shear flow (the third term of eq 1).

To solve eq 1 numerically, a discretization scheme is used, and meshes on the surface of a unit sphere are constructed. For those operators inside the brace brackets which represent the transport fluxes, we apply the central differences approximations. However, the rotation operator outside of the brace brackets needs to be discretized using the concept of transport fluxes through the boundaries of the mesh. In other words, the integral form of the eq 1 is invoked and applied to each of the mesh elements. To do this the identity, $(\hat{\mathbf{u}} \times \nabla_{\hat{\mathbf{u}}})\cdot\mathbf{F} = \nabla_{\hat{\mathbf{u}}}\cdot(\mathbf{F} \times \hat{\mathbf{u}})$ is used in order to transform the angular transport flux of a rod to the translational transport flux of one tip of that rod. It differs from the conventional method of discretizing a differential equation where the operators are written explicitly into the sum of the first- and second-order derivatives, and then the latter are approximated by selected difference schemes. The advantage of the current method is that, since neighboring meshes share boundaries, the fluxes leaving one mesh are always absorbed by the surrounding meshes and vice versa. Therefore, there is no loss and generation in the total amount of the ODFs as the computation proceeds (see Figure 1). In practice, a 40 × 80 mesh was used on the surface of a unit sphere with 40 equispaced grids in the polar angle and 80 equispaced grids in the azimuthal angle in a spherical coordinates. The right-hand side of eq 1 is discritized on the meshes according to the flux-conservative method mentioned above. A fourth order Adams' predictor-corrector method[20] was invoked to follow the time evolution of the ODF. More details will be published in a forthcoming paper.

The time-dependent ODF is now used to calculate the time-dependence of three parameters characterizing the flow behavior of a nematic phase: (1) θ describing the angle between the nematic director and flow direction, (2) the scalar magnitude of the director defined by the order parameter P_2, and (3) the total stress of an ensemble of flowing rods. The angle and magnitude of the order parameter are obtained from the order parameter tensor

$$\boldsymbol{S} = \oint \mathrm{d}\hat{\mathbf{u}}\ \hat{\mathbf{u}}\hat{\mathbf{u}}P(\hat{\mathbf{u}}, t) \tag{3}$$

The largest eigenvalue of the order parameter tensor λ, characterizes the degree of alignment of rods with respect to the director given by the corresponding eigenvector $\hat{\boldsymbol{n}}$. The largest eigenvalue of $\boldsymbol{S}$ is $^1/_3$ in the isotropic phase and 1 for a perfectly aligned nematic phase. Scalar order parameter P_2 is defined as $P_2 = (3\lambda - 1)/2$.

The stress σ_{12} is obtained from the deviatoric part of the stress tensor derived by Dhont and Briels[18]

$$\Sigma_D = \eta_0\dot{\gamma} + 3\bar{\rho}k_{\mathrm{B}}T\left\{\mathbf{S} - \frac{1}{3}\hat{\mathbf{I}} + \frac{L}{D}\phi\Sigma_I^D + \frac{1}{6}Pe_{\mathrm{r}}\left[\mathbf{S}^{(4)}\colon\ \hat{\mathbf{E}} - \frac{1}{3}\hat{\mathbf{I}}\mathbf{S}\colon\ \hat{\mathbf{E}}\right]\right\} \tag{4}$$

where

$$\Sigma_I^D = \frac{8}{3\pi}\oint d\hat{\mathbf{u}}\oint \mathrm{d}\hat{\mathbf{u}}'\hat{\mathbf{u}}\hat{\mathbf{u}} \times \frac{\hat{\mathbf{u}} \times \hat{\mathbf{u}}'}{|\hat{\mathbf{u}} \times \hat{\mathbf{u}}'|}\hat{\mathbf{u}}\cdot\hat{\mathbf{u}}'P(\hat{\mathbf{u}}, t)P(\hat{\mathbf{u}}', t) \tag{5}$$

and

$$\mathbf{S}^{(4)} = \oint \mathrm{d}\hat{\mathbf{u}}\ \hat{\mathbf{u}}\hat{\mathbf{u}}\hat{\mathbf{u}}\hat{\mathbf{u}}P(\hat{\mathbf{u}}, t) \tag{6}$$

Here, $\phi = \pi/4\ D^2L\bar{\rho}$ is the volume fraction of rods, and $Pe = \dot{\gamma}/D_{\mathrm{r}}$ the rotational Péclet number which is defined as the shear rate scaled with the rotational diffusion of a rod at infinite dilution. The first term between the brackets, $\boldsymbol{S} - {}^1/_3\hat{\mathbf{I}}$, stems from the Brownian contribution to the stress. The second term stems from the direct interaction between rods and describes the elastic contribution to the total stress. The proportionality constant $\phi\ L/D$ is the dimensionless rod concentration and is also called the nematic strength. The terms proportional to $\sim Pe_{\mathrm{r}}$ stem from the flow of the suspension and described the viscous contribution to the total stress. This term disappears instantaneously when the shear is switched off.

In Figure 2, we plot the evolution of the three parameters (angle θ, order parameter P_2, and stress σ_{12}) as a function of strain for different shear rates at a dimensionless rod concentration of $\phi\ L/D = 4.5$. For this calculation, we used an initial rod orientation in the flow-gradient plane. The flow behavior between Péclet numbers of 4.5 and 5.0 exhibits a sharp transition from tumbling behavior, where the director continuously rotates, to wagging behavior where the director hops back and forth between two well defined angles. At higher shear rates, the director is found to be flow aligning. The order parameter at low shear rates remains unchanged, but is significantly reduced at the point of the tumbling to wagging flow transition.

III. Materials and Methods

The viscosity and stress response were measured using an ARES strain controlled rheometer (TA instruments, Delaware). A double wall Couette geometry was used because of the fairly low viscosity of the samples. Polarized light microscopy images of *fd* under shear flow were taken using a Linkam CSS450 plate-plate shear cell.

The physical characteristics of the bacteriophage *fd* are its length $L = 880$ nm, diameter $D = 6.6$ nm, persistence length of 2200 nm, and a charge per unit length of around 10 e$^-$/nm at pH 8.2.[21] When in solution, *fd* exhibits isotropic, cholesteric, and

---

(20) Korn, G. A.; Korn, T. M. *Mathematical Handbook for Scientists and Engineers*; Mc-Graw and Hill: New York, 1968.

(21) Fraden, S. *Observation, Prediction, and Simulation of Phase Transitions in Complex Fluids*, volume 460 of *NATO-ASI − Series C*; Baus, M.; Rull, L. F.; Ryckaert, J. P., Eds.; Kluwer Academic Publishers: Dordrecht, The Netherlands, 1995; pp 113−164.

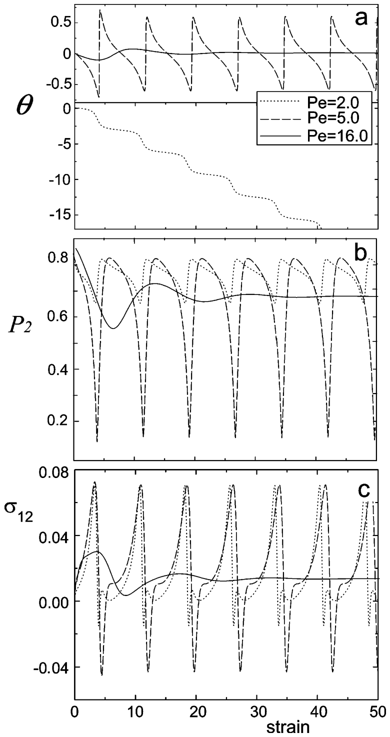

Figure 2. Three plots showing the behavior of the angle of the nematic director θ (a), the magnitude of the nematic order parameter(b), and the average stress (c) as a function of strain after a start up of the flow. The dimensionless rod concentration is $\phi\ L/D = 4.5$. Data are obtained by numerically solving eq 1 using the finite element method. The rods are initially placed in the flow-gradient plane. For the stress calculation only the elastic contribution (eq 4) was considered.

smectic phases with increasing concentration.[22,23] *fd* forms a cholesteric phase while the DEH theory is valid for nematic structures. In practice, nematic and cholesteric phase are locally almost identical and the free energy difference between these phases is very small.[24] In this paper, we do not distinguish between these two phases. The *fd* virus was prepared according to standard biological protocols using XL1-Blue strain of *E. coli* as the host bacteria.[25] The standard yields are approximately 50 mg of *fd* per liter of infected bacteria, and virus is typically grown in 6 L batches. The virus is purified by repetitive centrifugation (108 000 g for 5 h) and re-dispersed in a 20 mM Tris-HCl buffer at pH 8.2.

A. *fd* as a Model Hard Rod System. The Onsager theory for hard rod dispersions predicts a first order phase transition between a disordered, isotropic phase and an orientationally ordered, nematic phase. Due to hard core athermal interactions considered in the Onsager model, the phase diagram is temperature independent and the rod concentration is the only parameter that determines the location of the I−N phase transition. The two points spanning the region of isotropic−nematic coexistence are called the binodal points. The spinodal point is located at a rod concentration higher than the lower binodal point and is determined by the following condition $\phi\ L/D = 4$. *fd* viruses are not true hard rods, due to surface charge and limited flexibility. As a consequence, their equilibrium phase behavior differs from the ideal hard rod case described by Onsager based theory, e.g., DEH. The finite flexibility of *fd* viruses drives the concentration of the binodal points to a 30% higher value when compared to equivalent but perfectly stiff hard rods. In addition, flexibility also reduces the value of the order parameter of the coexisting nematic phase. For *fd*, the order parameter of the coexisting nematic is about 0.65, whereas Onsager theory for hard rods in equilibrium predicts the order parameter of 0.8.[15] The effect of surface charge is to increase the effective diameter of the rod D_{eff} and therefore the excluded volume interaction between charged rods. As a consequence, the charge reduces the real concentration of the phase transition.[26]

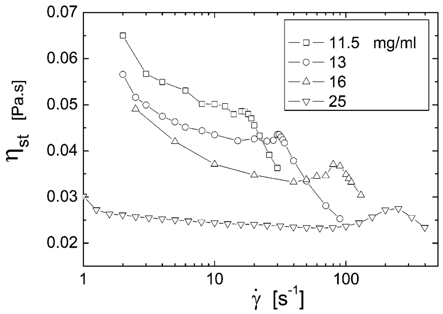

Figure 3. Stationary viscosity as a function of shear rate for four different concentration of *fd* virus at 11.5, 13, 16, and 25 mg/mL.

For the *fd* suspension used, the binodal point at high rod concentration c_{IN} occurs at 11 mg/mL. After taking the effects of flexibility and charge into account, it was shown that the order parameter of the nematic solution of *fd* is quantitatively described by the extensions of the Onsager theory to the semiflexible case.[15] Hence, even though *fd* is flexible and charged, it can be used to quantitatively test predictions of the DEH theory. It is, however, a very difficult and until now unfulfilled task to incorporate charge and flexibility into a nonequilibrium equation of motion such as eq 1. Therefore, in this paper, we use data from ref 15 to convert the measured concentration of *fd* to the nematic order parameter of the sample. After that, we compare experiments and theory at the same values of the order parameter.

IV. Results

A. Stationary Viscosity. The measurements of a stationary viscosity as a function of the shear rate for different *fd* concentrations are shown in Figure 3. For the lowest concentrations of *fd*, the viscosity decreases continuously with shear rate except for a small hesitation at a shear rate of 10 s^{-1}. This hesitation is similar to what is observed for solutions of PBG at low concentration in solvent *m*-cresol.[13,27] For *fd* at intermediate concentrations, shear thinning becomes less pronounced, the hesitation shifts to higher shear rates and turns into a local maximum. For the highest *fd* concentration, almost no shear thinning is observed, only a pronounced peak in the viscosity. This shear thickening behavior has not been previously reported.

A hesitation in the shear rate dependence of the viscosity was predicted theoretically by Larson.[5] It was argued that the transition from the tumbling regime to the wagging regime implies a broadening of the ODF which leads to higher dissipative stresses. The broadening of the ODF

---

[22] Dogic, Z.; Fraden, S. Smectic phase in a colloidal suspension of semiflexible virus particles. *Phys. Rev. Lett.* **1997**, *78*, 2417.

[23] Dogic, Z.; Fraden, S. Development of model colloidal liquid crystals and the kinetics of the isotropic-smectic transition. *Philos. Trans. R. Soc. London A* **2001**, *359*, 997.

[24] Dogic, Z.; Fraden, S. Cholesteric phase in virus suspensions. *Langmuir* **2000**, *16*, 7820−7824.

[25] Sambrook, J.; Fritsch, E. F.; Maniatis, T. *Molecular Cloning: A Laboratory Manual*, 2nd ed.; Cold Spring Harbor Laboratory Press: Plainview, NY, 1989; Chapter 4.

[26] Tang, J.; Fraden, S. Isotropic-cholesteric phase transition in colloidal dispersions of filamentous bacteriophage *fd*. *Liq. Cryst.* **1995**, *19* (4), 459−467.

[27] Kiss, G.; Porter, R. S. Rheolog of concentrated solutions of poly-(γ-benzyl-glutamate). *J. Polym. Sci.* **1978**, *65*, 193−211.

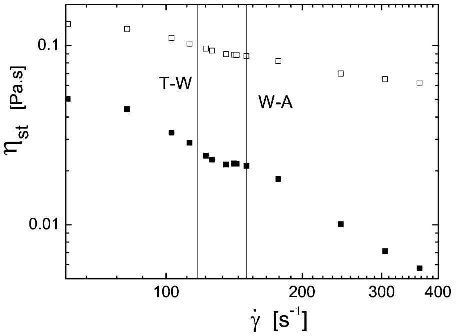

Figure 4. Theoretical time averaged viscosity at a dimensionless concentration of $L/D\ \phi = 4.5$ with (□) and without (■) the viscous contribution of the rods, as calculated by solving the equation of motion of the ODF for 20 independent initial orientations of the director. The lines indicate the transition from tumbling to wagging, and from wagging to flow aligning as found from Figure 2. The results are scaled to the experiment using a typical concentration of 16 mg/mL for $\bar{\rho}$ in eq 4 and $D^0_{\text{inf}} = 20\ s^{-1}$ for the rotational diffusion at infinite dilution.[15,28]

is illustrated in Figure 2b. As can be seen in Figure 2c, it is not straightforward that ODF broadening really has an effect on the stress. We calculated the time-dependent viscosity by numerically solving the equation of motion of the ODF for 20 different initial orientations of the director. From the time-dependent ODFs, we calculated the viscosity using either only the elastic term or both elastic and viscous terms. The viscosity is averaged over all 20 traces and a tumbling period after the transient start up flows have died out. The results are scaled to the experiment using a typical concentration of 16 mg/mL for $\bar{\rho}$ in eq 4 and the value of $D^0_{\text{inf}} = 20\ \text{s}^{-1}$, taken for the rotational diffusion at infinite dilution.[15,28] In Figure 4 the stationary viscosity decreases continuously with increasing shear rate and only shows a hesitation when the viscous contribution to the stress is not included. The shear rate where this hesitation occurs corresponds with the shear rate where the system nematic ordering is significantly reduced and the transition from tumbling to wagging takes place, as can be concluded from Figure 2. Comparing the model predictions to the experiments, it should be noted that the experimentally observed features are much more pronounced. Moreover, there is no real reason to leave out the viscous contribution although it does obscure the behavior we see in the experiment. Still, the maximum in the viscosity is interpreted as a signature of the transition from tumbling to a wagging state.

There are three observations to keep in mind when considering *fd* in the nematic phase under shear flow, which all point to very low stresses in such systems when compared to polymeric liquid crystals. First, the viscosity of *fd* in the nematic phase is two to 3 orders of magnitude lower than the viscosity of typical polymeric liquid crystals such as poly(benzyl glutamate) (PBG),[29] although the difference in solvent viscosity is only 1 order of magnitude. Second, the range over which the viscosity of *fd* suspension varies is more limited with changing shear rate and rod concentration: the viscosity lies between 70 times the solvent viscosity for low shear rate and low rod concentration and 20 times the solvent viscosity for high shear rate and rod concentration. Moreover, the viscosity as calculated from the equation of motion of the ODF is of the same order as the measured viscosity. Third, polymer nematics exhibit negative first normal stress differences for certain shear rates as was first observed for PBG solution.[26] This is a direct consequence of the tumbling of the nematic director. Attempts have been made to measure the first normal stress difference for nematic *fd* solutions but due to very low force the signals were too small to be measured.

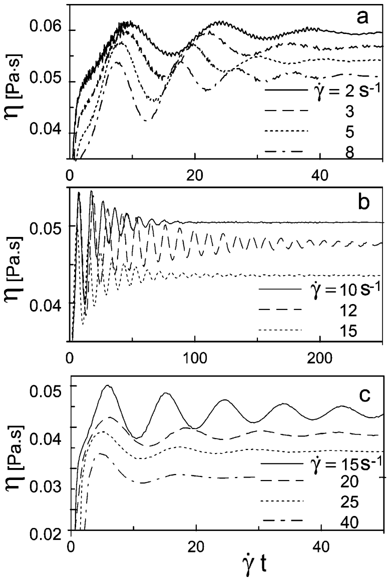

Figure 5. Viscosity of the nematic *fd* solution in a response to a flow reversals. The sample is sheared at shear rate $+\dot{\gamma}$ until the viscosity is equilibrated; at time $t = 0$ the shear rate is changed to $-\dot{\gamma}$. The concentration of *fd* is kept constant at 11.5 mg/mL. The data can be nicely fitted to eq 7. The fits are not shown for clarity.

B. Flow Reversal Experiments. In flow reversal experiments, the sample is first sheared at a constant shear rate in one direction until the steady state condition is reached. Subsequently, the direction of flow is suddenly reversed while keeping the magnitude of shear rate constant. Such experiments have been very useful in characterizing and understanding the dynamics of sheared liquid crystalline polymers.[13] In the present work, flow reversal experiments were performed covering a wide range of shear rates and *fd* concentrations. Typical flow reversal experiments are depicted in Figure 5 for a *fd* concentration of 11.5 mg/mL which corresponds to $c/c_{\text{IN}} = 1.05$. At the lowest shear rates, a damped oscillatory response is obtained which decays within few oscillations (Figure 5a). Increasing the shear rate results in a more pronounced oscillatory response, which damps out relatively slowly. The oscillatory response in Figure 5b is most pronounced at a shear rate of 12 s^{-1}. At even higher shear rates, the damping again increases (Figure 5c). To quantitatively characterize the response of a nematic to a flow reversal, the data is fitted to a damped sinusoidal superimposed onto a asymptotically decaying function of the following form:

$$\eta(t) = \eta_{\text{stat}}\left\{1 + A\mathrm{e}^{-\dot{\gamma}t/\tau_{\text{d}}}\sin\left(2\pi\frac{\dot{\gamma}t - \varphi}{P}\right)\right\}(1 - bg^{\dot{\gamma}t}) \quad (7)$$

---

(28) Kramer, H. Deggelmann, M.; Graf, C.; Hagenbtichle, M.; Johner, C.; Weber, R. Electric birefringence measurements in aqueous fd virus solutions. *Macromolecules* **1992**, *25*, 4325−4328.

(29) Vermant, J.; Moldenaers, P.; Picken, S. J.; Mewis. J. A comparison between texture and rheological behaviour of lyotropic liquid crystalline polymers during flow. *J. Non-Newtonian Fluid Mech.* **1994**, *53*, 1−23.

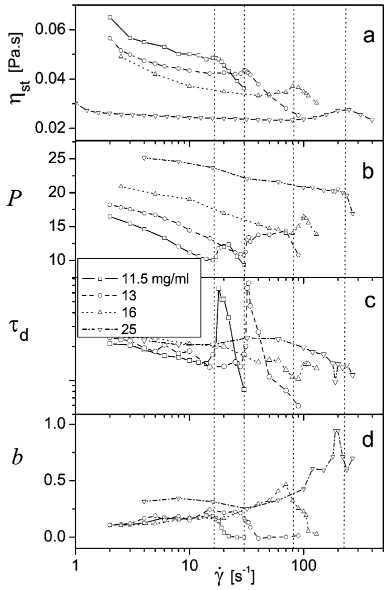

Figure 6. (a) Steady-state viscosity as function of the shear rate for *fd* virus at four different concentrations. All viscosity curves exhibit shear thinning at low shear rates followed by a local maximum in viscosity. (b–d) Behavior of the parameters obtained from fitting the response of the shear flow reversal experiments to eq 7. The vertical lines indicate the local maximum in viscosity curves. The local maximum in the steady-state viscosity curve corresponds to maximum of the tumbling period P and damping constant τ_d and minimum of asymptotic constat b in the flow reversal.

This is an empirical choice, but each variable in the fit contains important information about the behavior of rods in shear flow. Figure 6 shows the behavior of fit parameters as a function of the shear rate at few selected concentrations of *fd* virus. In this figure, we indicate with vertical dashed lines the shear rates at which the steady state viscosity exhibits a local maximum for four different concentrations. Interestingly, these are exactly the same shear rates at which the damping constant τ_d as well as the tumbling period P show a sharp increase. The asymptotic constant b, on the contrary, shows a decrease. These features disappear for the highest *fd* concentration. Presumably the three regions showing different flow reversal behavior correspond to tumbling, wagging and flow aligning regime. This will be discussed in more detail in section V.B. In the next section. we first discuss the concentration and shear rate dependence of the tumbling period in the regime where rods exhibit tumbling flow behavior.

C. Tumbling Period as a Function of Shear Rate and Rod Concentration. DEH theory predicts that as the *De* (or *Pe*) number is increased, that the "molecular" period of oscillation decreases with increasing shear rate in the tumbling regime.[5] This feature was never fully explored, since in most polymeric liquid crystals it was found that the tumbling period was strain scaling, implying that the response overlaps when the period is scaled with the applied shear rate and the stress is normalized by its steady state value. The strain scaling arises as a consequence of the presence of a large, non-Brownian, length scale in the sample that determines the time response, even at relatively high *De* (or *Pe*) numbers. This most probably is the domain size characterizing the nematic texture. The log–log plot of the tumbling period ($T = P/\dot{\gamma}$) as a function of the shear rate is shown in Figure 7. Here the data are only shown for a low shear rate region which is associated with the tumbling region. Strain scaling, if present, would give a slope of −1. However, as can be seen in the inset of Figure 7, the reciprocal indicating strain scaling is only approached and not reached at the highest rod concentration studied here.

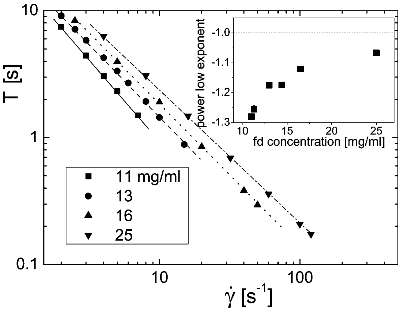

Figure 7. Dependence of the tumbling periods on the shear rate for different concentrations of the nematic *fd*. The figure shows that the tumbling period scales with a power low as a function of the shear rate. The inset shows the power law dependence of the tumbling period on the shear rate for different *fd* concentrations.

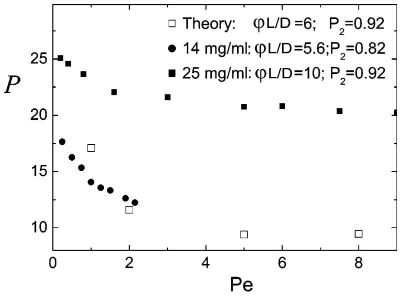

Figure 8. Period of the oscillations (in units of strain) as a function of the Péclet number, where the shear rate is scaled with the rotational diffusion of *fd* at infinite dilution.

The shear rate dependence of the tumbling period is compared to the theoretical prediction for the same rod concentration as well as the same order parameter, see Figure 8. The reason for using the order parameter to assess the theoretical predictions was discussed at length in section III.A. For purposes of comparison, the order parameter was obtained from X-ray experiments and the value of $D^0_{\text{inf}} = 20\ \text{s}^{-1}$. We emphasize that DEH theory is microscopic and that there are no adjustable parameters in the comparison between theory and experiments. Clearly there is a qualitative correspondence between theory and experiment, both showing a continuous decrease of the period. The quantitative correspondence, on the other hand, is limited. This is probably due to fact that texture, although not dominating the response, is still present. It will be shown later in section V.B that the shear rate and rod concentration dependence of a tumbling to wagging and wagging to flow-aligning transition agree much better with DEH theory.

The concentration dependence of the tumbling period is shown in Figure 9. Here, theory and experiments are compared at a fixed shear rate at which the tumbling to wagging flow transition occurs. The tumbling period increases with increasing rod concentration (Figure 9a) or, equivalently, increasing order parameter of the nematic phase (Figure 9b). The increase of the tumbling period

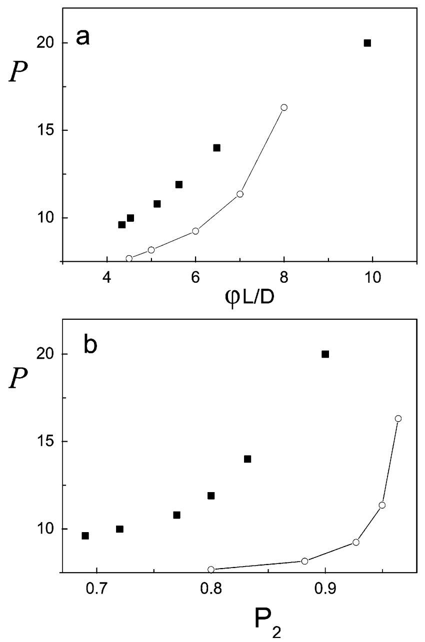

Figure 9. Period of the oscillations (in units of strain) as a function of the dimensionless concentration (a) and order parameter (b). The shear rate was chosen at the point we identify with the tumbling to wagging transition for experiment (■) and exact theory (○).

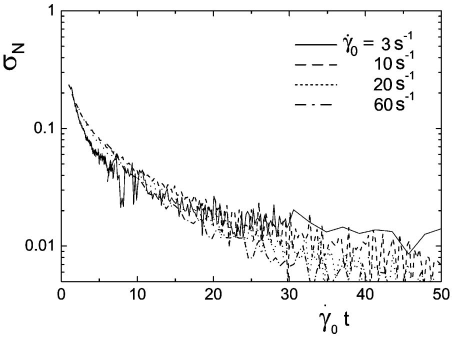

Figure 10. Stress relaxation after cessation of flow for *fd* at 25 mg/mL ($c/c^* = 2.3$), varying the initial shear rate. The time is scaled by the initial shear rate. The stress is normalized by the stress before the cessation of flow.

with increasing order parameter was already predicted using a linearized version of the DEH theory.[30]

In conclusion, the absence of strain scaling of the tumbling period and the qualitative agreement between theory and experiment the tumbling period indicates that the response of the suspension of *fd* virus is dominated by the molecular elasticity arising from the distortion of the ODF of particles.

D. Relaxation at High Concentration. To measure the relative magnitude of the elastic texture contribution to the overall stress, relaxation experiments were performed. For polymeric liquid crystals such as polybenzylglutamate (PBG) solutions in *m*-cresol, Walker et al.[12] showed that there are three different regimes of relaxation behavior, each of which is related to a distinct structural

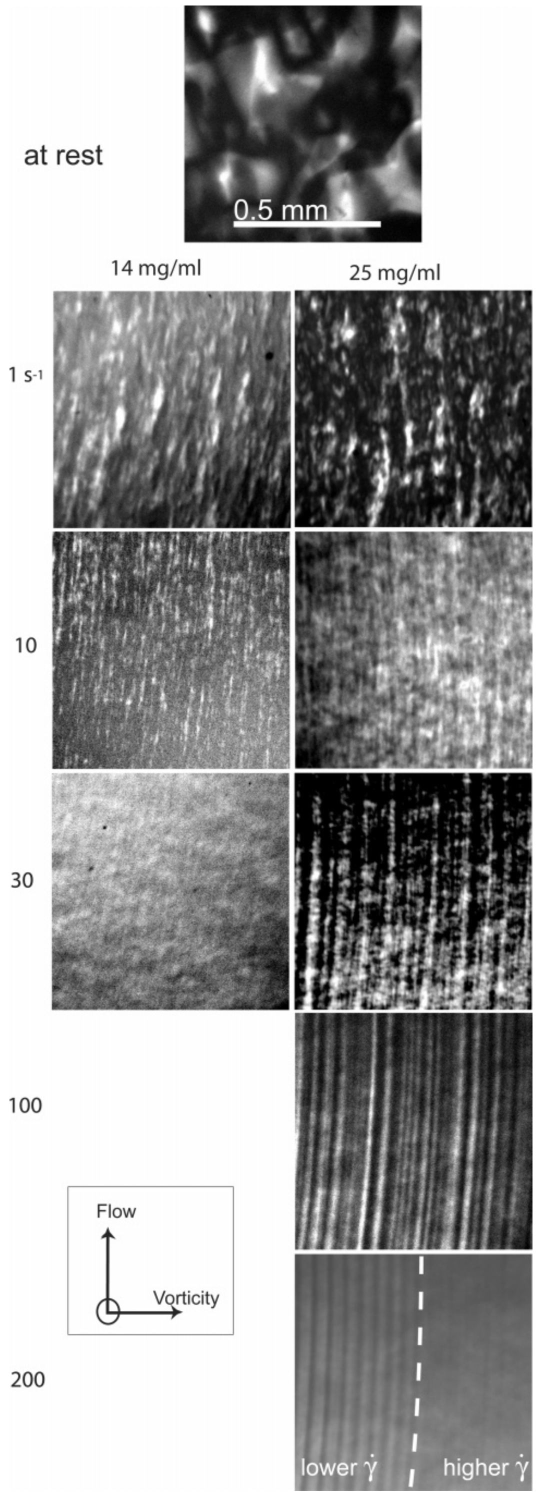

Figure 11. Polarization images of the nematic *fd* at 14 and 25 mg/mL for a range of different steady-state shear rates. The dashed line in the bottom right image indicates the border between the structured and unstructured regions.

---

(30) Kuzuu, N.; Doi, M. *J. Phys. Soc. Jpn.* **1984**, *53*, 1031.

relaxation. There is a "fast" relaxation of the nematic fluid; a "slower" relaxation that exhibits scaling with the shear rate before the cessation of flow, which is due to the indirect contribution of the texture to the overall stress; and a "long-time" relaxation due to the reorganization of the texture on a supramolecular level which will not be addressed here.

Stress relaxation experiments were performed in the low shear rate "tumbling" region, at shear rates smaller than those corresponding to the maximum in the viscosity. The sample used had a relatively high *fd* concentration of 25 mg/mL, corresponding with $c/c_{\mathrm{IN}} = 2.3$. Some typical responses to the cessation of flow are depicted in Figure 10. The stress is normalized to its value before the cessation of flow, and the time axis is scaled by the shear rate. The fast component of the decay takes place at less than a tenth of a second, which is comparable to the response of the force re-balanced transducer and therefore not shown. The slow component of the stress relaxation scales when time is multiplied with the previous shear rate, but only from the point that the stress has decayed to less than 30% of its original value, or less for higher initial shear rates. From Figure 10, it can be concluded that the contribution to the stress for the highest concentration used and for low shear rates is 30%. This is the absolute upper limit for the samples used in this paper. It should be noted that for PBG solutions 30% it was found to be the lower limit.[12]

E. In Situ Microscopy. The flow-induced changes of the liquid crystalline texture during steady-state shear flow were studied using a plate−plate geometry in combination with a polarization microscope. Measurements were performed for *fd* concentrations of 14 and 25 mg/mL. Typical images are shown in Figure 11 for different shear rates. Interestingly the characteristic size of the "domains" was very large. Birefringent regions of up to half a millimeter were observed under static conditions. When the sample is subjected to shear flow, these domains will elongate and eventually disappear, at values of the shear rate which correspond to the maximum in the viscosity (see Figure 6a). An important difference between the two concentrations is that the elongated domains merge into bands for high rod concentration, whereas for the low concentration the structure disappears before such bands are formed. Interestingly, this transition to a banded structure in the high concentration fluid takes place at a shear rate which is higher than the shear rate where the low concentration fluid loses its features.

V. Discussion

When comparing the flow behavior of the polymeric nematic phase and the colloidal nematic phase of the dispersed *fd* viruses, the most striking observation is the qualitative agreement between the two systems, despite the fact that *fd* is 1 order of magnitude larger. The viscosity of the *fd* nematic is much smaller, and the rotational diffusion of *fd* is much slower when compared to polymeric liquid crystals. Flow reversal experiments reveal typical transitions in the transient rheological behavior: damped oscillations occur at low shear rates changing to undamped oscillations at intermediate shear rate, which disappear if the shear rate is increased even further; the time scale of the oscillations of the stress transients is comparable. Also other well-known phenomena like the formation of very large bands upon cessation of flow along the vorticity direction which have been studied in detail in polymeric systems[31] can also be observed here (data not shown).

Having established that *fd* virus dispersions indeed undergo a tumbling motion under flow, the *dynamic* behavior of *fd* suspensions can be rationalized on the basis of the microscopic theoretical predictions for a homogeneous system of rods under shear. Doing so, one important prerequisite needs to be fulfilled, namely that the dominating contribution to the stress is coming from the nematic fluid and not from the texture. It will be argued here that this indeed is the case. Having done so, we will be able to map out a phase diagram of the dynamic transitions from tumbling to wagging to flow aligning.

A. Textural Evolution during Flow. The word "texture" refers to disclination points and lines where the director of the nematic phase changes discontinuously, marking domains in the sample. When a system containing these domains and disclinations is subjected to shear flow, part of the dissipated energy is used to destroy these structures. Figure 11 shows that the domains tend to elongate and align with the flow. Disclinations can also cause a direct contribution to the total stress resulting in a high viscosity and a very pronounced shear thinning behavior, typically referred to as region I.[32] Experiments on polymeric liquid crystals have revealed several features of the flow behavior of nematic liquid crystals which are attributed to the presence of texture in the nematic phase. Tumbling induces distortions in the director field and the defects arrest the tumbling, thereby inducing an elastic stress. The length scale over which this distortion occurs, i.e., the "domain" length scale, is an inherent non-Brownian length scale, see ref 33. As a consequence, stress patterns during flow reversal will display strain scaling. Also the damping of the oscillations is explained on the base of the presence of the polydomain structure, where, e.g., the "friction" between the domains would lead to a damping of the oscillations.[14,34] The scaling of the stress relaxation process after the flow is stopped with shear rate has been explained using the same arguments. From such an experiment, the relative contribution to the total stress of a homogeneous nematic phase and the polydomain texture can be estimated since the relaxation dynamics of the nematic phase is much faster than that of polydomain structure.[12]

The micrographs in Figure 11 clearly reveal that texture under flow exists in nematic *fd* dispersions. Their contribution to the rheology is, however, far less prominent when compared to polymeric liquid crystals such as PBG. This we can infer from several observations. First, very moderate shear thinning is observed in the low shear rate regime for the *low* concentrations, which gradually disappears with increasing concentration (Figure 6b). This is very similar to theoretical predictions for a homogeneous nematic phase (Figure 2b in ref 18). Also, the calculated and measured viscosities are of the same order of magnitude. In contrast, shear thinning can be fairly strong in the low shear rate region (region I) where texture dominates the response, and it will increase with increasing concentration,[35] although also other microstructural

---

(31) Vermant, J.; Moldenaers, P.; Mewis, J.; Picken, S. J. Band formation upon cessation of flow in liquid-crystalline polymers. *J. Rheol.* **1994**, *38* (5), 1571−1589.

(32) Walker, L. M.; Wagner, N. J. Rheology of region i flow in a lyotropic liquid-crystal polymer: The effects of defect texture) under shear and during relaxation. *J. Rheol.* **1994**, *38* (5), 1524−1547.

(33) Burghardt, W. R.; Fuller, G. G. Transient shear flow of nematic liquid crystals: Manifestations of director tumbling. *J. Rheol.* **1990**, *34* (6), 959−992.

(34) Kawaguchi, M. N.; Denn, M. M. A mesoscopic theory of liquid crystalline polymers. *J. Rheol.* **1999**, *43* (1), 111−124.

(35) Marrucci, G.; Greco, F. Flow behavior of liquid crystaline polymers. *Adv. Chem. Phys.* **1993**, *86*, 331.

features can contribute here.[36] Second, the tumbling period is not strain scaling (Figure 7), which could be due to either a smaller relative magnitude of the textural stress or due to the fact that we are not in a low enough *Pe* regime. Third, "strain" scaling is recovered for the slow "textural" relaxation process after the flow has been stopped. This experiment shows that at the highest rod concentrations used and at low shear rates the distortional textural contribution is about 30%. For most experiments done, this value is probably significantly lower. So, where texture is important, even dominating the stress response for molecular LCPs, molecular elasticity is far more dominating the *fd* virus. Though we just argued that the texture does not dominate the shear response of the system, this does not mean that the shear response is not influenced by texture. For one, the oscillations we observe are still strongly damped, and the damping only decreases when the transition to the flow aligning state is reached (see the behavior of τ_d in Figure 6). Moreover, the presence of texture might explain the discrepancy in the behavior of the period of the oscillations between experiment and theory (Figure 9). Most importantly, we know from microscopy that texture is present under shear (see Figure 11). It should be noted, however, that the size of the polydomain structure of the *fd* dispersions is 1 order of magnitude bigger as compared to PBG,[29] so that the density of disclination lines and points is about 3 orders of magnitude lower for *fd*. Note that the length scale of the texture during flow is still small compared to the dimension of the flow cell. Since the contribution of texture scales with the density of the disclinations,[35] texture will be far more dominating for e.g. PBG than for *fd*, even when elastic constants are almost the same for the two systems,[24,37]).

B. Phase Diagram of Dynamical Flow Transitions. In this section, the experimental results are combined and a nonequilibrium phase diagram of *fd* rods under shear flow is presented. The results for the four fit parameters plotted in Figure 6 show clear transitions at well-defined shear rates for all *fd* concentrations. Although they only give an indirect proof of the transitions, they can be used to infer information about the flow transitions. For all *fd* concentrations (except for the highest one) the shear rate where the maximum viscosity is reached is identical with the shear rate where the period as well as the damping constant start to increase (indicated by the vertical dashed lines in Figure 6). The microscopic observations are in fairly good agreement with the transitions inferred from the rheology. Upon approaching the tumbling to wagging transition from tumbling to flow aligning, the texture becomes too faint to resolve in the microscope and texture subsequently disappears upon reaching the FA region. For the high *fd* concentration, i.e., the sample showing shear banding (Figure 11 last), one can identify a sharp transition from a structured to an unstructured region in the same micrograph. Since this picture was taken in the plate−plate geometry, there is a shear rate distribution across the image: the shear rate is increasing going from the left side to the right. A sharp spatial transition therefore also represents a sharp transition at a given shear rate. Although, due to the method of zero gap-setting, the value of the shear rate is not exactly known (±20%), one can still identify the shear rate where structure disappears as the shear rate where the viscosity reaches its local maximum (the down pointing triangles in Figure 6a). For low *fd* concentration of (14 mg/mL) the structure disappears around the point where the viscosity reaches its local maximum, although the morphological transition for the lower concentration is less abrupt.

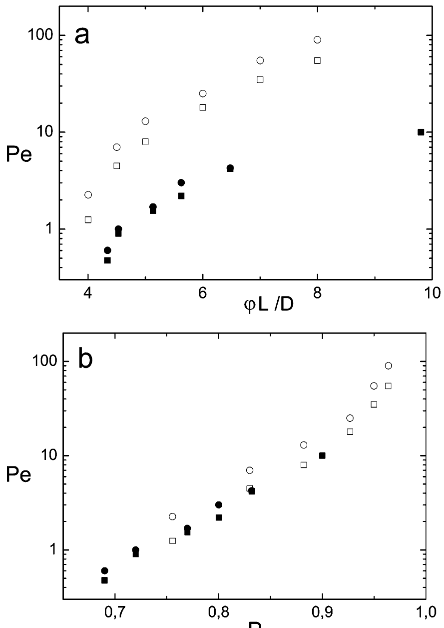

Figure 12. Phase diagram of flow transitions for the nematic *fd* phase as a function of dimensionless concentration (a) and order parameter (b). The experimental points indicate the Péclet numbers where the viscosity shows a local maximum (9) and where the damping constant τ_d (●) reaches a maximum. The theoretical points indicate tumbling to wagging (□) and wagging to flow aligning (○) transitions.

Figure 12 shows the behavior of flow transitions as a function of shear rate for various *fd* concentrations. For the experiment, we plotted the Péclet numbers where the viscosity shows a local maximum and where the damping constant reaches a maximum. The theoretical predictions for the tumbling to wagging and wagging to flow aligning transitions are obtained from the plots of the angle of the nematic director θ under flow, see Figure 2. Similar to the method used in Figure 9, the experimental concentration is scaled to the theoretical concentration in two different ways: effective concentration (Figure 12a) and the order parameter P_2 (Figure 12b). This figure was shown in a preliminary paper without a detailed explanation.[38] The shear rate is rescaled to the Péclet number by using the rotational diffusion coefficient at infinite dilution. Figure 12 allows us to draw some important conclusions. First, it is clear that scaling the concentration with the equilibrium order parameter gives better agreement when compared to the scaling by the dimensionless concentration. The fact that theory and experiment agree without using any fitting parameters (P_2 was obtained in a separate experiments[15]) leads to the conclusion that the DEH theory describes the flow behavior of the *fd* nematics quite well,

---

[36] Ugaz, V. M.; Cinader, D. K.; Burghardt, W. R. Origins of region I shear thinning in model lyotropic liquid crystalline polymers. *Macromolecules* **1997**, *30* (5), 1527−1530.

[37] Taratuta, V. G.; Hurd, A. J.; Meyer, R. B. Light-scattering study of a polymer nematic liquid crystal. *Phys. Rev. Lett.* **1985**, *55* (2), 246−249.

[38] Lettinga, M. P.; Dhont, J. K. G. Nonequilibrium phase behavior of rodlike viruses under shear flow. *J. Phys.: Condens. Matter* **2004**, *16*, 3929.

as long as the effects of flexibility and charge of the experimental rods are included in the calculation of the order parameter. A less convincing agreement is obtained when comparing the experimental and theoretically calculated periods (Figure 9). The reason for this could be the remaining textural contribution to the overall stress which, although small, cannot be neglected. Since we deduce from Figure 12b, that a dimensionless concentration of $\phi L/D = 4$ corresponds with a *fd* concentration of 16 mg/mL, we used this number a posteriori to scale the calculated molecular viscosity in Figure 4. The pure elastic contribution shows a very nice quantitative correspondence with the experimental data. Interestingly, when the viscous term is added, the theoretical viscosity is higher than the experimental viscosity, despite of the fact that no hydrodynamics is incorporated.

In the previous subsection, it was argued that the influence of textural contribution to the stress tensor of *fd* are relatively small, as compared to PLCs. There are however strong indications that the dynamic behavior is influenced by the macroscopic bands which are formed for the samples at the highest concentrations used (see Figure 11 end). As can be seen in Figure 6, the typical features for the transition to wagging disappear: there is no increase in the damping constant, nor in the period of the oscillations. Moreover, the theory shows only a moderate hesitation of the stationary viscosity (which even disappears when the viscous term is added, Figure 4), whereas in experiments a local peak is observed which is more pronounced with increasing concentration. The microscopy pictures show that at high concentrations the systems finds another way to handle the distortion of the particle distribution at high shear rates by forming shear bands where the overall orientational distribution is alternating, as was already observed and partially explained for the polymeric systems.[29,39,40] In the present work, the concentration dependence of the phenomenon at hand suggests that this merits further experimental as well as theoretical work. In this context, one should not forget that we compare experiments on charged and semiflexible *fd* with theory for hard and stiff rods. It could well be that these factors also play an important role. It will be a major challenge especially to take the semiflexibility into account in the equation of motion.

VI. Conclusions

Colloidal suspensions of rodlike *fd* viruses are an ideal model system to study the behavior of the nematic liquid crystalline phase under shear flow. Flow reversal experiments show signatures for tumbling, wagging, and flow aligning behavior, very similar to the behavior found in polymeric liquid crystals. The rigid rod nature of the *fd* suspension, possibly combined with a smaller relative textural contributions to the overall stress tensor make *fd* virus a suitable model system for the DEH theory. Important in this respect is that the overall viscosity is only one to 2 orders of magnitude higher than the solvent viscosity. Also it is important to note that stress relaxation experiments combined with the absence of strain scaling in flow reversal experiments suggest that there is only a limited contribution of textural aspects to the overall stress, even for the highest *fd* concentration used in this work. The shear thickening of the viscosity observed for a range of *fd* concentrations is as yet, unexplained. The maximum in the viscosity occurs at the critical shear rate where the tumbling to wagging transition takes place. Microscopic observations show that at this shear rate the morphological features disappear, suggesting a strong connection between the dynamic transitions and structure formation.

The experimental results have been compared to a microscopic theory for rod like molecules subjected to shear flow. A nonequilibrium phase diagram is constructed, describing the transitions from tumbling to wagging and from wagging to flow-aligning as a function of rod concentration and applied shear stress. When scaling the results to the concentration where the isotropic−nematic transition takes place, the experiment and theory show only a qualitative agreement, possibly due to the fact that the real rods are are both semiflexible and charged. However, when scaling the results using the order parameter, which is determined by the interactions between the rods, theory and experiment show an excellent agreement without using any fit parameters. Thus, it can be concluded that the DEH theory accurately captures the dynamic features of a hard rod system. *fd* dispersions constitute such a hard rod system as long as flexibility and charge are properly taken into account, which can be simply achieved by using the order parameter to scale the data. More theoretical work is needed, however, to explain the clear connection between the observed band formation at high concentrations and the dynamic transitions, and to incorporate the effect of flexibility of the rods.

Acknowledgment. We thank Jan Dhont for many discussions and critical reading of the manuscript. Pier-Luca Maffetonne is acknowledged for stimulating remarks. M.P.L. is supported by the Transregio SFB TR6, “Physics of colloidal dispersions in external fields”. Z.D. is supported by Junior Fellowship at Rowland Institute at Harvard. The authors acknowledge support of the EU (sixth FP) in the framework of the Network of Excelence “SOFTCOMP”.

LA050116E

---

(39) Larson, R. G. Roll-cell instabilities in shearing flows of nematic polymers. *Liq. Cryst. 37* (2), 175−197.

(40) Larson, R. G.; Mead, D. W. The ericksen number and deborah number cascades in sheared polymeric nematics. *Liq. Cryst.* **1993**, *5*(2), 151−169.

Chapter 11

Attractive colloidal rods in shear flow

Attractive Colloidal Rods in Shear Flow

M. Ripoll,[*] P. Holmqvist, R. G. Winkler, G. Gompper, J. K. G. Dhont, and M. P. Lettinga

Institut für Festkörperforschung, Forschungszentrum Jülich, D-52425 Jülich, Germany

(Received 19 March 2008; published 15 October 2008)

The effect of shear flow on the isotropic-nematic phase transition of attractive colloidal rods is investigated by a combination of simulations and experiments. The isotropic phase aligns with the flow, while the nematic phase undergoes a collective rotational motion which frustrates the merging of the coexisting regions. The location of binodals, spinodals, and the tumbling-to-aligning transition line in the shear-rate versus concentration plane are investigated. The phase diagrams in the shear-concentration plane for the various strengths of attractions can be mapped onto a master curve by appropriate scaling.

DOI: 10.1103/PhysRevLett.101.168302 PACS numbers: 82.70.−y, 64.60.−i, 83.50.−v

Phase transitions occurring in soft matter systems are significantly affected by flow. Both the nature and location of the phase transition lines are changed due to the applied flow [1]. The challenge is to find the parameters that determine the nonequilibrium steady states under flow conditions. One important parameter is the interfacial tension between coexisting phases [2], as is the case for crystal and liquid phases of spherical colloids under shear flow [3]. Colloidal-rod suspensions constitute a particularly interesting system to study the effect of flow on their phase behavior [4,5], since rod orientation is strongly coupled to the shear field. Rods in the isotropic (I) phase, align with the flow and become paranematic (P). This suggests that the transition to the nematic (N) phase, where rods have orientational order, is facilitated by shear. On the other hand, rods in the nematic phase undergo a collective tumbling motion in the presence of shear flow [6–8]. The question that then arises is how these two effects will affect isotropic-nematic coexistence. Apart from fundamental interest, a detailed understanding of the flow behavior of a model system of attractive colloidal rods is useful for industrial applications where shear alignment of elongated objects, such as carbon nanotubes [9], wormlike micelles [10], and polymers, play a role.

In this Letter, the nonequilibrium phase diagrams of attractive colloidal rods in shear flow are investigated by a combination of mesoscale hydrodynamic simulations, small-angle light-scattering (SALS) experiments, and rheology. The simulations allow for a microscopic understanding of the behavior of coexisting phases and their interface under shear, including the possible role of collective tumbling motion of rods. In addition, the binodals—which define the concentrations of coexisting paranematic and nematic states in the shear-rate versus concentration plane—are determined. Experiments allow for the determination of the full phase diagrams, including spinodals—where the homogeneous nematic state becomes unstable—binodals, and tumbling-to-aligning transition lines. Both in simulations and experiments, the attractive rod-rod interactions are systematically varied, which affects the phase behavior, interfacial properties of coexisting phases as well as tumbling behavior.

Earlier experimental studies have mostly focused on the shear-induced P-N transition of wormlike micelles [10], that can break and recombine. For dispersions of hydroxypropyl-cellulose, the P-N transition temperature has been shown to change due to shear flow [11]. Much less is known about suspensions of monodisperse rodlike colloids like fd-virus particles. These systems exhibit an I-N phase transition without flow. The I-N biphasic gap width in the absence of flow is known to increase significantly when polymer is added, which induces depletion attractions [12]. The nonequilibrium binodal under shear flow conditions for a single, fixed strength of attraction has been studied by rheological experiments on fd-virus dispersions, which show that the P-N transition concentration changes on applying flow [13]. Hence, both attractive interactions as well as flow have a pronounced effect on the location of P-N transition lines. Also the effect of shear on nematic-paranematic interfaces in systems of soft repulsive ellipsoids has been studied by simulations [14].

In our simulations, each rod consists of N_m monomers with a bond and a bending potential. The bond potential keeps the distance between monomers essentially fixed at l_b while the bending potential provides rigidity to each rod [15]. The interactions between the monomers of different rods are described by a Lennard-Jones potential with a minimum of ϵ (in units of the thermal energy k_BT) and a diameter σ. Molecular dynamics simulations of rodlike colloids are combined with a mesoscopic description of the solvent known as multiparticle-collision dynamics (MPC) (see Ref. [16] for details). The simulation box consists of $20 \times 22 \times 30$ cubic collision cells with lattice constant a, and 50 solvent particles per cell. We use the parameters $\sigma = l_b = a/4$. This hybrid approach has been shown to account for long-range hydrodynamic interactions between rods [15] and has been successfully applied to different systems in flow [17]. Lubrication forces, however, are not accounted for in MPC simulations. The rods have an aspect ratio of 20. Previous simulations indicate that *I*-*N* coexistence for such rods occurs in a small interval of packing fractions ϕ_0 around 0.125 [18], which we obtain by including 10^4 rods in the simulation box. To impose shear, Lees-Edwards boundary conditions are employed. For a homogeneous fluid, these boundary conditions result in a linear velocity profile $(v_x, v_y, v_z) = (\dot{\gamma}y, 0, 0)$, with $\dot{\gamma}$ the applied shear rate (where the x direction is the flow direction and the y direction is the gradient direction). Shear rates are expressed in simulation time units $\sqrt{ma^2/k_BT}$, where m is the mass of a solvent molecule.

The simulated system is first prepared in equilibrium with coexisting isotropic and nematic phases, where the director of the nematic phase is aligned parallel to the interface. A snapshot of *I*-*N* coexistence in equilibrium is shown in Fig. 1(a). Then, shear is applied with the imposed flow direction parallel to the interface. At small shear rates, rods in the isotropic phase flow-align, i.e., become paranematic, and portions of the nematic phase display collective rotations, as shown in Fig. 1(b) and in Ref. [19]. These periodic motions were also observed in simulations for hard rods in a full nematic phase [20]. This behavior is characterized by both the local concentration and the local orientational order parameter $S_x(y) \equiv [3\overline{\hat{u}_x\hat{u}_x} - 1]/2$, where $\hat{u}_x$ is the component of the unit vector connecting the end points of a rod along the flow direction, and the overline indicates averaging over the vorticity and flow directions. The time dependence of the density ϕ and orientational order parameter S_x of rods as a function of the position y along the gradient direction is plotted in Figs. 1(c) and 1(d). As can be seen from Fig. 1(c), the nematic phase has a higher concentration than the isotropic phase, as expected. More importantly, Fig. 1(d) demonstrates the periodic tumbling motion of rods in the nematic phase. This is seen for all nematic domains in coexistence with paranematic regions and for all strengths of attractions studied. At long times, both Figs. 1(c) and 1(d) show that the nematic phase is somewhat displaced and seems to split into two nematic domains. Such a behavior is also seen experimentally by confocal microscopy [19]. Binodals are determined at times where the density of the paranematic state has reached a stationary value (this happens approximately at $\dot{\gamma}t = 25$, 50, 100 for $\epsilon = 3.0$, 3.2, 3.5, respectively) by averaging over about one tumbling period. The binodals obtained in this way are plotted in Fig. 2(a) for different attractions. Here, the concentration is expressed in terms of φ_{nem} and the shear rate is scaled by a factor $\dot{\gamma}_{\mathrm{max}}$ such that all data points fall onto a master curve. This master curve is obtained from the combined set of data from both simulations and experiments (which will be discussed below). The scale factor $\dot{\gamma}_{\mathrm{max}}$ can be identified with the maximum of the binodal. Simulations for shear rates just above $\dot{\gamma}_{\mathrm{max}}$ indeed indicate a homogeneous state. The inset in Fig. 2(a) shows that the effect of the increasing attraction between rods is that the coexistence region widens and that $\dot{\gamma}_{\mathrm{max}}$ increases. Because of slowing down of the dynamics and large-scale correlations close to spinodals, considerably longer simulations with larger system sizes would be required to determine the location of spinodals.

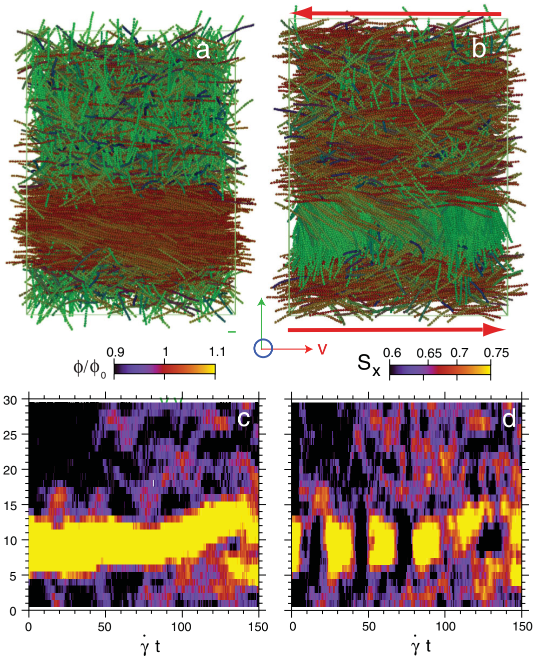

FIG. 1 (color). Snapshots of the simulation box with $\epsilon = 3.5$, (a) at equilibrium, and (b) in a tumbling event at $\dot{\gamma} = 0.003$. Colors in (a) and (b) are coding the rod orientation: horizontal is red, vertical is green, and perpendicular to plane of view is blue. Red arrows in (b) denote flow direction. (c) Time evolution of the normalized density ϕ/ϕ_0, and (d) of the orientational order parameter S_x along the gradient direction. For a movie see Ref. [19].

In our experiments, we use fd-virus suspensions where depletion attractions are varied through addition of dextran. fd virus is a long and thin rodlike particle (880 nm long, aspect ratio 120, persistence length 2.2 μm) [12]. Suspensions of varying colloid and dextran concentrations were prepared as follows. First, a homogeneous fd-virus suspension of 21.1 mg/ml fd virus with dextran (480 kd, Pharmacosmos) in 20 mM Tris buffer with 100 mM NaCl is allowed to macroscopically phase separate into an isotropic and nematic phase. A volume V_{nem} of the nematic phase is then mixed with a volume V_{iso} of the coexisting isotropic phase. The concentration of the fd rods is characterized by the fraction $\varphi_{\mathrm{nem}} = V_{\mathrm{nem}}/(V_{\mathrm{nem}} + V_{\mathrm{iso}})$ of the nematic phase that is present in the homogeneous mixture. This ensures that the polymer osmotic pressure (and hence the strength of attraction) in the homogeneous suspensions is independent of the rod concentration like for the simulations. The way the phase diagram is determined experimentally is conceptually different from simulations. We

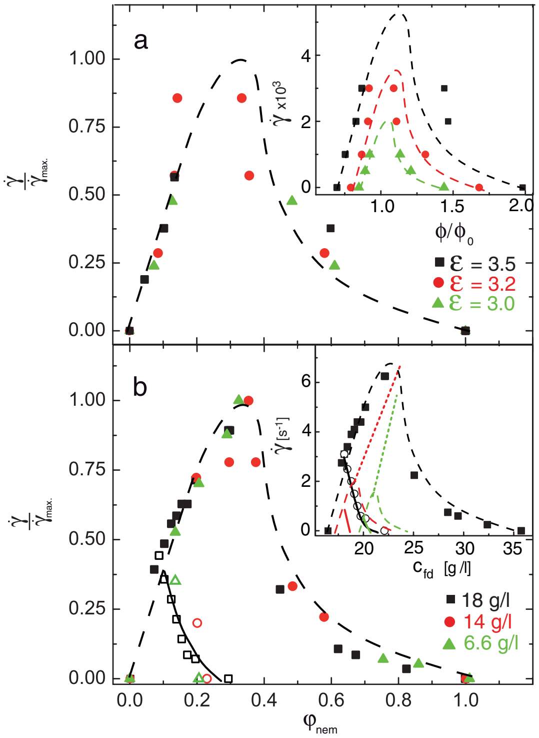

FIG. 2 (color online). (a) Nonequilibrium phase diagram obtained from simulations and (b) from experiments for various values of the strength of attraction interaction, with shear rates normalized by the maximum shear versus the fraction of equilibrium nematic phase. The open symbols in (b) are spinodal points. The insets present the unscaled data. Data points for the lower binodals in the inset in (b) are not shown for clarity. The dotted lines originating from the maximum of the binodal in the experimental diagram correspond to the tumbling-to-aligning transition lines. The solid lines in the inset in (b) at low shear rates indicate the location of the spinodals for the two lowest polymer concentrations. The dashed lines are the conjectured master curve, which are identical in (a) and (b).

obtain the binodal and spinodal experimentally by starting from a stable, homogeneous shear-induced nematic state at 100 s^{-1}, and taking data immediately after reducing the shear rate to a prescribed value. We measure the induction time for the formation of inhomogeneities, as probed with light scattering, after such a shear-rate quench. The induction time vanishes on approaching the spinodal line, while it diverges on approaching the binodal. In Figs. 3(a) and 3(b), the induction time and its inverse are shown as a function of concentration for several shear rates. The resulting experimental phase diagram is displayed in Fig. 2(b), scaled in the same way as for the simulations. The inset also displays the tumbling-to-aligning transition lines. As was shown for *fd*-virus suspensions in the fully nematic phase [7], this transition corresponds to the point in the flow curve where shear thickening occurs, as well as the shear rate at which nematic domains disappear. Both features can also be observed for flow-induced nematics with $\varphi_{\rm nem} > 0.4$. An example of a flow curve is given in Fig. 3(c). The middle inset in Fig. 3(c) shows an anisotropic scattering pattern typical for the sheared nematic structure, while after the peak in the viscosity only background scattering is observed (right inset). The tumbling-to-aligning transition lines obtained from these two different experiments coincide within experimental error. Note that the formation of vorticity bands reported earlier [21] does not affect the light-scattering results.

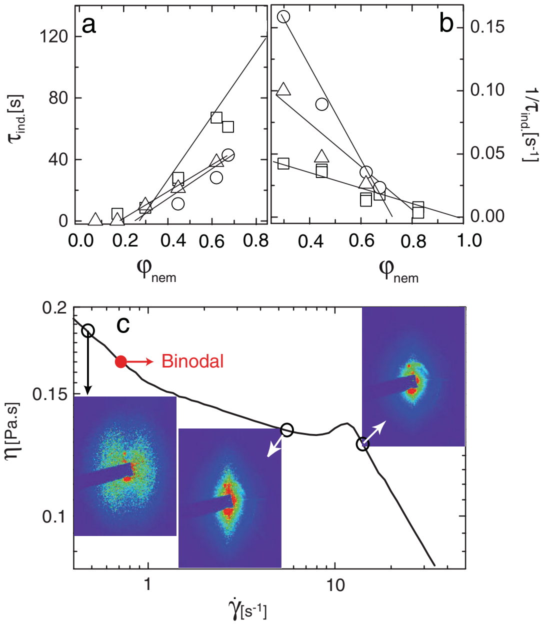

FIG. 3 (color). (a) Induction time and (b) inverse of the induction time after a shear-rate quench from 100 s^{-1} to 0 (□), 0.5 (○), and 1.5 s^{-1} (△) as a function of the fraction of nematic phase. Lines correspond to the extrapolated linear behavior. (c) Flow curve of a *fd*-dextran mixture with an equilibrium nematic volume fraction of 62%. The insets are snapshots of light scattering patterns at the indicated shear rates taken after 170 sec. All data correspond to a dextran concentration of 18 g/l.

The most striking feature of Fig. 2 is that the scaled experimental and simulation binodals overlap for different attractions, as do the scaled spinodals. Coexisting nematic states are in tumbling motion while the paranematic state is flow aligned, so that the interface between the two phases is highly dynamic. Time-averaged stresses across such interfaces must be obtained from dynamical equations for order parameters, together with an expression for the stress in terms of these order parameters, in order to calculate an effective interfacial tension. Moreover, the tumbling-to-aligning transition line ends at the maximum of the binodal, which is also the point where the tumbling nematic

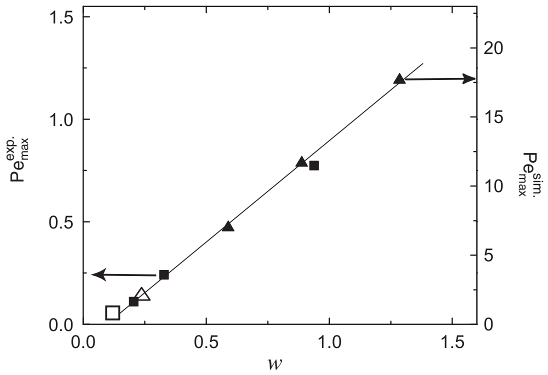

FIG. 4. The Peclet number at the maximum P_{max} as a function of the width of the equilibrium phase diagram w for simulations (▲, right axis) and experiments (■, left axis). The open symbols denote the extrapolation to the limit of hard rods, with $w = 0.1$ for an aspect ratio of 120 (□, left axis) and $w = 0.25$ for an aspect ratio of 20 (△, right axis).

and flow-aligned paranematic states merge. The spinodal line ends far below the maximum of the binodal. The spinodal displays the expected shear-rate dependence; i.e., shear stabilizes the nematic phase, in line with earlier experiments [5]. Note that the experiments show a nonmonotonic concentration dependence of the location of the maximum of the binodal as a function of the strength of attraction contrary to the simulations. This is probably due to the different forms of the interaction potentials in simulations and experiments.

Because of the observed scaling, the effect of attractive interactions on the phase diagram is reduced to two parameters, $\dot{\gamma}_{max}$ and the biphasic gap width w in the absence of flow, i.e., the difference in packing fractions between the isotropic and nematic phase in equilibrium, $w = (\phi_n - \phi_i)/\phi_0$ (with ϕ_0 the overall packing fraction). These two parameters are found to be linearly related, as shown in Fig. 4. Here, the bare rotational Peclet numbers are defined as $Pe_{max} = \dot{\gamma}_{max}/D_r^0$, where D_r^0 is the rotational diffusion coefficient at infinite dilution. For fd virus, D_r^0 is taken from Ref. [7], while for simulations it is calculated from the length and diameter of a rod [22]. The difference in slopes in Fig. 4 between the experimental and simulation results is due to different aspect ratios of the rods, which affects the rotational self-diffusion close to the phase transition [23]. The open symbols in Fig. 4 refer to an extrapolation to semiflexible rods with only hard-core repulsive interactions.

In conclusion, we have been able to establish generic features of the phase behavior of (attractive) rodlike colloids under flow conditions. Binodals and spinodals in the shear-concentration plane can be mapped onto a master curve for various strengths of attractions. Furthermore, the coexisting nematic is in tumbling motion, which explains why the tumbling-to-aligning transition line in the homogeneous state at higher shear rates ends at the maximum of the binodal.

We thank K. Mussawisade for his collaboration in the initial stage of this project. Financial support by the German Research Foundation (DFG) within SFB TR 6, and the European Network of Excellence SoftComp (Contract No. NMP3-CT-2004-502235) is gratefully acknowledged. M. R. thanks the Spanish MCYT (Project No. FIS2007-65869-C03-03) for partial support.

---

*m.ripoll@fz-juelich.de

[1] B. J. Ackerson and P. N. Pusey, Phys. Rev. Lett. **61**, 1033 (1988); P. D. Olmsted and P. M. Goldbart, Phys. Rev. A **46**, 4966 (1992).
[2] M. C. Cross and P. C. Hohenberg, Rev. Mod. Phys. **65**, 851 (1993).
[3] S. Butler and P. Harrowell, Nature (London) **415**, 1008 (2002).
[4] S. Hess, Z. Naturforsch. A **31**, 1034 (1976); H. See *et al.*, J. Chem. Phys. **92**, 792 (1990); P. D. Olmsted and C. Y. D. Lu, Phys. Rev. E **60**, 4397 (1999).
[5] T. A. J. Lenstra *et al.*, J. Chem. Phys. **114**, 10 151 (2001).
[6] R. Larson, Macromolecules **23**, 3983 (1990).
[7] M. P. Lettinga *et al.*, Langmuir **21**, 8048 (2005).
[8] J.-F. Berret *et al.*, Europhys. Lett. **32**, 137 (1995); T. Tiele *et al.*, J. Rheol. (N.Y.) **45**, 29 (2001).
[9] E. K. Hobbie and D. J. Fry, Phys. Rev. Lett. **97**, 036101 (2006).
[10] J.-F. Berret *et al.*, J. Phys. II (France) **4**, 1261 (1994); J.-F. Berret, Langmuir **13**, 2227 (1997).
[11] N. Grizzuti and P. L. Maffeteone, J. Chem. Phys. **118**, 5195 (2003).
[12] Z. Dogic *et al.*, Phys. Rev. E **69**, 051702 (2004).
[13] M. P. Lettinga and J. K. G. Dhont, J. Phys. Condens. Matter **16**, S3929 (2004).
[14] G. Germano and F. Schmid, J. Chem. Phys. **123**, 214703 (2005).
[15] R. G. Winkler *et al.*, J. Phys. Condens. Matter **16**, S3941 (2004).
[16] A. Malevanets and R. Kapral, J. Chem. Phys. **110**, 8605 (1999); T. Ihle and D. M. Kroll, Phys. Rev. E **63**, 020201 (R) (2001); M. Ripoll *et al.*, Europhys. Lett. **68**, 106 (2004).
[17] M. Ripoll *et al.*, Phys. Rev. Lett. **96**, 188302 (2006); H. Noguchi and G. Gompper, Proc. Natl. Acad. Sci. U.S.A. **102**, 14159 (2005).
[18] A. Yethiraj and H. Fynewever, Mol. Phys. **93**, 693 (1998).
[19] See EPAPS Document No. E-PRLTAO-101-038842 for movies of the dynamics *I-N* system under shear from simulations and experiments. For more information on EPAPS, see http://www.aip.org/pubservs/epaps.html.
[20] Y. G. Tao *et al.*, Phys. Rev. Lett. **95**, 237802 (2005).
[21] K. Kang *et al.*, Phys. Rev. E **74**, 026307 (2006).
[22] M. M. Tirado and J. García de la Torre, J. Chem. Phys. **73**, 1986 (1980).
[23] I. Teraoka and R. Hayakawa, J. Chem. Phys. **91**, 2643 (1989).

Chapter 12

Vorticity banding in rod-like virus suspensions

PHYSICAL REVIEW E **74**, 026307 (2006)

Vorticity banding in rodlike virus suspensions

Kyongok Kang,[1] M. P. Lettinga,[1] Z. Dogic,[2] and Jan K. G. Dhont[1]
[1]*Institute für Festkörper Forschung (IFF), Weiche Materie, Forschungszentrum Jülich, D52425 Jülich, Germany*
[2]*Rowland Institute at Harvard, 100 Edwin H. Land Boulevard, Cambridge, Massachusetts 02142, USA*

(Received 16 February 2006; published 28 August 2006)

Vorticity banding under steady shear flow is observed in a suspension of semiflexible colloidal rods (fd virus particles) within a part of the paranematic-nematic biphasic region. Banding occurs uniformly throughout the cell gap within a shear-rate interval $(\dot{\gamma}_-, \dot{\gamma}_+)$, which depends on the fd concentration. For shear rates below the lower-border shear rate $\dot{\gamma}_-$ only shear elongation of inhomogeneities, which are formed due to paranematic-nematic phase separation, is observed. Within a small region just above the upper-border shear rate $\dot{\gamma}_+$, banding occurs heterogeneously. An essential difference in the kinetics of vorticity banding is observed, depending on the morphology of inhomogeneities formed during the initial stages of the paranematic-nematic phase separation. Particle tracking and polarization experiments indicate that the vorticity bands are in a weak rolling flow, superimposed on the applied shear flow. We propose a mechanism for the origin of the banding instability and the transient stability of the banded states. This mechanism is related to the normal stresses generated by inhomogeneities formed due to the underlying paranematic-nematic phase transition.

DOI: 10.1103/PhysRevE.74.026307 PACS number(s): 47.20.Ft, 47.55.−t, 47.15.Fe, 82.70.−y

I. INTRODUCTION

At equilibrium, complex fluids undergo a variety of ordering transitions that are driven by purely thermodynamic forces (see, for example, Refs. [1,2]). External fields can greatly affect the phase behavior of these systems. For nonconservative fields such as a shear flow no thermodynamic analog is yet known, where the equality of scalar quantities in coexisting phases (the analogs to pressure and chemical potential) suffices to predict the location of phase transition lines as a function of the strength of the driving force. The search for such a formalism remains at the forefront of research in soft condensed matter and nonequilibrium physics [3,4]. In addition to nonequilibrium phases, systems driven by a shear flow frequently exhibit hydrodynamically driven pattern formation which have no equilibrium analogs. Some representative examples include Taylor-Couette flow at high shear rates and shear banding at much lower shear rates [5–7].

A particularly important example of a complex fluid whose phase behavior is greatly affected by a shear flow is a system of rodlike colloids. At equilibrium rods undergo a thermodynamically driven phase transition from an isotropic to a liquid crystalline nematic phase [2]. Shear flow strongly aligns rods and therefore affects the location of the isotropic (paranematic-) nematic phase transition [8–10]. An isotropic state under shear flow is referred to as a “paranematic” state to indicate that flow partially aligns otherwise isotropic rods. The paranematic-nematic *binodal* is defined as the locus of points that separates the one-phase region from the region where phase coexistence occurs. The *spinodal* under shear flow is defined as the locus of points where the system becomes unstable against infinitesimally small perturbations of the orientational order parameter. The spinodal and binodal referred to here and hereafter in the present paper are connected to the paranematic-nematic phase transition, that is, the shear-affected isotropic-nematic phase transition that also occurs in the absence of flow. Whenever a spinodal or binodal is mentioned in this paper, it refers to the shear-affected isotropic-nematic phase transition and not to the banding transition, except when explicitly mentioned otherwise.

Besides shifts of the equilibrium binodals and spinodals, shear flow can also lead to the formation of banded structures in a number of complex fluids including rodlike colloids studied here. In general two types of banding transitions can be distinguished: gradient banding and vorticity banding. In the case of gradient banding, coexisting regions (“bands”) extend along the gradient direction. The shear rate is essentially constant within these bands (see Refs. [11–16]). The gradient banding transition is relatively well understood and it occurs when the shear stress decreases with increasing shear rate [17–21]. In case of vorticity banding, regions of different internal structure are alternately stacked along the vorticity direction [9,10,22–24]. The origin and the mechanism of the vorticity banding transition are not yet known. It was suggested in Ref. [17] that vorticity banding can occur when the shear stress is a multivalued function of the shear rate. As far as we know, there are no systematic experimental studies of vorticity banding concerning shear-band formation kinetics, the characteristic features of vorticity-banded structures, the internal structure of individual bands, and the possible connection to the underlying nonequilibrium phase behavior.

In the present paper we systematically study pattern formation (vorticity-banding transition) under steady shear flow conditions of a suspension of rodlike colloids in shear flow, where bands of different orientational order are stacked along the vorticity direction. We quantify the relationship between pattern formation and the underlying nonequilibrium, shear-affected paranematic-nematic phase transition. Vorticity banding is observed within a part of the biphasic isotropic-nematic region, under both controlled shear-rate and shear-stress conditions. We propose a possible mechanism that describes the vorticity-banding instability and also explains the temporary stability of the quasistationary banded states. The proposed mechanism implies that there is no genuine stationary vorticity-banded state, and that its transient stability relies on the presence of inhomogeneities formed due to paranematic-nematic phase separation. The lifetime of the vorticity-banded state is thus set by the lifetime of the inhomogeneities. As soon as the inhomogeneities disappear, for example due to sedimentation, the vorticity-banded state also disappears. This process takes a few days as compared to the formation of bands within an hour. Since vorticity banding occurs only inside the biphasic paranematic-nematic region, the inhomogeneities that form after a shear-rate quench due to paranematic-nematic phase separation seem to play a crucial role in rendering the system unstable against vorticity banding. The kinetics of the banding transition is found to be fundamentally different depending on whether these inhomogeneities are isolated or form an interconnected structure. Furthermore, above the region where bands are formed homogeneously, there is a small shear-rate range where heterogenous banding is observed.

As an experimental model system we use the monodisperse rodlike virus fd. Extensive experiments have shown that the equilibrium isotropic-nematic phase transition of fd virus is quantitatively described by Onsager's theory [25] when it is extended to take into account fd flexibility and its surface charge [26–29]. Besides fd, numerous other systems of rodlike particles exhibit an isotropic-nematic phase transition, with important examples including DNA [30], tobacco mosaic virus [31] and synthetic Boehmite rods [32]. The phase behavior of fd has been studied in the presence of an external magnetic (conservative) field in Ref. [33]. The induced shift of isotropic-nematic binodals and spinodals for such a conservative external field can be defined thermodynamically, simply by adding the corresponding potential energy to the Hamiltonian. The analogous procedure is not allowed for the shear flow due to its nonconservative nature.

Besides previous experiments on fd [9,10], the only other experimental study of the paranematic-nematic phase transition of colloidal rods in shear flow, that we are aware of, is in dispersions of hydroxypropylcellulose [15]. However, there is significant work done on shear banding and phase transitions of related systems such as wormlike micelles [11,12,23,34] and thermotropic liquid crystals [13,14]. A complication of wormlike micelles systems, when compared to suspensions of rods, is that the worm-length distribution and the scission and recombination kinetics depend on the shear rate.

The main body of this paper is organized as follows. In Sec. II, details of the fd virus suspensions, the experimental setup, and the data analysis are given. The topology of the shear-induced nonequilibrium phase diagram is given in Sec. III. The kinetics of band formation is described in Sec. IV. In Sec. V we describe experiments which indicate that the bands are in rolling flow. Finally, we propose a mechanism for the vorticity-banding instability in Sec. VI. This mechanism is reminiscent of the well-known elastic instability of polymers [35–39], where nonuniform elastic deformation of the polymers leads to a rolling flow. In the present case, elastic deformations of inhomogeneities formed due to paranematic-nematic phase separation lead to the vorticity-banding transition and the associated rolling flow.

II. EXPERIMENTAL DETAILS

In this section we discus the colloidal system and the experimental setup together with the data analysis.

A. The colloidal system

We use monodisperse rodlike fd viruses which are a good model system for studies of liquid crystalline phase behavior [26–29]. The bacteriophage fd is a semiflexible filamentous molecule with a contour length $L=880$ nm and a diameter $D=6.6$ nm. The persistence length is $P=2200$ nm, which is more than twice its contour length. Fd virus is thus relatively stiff. The molecular weight of native fd is 1.64×10^7 g/mol. Bacteriophage fd was grown and purified following standard biological protocols, using the Xl1-blue strain of *Escherichia coli* as the host bacteria [40]. The standard yield was approximatively 15 mg of fd per liter of infected bacterial culture. The virus particles were purified by repeated centrifugation ($10^5 g$ for 5–6 h), and redispersed in high-ionic-strength buffer to screen electrostatic interactions (20 mM tris-HCl, *p*H 8.15, 100 mM NaCl). Dextran (507 kD, radius of gyration 16 nm, Sigma-Aldrich) was mixed with the fd dispersion in order to widen the biphasic region and enhance the phase-separation kinetics [29].

Two different dispersions are used in the experiments with two different dextran concentrations. To study the nonequilibrium kinetics and phase diagram we used a low dextran concentration (10.6 mg/ml dextran, 21.7 mg/ml fd). To study the internal structure of bands we used a high dextran concentration (14.5 mg/ml dextran, 21.7 mg/ml fd). Suspensions on which experiments were performed have been prepared as follows. The homogeneous mixtures were allowed to phase separate for a few hours, after which full phase separation was achieved by gentle centrifugation ($10^4 g$ overnight). The binodal concentrations with added low concentration of dextran are determined to be 17.5 ± 0.5 and 29.0 ± 1.5 mg/ml. The width of the phase-coexistence region is considerably wider when compared to a pure fd suspension, where binodal points are at 21 and 23 mg/ml, respectively. A volume V_{iso} from the isotropic phase is mixed with a volume V_{nem} of the coexisting nematic phase. The concentration of fd virus particles in such a mixture is expressed in terms of the quantity $\varphi_{\mathrm{nem}}\equiv V_{\mathrm{nem}}/(V_{\mathrm{nem}}+V_{\mathrm{iso}})$, which varies from 0 for the lower binodal concentration (17.5 ± 0.5 mg/ml) to 1 for the upper binodal concentration (29.0 ± 1.5 mg/ml) in the absence of flow. Homogenized mixtures within the biphasic region at various concentrations φ_{nem} are used for the vorticity-banding experiments. Such mixtures are prepared to be at constant dextran chemical potential, independent of the fd concentration. The samples with higher dextran concentration form thicker and more regular vorticity bands, and are thus more suitable to study the internal structure of the bands.

The variable φ_{nem} defined above is not introduced here as an "order parameter," but rather as a convenient measure for the concentration of a sample relative to the two binodal concentrations. In all our experiments the actual fd concentration is always between the two binodal concentrations, so that φ_{nem} always lies between 0 and 1.

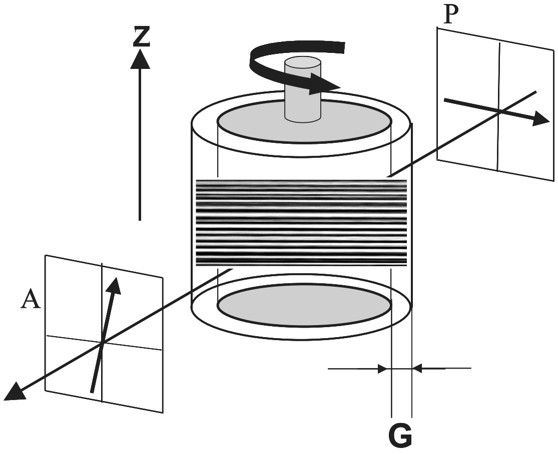

FIG. 1. Schematic of the experimental setup. The optical shear cell is placed between two polarizers, and spatial-temporal images of the banded structure are recorded with a CCD camera equipped with a telecentric lens. Additionally we show an image of a typical banded structure. The polarizers are not exactly crossed for the reasons discussed in Sec. V. The unit vector $\hat{z}$ indicates the vorticity direction.

B. Experimental setup and data analysis

Transparent couette shear cells are used with gap widths ranging from 1.0 to 2.0 mm. The rotating inner cylinder has a radius of 24 mm while the outer cylinder is fixed. The experiments are performed under controlled-rate conditions. For one concentration, the determination of the border shear rates is repeated under controlled-stress conditions, using a Bohlin rheometer (CVO). The optical couette cell is placed between a polarizer and an analyzer and is illuminated from one side with a white light source, as sketched in Fig. 1. The polarizer P is oriented along the flow direction. The optimal contrast between vorticity bands is obtained when the polarizer and analyzer A are not exactly crossed. Typically, the angle between the analyzer and the flow direction is 80°. The reason for this is related to the weak rolling flow within the bands and is discussed in Sec. V. The transmitted light intensity is monitored with a 12-bit charge-coupled device CCD camera (RS Princeton Instruments) equipped with a telecentric lens (Computar 5.5 mm). One pixel corresponds to 8.8 μm in real space, which sets the spatial resolution in the vorticity direction of our setup. The depth of the focus is about 1 mm. Therefore, an image is smeared along the gradient direction over a large part of the gap. Since the orientational order differs in the two types of vorticity bands, they appear in transmission as alternating bright and dark stripes, stacked along the vorticity direction (see the inset in Fig. 1).

For lower dextran concentrations, the extent of a single dark or bright band is between 50 and 120 μm. A single image at each time covers a region that includes about 50 vorticity bands divided over 582 pixels. The intensity at a particular height is the average over 80–100 adjacent pixels along the flow direction. Typically, ten such cuts from a single image are analyzed as described below and averaged. To probe the evolution of banded structures right after a shear-rate quench, optical morphologies are recorded every 10–60 s, depending on the rate of band formation, which is a function of the cell gap width, fd concentration, and shear rate. The total recording time varies from 1 to 3 h, which is the time to reach the quasistationary banded state.

The intensity profiles are analyzed as follows. An intensity profile $I(z,t)$ at a particular time t obtained from images as described above is first represented by a Fourier series as

$$I(z,t) = I_0(t) + \sum_{n=1}^{N_{\max}} [\alpha_n(t)\sin(2\pi z/L) + \beta_n(t)\cos(2\pi z/L)], \tag{1}$$

where I_0 is the average intensity, L is the total height of the image, and $0 \leqslant z \leqslant L$ is the height variable along the vorticity direction. In order to avoid high-frequency peaks due to noise being identified as a vorticity band, we averaged three adjacent intensities, corresponding to 26 μm. The maximum number of Fourier modes $N_{\max}$ is therefore equal to one-third of the number of image pixels. A band thus encompasses at least three pixels. The average number $\bar{n}$ of bright and dark bands is now obtained from

$$\bar{n}(t) = \sum_{n=N_{\min}}^{N_{\max}} nP_n(t), \tag{2}$$

where $N_{\min}$ is chosen equal to 3 in order to eliminate spurious long-wavelength variations in light intensity which are much longer than a typical bandwidth, while

$$P_n(t) = \frac{\sqrt{\alpha_n^2(t) + \beta_n^2(t)}}{\sum_{n=N_{\min}}^{N_{\max}} \sqrt{\alpha_n^2(t) + \beta_n^2(t)}} \tag{3}$$

is the normalized probability for a Fourier mode of order n. The average width at a given time of a vorticity band is then obtained from

$$H(t) = L/2\bar{n}(t). \tag{4}$$

As mentioned above, the choices for $N_{\max}$ and $N_{\min}$ are such that high-frequency contributions (due to noise) are eliminated and low-frequency variations (due to nonuniform illumination) do not lead to erroneous results. We confirmed by counting the number of bands by hand for a number of experiments that the procedure described above gives the correct number of bands.

III. THE NONEQUILIBRIUM PHASE DIAGRAM

The paranematic-nematic and vorticity-banding phase diagram in the shear rate versus fd concentration plane is presented in Fig. 2 (similar phase diagrams can be found in Refs. [9,10]). For fd virus suspensions, vorticity banding is observed within a part of the two-phase paranematic-nematic region which is bounded by the binodal. Dextran is added to fd rods, which induces depletion attractions. This in turn leads to a widening of the biphasic region [29] and an en-

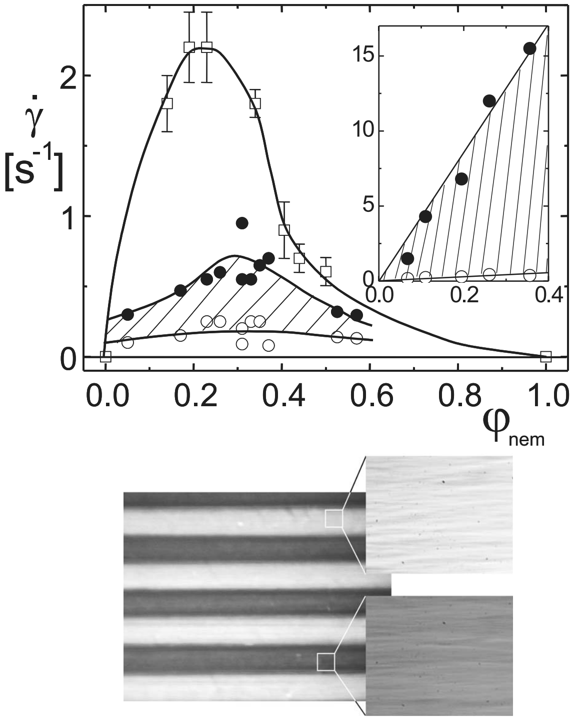

FIG. 2. The nonequilibrium phase diagram in the shear rate versus concentration plane for an overall fd concentration of 21.0 mg/ml and an overall dextran concentration of 10.6 mg/ml. The fd concentration is expressed in terms of φ_{nem} as defined in Sec. II A. The upper solid curve is the paranematic-nematic binodal and the shaded area is the region where vorticity banding is observed. The ○ are experimental points where banding occurs for the first time on increasing the shear rate while the ● are the experimental data where banding ceases to occur. The inset shows part of the vorticity-banding region for an overall dextran concentration of 14.5 mg/ml. Here, the binodal is not shown. The lower figure (which is taken from Ref. [9]) shows a banded state for the same dextran concentration of 14.5 mg/ml. The bandwidth is about 2 mm. The two enlargements on the right show the inhomogeneities that are present within the bands. The thickness of these inhomogeneities is of the order of 10–20 μm.

hancement of both phase-separation and vorticity-banding kinetics. It is still uncertain whether banding occurs in fd suspensions without any dextran.

We first turn our attention to determining the location of the paranematic-nematic binodal under flow, which was accomplished using time-resolved shear-stress measurements after a shear-rate quench [10]. Starting at a high shear rate, where the homogeneous state is stable, the shear rate is quenched to a lower value and the shear stress is measured as a function of time. If the system crosses the binodal, inhomogeneities in concentration and orientation order develop with time, giving rise to an increase of the shear stress. On quenching from a high to a lower shear rate, isotropic inhomogeneities are formed in a nematic background. Since these isotropic inclusions have a higher viscosity as compared to the nematic background, their growth is accompanied by an increase in the shear viscosity. Such time-resolved stress measurements allow the determination of the paranematic-nematic binodal in the fd concentration versus shear rate plane and lead to the upper solid curve in Fig. 2. The binodal determined in this way marks the concentrations of phase coexistence after completion of phase separation, since the homogeneous phases that coexist become metastable or unstable on increasing (for the lower binodal) or decreasing (for the upper binodal) the fd concentration. Note that this binodal is not connected to a shear-induced phase transition, contrary to many wormlike micellar systems. Here, the binodal is merely shear affected, and also occurs in the absence of flow.

The above-described method is not suitable for determining the paranematic-nematic binodal for the case of either high dextran concentration or high fd concentration. With increasing dextran concentrations the binodal is located at increasingly higher shear rates. As a result, the difference in the orientational order across the binodal is not as pronounced as for samples with lower dextran concentration. This leads to a decrease of the stress response after a shear-rate quench and renders the experimental determination of the binodal difficult. For this reason we have not shown the binodal in the inset of Fig. 2. At high fd concentration ($\varphi_{\text{nem}}>0.7$) close to the homogeneous nematic phase, states with periodic tumbling or wagging of rods in shear flow are observed [10,41]. This is evidenced by an oscillating shear-stress response subsequent to a shear-rate quench. For homogeneous nematic phases, theory predicts such behavior for certain rod concentrations and shear rates [37,42–46]. Due to the oscillatory response, the location of the binodal as well as the extent of the vorticity-banding transition cannot be determined for $\varphi_{\text{nem}}>0.7$. Therefore, the measurements of the binodal and vorticity banding are limited to lower fd concentrations. More details about the experimental determination of the binodal are available in Ref. [10].

The vorticity-banding region is determined from profiles taken at various shear rates similar to the ones shown in Fig. 3. The profiles in Fig. 3 persist for more than a week and are taken for a fixed fd concentration ($\varphi_{\text{nem}}=0.23$). The shear rate $\dot{\gamma}_-$ is the lower-border shear rate of the vorticity-banding region (the lower bound of the shaded region in the phase diagram in Fig. 2), and $\dot{\gamma}_+$ is the upper-border shear rate. As can be seen in Fig. 3, for shear rates below $\dot{\gamma}_-$, no clear bright and dark bands are formed. Inhomogeneities that are formed due to phase separation are stretched to a certain extent (leftmost profile in Fig. 3), but do not give rise to the formation of vorticity bands. For shear rates ($\dot{\gamma}_-<\dot{\gamma}<\dot{\gamma}_+$) within the vorticity-banding region, clear bright and dark bands are formed (two middle profiles in Fig. 3). These profiles exhibit relatively large intensity variations and a longer-wavelength structure when compared to those outside the banding region. For shear rates slightly above $\dot{\gamma}_+$, heterogeneous vorticity banding is observed (rightmost profile in Fig. 3). The shear-rate range ($\dot{\gamma}_+<\dot{\gamma}<\dot{\gamma}_{het}$) where heterogeneous banding occurs is about 5–10 % of the homogenous vorticity-banding shear-rate range ($\dot{\gamma}_-<\dot{\gamma}<\dot{\gamma}_+$). Experiments of this kind are repeated for different fd concentrations

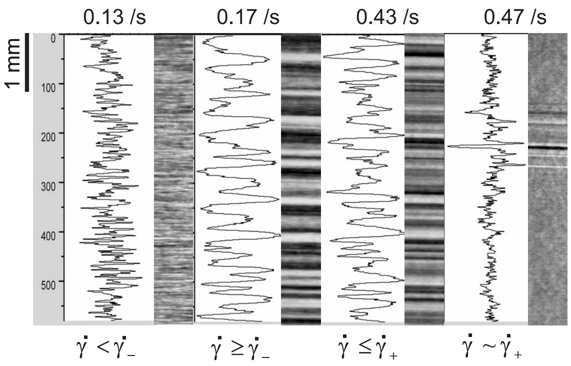

FIG. 3. Quasistationary intensity profiles taken a few hours after the shear-rate quench into the vorticity-banding region. The gap width is 2.0 mm and the fd concentration is $\varphi_{\text{nem}}=0.23$. The overall dextran concentration is 10.6 mg/ml, which complies with the phase diagram in Fig. 2. The border shear rates $\dot{\gamma}_-$ and $\dot{\gamma}_+$ are the lower and higher shear rates that bound the vorticity-banding region in the phase diagram. The leftmost profile shows an image for a shear rate just below $\dot{\gamma}_-$. The two middle profiles are for shear rates within the banding region, while the rightmost profile is taken for the shear rate just above $\dot{\gamma}_+$, where heterogeneous banding occurs. The vertical axis is given in camera-pixel number and a scale bar is added on the left side. The intensity scales are the same for all four profiles.

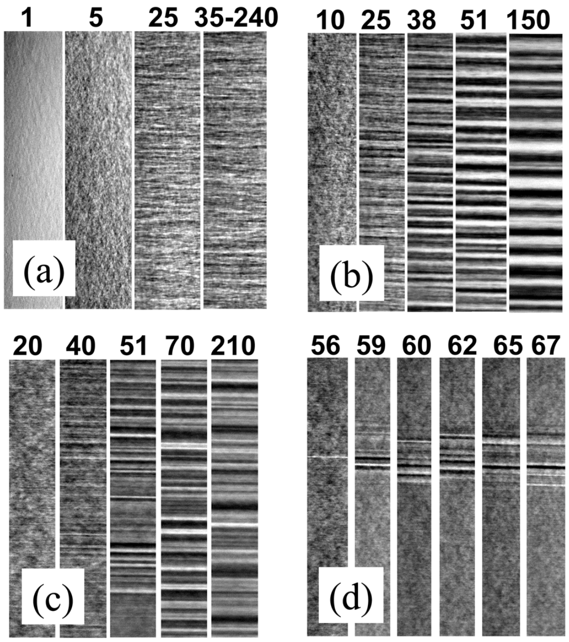

FIG. 4. Temporal evolution of the vorticity banding morphologies at various shear rates for an fd concentration of $\varphi_{\text{nem}}=0.23$ and a gap width of 2.0 mm. The overall dextran concentration is 10.6 mg/ml. The numbers above the intensity profile images refer to the time after the shear-rate quench in minutes. (a), (b) Shear rates 0.15 and 0.17 s^{-1} just below and above the lower-border shear rate $\dot{\gamma}_-=0.16\ \text{s}^{-1}$, respectively. (c), (d) Shear rates 0.45 and $\dot{\gamma}_+=0.47\ \text{s}^{-1}$ just below and above the upper-border shear rate $\dot{\gamma}_+=0.46\ \text{s}^{-1}$, respectively. Heterogeneous banding is observed in (d) just above the upper-border shear rate.

to determine the entire vorticity-banding region in the fd concentration vs shear rate plane. For each fd concentration the final shear rate in the two-phase region is systematically varied in steps of 0.02–0.04 s^{-1}. The prequench shear rate is always 10 s^{-1}, which is far above the binodal.

Due to sedimentation, the system will eventually phase separate into a coexisting paranematic and a sheared nematic bulk phase. This can be seen in Fig. 4 in Ref. [9], which shows a partly demixed system where sedimentation of denser nematic inhomogeneities occurred to some extent. The upper phase in this figure is a homogeneous paranematic phase that does not contain any inhomogeneities. The absence of a banded structure in the upper phase demonstrates that the lower binodal in Fig. 2 coincides with the lower bound of the vorticity-banding region.

The inset in Fig. 2 shows the vorticity-banding region (up to $\varphi_{\text{nem}}=0.4$) for the higher dextran concentration of 14.5 mg/ml. In this case the vorticity-banding region extends to much higher shear rates since the attractions between the rods are increased. Still, this region is contained within the biphasic region as bounded by the binodal. The vorticity bands at higher overall dextran concentrations are larger and more regular. Such bands are used for experiments on the internal flow and orientational order within the bands as described in Sec. V. The typical quasistationary banded structures that is observed for these higher dextran concentrations are shown in the lower part of Fig. 2. On the right-hand side there are two microscopy images that show the inhomogeneous microstructure found within each of the bands. These inhomogeneities are due to paranematic-nematic phase separation and are formed right after the shear-rate quench. In the proposed mechanism that underlies vorticity banding as presented in Sec. VI, these inhomogeneities play an essential role in the stabilization of the banded state.

IV. KINETICS OF VORTICITY BANDING

The experiments discussed in the present section are done on fd-dextran suspensions with the lower overall dextran concentration of 10.6 mg/ml. Figure 4 shows time-dependent banded intensity profiles subsequent to a quench from an initial shear rate of 10 s^{-1} to four final shear rates located in the biphasic paranematic-nematic region. The profiles in Fig. 4(a) are for a final shear rate 0.15 s^{-1} just below the lower-border shear rate $\dot{\gamma}_-=0.16\ \text{s}^{-1}$. No banding is observed. Here, the striped pattern is due to inhomogeneities that are formed due to paranematic-nematic phase separation and are elongated in shear flow. For Fig. 4(b), the final shear rate 0.17 s^{-1} is just above $\dot{\gamma}_-$. Here, the growth of the vorticity bands is clearly visible as the appearance and coarsening of bright and dark bands. Similarly, for a shear rate 0.45 s^{-1} just below the upper-border shear rate $\dot{\gamma}_+=0.46\ \text{s}^{-1}$, the banding transition is clearly observed in Fig. 4(c). In a small

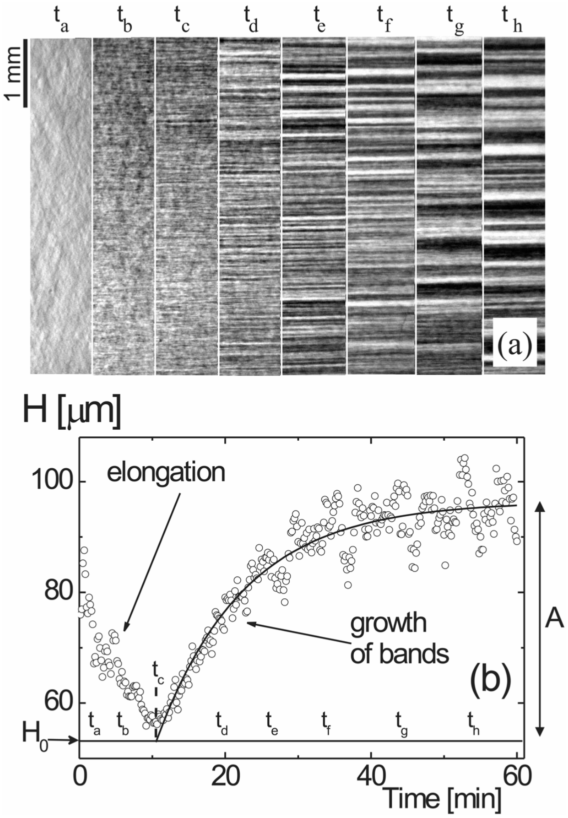

FIG. 5. (a) Temporal development of vorticity profiles right after a shear-rate quench into the banding region. (b) The bandwidth H as a function of time right after a shear quench, as measured from profiles as given in (a). The solid line is an exponential fit to the data according to Eqs. (4) and (6). Here, the times t_a–t_c in both figures are related to shear stretching of inhomogeneities at several times after the quench, while t_d–t_h relate to growth of vorticity bands. The fd concentration is $\varphi_{\mathrm{nem}}=0.23$, the shear-cell gap width is 2.0 mm, and the shear rate is 0.25 s^{-1}. The overall dextran concentration is 10.6 mg/ml. The shear rate is located in the middle of the vorticity-banding region.

shear-rate region just above the upper-border shear rate $\dot{\gamma}_+$, heterogeneous banding occurs, as can be seen in Fig. 4(d).

In order to quantify the growth kinetics of vorticity bands, the time-dependent bandwidth is obtained from intensity profiles by the Fourier-mode analysis described in Sec. II B. A typical result of such an analysis is shown in Fig. 5(b). There is a well-defined time t_0, beyond which vorticity banding occurs. Afterward the bandwidth increases continuously until it saturates at long times (the times indicated as t_d–t_h are in this regime). The time t_0 corresponds to the profile marked with t_c. From the corresponding image in Fig. 5(a) it can be seen that, indeed, at the time t_0 clear bright and dark stripes begin to appear. On average the bright and dark regions have an equal width during their growth.

It is much harder to ascertain the behavior of the system prior to the onset of the shear-banding transition. Since the depth of the camera focus is 1 mm, the acquired image is a superposition of spatial variations of inhomogeneities along the gradient direction. Therefore, the apparent bandwidth found in this region using image analysis is highly susceptible to artifacts. The best way to study the behavior of inhomogeneities formed in this region is with small-angle light scattering (SALS). SALS data showing the evolution of coexisting droplets (inhomogeneities) upon a shear-rate quench into a biphasic region are shown in Ref. [9]. The conclusion drawn from these experiments is that right after the shear-rate quench the inhomogeneities formed due to paranematic-nematic phase separation are shear stretched along the flow direction. This process is usually complete in about 10 min. After this initial stage we do not see any significant change in the SALS pattern. This indicates that any further coarsening process of coexisting phases is suppressed by the shear flow. Even after vorticity bands are fully developed it is possible to observe the presence of inhomogeneities in both bands (see lower panel of Fig. 2).

The relevant parameters obtained from growth curves like the one in Fig. 5(b) are the growth time and final bandwidth in the stationary state. These parameters are extracted as follows. We write

$$H(t) = H_0 + H'(t) \quad \text{for } t \geqslant t_0, \tag{5}$$

where t_0 is the time at which banding sets in, H_0 is the bandwidth at time t_0, and H' describes the growth of the bands. The time dependence of the vorticity-bandwidth, to within experimental error, can be described with a single time exponential,

$$H'(t) = A\{1 - \exp[(t_0 - t)/\tau]\} \quad (t \geqslant t_0), \tag{6}$$

where A is the total increase of the bandwidth at long times. This will be referred to as *the growth amplitude* while τ is the *band-growth time*. The final bandwidth is equal to $H_0 + A$ (see Fig. 5). The solid line in Fig. 5(b) is a best fit to Eqs. (4) and (6) for $t > t_0$. The parameters A and τ characterize the growth kinetics of the vorticity bands.

An exponential growth of the bandwidth is observed to within experimental error. The growth time τ is therefore the relevant experimental measure for the growth rate of bands. There is as yet no theory concerning band-growth kinetics that explains exponential growth or possible deviations from exponential growth at longer times.

The growth time τ and the growth amplitude A are measured as functions of shear rate and fd concentration (within the shaded region in Fig. 2). To compare such measurements for different fd concentrations, the shear rate is normalized in dimensionless units as

$$\dot{\gamma}_N \equiv \frac{\dot{\gamma} - \dot{\gamma}_-}{\dot{\gamma}_+ - \dot{\gamma}_-}. \tag{7}$$

Here, $\dot{\gamma}_-$ and $\dot{\gamma}_+$ are the lower-border and upper-border shear rates, respectively.

Systematic measurements of kinetic parameters are done for two different fd concentrations $\varphi_{\mathrm{nem}}=0.23$ and 0.35. The final bandwidth H_0+A and the growth time τ are given in Figs. 6(a) and 6(b) as a function of the normalized shear rate.

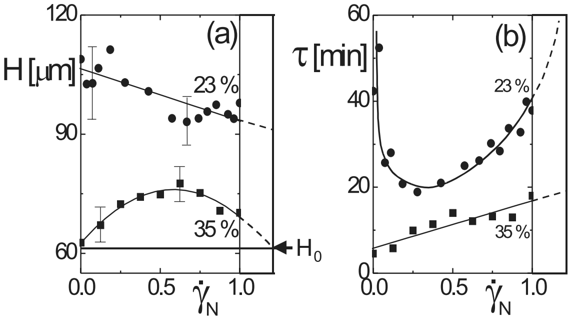

FIG. 6. (a) The final bandwidth as a function of the normalized shear rate as defined in Eq. (7) for two fd concentrations $\varphi_{\text{nem}}=0.23$ and 0.35, as indicated in the figure. In both cases the overall dextran concentration is 10.6 mg/ml. (b) The band-growth time τ as a function of shear rate for the same fd concentrations. Above the upper-border shear rate $\dot{\gamma}_+$, heterogeneous banding occurs for both concentrations. The dotted lines are estimates of bandwidths and growth rates from intensity profiles like in Fig. 4(d).

The relatively small shear-rate range beyond $\dot{\gamma}_+$ where heterogeneous banding occurs is also indicated in this figure. Since a Fourier-mode analysis in this region is not possible, the dashed lines are simple estimates from profiles such as the one given in Fig. 4(d).

We find an important difference in the kinetic behavior depending on the fd concentration. For both cases the bandwidth at the instant of time where banding sets in is $H_0=60\pm5$ μm. The final bandwidth is always larger than the bandwidth H_0 when banding starts. The final bandwidth for lower fd concentration $\varphi_{\text{nem}}=0.23$ varies by about 10% throughout the banding region. The band-growth time τ diverges both in the vicinity of the lower-border shear rate $\dot{\gamma}_-$ and below the shear rate $\dot{\gamma}_{\text{het}}$ where heterogeneous banding ceases to occur. Hence, for low fd concentration, banding ceases to occur for shear rates lower than $\dot{\gamma}_-$ or higher than $\dot{\gamma}_{\text{het}}$ due to a vanishing growth rate $1/\tau$. In contrast, for high fd concentration ($\varphi_{\text{nem}}=0.35$) band-growth rates are finite throughout the banding region [lower curve in Fig. 6(b)]. The reason that banding ceases to occur in this case, for shear rates below $\dot{\gamma}_-$ and above $\dot{\gamma}_{\text{het}}$, is that the growth amplitude A vanishes [lower curve in Fig. 6(a)].

Additionally we note that the time t_0 is constant throughout the region where homogeneous banding occurs, to within experimental error. For $\varphi_{\text{nem}}=0.23$, $t_0=11\pm2$ min, while for $\varphi_{\text{nem}}=0.35$, $t_0=8\pm2$ min.

Assuming that the inhomogeneities formed due to phase separation are at the origin of the vorticity-banding instability, the different banding kinetics for the two fd concentrations are probably related to the different morphology and mechanical properties of these inhomogeneities. Figure 7 shows the morphologies for three different fd concentrations during the early stages of phase separation, obtained by confocal microscopy. These images are taken after a shear-rate quench to a zero shear rate. For the lowest concentration, an interconnected morphology is observed during the initial stages of phase separation. This is reminiscent of spinodal decomposition. After about 10 min, the connectedness is lost, and a blurry morphology of inhomogeneities is formed. At the highest fd concentration, nucleation of isotropic tactoids in a nematic background is observed. A somewhat ordered, noninterconnected structure exists after about 10 min. For the middle concentration, which is close to the spinodal, interconnectedness still exists to some extent after 10 min. Slow phase separation in the vicinity of the spinodal leads to a still interconnected structure after a relatively long time. The fact that spinodal decomposition is observed at low fd concentration and nucleation and growth at high concentration is due to the residual alignment of the fd rods subsequent to a shear quench [47,48]. A quantitative analysis of this type of phase-separation kinetics is given in Ref. [48], where the relevant spinodal concentration is found to be around an fd concentration of $\varphi_{\text{nem}}=0.6$. The morphologies shown in Fig. 7 will be strongly deformed under shear flow, but will probably still be very different with changing fd concentrations. Different mechanical properties of these shear-deformed inhomogeneities might be at the origin of the observed difference in the banding kinetics for the two fd concentrations. A more systematic microscopic investigation is necessary to quantify the relation between the shear-deformed morphology of inhomogeneities and the observed vorticity-banding kinetics.

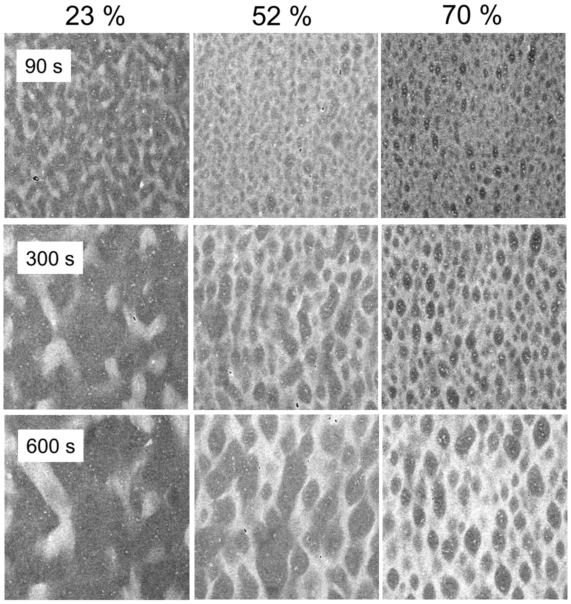

FIG. 7. Confocal images taken in reflection mode of the morphology of phase-separating suspensions, 90, 300, and 600 s after a shear-rate quench to zero shear rate, for three different fd concentrations, $\varphi_{\text{nem}}=0.23$, 0.52, and 0.70, as indicated in the figure. The bright regions are nematic, the dark regions are isotropic. The field of view is 180 μm.

As mentioned before, the spinodal and binodal referred to here are connected to the paranematic-nematic phase transition, that is, the shear-affected isotropic-nematic phase transition which also occurs in the absence of flow. It refers to the shear-affected isotropic-nematic phase transition and not to the banding transition.

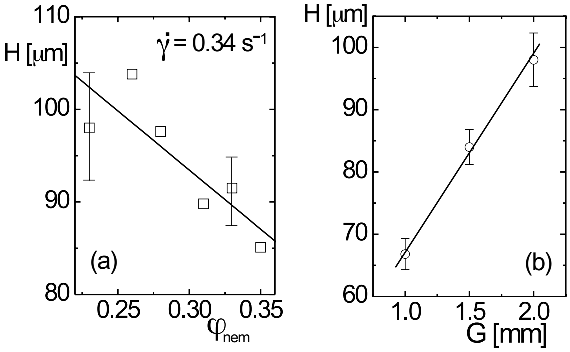

FIG. 8. (a) The concentration dependence of the final bandwidth H for a shear rate equal to 0.34 s^{-1} and for the lower overall concentration of 10.6 mg/ml. The gap width of the shear cell is 2.0 mm. (b) The gap-width dependence of the final bandwidth for $\varphi_{\text{nem}}=0.23$. The data points are averages over shear rates within the banding region, and the error bars relate to the spread in bandwidth on variation of the shear rate [see the upper curve in Fig. 6(a)].

As will be discussed in Sec. VI, gradients in shear rate determine the normal stress that is generated by the inhomogeneities, which in turn stabilizes the quasistationary state. Since the morphology of inhomogeneities at the time that banding sets in depends on the overall fd concentration, as discussed above, the final bandwidth, therefore, might be concentration dependent. As can be seen from Fig. 8(a), the final bandwidth is indeed seen to be depending on the fd concentration. The final bandwidth decreases with increasing fd concentration. There should also be a gap-width dependence of the final bandwidth due to the fact that the gradients in shear rate increase with increasing gap width. Such a gap-width dependence is indeed found, as shown in Fig. 8(b). As can be seen, the bandwidth increases as the gradients in shear rate become larger.

V. STRUCTURE OF QUASISTATIONARY VORTICITY-BANDED STATE

Two experiments provide strong indication that the vorticity banding is due to a weak rolling flow superimposed onto the applied shear flow. For both of these experiments we have used a somewhat higher dextran concentration of 12.3 mg/ml to produce large and regularly stacked vorticity bands. The width of the quasistationary bands under these conditions is about 1 mm. In a first experiment we use polarization optics to probe the orientational order of fd rods within adjacent bands. The couette cell is placed between an exactly crossed polarizer and analyzer (see Fig. 1). A $\lambda/2$ plate is placed between the couette cell and the analyzer, with a variable angle Θ with respect to the polarization direction of the analyzer. When the optical axis of the $\lambda/2$ plate is perpendicular (or parallel) to A there is no visible contrast between the two bands [middle image in Fig. 9(a)]. This implies that the orientational order averaged along the gradient direction is the same in both bands. However, all the rods along the gradient direction are not necessarily aligned in the same direction. In other words the rod orientation can form a left- or right-handed helix. This can be shown by changing the angle of the $\lambda/2$ plate. The polarized light is rotated equally by the two bands but in exactly opposite directions. This is nicely demonstrated by the leftmost and rightmost images in Fig. 9(a), where the $\lambda/2$ plate is at angles 80° and 100° with respect to A. The brightness of a band in the left image is equal to the brightness of adjacent bands in the right image. The transmitted intensity in the two bands as a function of the angle Θ is plotted in Fig. 9(b). Such behavior is consistent with banded structures that are in a rolling motion [as depicted in Fig. 10(b)]. Since the rolling motion is opposite in direction for two adjacent bands, the change of the polarization direction of light is equal but opposite in sign for the two bands. This optical phenomenon is similar to propagation of light in cholesteric liquid crystals [49].

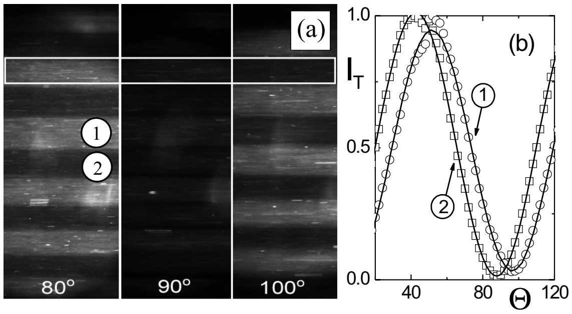

FIG. 9. (a) Images of shear bands illuminated with white light with a polarization direction parallel to the flow and the crossed analyzer directed along the vorticity direction. Between the analyzer and the couette cell there is a $(1/2)\lambda$ platelet with its optical axis at an angle of 80°, 90°, and 100° with respect to the analyzer (from left to right). The height of the images is 6.5 mm. (b) The transmitted intensity of two adjacent bands (the bands marked as 1 and 2 as a function of the angle Θ. Θ is the angle between the analyzer and the $(1/2)\lambda$ platelet. The solid lines are best fits to a linear combination of a sine and cosine with the same period and the same offset phase. The overall dextran concentration is 12.3 mg/ml, the shear rate is 0.26 s^{-1}, and $\varphi_{\text{nem}}=0.17$.

In the second experiment focused on determining the structure of vorticity bands we have tracked tracer particles within a vorticity band. Here, a couette cell is used with two counter-rotating cylinders. The height of the cell is adjusted to keep track of the particle along the vorticity direction. The position of the tracer particle in the gradient direction is probed by changing the relative angular velocity of the two cylinders so as to shift the plane of zero velocity in order to keep the particle within the field of view. The relative angular velocities are adjusted in such a way that the average shear rate remains unchanged. As can be seen from Fig. 10(a), the height z of the tracer sphere, which is the component of its position along the vorticity direction, oscillates in time with an amplitude that is roughly equal to the bandwidth. There is drift of the z position due to sedimentation of the large tracer particle. The experimental measure for the location of the tracer sphere in the gradient direction is the so-called speed ratio S. S is defined as

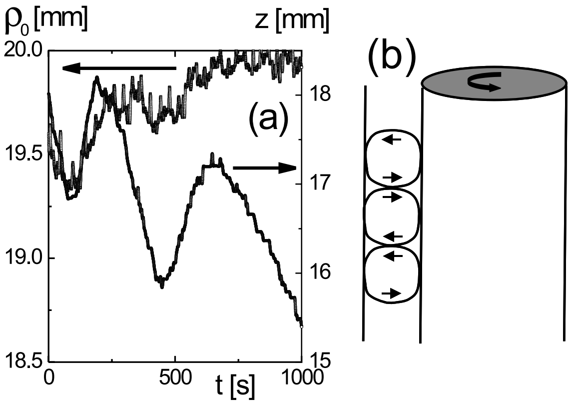

FIG. 10. (a) On the right axis, the position z in the vorticity direction of a tracer sphere with a diameter of 50 μm is shown as a function of time in the quasistationary banded state as measured by video microscopy with a counter-rotating couette cell, where the radii of the inner and outer cylinders are 18.5 and 20.0 mm, respectively. The time $t=0$ is the time after which the optical trapping of the tracer sphere is released. The radial position ρ_0 of the tracer sphere is shown on the left axis. The overall dextran concentration is 12.3 mg/ml, the fd concentration is $\varphi_{\mathrm{nem}}=0.17$, and the shear rate is 0.88 s^{-1}. The bandwidth is about 1 mm. (b) A sketch of the rolling flow that complies with the observed oscillatory behavior of the position coordinate of the tracer particle.

$$S=\frac{\Omega_o}{\Omega_i+\Omega_o}, \qquad (8)$$

where Ω_i and Ω_o are the (absolute values of) the rotational velocities of the counter-rotating inner and outer cylinders, respectively. The rolling velocity is simply superimposed onto the velocity v_0 in the perpendicular direction that one would have for a Newtonian fluid in a couette cell. Indeed, heterodyne dynamic light scattering experiments within the banded state show an essentially linear velocity profile as for a Newtonian fluid. The fluid flow velocity v_0 is given as a function of the radial distance ρ from the centerline of rotation as

$$v_0(\rho)=\frac{\rho}{R_o^2-R_i^2}\left(\Omega_o R_o^2+\Omega_i R_i^2-(\Omega_o+\Omega_i)\frac{R_o^2 R_i^2}{\rho^2}\right), \qquad (9)$$

where R_i and R_o are the radii of the inner and outer cylinders, respectively. The location ρ_0 of the plane of zero velocity is thus equal to

$$\rho_0=R_o R_i\sqrt{\frac{\Omega_o+\Omega_i}{\Omega_o R_o^2+\Omega_i R_i^2}}=\frac{R_o R_i}{\sqrt{S R_o^2+(1-S)R_i^2}}, \qquad (10)$$

where the definition of the experimental parameter S in Eq. (8) has been substituted. This relation is used to construct the plot in Fig. 10(a) for the radial position of the tracer particle. Although there is a drift of the particle toward the outer cylinder due to gradients in the shear rate, the radial position seems to exhibit an oscillatory behavior. Since the tracer particle will migrate to the outer cylinder due to gradients in shear rate and its initial radial position is in the middle of the gap of the shear cell, these oscillations are not very pronounced. Therefore, the data for ρ_0 are too noisy to unambiguously correlate the height and the radial position in order to prove that there is a rolling flow. The data in Fig. 10, however, strongly indicate the existence of a rolling flow, as depicted in Fig. 10(b).

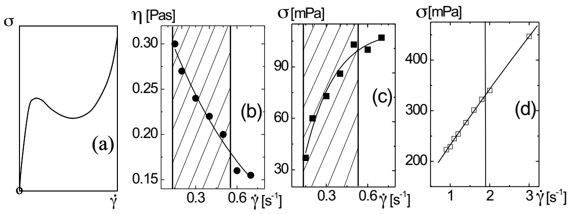

FIG. 11. (a) A typical van der Waals looplike shear-rate dependence of the shear stress for a homogeneously sheared system that will exhibit gradient banding. The viscosity η and the shear stress $\sigma=\dot\gamma\ \eta$ as a function of shear rate are shown in (b) and (c), respectively. Vorticity banding is observed within the shaded region. The vertical bounds of the shaded area correspond to the lower- and upper-border shear rates. The data points are measured 5 min after a shear-rate quench, just before vorticity banding occurs. The fd concentration is $\varphi_{\mathrm{nem}}=0.35$. (d) The shear stress for higher shear rates, for $\varphi_{\mathrm{nem}}=0.33$. The overall dextran concentration is 10.6 mg/ml. The vertical line indicates the location of the binodal. The gap width is 1.0 mm.

Typically, 1–5 h are needed to establish a banded state that remains unchanged for at least a week. There is a difference between density of nematic and paranematic phase and therefore the inhomogeneities will slowly sediment over a long period of time. This will eventually lead to a state where two homogeneous bulk phases coexist: a paranematic and a sheared nematic phase (see Fig. 4 in Ref. [9].). Microscopy images and small-angle light scattering experiments indicate that inhomogeneities are present within the bands [9,10]. These inhomogeneities are necessary to maintain a normal stress along the gradient direction that stabilizes the vorticity bands. As soon as these inhomogeneities coalesce, for example due to sedimentation, the stabilizing normal stress ceases to exist, and bands will disappear. The banded structure is therefore a long-lived, transient state. In this sense the banded structure is referred to as quasistationary, since the inhomogeneities will not persist for ever.

VI. POSSIBLE MECHANISM FOR VORTICITY BANDING

We have measured the flow curve of fd-dextran mixtures for the possible rheological signs of a gradient-banding transition. In the case of gradient banding, the flow curve of the homogeneous system, before banding occurs, exhibits a van der Waals looplike dependence on the shear rate. That is, there is a region of shear rates where the shear stress of the homogeneously sheared suspension decreases with increasing shear rate [see Fig. 11(a)]. A mechanism similar to gradient banding would play a role in the present system when the shear stress of the suspension just before banding sets in would exhibit such a decrease of the shear stress with increasing shear rate. When gradient bands are allowed to fully develop before a stress measurement is done, a plateau in the shear stress as a function of shear rate is observed under controlled shear-rate conditions [17–21]. This plateau can be tilted when the stress couples strongly to variables such as concentration [17]. There is no such signature in the flow curve for the fd suspensions within the vorticity-banding region as seen in Figs. 11(b) and 11(c). Here, the shaded area indicates the vorticity-banding region, that is, the shear-rate range $(\dot{\gamma}_-, \dot{\gamma}_+)$ in the phase diagram in Fig. 2 where vorticity banding is observed. The stress and viscosity data in Figs. 11(b) and 11(c) are obtained 5 min after a shear-rate quench. Vorticity banding sets in after 10 min. These data essentially do not change when measured within a time window of about 5–10 min after the quench. In the case of gradient banding such curves would exhibit a van der Waals looplike behavior as depicted schematically in Fig. 11(a). The system is only weakly shear thinning [see Fig. 11(b)] and does not show any sign of a van der Waals loop nor a stress plateau. In addition, we have repeated the determination of the border shear rates for one concentration under controlled stress conditions. No differences were found with the controlled rate experiments: both border shear rates are the same. The mechanism for vorticity banding is thus clearly different from that of gradient banding. Finally we confirmed that the shear stress is also well behaved throughout the entire biphasic region, as shown in Fig. 11(d). Here, the vertical line indicates the location of the binodal.

In view of the rolling flow within the bands (see Sec. V), the vorticity-banding instability might have a similar origin as the elastic instability studied in polymeric systems [35–39]. The origin of this well-known instability is as follows. When there is a gradient in shear rate, as in a couette cell, the shear-induced stretching of polymer chains leads to normal stresses along the gradient direction. Chains which are not perfectly aligned along the streamlines are stretched in a nonuniform way due to gradients in the shear rate [Fig. 12(a)]. On average, such nonuniform stretching of chains leads to normal stresses that pull a volume element toward the rotating inner cylinder [also depicted in Fig. 12(a)]. These “hoop stresses” set the fluid in motion toward the inner cylinder. This leads to a rolling flow [as sketched in Fig. 10(b)], since at the inner cylinder the flow velocity must change to the vorticity direction. In case of a free surface, the fluid may climb the inner cylinder, in which case the increase in hydrostatic pressure compensates the normal stress in the gradient direction. This is known as the Weissenberg or rod-climbing effect.

We propose that, in a similar way, nonuniform shear-induced deformation of the inhomogeneities (instead of polymer chains) may be at the origin of the vorticity-banding instability, as depicted in Fig. 12(b). Nonuniform deformation of inhomogeneities (formed during the initial stages of paranematic-nematic phase separation) due to gradients in shear rate are thus responsible for the vorticity-banding instability and the stabilization of the banded structures.

There are, however, additional forces that might play a role here. Since inhomogeneities are very much extended along streamlines, bending elasticity might give rise to significant normal stresses in the opposite direction, away from the center of the couette cell [see Fig. 12(c)]. Bending elasticity [49] might counteract the stretching forces in generating hoop stresses.

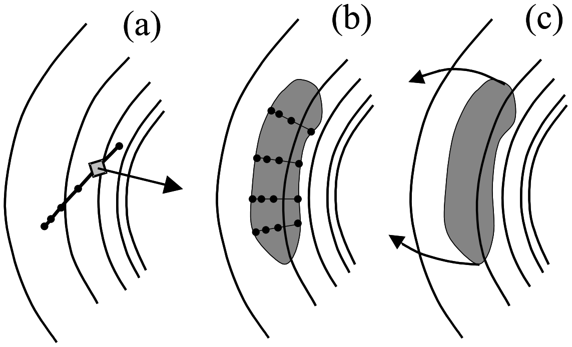

FIG. 12. (a) The origin of the well-known elastic instability of polymer systems. The dots on the polymer chain are used to indicate the degree of stretching. Without stretching or for uniform stretching, the dots would be equally spaced. When a chain is not aligned along streamlines, stretching is nonuniform and normal stresses are generated. The resulting forces pull a volume element toward the rotating inner cylinder, as indicated by the arrow. (b) Similar stretching of the inhomogeneities that are formed due to nonequilibrium paranematic-nematic phase separation. The dots are used to visualize nonuniform stretching. (c) In comparison to flexible polymer chains, bending elasticity may play a role as well. In such cases normal stresses act in the opposite direction, as depicted by the arrows in the figure.

The following experimental observations can be intuitively understood on the basis of the above-proposed mechanism.

(i) At a given overall shear rate, gradients in the shear rate in a couette cell increase with increasing gap width of the couette cell. Therefore the driving force for rolling flow will increase with increasing gap width. This will probably lead to an increase of the bandwidth. Indeed an increase of the bandwidth with increasing gap width is observed [see Fig. 8(b)].

(ii) Shear gradients in a couette cell are large when the overall shear rate is large. This might explain why vorticity banding occurs only at sufficiently high shear rates, that is, the lower-border shear rate $\dot{\gamma}_-$ is larger than zero. Gradients in shear rate are not sufficiently pronounced for shear rates below $\dot{\gamma}_-$ to render the normal stresses strong enough to induce vorticity banding.

(iii) At larger shear rates, close to the upper-border shear rate, inhomogeneities are relatively thin due to shear stretching. This diminishes the nonuniform stretching within the inhomogeneity [see Fig. 12(b), where now the inhomogeneity is very thin]. In addition, the bending forces will be smaller, since a thinner inhomogeneity is more easily bent as compared to a thick inhomogeneity. This might explain why banding ceases to occur above the upper-border shear rate $\dot{\gamma}_+$, which is well within the two-phase region.

(iv) Contrary to gradient banding, the region where vorticity banding occurs and the final bandwidth are independent of whether the shear rate or shear stress is controlled. This agrees with the mechanism proposed above, since normal stresses are important instead of shear-gradient stresses.

Although the mechanism proposed above is in accord with a number of experimental observations, more theoretical and experimental work is needed to validate these suggestions. Measurements of normal stresses along the gradient direction during the initial stages of banding could be performed. This will not be straightforward since, in weak rolling motion, these stresses are probably quite small. In addition, a detailed experimental study of the dependence of the flow pattern within the bands on varying gap width would be valuable.

Stationary vorticity-banded states are also found in aggregated nanotube suspensions [50]. Instead of the inhomogeneities formed due to phase separation as in our fd virus suspensions, here, similar deformation of the nanorod aggregates may be at the origin of the vorticity banding. Normal stress measurements reported in Ref. [50] indeed indicate that such stresses play a role in vorticity banding. Stationary vorticity banding has also been observed in wormlike micellar systems [23]. There are two possibilities here: either inhomogeneities are formed due to a shear-induced paranematic-nematic phase transition, or the wormlike micelles themselves are nonlinearly stretched (like polymer chains in the elastic instability of polymer systems). In those wormlike micellar systems where a shear-induced paranematic-nematic phase transition occurs and no vorticity banding is observed, the mechanical properties related to stretching of the inhomogeneities are probably such that normal stresses are not large enough to give rise to rolling flow. In the weakly flocculating systems in Ref. [22], the nonuniform stretching of flocs of colloidal particles is probably at the origin of the observed vorticity banding.

VII. SUMMARY

We have performed experiments under steady shear-flow conditions on the structure and kinetics of vorticity banding in sheared suspensions of rodlike fd virus. We determined the vorticity- banding region which is entirely enclosed by the paranematic-nematic binodal. Under both controlled shear-rate and shear-stress conditions banding occurs between the lower- and upper-border shear rates $\dot{\gamma}_-$ and $\dot{\gamma}_+$, respectively, where $\dot{\gamma}_-$ is larger than zero. After a shear-rate quench from a high shear rate into this region, inhomogeneities are formed due to phase separation. These inhomogeneities are shear elongated up to a well-defined time after which vorticity banding occurs. The growth of the vorticity-bandwidth can be described, to within experimental error, by a single-exponential function of time. There are two important parameters that characterize the kinetics of band formation: (i) the band-growth time τ in the exponential, the inverse of which measures the growth rate of band formation, and (ii) the amplitude A of the time exponential, which is related to the total growth of the bandwidth as compared to the initial apparent bandwidth of shear-stretched inhomogeneities. The growth kinetics depends on the morphology and the mechanical properties of the inhomogeneities formed due to the phase separation. Two different scenarios have been found. For small fd concentration, τ diverges at the border shear rates, while the amplitude A remains finite. The growth rate of bands thus vanishes. For larger fd concentration, the amplitude A vanishes at the border shear rates, while τ remains finite.

Experiments indicate that there is a weak rolling flow within the bands. A possible mechanism that is at the origin of the banding instability as well as the stabilization of quasistationary banded states is proposed, where the mechanical properties of the inhomogeneities are essential. The proposed mechanism is similar to the elastic instability for polymer systems, where the inhomogeneities play the role of the polymer chains.

The proposed mechanism explains, on an intuitive level, a number of the observed phenomena, like the gap-width dependence of the vorticity-bandwidth, the large bandwidth with increasing dextran concentration, and the fact that banding occurs only beyond a certain nonzero shear rate and ceases to occur above another shear rate. Moreover, the proposed mechanism explains why the border shear rates are independent of whether controlled shear rates or controlled shear stresses are applied. Just above the upper-border shear rate there is a finite probability to have a localized assembly of neighboring inhomogeneities which are still thick enough to give rise to banding. This leads to the observed heterogeneous band formation.

More experiments are necessary to unambiguously validate the proposed mechanism. In addition, theory should be developed to confirm such a scenario. In particular, the expression for the stress tensor as obtained in Ref. [51], which is valid for highly inhomogeneous systems of stiff, long, and thin rods, could serve as a starting point for the theoretical validation of the proposed mechanism. Simulations also might provide a better understanding of the behavior of colloidal rods under shear flow [52,53].

ACKNOWLEDGMENTS

This work was performed within the framework of the Transregio SFB TR6 “Physics of Colloidal Dispersions in External fields,” and is also part of the research being performed within the European Network of Excellence “Soft Matter Composites” (SoftComp). Z.D. is supported by the Rowland Institute at Harvard. The confocal microscopy experiments have been done in cooperation with D. Derks, A. Imhof, and A. van Blaaderen, from the Utrecht University in The Netherlands. The tracking experiment has been done in cooperation with M. Lenoble and B. Pouligny from the Centre Recherche Paul Pascal, CNRS, Pesac in France.

[1] W. C. K. Poon and P. N. Pusey, in *Observation, Prediction, and Simulation of Phase Transitions in Complex Fluids*, edited by M. Baus, L. F. Rull, and J. P. Ryckaert (Kluwer Academic Publishers, Dordrecht, 1995).
[2] G. J. Vroege and H. N. W. Lekkerkerker, Rep. Prog. Phys. **8**, 1241 (1992).
[3] A. Baranyai and P. T. Cummings, Phys. Rev. E **60**, 5522 (1999).
[4] S. Butler and P. Harrowell, Nature (London) **415**, 1008 (2002).
[5] M. C. Cross and P. C. Hohenberg, Rev. Mod. Phys. **65**, 851 (1993).
[6] J. F. Berret, Langmuir **13**, 2277 (1997).
[7] P. Boltenhagen, Y. Hu, E. F. Matthys, and D. J. Pine, Phys. Rev. Lett. **79**, 2359 (1997).
[8] T. A. J. Lenstra, Z. Dogic, and J. K. G. Dhont, J. Chem. Phys. **114**, 10151 (2001).
[9] J. K. G. Dhont, M. P. Lettinga, Z. Dogic, T. A. J. Lenstra, H. Wang, S. Rathgeber, P. Carletto, L. Willner, H. Frielinghaus, and P. Lindner, Faraday Discuss. **123**, 157 (2003).
[10] M. P. Lettinga and J. K. G. Dhont, J. Phys.: Condens. Matter **16**, S3929 (2004).
[11] J.-F. Berret, Langmuir **13**, 2227 (1997).
[12] E. Fischer and P. T. Callaghan, Phys. Rev. E **64**, 011501 (2001).
[13] C. Pujolle-Robic and L. Noirez, Nature (London) **409**, 167 (2001).
[14] P. T. Mather, A. Romo-Uribe, C. D. Han, and S. S. Kim, Macromolecules **30**, 7977 (1997).
[15] N. Grizzuti and P. L. Maffettone, J. Chem. Phys. **118**, 5195 (2003).
[16] S. Lerouge, J. P. Decruppe, and C. Humbert, Phys. Rev. Lett. **81**, 5457 (1998).
[17] P. D. Olmsted and C.-Y. David Lu, Phys. Rev. E **60**, 4397 (1999).
[18] C.-Y. David Lu, P. D. Olmsted, and R. C. Ball, Phys. Rev. Lett. **84**, 642 (2000).
[19] P. D. Olmsted, O. Radulescu, and C.-Y. Lu, J. Rheol. **44**, 257 (2000).
[20] J. L. Goveas and P. D. Olmsted, Eur. Phys. J. E **6**, 79 (2001).
[21] J. K. G. Dhont, Phys. Rev. E **60**, 4534 (1999).
[22] J. Vermant, L. Raynaud, J. Mewis, B. Ernst, and G. G. Fuller, J. Colloid Interface Sci. **211**, 221 (1999).
[23] D. Bonn, J. Meunier, O. Greffier, A. Al-Kahwaji, and H. Kellay, Phys. Rev. E **58**, 2115 (1998).
[24] P. Fischer, E. K. Wheeler, and G. G. Fuller, Rheol. Acta **41**, 35 (2002).
[25] L. Onsager, Ann. N.Y. Acad. Sci. **51**, 62 (1949).
[26] Z. Dogic and S. Fraden, in *Soft Condensed Matter*, edited by G. Gompper and M. Schick (Viley-VCH, Weinheim, 2006).
[27] J. Tang and S. Fraden, Liq. Cryst. **19**, 459 (1995).
[28] E. Grelet and S. Fraden, Phys. Rev. Lett. **90**, 198302 (2003).
[29] Z. Dogic, K. R. Purdy, E. Grelet, M. Adams, and S. Fraden, Phys. Rev. E **69**, 051702 (2004).
[30] F. Livolant, Physica A **176**, 117 (1991).
[31] S. Fraden, G. Maret, D. L. D. Caspar, and R. B. Meyer, Phys. Rev. Lett. **63**, 2068 (1989).
[32] M. P. B. van Bruggen, J. K. G. Dhont, and H. N. W. Lekkerkerker, Macromolecules **32**, 7037 (1999).
[33] J. Tang and S. Fraden, Phys. Rev. Lett. **71**, 3509 (1993).
[34] J.-F. Berret, D. C. Roux, and G. Porte, J. Phys. II **4**, 1261 (1994).
[35] K. Weissenberg, Nature (London) **159**, 310 (1947).
[36] C. W. Macosko, *Rheology, Principles, Measurements and Applications* (VCH Publishers, Cambridge, U.K., 1994).
[37] R. G. Larson, S. J. Muller, and E. S. G. Shaqfeh, J. Fluid Mech. **218**, 573 (1990).
[38] P. Pakdel and G. H. McKinley, Phys. Rev. Lett. **77**, 2459 (1996).
[39] A. Groisman and V. Steinberg, Phys. Fluids **10**, 2451 (1998).
[40] T. Maniatis, J. Sambrook, and E. F. Fritsch, *Molecular Cloning: A Laboratory Manual*, 2nd ed. (Cold Spring Harbor Laboratory Press, Plainview, NY, 1989).
[41] M. P. Lettinga, Z. Dogic, H. Wang, and J. Vermant, Langmuir **21**, 8048 (2005).
[42] S. Hess, Z. Naturforsch. A **31**, 1034 (1976).
[43] G. Rienäcker, M. Kröger, and S. Hess, Phys. Rev. E **66**, 040702(R) (2002).
[44] S. Hess and M. Kröger, J. Phys.: Condens. Matter **16**, S3835 (2004).
[45] M. G. Forest, Q. Wang, and R. Zhou, Rheol. Acta **44**, 80 (2004).
[46] M. G. Forest, X. Zheng, R. Zhou, Q. Wang, and R. Lipton, Adv. Funct. Mater. **15**, 2029 (2005).
[47] J. K. G. Dhont and W. J. Briels, Phys. Rev. E **72**, 031404 (2005).
[48] M. P. Lettinga, K. Kang, A. Imhof, D. Derks, and J. K. G. Dhont, J. Phys.: Condens. Matter **17**, S3609 (2005).
[49] P. G. de Gennes and J. Prost, *The Physics of Liquid Crystals*, 2nd ed. (Clarendon Press, Oxford, 1999).
[50] S. Lin-Gibson, J. A. Pathak, E. A. Grulke, H. Wang, and E. K. Hobbie, Phys. Rev. Lett. **92**, 048302 (2004).
[51] J. K. G. Dhont and W. J. Briels, J. Chem. Phys. **117**, 3992 (2002); **118**, 1466 (2003).
[52] R. Zhou, M. G. Forest, and Q. Wang, Multiscale Model. Simul. **3**, 853 (2005).
[53] G. Germano and F. Schmid, J. Chem. Phys. **123**, 214703 (2005).

Chapter 13

Is vorticity-banding due to an elastic instability?

Rheol Acta (2008) 47:499–508
DOI 10.1007/s00397-007-0238-z

ORIGINAL CONTRIBUTION

Is vorticity-banding due to an elastic instability?

Kyongok Kang · M. Paul Lettinga · Jan K. G. Dhont

Received: 11 May 2007 / Accepted: 19 August 2007 / Published online: 21 February 2008

Abstract A possible mechanism for the vorticity-banding instability is proposed on the basis of experiments with colloidal rod-like particles that exhibit an isotropic–nematic phase transition. The proposed mechanism is similar to the well-known elastic instability for polymer systems that is due to nonuniform elastic deformation of polymer chains as a result of gradients in the local shear rate (the Weissenberg effect). However, the role of polymer chains is now played by inhomogeneities that exist in systems exhibiting vorticity banding. For the rod-like colloidal system investigated here, inhomogeneities are formed during the early stages of phase separation. Nonuniform deformation of these inhomogeneities are thus proposed to lead to hoop stresses which give rise to banded structures where there is secondary, weakly rolling flow within each of the bands. Many of the features found experimentally for the rod-like colloidal system can be understood on the basis of this proposed mechanism. For different types of systems that also show vorticity banding, inhomogeneities can be identified, which might lead to vorticity banding for the same reasons as for the rod-like colloidal systems studied here.

Keywords Instability · Dispersions · Phase separation

Introduction

Two types of banding transitions have been found experimentally in various types of complex solutions, which are referred to as gradient banding and vorticity banding. In case of gradient banding, typically two regions with different shear rates coexist in the stationary state, where in each of the two regions the shear rates are essentially constant, independent of position (see, for example, Berret 1997; Olmsted et al. 2000). The gradient-banding instability occurs when the shear stress (the flow-gradient component of the stress tensor) of the homogeneously sheared system decreases with increasing shear rate. The molecular origin of the accompanied severe shear-thinning behavior is relatively well understood. The origin of the vorticity-banding instability, however, is not yet understood. In the present paper, we propose a possible mechanism for this instability that is related to hoop-stresses generated by nonuniform shear-induced stretching of inhomogeneities. These inhomogeneities can be due to early stage phase separation; they can be self-assembled structures like in worm-like micellar, or they can be aggregates in weakly flocculating colloids. The nonuniform deformation of such inhomogeneities gives rise to elastic normal forces which set the fluid in weakly rolling motion. The rolls correspond to the observed bands that are stacked in the vorticity direction. The mechanism underlying the vorticity-banding instability is thus analogous to the well-known elastic instability of polymer systems, leading to the Weissenberg effect (see Weissenberg 1947), where the role of polymer chains is now played by the inhomogeneities.

Experiments on fd-virus suspensions will be discussed, where vorticity banding is found within the isotropic–nematic two-phase region, which partly extend on earlier work by Kang et al. (2006). Fd virus is a stiff, long, and thin colloidal rod, suspensions of which are model systems

Paper presented at 4th Annual European Rheology Conference, AERC, April 12–14, Napels, Italy.

K. Kang (✉) · M. P. Lettinga · J. K. G. Dhont
Institute für Festkörper Forschung (IFF), Weiche Materie,
Forschungszentrum Jülich,
52425 Jülich, Germany
e-mail: k.kang@fz-juelich.de

for monodisperse rods. Inhomogeneities are, in this case, due to early stage isotropic–nematic phase separation. The experimental findings discussed in the present paper that can be understood on the basis of the proposed mechanism mentioned above include (1) the different vorticity-banding kinetics depending on whether phase separation leads to bi-continuous structures or isolated inhomogeneities just before banding occurs, (2) the finite shear-rate range where vorticity banding is found, (3) the couette-cell gap-width dependence of the shear-rate region where banding occurs, (4) the gap-width dependence of the final vorticity-band width, and (5) the observed rolling flow within the bands.

This paper is organized as follows. In Section Experiments with fd-virus suspensions, we discuss experimental results on fd-virus suspensions, some of which are also discussed by Kang et al. (2006). The mechanism leading to vorticity banding, as mentioned above, will be discussed in Section A possible mechanism for vorticity banding. Experimental findings will be interpreted on the basis of the proposed mechanism in Section Intuitive explanation of vorticity-banding characteristics of fd-virus suspensions and of other systems, where other vorticity-banding systems are also discussed within the scope of the proposed mechanism.

Experiments with fd-virus suspensions

Fd virus is a stiff, rod-like virus of colloidal dimensions, with a thickness of D=6.6 nm, a length of L=880 nm, and a persistence length of 2,200 nm. We used suspensions with a high ionic strength (20 mM TRIS buffer, pH=8.15 with 100 mM added NaCl) where dextran is added (radius of gyration 16 nm) to enhance isotropic–nematic phase separation and vorticity-band formation. Samples were prepared as follows. First, we prepare a homogeneous solution of fd virus at an overall concentration of 22.1 mg/ml and the appropriate dextran concentration. This mixture is then left to phase separate under gentle centrifugation for about 24 h, to establish separation into two bulk phases. Then a volume V_{nem} from the lower, nematic bulk phase and a volume V_{iso} from the upper, isotropic bulk phase are mixed. This is the mixture that is used in our shear experiments. This procedure of sample preparation ensures that the chemical potential of dextran is independent of the total fd-virus concentration. Experiments are performed for two rod concentrations Φ_{nem}= 0.23 and 0.35, where $\Phi_{\mathrm{nem}}=V_{\mathrm{nem}}/(V_{\mathrm{nem}}+V_{\mathrm{iso}})$. Unless stated otherwise, the dextran concentration in the inhomogeneous suspension is 10.6 mg/ml.

Shear experiments are done in an optical couette cell with a stationary outer cylinder and a rotating inner cylinder. The gap width of the couette cell can be varied from 1.0 to 2.5 mm. The sample is pre-sheared at a shear rate of 10 s^{-1} for at least 10 min. This shear rate is far above the highest shear rate that bounds the two-phase region. Experiments are done by quenching from this high shear rate to a lower shear rate where vorticity banding occurs. Vorticity banding of fd-virus suspensions is observed both under controlled shear rate and controlled shear stress conditions, within a limited part of the two-phase paranematic–nematic region as bounded by the isotropic–nematic binodal in the shear-rate vs fd-concentration plane (see also Kang et al. 2006). For a fixed fd-concentration, banding occurs within a shear-rate interval $\left(\dot{\gamma}_+,\dot{\gamma}_+\right)$, where the "border shear rates" $\dot{\gamma}_-$ and $\dot{\gamma}_+$ lie within the two-phase region.

Vorticity bands are visualized by placing the couette cell between polarizers that are slightly off from a crossed alignment of polarizations. Time resolved transmitted intensity profiles are recorded with a CCD camera equipped with a telecentric lens. An example of such intensity profiles is given in Fig. 1. The two types of bands appear as alternating dark and bright regions. Average band widths are obtained through a Fourier mode analysis of the resulting transmitted intensity profiles, where the height of bright and dark bands is equal. Details are given by Kang et al. (2006).

The banded patterns that are discussed here are similar to that found for the well-known Taylor instability. The Taylor instability for the fd-virus suspensions has been observed to occur at a shear rate typically equal to about 25 s^{-1}. This shear rate is about a factor of 50–100 larger than the typical shear rates where vorticity banding is seen. We are thus far below the critical shear rates at which the Taylor-banding instability occurs.

Outside the banding region, the suspension merely phase separates into a sheared bulk isotropic state (the "paranematic phase") and a sheared bulk nematic phase, without the occurrence of a banded structure. Confocal images of morphologies of phase separating fd-virus suspensions at various concentrations after a shear-rate quench from 10 s^{-1} to a zero shear rate are shown in Fig. 2. These images are taken 10 min after the shear quench. The bright regions are nematic regions, the dark regions are isotropic. On increasing the rod concentration, the difference in rate of decomposition leads to isolated inhomogeneities at high rod concentrations and a bi-continuous structure at low concentrations at the instant where banding sets in. The observed spinodal decomposition at low concentration and nucleation and growth at higher concentration indicates that the initial state, before demixing occurred, is aligned due to the high shear rate before the shear-rate quench. Demixing kinetics of fd-virus suspensions is studied in detail by Lettinga et al. (2005).

Vorticity banding is only found within the isotropic–nematic two-phase region, which indicates that the inhomogeneities that are formed after the quench are essential for the banding instability. Without these inhomogeneities,

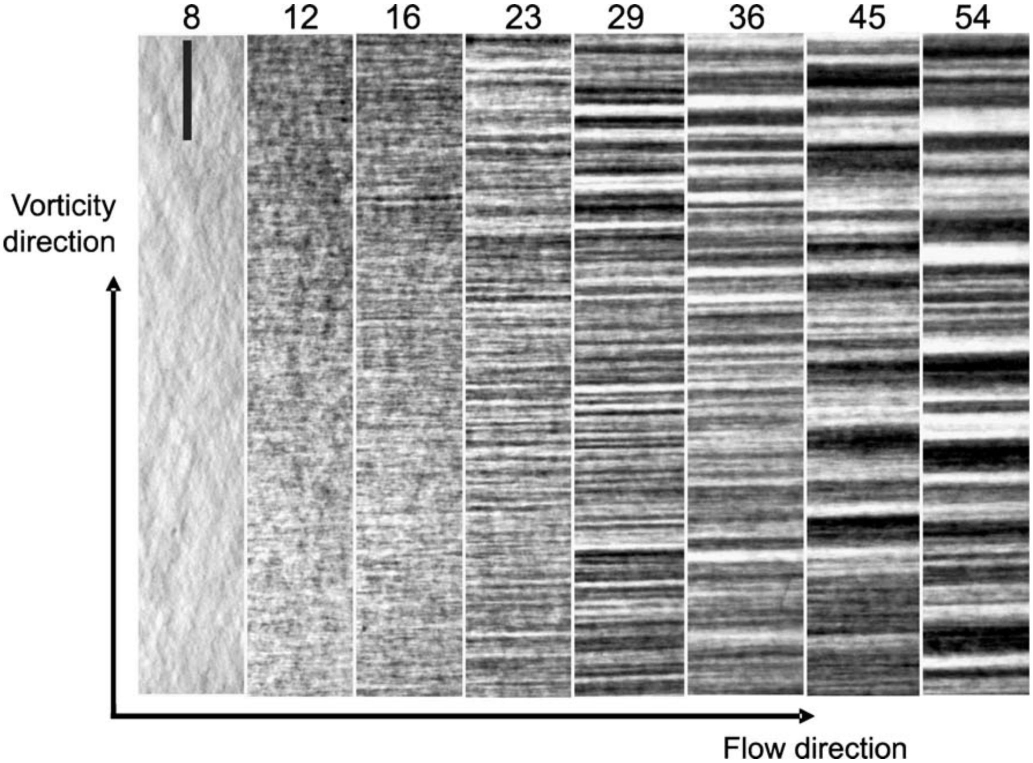

Fig. 1 An example of intensity profiles at different times. The numbers are times in minutes after the shear-rate quench. The *bright and dark bands* are the two types of vorticity bands that are formed. The *left upper bar* is 1 mm long. Banding sets in 10 min after the quench. The *most left figure* taken 8 min after the quench thus shows shear-stretched inhomogeneities, before banding occurred

vorticity banding does not occur. It is therefore to be expected that the kinetics of vorticity-band formation depends on the fd concentration, as according to Fig. 2, the morphology of inhomogeneities that is formed during the initial stages of demixing varies with the fd concentration. This is indeed the case as can be seen from Fig. 3, where the band width as a function of time right after the shear quench is plotted. Right after the quench, inhomogeneities are shear-stretched, giving rise to a decrease of the apparent "band width". At a well-defined time, vorticity banding sets in, and the band width increases with time. The two plots (a) and (b) on the left are for 23% and the two plots (c) and (d) on the right are for 35%. The time where banding sets in is 10 min for 23% and 15 min for 35%. For the two upper plots (a) and (c), the shear rate is close to the lower border shear rate. The two lower figures,

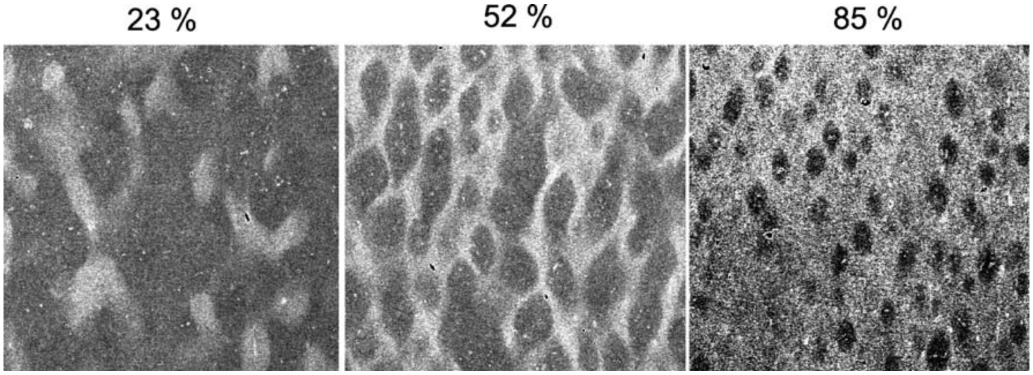

Fig. 2 Confocal images of fd-suspensions with increasing Φ_{nem} (*from left to right*, as indicated in the figure), after a quench from shear rate 10 s^{-1} to a zero shear rate, taken 10 min after the shear quench. The spinodal is located at approximately 52% (Lettinga et al. 2005)

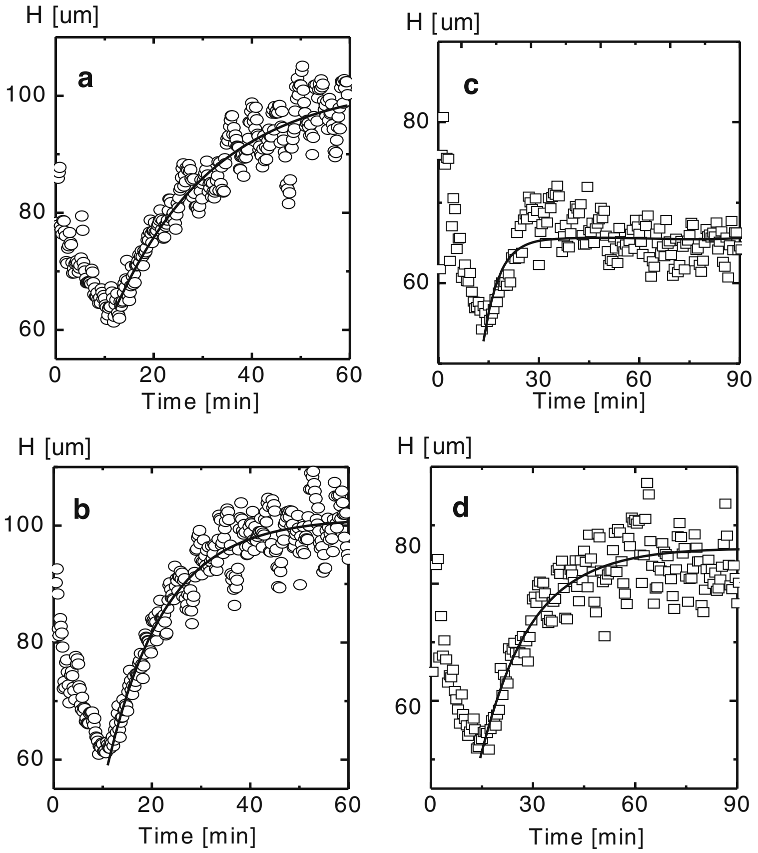

Fig. 3 The time dependence of the band width for two different fd-rod concentrations: **a** and **b** for $\Phi_{\mathrm{nem}}=0.23\%$, and **c** and **d** for 0.35%. **a** $\dot{\gamma}=0.17\ \mathrm{s}^{-1}$ close to the lower border shear rate and **b** $\dot{\gamma}=0.29\ \mathrm{s}^{-1}$ in the middle of the banding region for 23%, and similarly **c** $\dot{\gamma}=0.29\ \mathrm{s}^{-1}$ and **d** $\dot{\gamma}=0.40\ \mathrm{s}^{-1}$ for 35%

(b) and (d) are for a shear rate in the middle of the shear-rate interval $\left(\dot{\gamma}_-,\dot{\gamma}_+\right)$ where vorticity banding occurs. The solid curves are a fit to a single time exponential. For the lower concentration of 23%, close to the lower border shear rate $\dot{\gamma}_-$ (see Fig. 3a), the growth time is much larger than for the shear rate in the middle of the banding interval (see Fig. 3b). The total increase of the band width, however, is approximately the same for both cases (~40 μm). On the contrary, for the higher concentration of 35%, the growth time is approximately the same for the two shear rates, but the total increase of the band width is much smaller at the lower-border shear rate (see Fig. 3c and d). Hence, vorticity banding ceases to occur due to the divergence of the growth time in the case of a bi-continuous, spinodal-like structure, and banding ceases to occur due to a vanishing amplitude in the case of isolated inhomogeneities. Interestingly, the shear-rate interval $\left(\dot{\gamma}_-,\dot{\gamma}_+\right)$ where vorticity banding occurs depends on the gap width of the shear cell, as can be seen from Fig. 4. For the lower fd concentration with $\Phi_{\mathrm{nem}}=0.23$, where we have a bi-continuous structure, the shear-rate region where banding occurs widens with increasing gap width. For the higher fd concentration, however, where isolated inhomogeneities are formed, both border shear rates decrease with increasing gap width. The shear rate interval where banding occurs now decreases with increasing gap width. As will be discussed in Section Intuitive explanation of vorticity-banding characteristics of fd-virus suspensions and of other systems, the gap-width dependence of both $\dot{\gamma}_-$ and $\dot{\gamma}_+$ is probably due to the change of gradients in local shear rates. The different behavior for the two concentrations is due to differences of the elastic properties of the inhomogeneities formed during the initial stages of demixing for $\Phi_{\mathrm{nem}}=0.23$ and 0.35. As can be seen from Fig. 4c, the band width in the stationary state depends on the gap width. Vorticity bands become broader on increasing the gap width of the shear cell.

To investigate whether the shear rate is constant throughout the vorticity bands or whether they exhibit internal rolling flow, we tracked the position of a tracer sphere along the vorticity direction. This experiment is performed on a sample with a relatively high dextran concentration (12.3 mg/ml) and a relatively low fd concentration ($\Phi_{\mathrm{nem}}=0.17$) leading to more pronounced bands with a typical band width of about 1 mm. The cell gap width in this experiment is 1.5 mm, and the shear rate is $0.88\ \mathrm{s}^{-1}$. As can be seen in Fig. 5, there is an oscillatory

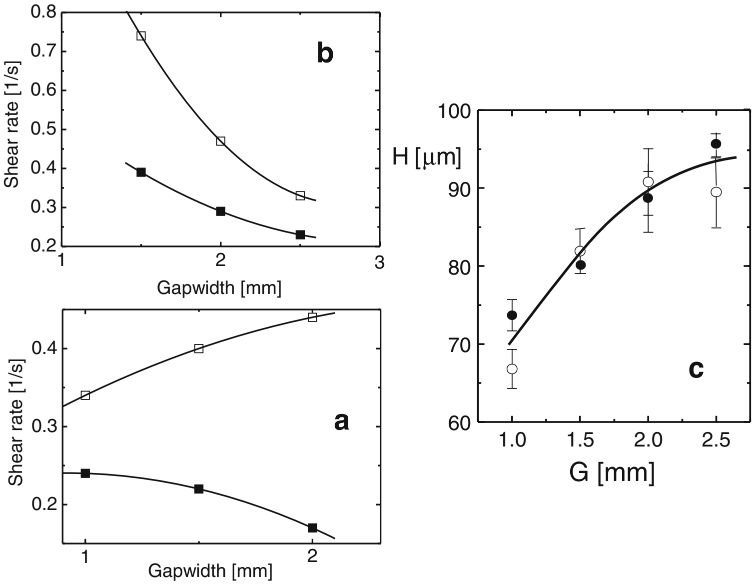

Fig. 4 The variation of the upper-border shear rates (*empty squares*) and lower-border shear rates (*filled squares*) with the cell gap width for the two concentrations Φ_{nem}=23% (**a**) and 35% (**b**). **c** The band width in the quasi stationary state as a function of the couette cell gap width. The data points are for 23% at shear rates 0.29 s^{-1} (*empty circles*) and 0.34 s^{-1} (*filled circles*)

motion of the tracer sphere along the vorticity direction, indicating that the bands are in (weakly) internal rolling flow. There is also a drift downwards as a result of sedimentation. No oscillations of the shear stress under controlled shear-rate conditions have been observed in the stationary vorticity-banded state. In Section A possible mechanism for voricity banding, we will discuss a possible mechanism leading to rolling flow. Furthermore, the rod concentration is the same within the two bands, as can be seen from the fluorescent image in the right panel in Fig. 6, where the fd rods are fluorescently labeled. The left panel shows the banded structure as visualized through birefringence. The right figure probes the same area, and shows the fluorescent intensity from a laser beam directed along the vorticity direction. As can be seen, the fluorescent intensity is homogeneous along the vorticity direction, implying that the concentrations within the bands are similar. Within experimental noise (about 2%), no contrast between bands could be seen.

A possible mechanism for vorticity banding

A recently proposed mechanism by Fielding (2007) for vorticity banding involves the formation of a gradient banded flow, before vorticity banding occurs. The gradient-banded interface generates normal body forces that set the suspension in motion along the gradient direction. This would ultimately lead to vorticity banding where the bands are in internal rolling flow. Kang et al. (2006) report on stress measurements for fd-virus suspensions just before vorticity banding occurs. The shear stress is found to be a monotonically increasing function of shear rate. Furthermore, no decrease of the measured shear stress is observed during banding (experiments like in Fig. 1 given by Lettinga and Dhont 2004 have been extended to a much larger time range). We neither found a van der Waals loop-like behavior of the stress nor observed a stress plateau. There is thus no sign that gradient banding plays a role in the formation of vorticity bands in the fd-virus suspensions.

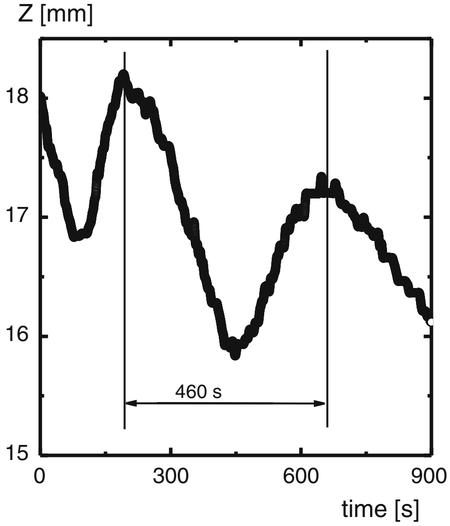

Fig. 5 The position of a tracer sphere (diameter 50 μm) in the vorticity direction within a band as a function of time. The dextran concentration was 12.3 mg/ml, the cell gap width is 1.5 mm and Φ_{nem}=0.15

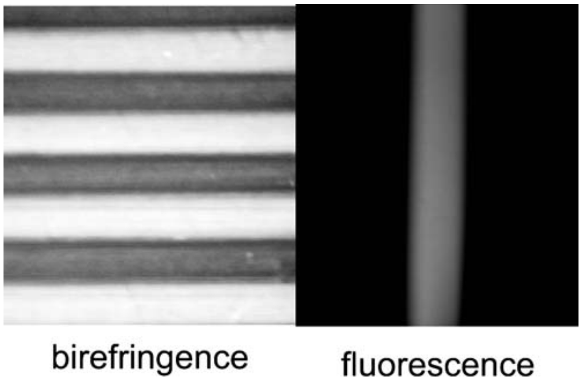

Fig. 6 *Left figure*: the banded structure. The dextran concentration here is 12.3 mg/ml. *Right figure:* the same are as in the left figure, where now the fluorescent intensity of a laser beam along the vorticity direction is probed. Here, the fd virus is fluorescently labeled

This suggests that a different mechanism is probably involved for vorticity banding of fd-virus suspensions. Schmitt et al. (1995) proposed a mechanism for the development of a banded structure along the vorticity direction that involves spinodal decomposition, where the mass diffusion coefficient is negative. For our fd-virus suspensions, however, banding is found throughout the two-phase region, including the meta-stable region where the mass diffusion coefficient (and also the orientational diffusion coefficient) is positive. This indicates that the proposed mechanism by Schmitt et al. (1995) does not apply to our system of rod-like colloids. The rolling flow within the bands and the monotonically increasing shear stress with increasing shear rate show that the stationary state is not a state where the shear rate is constant throughout the gap, as was assumed in earlier theories by Olmsted and Lu (1999), Olmsted (1999), Goveas and Olmsted (2001), and Aradian and Cates (2006).

In view of the experimental results presented in the previous section, we propose a mechanism that is similar to the elastic instability for polymer systems, known as the Weissenberg effect. The Weissenberg effect is due to normal stresses in the gradient direction, so-called hoop stresses, which are generated by nonuniform elastic deformation of polymer chains (see, for example, Weissenberg 1947; Larson et al. 1990; Pakdel and McKinley 1996, and Groisman and Steinberg 1998). This elastic instability has the following microscopic origin. In a couette geometry, the local shear rate increases slightly towards the inner cylinder. This leads to a more pronounced stretching of the part of a polymer chain that is closer to the inner cylinder and to a less pronounced stretching of the part of a polymer chain further away from the inner cylinder (see Fig. 7a). On average, this nonuniform stretching leads to a body force that is directed towards the inner cylinder. When these normal forces are large enough, this leads to a flow towards the inner cylinder. We note that volume elements do not immediately move towards the inner cylinder once the instability occurs. The flow towards the inner cylinder is initiated in the bulk of the suspension and is accompanied by a back flow (see the stability analysis later in this section). In the resulting stationary state, this leads to bands assembled along the vorticity direction, where there is a secondary, rolling flow within the bands. Near the surface of the polymer system, the upwards flow along the inner cylinder leads to the well- known "rod-climbing" effect. The vorticity-banding instability is proposed to be of the same origin, where the role of polymer chains is now played by inhomogeneities (see Fig. 7b). In the case of the fd-virus suspensions discussed above, the inhomogeneities formed during the initial stages of phase separation are nonuniformly deformed, leading to hoop stresses which give rise to banding.

The proposed mechanism that underlies the vorticity instability can be specified in somewhat more detail by means of a stability analysis. The crude stability analysis described below explains the major features of the vorticity instability. For sufficiently shallow inhomogeneities, the internal structure of the inhomogeneities will be able to adjust to the imposed flow such that the body force B_y in the y direction (the gradient direction) is zero. When inhomogeneities become more pronounced, however, such an adjustment may not be possible anymore, resulting in a nonzero body force, which leads to flow along the gradient direction. We ask for the amplitude of inhomogeneities under which a change in the amplitude of the inhomogeneities leads to flow in the gradient direction of the initial flow profile. Within the "Weissenberg scenario for vorticity banding", a nonzero flow velocity u_y along the y- direction

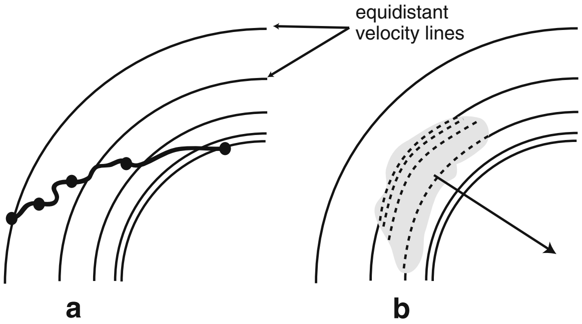

Fig. 7 **a** A schematic of the origin of the Weissenberg effect, where polymer chains are nonuniformly stretched, as indicated by the dots, which would be equidistant for uniform stretching. **b** Nonuniform deformation of an inhomogeneity. The *dotted lines* indicate the nonuniform deformation, like the dots for the polymer chain. The lines are equidistant flow velocity lines. The *arrow* represents the normal force towards the inner cylinder

initiates vorticity banding. As the discrete nature of the inhomogeneities along the flow direction is relatively unimportant, the gradient component of the Navier–Stokes equation reads,

$$\rho_m \left[\frac{\partial}{\partial t} + u_y \frac{\partial}{\partial y} + u_z \frac{\partial}{\partial z} \right] u_y(y,z,t) = B_y(y,z,t), \tag{1}$$

where u_z is the flow velocity in the z direction (the vorticity direction). Let δu_y be the small change of u_y due to a change of the amplitude of inhomogeneities, and δB_y the accompanied change of the body force. As u_z=0 before banding occurs, linearization of the Navier–Stokes Eq. 1 gives,

$$\rho_m \frac{\partial \delta u_y(y,z,t)}{\partial t} = \delta B_y(y,z,t). \tag{2}$$

The z dependence of both δu_y and δB_y is approximately sinusoidally ~exp$\{ikz\}$, where Λ=2π/k is the typical distance between inhomogeneities (as sketched in Fig. 8a). This wavelength corresponds to the most pronounced Fourier mode of the intensity profile taken at 12 min as given in Fig. 1. The y dependence of δB_y is much more complicated and is related to the nonlinear deformation of the inhomogeneities along the gradient direction. Substitution of the forms,

$$\begin{aligned} \delta u_y(y,z,t) &= \overline{\delta u_y}(y)\ \exp\{ikz - \Gamma t\}, \\ \delta B_y(y,z,t) &= \overline{\delta B_y}(y)\ \exp\{ikz - \Gamma t\}. \end{aligned} \tag{3}$$

into Eq. 3 leads to,

$$-\rho_m \Gamma \overline{\delta u_y}(y) = \overline{\delta B_y}(y). \tag{4}$$

Here, $\Gamma > 0$ is the flow relaxation time in case no vorticity banding occurs, while $\Gamma < 0$ when the system is unstable against vorticity banding. A theoretical prediction for the behavior of the body force B_y for rod-like colloids can be based on the equations of motion for the density and order parameter, and the constitutive equation for inhomogeneous suspensions as derived by Dhont and Briels (2002, 2003). Here, the body force is expressed in terms of integrals over the probability density $\rho(r,\hat{u},t)$ for the position **r** of a rod and its orientation specified by the unit vector $\hat{u}$. The constitutive equation derived by Dhont and Briels (2003) contains three distinct contributions: there is a Brownian body force, a contribution due to rod–rod interactions and a contribution due to direct coupling of flow to microstructural order. The Brownian body force and the coupling contribution are linear in the probability density, while the interaction contributions to the body force are bilinear. The probability density is now written as $\rho(\mathbf{r},\hat{u},t) = A\hat{\rho}_0(\mathbf{r},\hat{u}) + \delta A\hat{\rho}_1(\mathbf{r},\hat{u},t)$, where $\hat{\rho}_0$ and $\hat{\rho}_1$ are re-normalized densities, where their prefactors A and δA specify their amplitude. The density $\hat{\rho}_0$ is supposed to lead to a zero body force in the gradient direction. We are looking for those amplitudes A, above which the probability density is not able anymore to adjust itself to the imposed flow profile such that the body force remains zero. Upon linearization of the above mentioned contributions to the body force with respect to δA, the following possible contributions to δB_y result. The linear terms in the density give rise to contributions that do not involve the amplitude A. Normal body forces vary like $\sim \left(\dot{\gamma}\tau\right)^2$ for small shear rates, where τ is the relaxation time of shear-induced deformations of inhomogeneities. For high shear rates, normal forces shear-thin to a relatively small value. Hence, the linear terms in density give rise to contributions of the form $\sim \left(\dot{\gamma}\tau\right)^2 f\left(\dot{\gamma}\tau\right)\delta A$, where f tends to a nonzero constant for small shear rates and tends essentially to zero for high shear rates. For convenience, we shall use the simplest function with these limiting properties: $f\left(\dot{\gamma}\tau\right) = 1\Big/\left[1+\left(\dot{\gamma}\tau\right)^4\right]$. The rod–rod interaction contributions to the body force which are bilinear in the density similarly lead to contributions of the form $\sim \left(\dot{\gamma}\tau\right)^4$

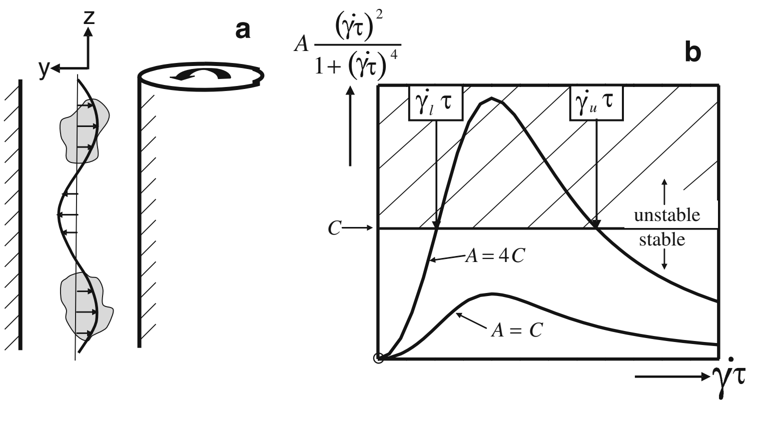

Fig. 8 **a** The flow field along the gradient direction in the initial stage of vorticity banding. The *light grey inclusions* represent inhomogeneities. **b** Stability diagram for vorticity banding within the "Weissenberg scenario". A measures the magnitude of inhomogeneities. For the lower curve, A=C, while for the upper curve, A=4C. The system is unstable in the shear-rate interval $\left(\dot{\gamma}_l, \dot{\gamma}_u\right)$, where $\dot{\gamma}_l$ is "the lower border shear rate" and $\dot{\gamma}_u$ is the "upper border shear rate"

$f^2\left(\dot{\gamma}\tau\right)A\delta A$, as $\hat{\rho}_0$ and $\hat{\rho}_1$ are essentially equal. The linear change of the body force due to a slight change of the density is thus of the form,

$$\delta \bar{B}_y = \left\{ C_1 + C_2 A \frac{\left(\dot{\gamma}\,\tau\right)^2}{1+\left(\dot{\gamma}\,\tau\right)^4} \right\} \frac{\left(\dot{\gamma}\,\tau\right)^2}{1+\left(\dot{\gamma}\,\tau\right)^4}\,\delta A, \tag{5}$$

where the constant C_1 is linear in $\hat{\rho}_1$ and C_2 is bilinear in $\hat{\rho}_0$ and $\hat{\rho}_1$. These constants are determined by the internal structural properties of the inhomogeneities. Without loss of generality, A and δA can be taken positive. Suppose that δu_y is negative, implying that the flow is directed towards the inner cylinder at positions where inhomogeneities are present and a "backflow" occurs in between the inhomogeneities, as sketched in Fig. 8a (the analysis given below proceeds similarly when δu_y is negative). From Eqs. 4 and 5, the following instability criterion for which $\Gamma<0$ is then found,

$$C_1 + C_2 A \frac{\left(\dot{\gamma}\,\tau\right)^2}{1+\left(\dot{\gamma}\,\tau\right)^4} < 0. \tag{6}$$

As no banding is expected when interactions are absent (in which case C_2=0), the constant C_1 must be positive. Banding can thus occur when $C_2<0$. The instability condition can thus be rewritten as,

$$A \frac{\left(\dot{\gamma}\,\tau\right)^2}{1+\left(\dot{\gamma}\,\tau\right)^4} > C, \tag{7}$$

where $C = -C_1/C_2 > 0$. The corresponding stability diagram is given in Fig. 8b. The form $\left(\dot{\gamma}\tau\right)^2 \Big/ \left[1+\left(\dot{\gamma}\tau\right)^4\right]$ has a single maximum at $\dot{\gamma}\,\tau = 1$, with a maximum value of 1/2. Hence, when $A<2C$, there is no instability (see the lower curve in Fig. 8b, for which A=C). In this case, inhomogeneities are not sufficiently pronounced to produce body forces which lead to flow along the gradient direction. That a minimum strength of inhomogeneities is required for vorticity banding is evidenced by the fact that banding occurs only at a characteristic time after the shear-rate quench, where phase separation led to sufficient inhomogeneities (see Fig. 3). When $A>2C$, an instability occurs only in a limited shear-rate range $\left(\dot{\gamma}_l, \dot{\gamma}_u\right)$, with $\dot{\gamma}_l > 0$ (as indicated in the upper curve in Fig. 8b, for which A=4C). This is also seen in our experiments, where for a given fd concentration, banding indeed occurs in a shear-rate range where the lower border shear rate is nonzero. A threshold shear rate is needed to produce body forces along the gradient direction, while shear thinning of normal stresses leads to zero body forces, rendering the system stable again at higher shear rates. A more precise analysis can be performed using the constitutive relation as derived by Dhont and Briels (2002, 2003).

To further validate the proposed mechanism, the gap width dependence of the shear rate for the onset of elastic instability, as given in Fig. 4a and b, could be compared to theory. Larson et al. (1990) predicts a $G^{1/2}$-dependence on the gap width G. However, there are too few data points in Fig. 4a and b to confirm this prediction. It is also not possible to estimate the critical Weissenberg number where banding first occurs, as this involves the relaxation time of the nonuniformly stretched inhomogeneities to their homogeneous state. It is not clear how to measure or estimate such a relaxation time.

The volume fraction of dextran is about 0.15, and therefore below the overlap concentration. The dextran is therefore dilute and far from being entangled. Dextran as such is therefore not at the origin of the observed banding. In fact, for a given dextran concentration, vorticity banding ceases to occur outside the paranematic–nematic two-phase region. The role of dextran is to induce depletion attractions between the rods, which apparently has an appreciable effect on the mechanical properties of the inhomogeneities.

Intuitive explanation of vorticity-banding characteristics of fd-virus suspensions and of other systems

Assuming that the mechanism described in the previous section is at the origin of vorticity banding, a number of the experimental findings for the fd-virus suspensions can be understood intuitively.

Based on the proposed mechanism, it is immediately clear why banding is observed only within the two-phase region. Without the presence of elastically deformable inhomogeneities that are formed due to phase separation, hoop stresses cannot be generated, and banding will not occur.

Banding is observed only within a limited shear-rate region $\left(\dot{\gamma}_-, \dot{\gamma}_+\right)$, with $\dot{\gamma}_- > 0$. The overall shear rate must exceed a minimum value to lead to normal stresses that are sufficiently large to lead to rolling flow. Banding probably ceases to occur at higher shear rates because the extent of inhomogeneities in the gradient direction becomes too small to achieve sufficient nonuniform deformation in that direction.

For a couette geometry, local gradients in shear rate increase with increasing gap width. Such larger gradients in shear rate lead to stronger nonuniform stretching and therefore to larger hoop stresses. This explains why $\dot{\gamma}_-$ decreases with increasing gap width (see Fig. 4a and b). That the upper border shear rate $\dot{\gamma}_+$ decreases for increasing gap width in case of isolated inhomogeneities and increases in case of a bi-continuous structure is unclear. It reflects the different elasticity of inhomogeneities in a bi-continuous, spinodal-like structure or isolated inhomogeneities. The stronger hoop stresses for larger gap widths evidently leads to larger band widths, which is indeed observed (see Fig. 4c).

Vorticity banding is found, independent of whether the shear rate or shear stress is controlled. This agrees with the proposed mechanism, as normal stresses are important, independent of whether shear rate or shear stress is controlled during the experiment.

Finally, the same observed rolling flow within the bands for the polymer systems is expected, as the same mechanism is responsible for the observed banding.

Vorticity banding is observed in different kinds of systems. Inhomogeneities can be identified in all these systems that might be elastically nonuniformly deformed, leading to banding as proposed above. Vorticity banding has been seen in nanotube suspensions by Lin-Gibson et al. (2004), which are partly aggregated. These aggregates are the necessary inhomogeneities to induce the hoop stresses leading to banding. The normal stress measurements by Lin-Gibson et al. (2004) indeed indicate that such stresses play a role in vorticity banding for these systems. Similar aggregates of weakly flocculating spherical colloidal particles are reported by Vermant et al. (1999) to give rise to vorticity banding. Stationary vorticity banding has also been observed by Bonn et al. (1998) for worm-like micellar systems. Either the worm-like micelles serve here as the inhomogeneities or a shear-induced nematic phase is formed, leading to the same kind of inhomogeneities for our fd-virus suspension.

Vorticity banding is occasionally connected to a strong shear thickening (like for the worm- like micelles found by Bonn et al. 1998), where the shear stress exhibits a discontinuity, as schematically depicted in Fig. 9. Assuming that the shear rate is spatially constant and equal to the applied shear rate throughout the system, the accompanied multi-valued form of the flow curve is a necessary condition for the existence of vorticity bands. The two shear stresses indicated in Fig. 9 correspond, in that case, to the stresses carried by the two different microstructures (or phases) that exist within the bands. However, such a shear-thickening behavior is not observed in our fd-virus suspensions. What might happen for systems that exhibit such a shear thickening is that inhomogeneities exist due to a shear-induced phase transition of a phase with a much higher shear viscosity compared to structure at low shear-rates. Highly viscous inhomogeneities could be formed during the initial stages of this shear-induced phase transition, which then lead to vorticity banding according to the proposed mechanism in the previous section (personal communication with John R. Melrose).

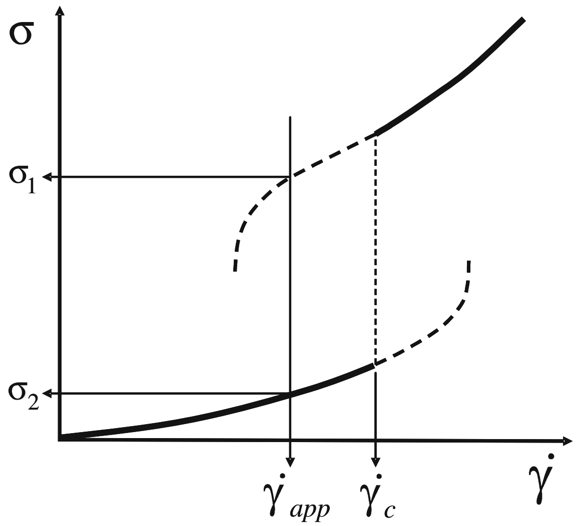

Fig. 9 The shear viscosity as a function of shear rate, where beyond a critical shear rate $\dot{\gamma}_c$, a shear-induced, very viscous phase is formed. The *two dashed branches* are (meta-table) states. In case the shear rate is equal to the applied shear rate $\dot{\gamma}_{\mathrm{app}}$ throughout the gap, the two types of vorticity bands support the stresses σ_1 and σ_2

Summary

Experiments on vorticity banding of suspensions of colloidal rod-like particles (fd virus) reveal the importance of inhomogeneities that are formed during the initial stages of isotropic–nematic phase separation. Vorticity banding occurs only within the two-phase region and banding kinetics depends on whether the inhomogeneities are formed due to spinodal decomposition or a mix of spinodal decomposition and nucleation and growth. Furthermore, the shear-rate region where banding occurs and the final band width depend on the gap width of the couette cell, and there is a secondary weakly rolling flow within the bands. This lead us to propose a mechanism that gives rise to the vorticity-banding instability, which is similar to the well-known elastic instability of polymer systems (the Weissenberg effect). Instead of nonuniform deformation of polymer chains that lead to hoop stresses giving rise to band formation, the inhomogeneities are nonuniformly deformed in case of vorticity banding. The vorticity-banding instability is thus proposed to be similar to the Weissenberg effect, where the role of polymer chains is now played by inhomogeneities. Many of the observed banding characteristics can be understood intuitively on the basis of this mechanism.

Inhomogeneities can be identified in other systems that exhibit vorticity banding. It remains, however, to be further investigated whether these other systems also exhibit banding due to the proposed elastic instability. The main features that should be investigated are whether there is a secondary, rolling flow within the bands and whether the banding characteristics depend on the properties of the inhomogeneities that are present. A quantitative understanding requires a theory that includes stresses generated by nonuniformly stretched inhomogeneities.

It would be interesting to perform normal stress measurements in a cone-plate geometry. However, in view of the very long oscillation time of the rolling flow, the normal stress differences for the fd-virus suspensions might be too small to measure with the present available rheometers.

References

Aradian A, Cates ME (2006) Phys Rev E 73:041508

Berret J-F (1997) Langmuir 13:2227

Bonn D, Meunier J, Greffier O, Al-Kahwaji A, Kellay H (1998) Phys Rev E 58:2115

Dhont JKG, Briels WJ (2002) J Chem Phys 117:3992

Dhont JKG, Briels WJ (2003) J Chem Phys 118:1466

Fielding SM (2007) Phys Rev E 76:016311

Goveas JL, Olmsted PD (2001) Eur Phys J E 6:79

Groisman A, Steinberg V (1998) Phys Fluids 10:2451

Kang K, Lettinga MP, Dogic Z, Dhont JKG (2006) Phys Rev E 74:026307

Larson RG, Shaqfeh ESG, Muller SJ (1990) 218:573

Lettinga MP, Dhont JKG (2004) J Phys Cond Mat 38:S3929

Lettinga MP, Kang K, Imhof A, Derks D, Dhont JKG (2005) J Phys Cond Mat 17:3609

Lin-Gibson S, Pathak JA, Grulke EA, Wang H, Hobbie EK (2004) Pys Rev Lett 92:048302

Olmsted PD, Lu C-Y (1999) Phys Rev E 60:4397

Olmsted PD (1999) Europhys Lett 48:339

Olmsted PD, Radulescu O, Lu C-Y (2000) J Rheol 44:257

Pakdel P, McKinley GH (1996) Phys Rev Lett 77:2459

Schmitt V, Marques CM, Lequeux F (1995) Phys Rev E 52:4009

Vermant J, Raynaud L, Mewis J, Ernst B, Fuller GG (1999) J Coll Int Sci 211:221

Weissenberg K (1947) Nature 159:310

Part IV

Flow instabilities in dispersions of worm-like particles

Chapter 14

Multiple Shear-Banding Transitions in a Supramolecular Polymer Solution

Multiple Shear-Banding Transitions in a Supramolecular Polymer Solution

J. van der Gucht,[1,*] M. Lemmers,[1] W. Knoben,[1] N. A. M. Besseling,[1] and M. P. Lettinga[2]
[1]*Laboratory of Physical Chemistry and Colloid Science, Wageningen University, PO Box 8038, 6700 EK Wageningen, The Netherlands*
[2]*Forschungszentrum Jülich, IFF, Weiche Materie, 52425, Jülich, Germany*

(Received 6 June 2006; published 7 September 2006)

We report on the nonlinear rheology of a reversible supramolecular polymer based on hydrogen bonding. The coupling between the flow-induced chain alignment and breakage and recombination of bonds between monomers leads to a very unusual flow behavior. Measured velocity profiles indicate three different shear-banding regimes upon increasing shear rate, each with different characteristics. While the first of these regimes has features of a mechanical instability, the second shear-banding regime is related to a shear-induced phase separation and the appearance of birefringent textures. The shear-induced phase itself becomes unstable at very high shear rates, giving rise to a third banding regime.

DOI: 10.1103/PhysRevLett.97.108301 PACS numbers: 83.60.Rs, 47.50.−d, 83.60.Wc, 83.80.Rs

Coupling between fluid microstucture and flow yields a rich scala of non-Newtonian behavior in complex fluids. Many complex fluids display flow instabilities or flow-induced phase transitions above a critical shear rate or stress. Solutions of wormlike micelles, for example, undergo a shear-banding instability in which the fluid separates in the gradient direction into coexisting regions (bands) supporting different shear rates (“gradient banding”) [1,2]. Rod-like colloids, on the other hand, display “vorticity banding,” in which the different shear bands are separated in the vorticity direction [3]. Several other systems, such as attractive emulsions or carbon nanotube suspensions, show an elastic instability that leads to the formation of shear-induced aggregates aligned in the vorticity direction [4,5].

Several aspects of these instabilities can be reproduced by phenomenological models, see e.g. [6]. Shear banding in the gradient direction, for example, can be related to a nonmonotonic constitutive equation relating the shear stress σ and the shear rate $\dot{\gamma}$. When a shear rate is applied in the region where σ decreases with $\dot{\gamma}$, an initially homogeneous flow becomes mechanically unstable. In the simplest scenario, the system then separates into a weakly sheared band that flows at $\dot{\gamma}_1$ and a highly sheared band that flows at $\dot{\gamma}_2$ [1]. Increasing the overall shear rate within the unstable region leads to an increase of the width of the high shear band, while the stress remains constant. The microscopic origin of the shear-banding instability varies for different systems. For wormlike micelles, two alternative mechanisms for shear banding have been proposed. Cates and coworkers predicted a nonmonotonic constitutive equation leading to a shear-banding instability, based on the Doi and Edwards reptation model for polymers [1]. This purely mechanical instability is responsible for shear banding in semidilute solutions of wormlike micelles, far from an equilibrium phase transition [2]. In more concentrated systems, on the other hand, the appearance of a banded flow is related to a first-order phase transition induced by the flow, such as an isotropic-to-nematic transition [6,7]. In this case, the two shear bands correspond to two structurally different coexisting phases.

Most experimental studies on shear banding have been performed with solutions of wormlike micelles. These have been successfully described as reversible equilibrium polymers that can break and recombine on experimental timescales [8]. In recent years, various other types of reversible supramolecular polymers have been synthesized, based on more specific reversible interactions, such as metal coordination complexes and hydrogen bonding [9]. The availability of these polymers paves the way for experiments that will lead to a more general understanding of the flow behavior of reversible polymers.

In this Letter, we report for the first time on shear banding in a solution of reversible supramolecular polymers based on hydrogen bonding. The unique feature of this system is that we observe *three* different shear-banding regimes upon variation of the shear rate, each with different characteristics. While the banded state at low shear rates has features of a mechanical instability, the second shear-banding regime is related to a shear-induced phase transition and the appearance of texture. In this region, we find a very unusual relation between the relative widths of the two shear bands and the overall shear rate: the width of the high-shear band *decreases* when the global shear rate increases. At very high shear rates, the shear-induced phase becomes itself unstable, giving rise to a third banding regime.

The system under examination is a solution of bis-urea-substituted toluene (EHUT), a bifunctional monomer that assembles reversibly into long, semiflexible polymer chains by multiple hydrogen bonds [10]. The persistence length of EHUT polymers was estimated to be at least 100 nm [11], which is an order of magnitude larger than for most wormlike micelles [8]. We study solutions of EHUT in dodecane at concentrations up to 6.4 g/l at 20 °C. No evidence for an isotropic-to-nematic phase transition (at rest) was observed for this concentration range and temperature. Rheological measurements were performed on a Paar Physica MCR 300 rheometer in controlled strain mode using a Couette geometry of 26.66 mm inner diameter and 1.13 mm gap width and a solvent trap to minimize evaporation. It was checked that a different Couette geometry gave only small differences. Spatially resolved velocity profiles were measured in a closed transparent Couette cell (43 mm inner diameter, 2.5 mm gap) using heterodyne dynamic light scattering in combination with a differential Laser Doppler velocimeter [12]. The rheo-optical properties of the sheared solutions were studied by placing a transparent Couette cell (43 mm inner diameter, 2.5 mm gap) between crossed polarizers. Images were taken in the plane defined by the flow and vorticity directions so that the measured birefringence is an average over the gap.

Figure 1 shows the steady state shear stress σ as a function of the shear rate $\dot{\gamma}$ for a 5.9 g/l EHUT solution at 20 °C. Several regimes are indicated in this figure. In regime A ($\dot{\gamma} < \dot{\gamma}_{\mathrm{I}} \approx 0.01\ \mathrm{s}^{-1}$), the stress increases linearly with the shear rate. The solution behaves as a Maxwell fluid in this regime with a viscosity η of 368 Pa · s, plateau modulus G_0 of 16 Pa and a relaxation time τ_0 of 23 s as obtained from the transient stress response after startup of shear flow and from dynamic linear rheology measurements. At $\dot{\gamma} = \dot{\gamma}_{\mathrm{I}} \approx 0.01\ \mathrm{s}^{-1}$ and $\sigma = \sigma_B \approx 3.3$ Pa, there is an abrupt change of slope, after which the stress decreases slightly with increasing shear rate. After reaching a minimum, the stress increases again, but with a much lower slope than in the linear regime. Region B is characterized by stress overshoots, very slow transient behavior (it may take hours before a steady state is reached), and metastability. At $\dot{\gamma} > \dot{\gamma}_{\mathrm{II}} \approx 0.06\ \mathrm{s}^{-1}$, the stress exceeds σ_B and increases with increasing shear rate with a slope of about 0.3 (regime C). In regime D, the slope of the flow curve decreases and reaches a minimum of around 0.08 at $\dot{\gamma} \simeq 30\ \mathrm{s}^{-1}$. In regime E, the slope increases again, and it eventually reaches a value of around 0.5 in regime F. Regimes D and E are again characterized by slow transient behavior. Care was taken to ensure that the points in Fig. 1 really correspond to the steady state values for the stress. Different shear histories were applied to the solution, which all resulted in the same steady state value. We also measured a flow curve in controlled stress mode. This gave the same result, except that no points could be measured in regime B: at $\sigma = \sigma_B$, the shear rate "jumps" from $\dot{\gamma}_{\mathrm{I}}$ to $\dot{\gamma}_{\mathrm{II}}$. As indicated in the inset in Fig. 1, flow curves at different concentrations exhibit qualitatively the same characteristics. The onset of regime B occurs at the same normalized shear rate $\dot{\gamma}_{\mathrm{I}}\tau_0 = 0.20 \pm 0.03$ and stress $\sigma_B/G_0 = 0.18 \pm 0.03$ for all concentrations, where G_0 and τ_0 both increase with increasing concentration [11]. At higher shear rates, the normalized flow curves do not superimpose, and the normalized stress at a certain normalized shear rate decreases with increasing concentration.

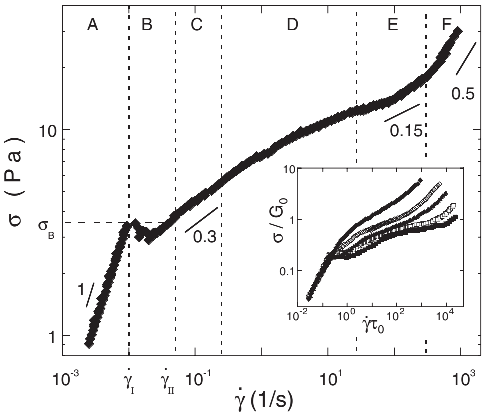

FIG. 1. Shear stress as a function of shear rate for a 5.9 g/l EHUT solution at 20 °C (measured under controlled shear rate). A–F indicate different flow regimes. In regimes B, D, and E, a banded flow is observed. Inset: flow curves for EHUT concentrations of 1.4 (◆), 2.0 (◇), 3.1 (▲), 5.9 (□), and 6.4 (■) g/l; $\dot{\gamma}$ is normalized by the terminal relaxation time τ_0 and σ is normalized by the plateau modulus G_0.

Figure 2 shows velocity profiles in the gap of the Couette cell measured at different applied overall shear rates. The lowest shear rate for which a velocity profile could be

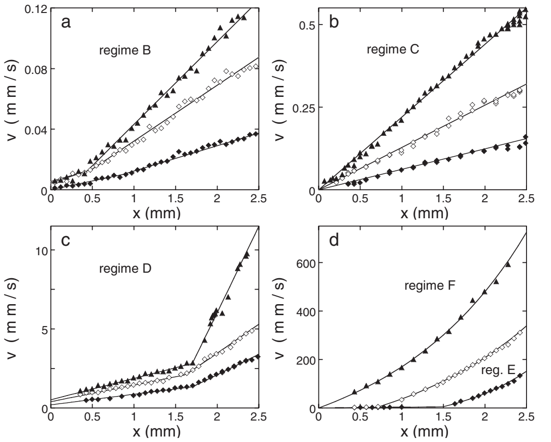

FIG. 2. Velocity profiles in the Couette cell at different applied shear rates $\dot{\gamma}$. (a) Regime B, $\dot{\gamma} = 0.015$ (◆), $\dot{\gamma} = 0.025$ (◇), and $\dot{\gamma} = 0.05$ (▲) s^{-1}. Drawn lines are linear fits for both bands. (b) Regime C, $\dot{\gamma} = 0.066$ (◆), $\dot{\gamma} = 0.14$ (◇), and $\dot{\gamma} = 0.23$ (▲) s^{-1}. Drawn lines corresponds to $v = \dot{\gamma}x$. (c) Regime D, $\dot{\gamma} = 0.59$ (◆), $\dot{\gamma} = 1.5$ (◇), and $\dot{\gamma} = 4.9$ (▲) s^{-1}. Lines are linear fits for both bands. (d) Regime E, $\dot{\gamma} = 64$ (◆) and $\dot{\gamma} = 147$ (◇) s^{-1}, and beginning of regime F, $\dot{\gamma} = 308\ \mathrm{s}^{-1}$ (▲). Drawn lines correspond to a linear profile for the low shear band and a power-law fluid ($\sigma \sim \dot{\gamma}^{0.15\pm0.02}$) for the high shear band. No slip was observed at the moving wall in all cases.

measured was 0.01 s^{-1}, just on the boundary of regimes A and B. The velocity profile is linear, as expected for a Newtonian solution. At shear rates between 0.015 and 0.066 s^{-1} (regime B, Fig. 2(a)], the profiles exhibit a "kink" indicating a banded structure. The kink becomes more pronounced with increasing shear rate. The measured velocity profiles also enable a quantification of wall slip. In regime B, there is a marginal slip at the stationary outer cylinder. At shear rates between 0.066 and 0.25 s^{-1} (regime C, Fig. 2(b)), the profiles are linear, indicating that the flow is homogeneous. Slip is negligible in this regime. An unambiguous banded state is observed again in regimes D and E, at shear rates between 0.25 and 300 s^{-1}. In regime D, between 0.25 and 30 s^{-1}, the velocity profile in both shear bands is approximately linear [Fig. 2(c)], while in regime E, above 30 s^{-1}, the high-shear band has a strongly curved profile [Fig. 2(d)]. At the highest shear rate applied ($\dot{\gamma} = 308$ s^{-1}), the low shear band has disappeared and only one band is left, also with a curved velocity profile (regime F, Fig. 2(d)]. The curved velocity profiles in regimes E and F are an indication for strong shear thinning in these regimes [12]. The profile for $\dot{\gamma} = 308$ s^{-1} can be fitted with a power-law fluid $\sigma \sim \dot{\gamma}^a$ with an exponent $a = 0.15$ [13]. The same shear-thinning exponent accounts for the profiles in the high shear band in regime E. A slope of 0.15 is also indicated in the flow curve shown in Fig. 1. It can be seen in this figure that this exponent is in reasonable agreement with the slope of the measured flow curve in the relevant region (regime E and the beginning of regime F).

Solutions of EHUT thus exhibit *three* different shear-banding regimes. The onset of the first shear-banding regime (B) occurs at the same normalized shear rate $\dot{\gamma}_I \tau_0$ and stress σ_B/G_0 for different EHUT concentrations (Fig. 1, inset), suggesting that the origin of shear banding in this regime is a mechanical instability of the underlying constitutive relation, such as proposed by Spenley and Cates [1]. Indeed, birefringence images show no evidence for a shear-induced phase transition in regime B [Fig. 3(a)]: no significant increase of the birefringence could be detected in regimes B and C. The unstable flow behavior is also supported by the jump in the flow curve when measured under controlled stress. The shear-banded flow at higher shear rates, in regimes D and E, on the other hand, is accompanied by the appearance of birefringent textures in the solution [Fig. 3(b)–3(d)]. These textures could be seen for the first time at a shear rate of about 1 s^{-1} (i.e. in regime D). They appear a few seconds after startup of shear flow and remain visible for many hours under steady flow. After cessation of the shear flow, the textures disappear again on the timescale of several seconds. With increasing shear rate, the overall birefringence increases and the textures become finer and at very high shear rates, they seem to disappear [Fig. 3(d)]. Without polarized incoming light, no texture could be seen. The textures can be interpreted as domains of a new phase induced by the shear flow and suggest that, contrary to regime B, the banded structure in regimes D and E is related to a shear-induced phase separation (for example between an isotropic and a nematic phase). Similar domain patterns have been seen in other multiphase flows where they were attributed to a viscoelastic asymmetry between the two phases [5]. In wormlike micelle solutions, a shear-induced phase transition is observed only for very concentrated micellar solutions, close to an equilibrium phase transition [7]. For EHUT solutions, we did not see evidence for a phase transition at rest for the concentrations used, but, nevertheless, a transition is induced by the flow. This suggests that the flow couples more strongly to chain alignment and growth for EHUT than for wormlike micelles, probably because of the longer persistence length of EHUT polymers [8,11].

In order to obtain more detailed information about the behavior in the three different shear-banding regimes, we extract from the velocity profiles displayed in Fig. 2 the average shear rates in both shear bands and the width of the two bands. These are shown in Fig. 4 as a function of the overall applied shear rate. Clearly, our observations do not correspond to the simple picture in which a change of the applied shear rate only affects the relative proportion of

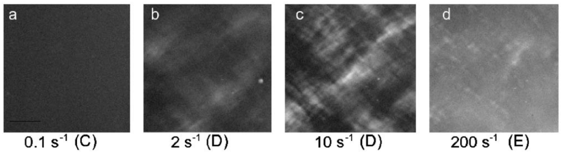

FIG. 3. Birefringence images taken in the plane defined by the flow and vorticity directions of a 5.9 g/l EHUT solution at 20 °C under shear flow for different applied shear rates (as indicated). The flow regime is indicated in parentheses. Each image is 1 × 1 cm.

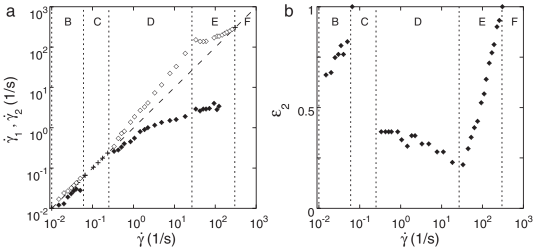

FIG. 4. (a) Average shear rates $\dot{\gamma}_1$ in the low shear band (◆) and $\dot{\gamma}_2$ in the high shear band (◇) as a function of the overall shear rate. + indicates shear rates in regime C, where no shear-banding is observed. The diagonal dashed line denotes homogeneous flow. (b) Fraction ε_2 of the gap occupied by the high shear band as a function of the overall shear rate. Note that there is only one band in regimes A, C, and F. Vertical dashed lines in both figures indicate different regimes A–F.

each layer, while the shear rates in both bands and the value of the stress remain constant [1]. In regime *B*, we find that both the shear rate in the low shear band $\dot{\gamma}_1$ and that in the high shear band $\dot{\gamma}_2$ increase with increasing $\dot{\gamma}$. Moreover, we do not see a clear stress plateau in the flow curve (Fig. 1). These observations may be due to the inherent stress gradient of the Couette cell. Alternatively, the compositions of the two bands could be different and vary when the overall shear rate is varied [6]. The relative width of the high shear band ϵ_2 increases with the overall shear rate $\dot{\gamma}$ in regime *B*, as expected [1]. It approaches unity as regime *C* is approached, where the banded structure disappears. The difference in viscosity between the two bands in regime *B* is rather small: the ratio $\dot{\gamma}_2/\dot{\gamma}_1$ varies between 1 and 2. In regime *D*, where shear banding is related to a phase transition (as seen from birefringence images), the variation of $\dot{\gamma}_1$, $\dot{\gamma}_2$, and ϵ_2 with $\dot{\gamma}$ is rather unusual. Upon increasing the shear rate, ϵ_2 first remains more or less constant and then *decreases*, while the ratio between the shear rates in both bands ($\dot{\gamma}_2/\dot{\gamma}_1$) increases from 1 to approximately 50. Clearly, such behavior cannot be explained by current theory. It suggests a complex interplay between the structure of the two phases, the concentrations and length distributions in both phases, and the shear flow. In regime *E*, the behavior is more or less as expected. Upon increasing the overall shear rate, the shear rates in the two bands remain approximately constant, while ϵ_2 increases monotonically to unity at the boundary between regimes *E* and *F*, where also the textures disappear. The behavior of $\dot{\gamma}_1$, $\dot{\gamma}_2$, and ϵ_2 upon variation of the overall shear rate changes very abruptly at $\dot{\gamma} \approx 30\ \mathrm{s}^{-1}$, between regimes *D* and *E*. As noted above, the shapes of the velocity profiles also change here: in regime *D* the profiles are linear in both bands, while in regime *E* the high shear band is strongly curved [Fig. 2(c) and 2(d)]. These observations suggest that the shear-induced phase that is formed in regime *D* becomes unstable in regime *E*, thus giving rise to a third shear-banding regime. Whether this instability is a mechanical instability or a phase transition to a new shear-induced phase or structure is unclear. It would be useful to extend the present rheological study with scattering techniques, microscopy, or birefringence imaging in the vorticity direction to obtain information about the microstructure of the two phases.

In summary, we studied the nonlinear rheology of a solution of hydrogen-bonded supramolecular equilibrium polymers. Upon variation of the shear rate, these polymers exhibit a very rich and complex behavior with three different shear-banding regimes. For the first time, we observe within the same system the two different types of gradient shear banding that have been described: a mechanical instability at low shear rates and a shear-induced phase transition at higher shear rates. The characteristics of the banded flow regimes cannot be fully explained by current theories and ask for a detailed microscopic modeling of equilibrium polymers under flow that takes into account the coupling between flow alignment, reversible breakage and recombination reactions, and concentration gradients in the gap. By comparing with other types of reversible supramolecular polymers and contrasting to wormlike micelles, we may be able to extract the role of specific bonding interactions and chain flexibility in these systems. Alternatively, by adding monofunctional monomers that block chain ends and prevent their recombination [14], one could investigate the role of recombination reactions, while adding trifunctional monomers would give the possibility of bundle or network formation.

The authors thank L. Bouteiller for supplying EHUT samples and H. Kriegs for assistance with the heterodyne light scattering measurements.

---

[*] Electronic address: jasper.vandergucht@wur.nl

[1] N. A. Spenley, M. E. Cates, and T. C. B. McLeish, Phys. Rev. Lett. **71**, 939 (1993).

[2] H. Rehage and H. Hoffmann, Mol. Phys. **74**, 933 (1991).

[3] M. P. Lettinga and J. K. G. Dhont, J. Phys. Condens. Matter **16**, S3929 (2004).

[4] A. Montesi, A. Peña, and M. Pasquali, Phys. Rev. Lett. **92**, 058303 (2004).

[5] E. K. Hobbie, S. Lin-gibson, H. Wang, J. A. Pathak, and H. Kim, Phys. Rev. E **69**, 061503 (2004).

[6] S. M. Fielding and P. D. Olmsted, Eur. Phys. J. E **11**, 65 (2003).

[7] J. F. Berret, D. C. Roux, and P. Lindner, Eur. Phys. J. B **5**, 67 (1998).

[8] M. E. Cates and S. J. Candau, J. Phys. Condens. Matter **2**, 6869 (1990).

[9] L. Brunsveld, B. J. B. Folmer, E. W. Meijer, and R. P. Sijbesma, Chem. Rev. **101**, 4071 (2001).

[10] S. Boileau, L. Bouteiller, F. Lauprêtre, and F. Lortie, New Journal of Chemistry **24**, 845 (2000).

[11] J. Van der Gucht, N. A. M. Besseling, W. Knoben, L. Bouteiller, and M. A. Cohen Stuart, Phys. Rev. E **67**, 051106 (2003).

[12] J.-B. Salmon, A. Colin, and S. Manneville, Phys. Rev. Lett. **90**, 228303 (2003).

[13] The velocity profile for a power law fluid with $\sigma \sim \dot{\gamma}^a$ in a Couette geometry is $v(r) = \omega_0 r(r^{-2/a} - R_2^{-2/a})/(R_1^{-2/a} - R_2^{-2/a})$, with ω_0 the applied angular velocity, R_1 the radius of the inner cylinder, R_2 that of the outer cylinder, and $r = R_2 - x$ the distance from the center of the cylinders [12].

[14] W. Knoben, N. A. M. Besseling, L. Bouteiller, and M. A. Cohen Stuart, Phys. Chem. Chem. Phys. **7**, 2390 (2005).

Chapter 15

Dynamic response of block copolymer worm-like micelles to shear flow

IOP PUBLISHING JOURNAL OF PHYSICS: CONDENSED MATTER

J. Phys.: Condens. Matter **20** (2008) 404207 (11pp) doi:10.1088/0953-8984/20/40/404207

Dynamic response of block copolymer wormlike micelles to shear flow

B Lonetti[1], **J Kohlbrecher**[2], **L Willner**[1], **J K G Dhont**[1] **and**
M P Lettinga[1]

[1] Institut für Festkörperforschung, Forschungszentrum Jülich, D-52425 Jülich, Germany
[2] Laboratory for Neutron Scattering, ETH Zürich and Paul Scherrer Institut, 5232 Villigen PSI, Switzerland

Received 2 May 2008
Published 10 September 2008
Online at stacks.iop.org/JPhysCM/20/404207

Abstract
The linear and nonlinear dynamic response to an oscillatory shear flow of giant wormlike micelles consisting of Pb–Peo block copolymers is studied by means of Fourier transform rheology. Experiments are performed in the vicinity of the isotropic–nematic phase transition concentration, where the location of isotropic–nematic phase transition lines is determined independently. Strong shear-thinning behaviour is observed due to critical slowing down of orientational diffusion as a result of the vicinity of the isotropic–nematic spinodal. This severe shear-thinning behaviour is shown to result in gradient shear banding. Time-resolved small-angle neutron scattering experiments are used to obtain an insight into the microscopic phenomena that underlie the observed rheological response. An equation of motion for the order parameter tensor and an expression of the stress tensor in terms of the order parameter tensor are used to interpret the experimental data, both in the linear and nonlinear regimes. Scaling of the dynamic behaviour of the orientational order parameter and the stress is found when critical slowing down due to the vicinity of the isotropic–nematic spinodal is accounted for.

1. Introduction

Dispersions of surfactant wormlike micelles form a class of systems that has been intensively studied during the past two decades. Wormlike micellar systems sometimes exhibit extreme shear-thinning behaviour (Berret 2004), resulting in shear-induced structure formation like shear banding (Manneville 2008). Strong shear thinning is of practical interest, since often systems are required in practical applications that exhibit extreme differences in viscosity between the sheared and quiescent states. The reason for the popularity of wormlike micelles lies in their complex rheological behaviour like shear banding and chaotic response, which are connected to the thinning behaviour of these systems (Berret 2004). It is therefore important to understand the microscopic mechanism underlying the very strong shear-thinning behaviour of wormlike micelles. There are several possible microscopic mechanisms that could be responsible for the occurrence of strong shear thinning (Cates and Candau 1990). One mechanism is related to the breaking and/or merging of worms. Scission due to shearing forces and merging of worms through stressed entanglement points (Briels *et al* 2004) can lead to strong shear thinning. Another possible mechanism for strong shear thinning is connected to the fact that wormlike systems can undergo an isotropic–nematic (I–N) phase transition. Rotational diffusion close to I–N spinodal lines in the phase diagram is very slow, so that a relatively strong alignment on applying shear flow occurs. Such a strong increase in the degree of alignment leads in turn to strong shear thinning. We shall hereafter refer to the slowing down of rotational diffusion close to the I–N spinodals simply as '*critical slowing down*'. By definition, the rotational diffusion coefficient at the spinodal changes sign, and is therefore zero at the spinodal, which implies very slow rotational Brownian motion.

For most studied surfactant wormlike micellar systems, the I–N transition occurs at relatively high volume fractions of around 10%. At this high concentration the viscosity of the system is quite large, and moreover a transition to a gel phase can interfere. For CPLC/NaSal inbrine, for example, gelling occurs in the vicinity of the I–N transition on changing the temperature by just a few degrees. Furthermore, the I–N transition is only found under flow conditions. These features complicate detailed studies on the rheological response of wormlike micelles and its microscopic origin. We therefore study here a system that exhibits many of the properties of wormlike micellar systems that are responsible for their interesting rheological behaviour, but that does not have the above-mentioned complications of surfactant wormlike micellar systems. For an I–N transition to occur without flow, we need a system where the persistence length l_p is much larger than the thickness d of the chains. The ratio l_p/d should be larger compared to typical values for wormlike micelles. A candidate system could be micelles formed from block copolymers. A well-studied system is the poly(butadiene)–poly(ethylene oxide) (Pb–Peo) diblock copolymer with a 50–50 block composition in aqueous solution. The main advantage of this system is that it is very stiff, with a persistence length of around 500 nm and a diameter of 14 nm. The contour length of the Pb–Peo worms is around 1 μm. As a result of the large ratio l_p/d compared to common surfactant micellar systems, the diblock copolymer system shows an I–N transition at a modest concentration of about 5%, although the transition concentration has not been determined accurately yet (Won *et al* 1999). Other advantages of the Pb–Peo system are that it is possible to tune the monomer-exchange kinetics between the polymers (Lund *et al* 2006) or its morphology (Denkova *et al* 2008) by using different solvent mixtures. Furthermore, these polymers are easily marked with fluorescent dyes, which enables their visualization with fluorescence microscopy. In a recent study Förster *et al* used this system, amongst others, for Rheo-SANS measurements, where stationary shear measurements were combined with small-angle neutron scattering (SANS) (Förster *et al* 2005). A feature of this diblock copolymer system that is probably not shared with micellar systems is that the polymers do not easily break and merge under flow. We thus focus on the microscopic mechanism mentioned above, related to critical slowing down of rotational diffusion close to the I–N transition.

In section 2, a well-known theoretical framework for the dynamics and rheological behaviour of stiff rods is summarized. This theory does not include flexibility of single polymer chains, but does include the slowing down of rotational diffusion due to the vicinity of the I–N spinodal. This theory will be used to assess the effect of the vicinity of the I–N transition on rheological response. A comparison of our experiments with predictions based on this theory can only be done on a qualitative level, since flexibility is neglected in the theory. After the materials section we describe a newly developed time-resolved SANS set-up, and the couette cells and rheometers that were used. In section 5 we first discuss the flow curve of the system and determine the corresponding flow profiles. It is also shown in this section how the (non-equilibrium) binodal line can be found from shear step-down experiments. Then we discuss SANS experiments on quiescent and stationary sheared systems, which we need as an input in the last subsection on dynamic experiments. In the latter subsection we connect the time-resolved SANS measurements with Fourier transform rheology results. The spinodal point is determined in order to establish whether the concept of critical slowing down indeed applies.

2. Theory

2.1. Concentration dependence of the rotational diffusion coefficient

On approach of the isotropic–nematic (I–N) spinodal, the *collective* rotational diffusion coefficient vanishes and becomes negative in the unstable part of the phase diagram. As will be discussed later, this rotational diffusion coefficient describes the dynamics of small perturbations of the orientational order parameter from its value in a stationary state. For a system of very long and thin, rigid rods with repulsive interactions that have a range that is small compared to the length of the rods, critical slowing is described by the equation of motion for the orientational order parameter tensor $\mathbf{S} \equiv \langle \hat{\mathbf{u}}\hat{\mathbf{u}} \rangle$, where $\hat{\mathbf{u}}$ is the unit vector along the long axis of a rod, which specifies the orientation of the rod, and where the brackets indicate ensemble averaging. Starting from the Smoluchowski equation for rod-like colloids with hard-core interactions, an equation of motion for $\mathbf{S}$ can be derived (Dhont and Briels 2003a), which is similar to the Doi–Edwards equation of motion (Doi and Edwards 1986):

$$\frac{\mathrm{d}}{\mathrm{d}t}\mathbf{S} = -6D_\mathrm{r}\left\{\mathbf{S} - \tfrac{1}{3}\hat{\mathbf{I}} + \tfrac{L}{D}\varphi\left(\mathbf{S}^{(4)}{:}\mathbf{S} - \mathbf{S}\cdot\mathbf{S}\right)\right\} + \dot{\gamma}\left\{\hat{\mathbf{\Gamma}}\cdot\mathbf{S} + \mathbf{S}\cdot\hat{\mathbf{\Gamma}}^\mathrm{T} - 2\mathbf{S}^{(4)}{:}\hat{\mathbf{E}}\right\}, \tag{1}$$

where D_r is the rotational diffusion coefficient at infinite dilution, L is the length of the rods, d their core diameter, φ is the volume fraction of rods, $\dot{\gamma}$ is the shear rate, $\hat{\mathbf{\Gamma}}$ is the velocity-gradient tensor and $\hat{\mathbf{E}} = \frac{1}{2}[\hat{\mathbf{\Gamma}} + \hat{\mathbf{\Gamma}}^\mathrm{T}]$ is the symmetrized velocity-gradient tensor (where the superscript ‘T’ stands for ‘transpose’). Furthermore, $\mathbf{S}^{(4)} \equiv \langle \hat{\mathbf{u}}\hat{\mathbf{u}}\hat{\mathbf{u}}\hat{\mathbf{u}} \rangle$ is a fourth-order tensor. A closure relation that expresses contractions of the form $\mathbf{S}^{(4)}{:}\mathbf{M}$ in terms of $\mathbf{S}$ for arbitrary second rank tensors $\mathbf{M}$ is discussed in (Dhont and Briels 2003a):

$$\langle \hat{\mathbf{u}}\,\hat{\mathbf{u}}\,\hat{\mathbf{u}}\,\hat{\mathbf{u}} \rangle{:}\mathbf{M} = \tfrac{1}{5}\left\{\mathbf{S}\cdot\overline{\mathbf{M}} + \overline{\mathbf{M}}\cdot\mathbf{S} - \mathbf{S}\cdot\mathbf{S}\cdot\overline{\mathbf{M}} - \overline{\mathbf{M}}\cdot\mathbf{S}\cdot\mathbf{S} + 2\mathbf{S}\cdot\overline{\mathbf{M}}\cdot\mathbf{S} + 3\mathbf{S}\mathbf{S}{:}\overline{\mathbf{M}}\right\}, \tag{2}$$

where $\overline{\mathbf{M}} = \frac{1}{2}[\mathbf{M} + \mathbf{M}^\mathrm{T}]$ is the symmetric part of the tensor $\mathbf{M}$. For simple shear flow, the velocity-gradient tensor has the form

$$\hat{\mathbf{\Gamma}} = \begin{pmatrix} 0 & 1 & 0 \\ 0 & 0 & 0 \\ 0 & 0 & 0 \end{pmatrix}, \tag{3}$$

which corresponds to a flow in the x direction with its gradient in the y direction.

The largest eigenvalue λ of $\mathbf{S}$, the ‘orientational order parameter’, is a measure of the degree of alignment (for the isotropic state $\lambda = 1/3$ and for a perfectly aligned state, $\lambda = 1$). In order to illustrate critical slowing down of orientational diffusion, we consider first an isotropic state which is slightly perturbed. The equation of motion for a small perturbation $\delta\lambda$ of $\lambda = 1/3$ in the isotropic state, in the absence of flow, is readily obtained from equation (1) together with the closure relation (2):

$$\frac{\mathrm{d}\delta\lambda}{\mathrm{d}t} = -6D_\mathrm{r}\left\{1 - \frac{1}{4}\frac{L}{d}\phi\right\}\delta\lambda = -6D_\mathrm{r}^\mathrm{eff}\delta\lambda \tag{4}$$

where

$$D_{\mathrm{r}}^{\mathrm{eff}} = D_{\mathrm{r}}\left\{1 - \frac{1}{4}\frac{L}{d}\phi\right\} \tag{5}$$

is the effective rotational diffusion coefficient. Hence,

$$\delta\lambda(t) = \delta\lambda(t=0)\exp\{-6\,D_{\mathrm{r}}^{\mathrm{eff}}t\}. \tag{6}$$

From equation (5) it can be seen that $D_{\mathrm{r}}^{\mathrm{eff}} \to 0$ as $(L/d)\varphi \to 4$. Collective rotational diffusion thus becomes very slow on approach of the spinodal concentration where $(L/d)\varphi = 4$. For larger concentrations, where $D_{\mathrm{r}}^{\mathrm{eff}} < 0$, the isotropic state is unstable, and the initially small orientational order parameter increases in time. In the presence of shear flow, the above analysis must be done numerically, since the unperturbed (stable or unstable) stationary state under shear flow is not known analytically. The effective rotational diffusion coefficient is now a tensorial quantity rather than a scalar as for the isotropic state discussed above. The phenomenon of critical slowing down, however, is unchanged: rotational diffusion becomes very slow on approach of the spinodal (where at least one of the eigenvalues of the rotational diffusion tensor changes sign). This slowing down of rotational diffusion has pronounced effects on the shear-thinning behaviour, as will be discussed later.

2.2. *Dynamic response of stress and orientational order*

From microscopic considerations, an expression for the stress tensor $\mathbf{\Sigma}$ can be obtained (Dhont and Briels 2003b), which is similar to an earlier derived expression by Doi and Edwards (Doi and Edwards 1986):

$$\mathbf{\Sigma}_D = 2\eta_0\dot{\gamma}\left[\hat{\mathbf{E}} + \frac{(L/D)^2}{3\ln\{L/D\}}\varphi \times\left\{\hat{\mathbf{\Gamma}}\cdot\mathbf{S} + \mathbf{S}\cdot\hat{\mathbf{\Gamma}}^{\mathrm{T}} - \mathbf{S}^{(4)}{:}\hat{\mathbf{E}} - \frac{1}{3}\hat{\mathbf{I}}\mathbf{S}{:}\hat{\mathbf{E}} - \frac{1}{\dot{\gamma}}\frac{\mathrm{d}\mathbf{S}}{\mathrm{d}t}\right\}\right]. \tag{7}$$

For an oscillatory shear flow, the shear rate $\dot{\gamma}$ in equations (1) and (7) is time-dependent:

$$\dot{\gamma}(t) = \dot{\gamma}_0\cos\{\omega t\}, \tag{8}$$

where $\dot{\gamma}_0 = A\omega$ is the shear amplitude, with A the strain amplitude and ω the frequency of oscillation.

The linear and nonlinear response of suspensions or rigid rods, within the approximations involved in the theory, can be obtained from numerical solutions of equations (1) and (7) (Dhont and Briels 2003a). In particular, dynamic response functions can be obtained from a Fourier analysis of the time dependence of the stress tensor after transients have relaxed. For sufficiently large shear rates, higher-order nonlinear response functions come into play. For these higher shear amplitudes, the time-dependent stress tensor must be Fourier-expanded as

$$\mathbf{\Sigma}_D = 2\dot{\gamma}_0\hat{\mathbf{E}}\sum_{n=0}^{\infty}|\eta|_n\sin(n\omega t + \delta_n), \tag{9}$$

where $|\eta|_n$ and δ_n are the amplitude and phase shift of the Fourier components, respectively. Similarly, the scalar orientational order parameter will respond in a nonlinear fashion, so that

$$P_2(t) = \sum_{n}^{\infty}|P_2|_n\cos(\omega t + \epsilon_n), \tag{10}$$

where $P_2 = \frac{1}{2}[3\lambda - 1]$ (as before, λ is the largest eigenvalue of $\mathbf{S}$). It should be mentioned that in scattering experiments only projections of the orientational order parameter tensor are probed. In that case, P_2 in equation (10) does not correspond to the largest eigenvalue of $\mathbf{S}$, but only to the corresponding projection of $\mathbf{S}$. In the experiments described in this paper the vorticity-flow plane is probed, for which it is readily shown from equation (1) by expanding $\mathbf{S}$ for small shear rates that the leading term in shear rate varies like $\sim\dot{\gamma}^2$. The time dependence of the experimentally determined orientational order parameter term has therefore the double frequency of the applied shear flow.

One may ask about the shear rate beyond which nonlinear response is expected, and beyond which a frequency phase shift will be found. An analysis of the equation of motion (1) and the expression (7) for the stress tensor for the isotropic state and to leading order in nonlinearity reveals that the so-called effective Peclet number,

$$Pe_{\mathrm{eff}} = \dot{\gamma}_0/D_{\mathrm{r}}^{\mathrm{eff}}, \tag{11}$$

and the effective Deborah number:

$$\Omega_{\mathrm{eff}} = \omega/D_{\mathrm{r}}^{\mathrm{eff}}, \tag{12}$$

measure the nonlinearity and phase shift. Here, the effective rotational diffusion coefficient is given in equation (5).

3. Material

In this study we used a symmetric Pb–Peo block copolymer prepared by living anionic polymerization; the synthesis follows a two-step procedure since the polymerization conditions for ethylene oxide are different from those for butadiene. Details of the two-step procedure can be found in an earlier publication (Allgaier *et al* 1997). The Pb–Peo block copolymer was characterized by size exclusion chromatography (SEC) using a mixture of tetrahydrofuran/dimethylacetamide 90/10 v/v as eluant. The polydispersity, Mw/Mn, of the block copolymer was smaller than 1.04. No signs of PEO and PB homopolymers were found in the SEC chromatograms. Absolute molecular weights were determined by 1H-NMR measurements in $CDCl_3$. Thereby, the signal of the t-butyl initiator group was taken as an internal reference. The number average molecular weights, Mn, are 2.6 kg mol^{-1} for PB and 2.64 kg mol^{-1} for PEO. Polymer solutions were prepared by dissolving the polymer in D_2O (Chemotrade, $\%D = 99.8\%$) and, in order to guarantee its complete dissolution, especially in the case of high concentration samples, they were kept for half an hour at 56 °C and then left to cool down slowly to the ambient temperature. When not specified otherwise, the concentrations will be expressed as a weight fraction.

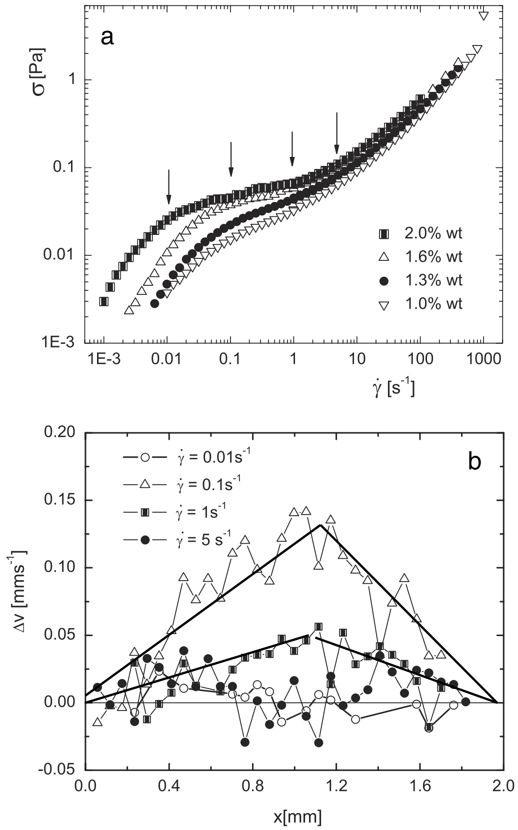

Figure 1. (a) Flow curves for different Pb–Peo concentrations. (b) The relative flow velocity $\Delta v(x) = V(x) - \dot{\gamma}x$ throughout the gap of the couette cell for various applied shear rates as indicated by the arrows in (a): 0.01, 0.1, 1 and 5 s^{-1}. The lines indicate two shear bands.

4. Experimental details

SANS experiments have been performed at the SANS I instrument at the SINQ spallation source at the Paul Scherrer Institute (PSI) in Villigen, Switzerland (Kohlbrecher and Wagner 2000). We used thermal neutrons of wavelength $\lambda = 0.8$ nm with a wavelength spread $\Delta\lambda/\lambda$ of about 0.1. The data analysis was performed using the BerSANS software package (Keiderling 2002). A standard water sample was used for calibration of absolute scattering intensities and also to account for non-uniform detector efficiency. For the Rheo-SANS experiments a Rheowis strain-controlled rheometer with a couette type shear cell (bob: 48 mm radius, cup: 50 mm radius) was placed in the neutron beam in the so-called radial configuration. In this configuration the neutron beam passes through the centre of the sapphire cell, transparent for neutrons, and is parallel to the gradient direction so that the flow-vorticity plane is probed by the 2D detector. The accessible torque range is between 10^{-7} and 0.046 N m, the frequency range between 5×10^{-3} and 10 Hz and the amplitude range between 5×10^{-2} and 45. Both steady state and oscillatory experiments were performed. In order to probe the time-dependent structural changes with SANS under oscillating shear, a stroboscopic data acquisition scheme, implemented on the SANS-1 instrument, has been used. The electronics of the rheometer supplies a low and high signal depending on the turning direction. The falling edge of this rectangular signal has been used to trigger the data acquisition of the scattered neutrons, producing histograms of 128×128 pixels of 0.75×0.75 cm^2 spatial resolution and at least $n = 100$ time channels of widths $\Delta t = (n \times \omega/2\pi)^{-1}$, where $\omega/2\pi$ is the frequency of the applied oscillating shear. The time of flight t_{tof} of the scattered neutrons between sample and detector has been corrected to obtain the exact phase between applied shear and scattered neutrons. However, this correction can be practically neglected as the applied shear frequencies are much lower than $1/t_{\mathrm{tof}}$. Before starting the neutron data acquisition the rheometer was oscillating for several cycles to ensure that no transient effects were measured. To obtain sufficient counting statistics for each time channel, the histograms of many shear cycles were summed up over a time going from 1 h to 15 min for the lowest and highest concentration, respectively. With this technique the temporal evolution of the structural alignment of the diblock copolymers during a whole shear cycle could be measured.

Fast Fourier transform rheological experiments were performed on a strain-controlled rheometer (ARES, TA instruments), using a couette geometry (bob: 32 mm radius, cup: 34 mm radius). The stress response to dynamic strain experiments has been simultaneously recorded with a Analog Digital Card and analysed with fast Fourier transform software as described in (Wilhelm *et al* 1998). The same instrument was used for step-rate experiments and to obtain flow curves. Spatially resolved velocity profiles were measured on a homebuilt heterodyne dynamic light scattering set-up using a closed, transparent couette cell (2 mm gap), see e.g. (Salmon *et al* 2003).

5. Results and discussion

5.1. Flow curve and step-down rheology

The Pb–Peo block copolymer under study forms wormlike micelles in water solution. As molecular wormlike micelles, consisting of surfactant molecules, these giant wormlike micelles show a pronounced shear-thinning behaviour. Figure 1(a) shows the stress as a function of the shear rate for Pb–Peo solutions with volume fraction between 1% and 2%. These concentrations lie close to the suggested literature value for the I–N transition (Won *et al* 1999), but are still in the isotropic phase. All the curves in figure 1(a) exhibit a shear-thinning region which extends to lower shear rates with increasing volume fraction of micelles, while the corresponding stress plateau becomes flatter. For the sample with the highest concentration, i.e. $[\mathrm{Pb-Peo}] = 2\%$, we tested if the sample shows shear banding, as is expected for extreme shear-thinning samples (Dhont and Briels 2008, Olmsted 2008). A few typical velocity profiles relative to the applied shear rate within the gap of the couette cell are

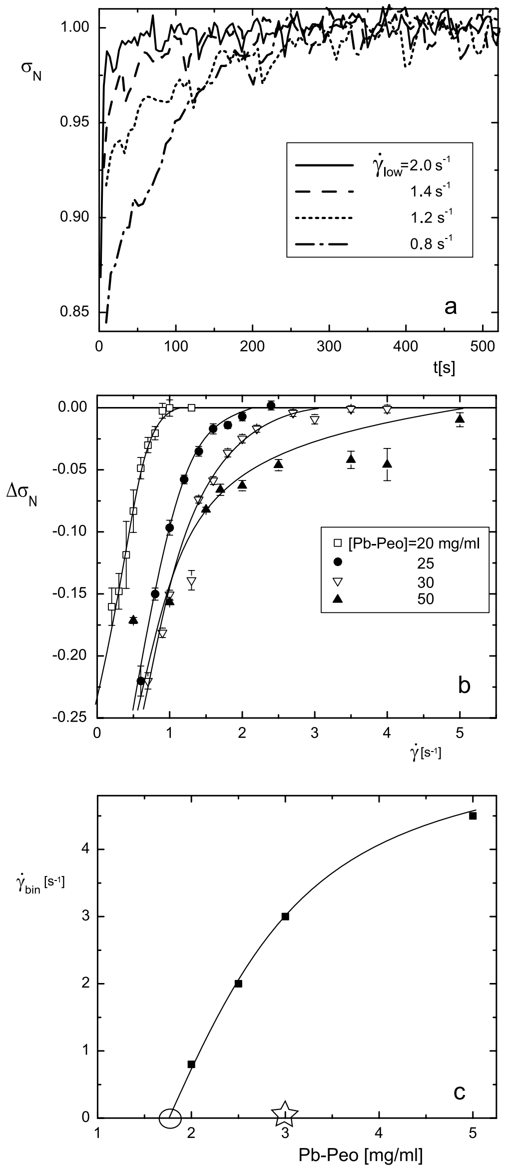

Figure 2. (a) The response of the normalized stress $\sigma_N(t) = \sigma(t)/\sigma(t \to \infty)$ to shear rate quenches from the fully nematic state into the biphasic region. The initial shear rate was $\dot{\gamma} = 7\ s^{-1}$ and the low shear rates were varied between $\dot{\gamma} = 0.8\ s^{-1}$ (bottom) and $\dot{\gamma} = 2.0\ s^{-1}$ (top). (b) The magnitude of the stress response $\Delta\sigma_N$, obtained from the fit to $\sigma_N(t) = 1 - \Delta\sigma_N\, e^{-t/\tau}$ as a function of the shear rate. Lines are guides to the eye. (c) The resulting binodal points obtained from the shear rate in (b) where $\Delta\sigma_N$ becomes zero. The circle indicates the equilibrium I–N binodal, that is, the binodal point in the absence of flow. The line is a guide to the eye, representing the non-equilibrium binodal. The open star indicates the location of the spinodal at zero shear rate.

plotted in figure 1(b), as obtained from spatially resolved heterodyne light scattering measurements. Shear banding is observed between 0.1 and 0.75 s^{-1}, which corresponds to the flat region in the flow curve in figure 1(a). At the lowest investigated shear rate, 0.01 s^{-1}, the velocity profile is linear (see figure 1(b)). Increasing the shear rate to 0.1 s^{-1}, inside the stress plateau region, a banded structure can be recognized and the velocity profile shows a characteristic kink, as can be seen from figure 1(b). In the investigated overall shear-rate range, the average shear rate in the high shear-rate band is twice that of the lower shear-rate band. The fraction of the gap occupied by the high shear-rate band increases with the overall shear rate, and for shear rates higher than 1 s^{-1} the low shear-rate band disappears and a linear profile is re-established.

In order to locate the isotropic–nematic binodal, i.e. the point where the isotropic phase becomes metastable, rheology is a very useful tool as the viscosity of the micellar solution is very sensitive to the local orientation of the worms. To exploit the large difference between the viscosity of the isotropic and nematic phases, we performed step-down experiments in the concentration region between 2% and 5%. As we have shown in an earlier paper on rod-like viruses (Lettinga and Dhont 2004), the viscosity of the system will increase in time when the system is quenched from a high shear rate, where the nematic phase is stable, to a lower shear rate, where the nematic phase becomes meta- or unstable. Figure 2(a) shows an example of the normalized stress $\sigma_N(t) = \sigma(t)/\sigma(t \to \infty)$ (where σ is the shear stress) as a function of time after the shear rate was quenched from 7 s^{-1} to a final value ranging from 2 to 0.8 s^{-1}. The curves are fitted to a single exponential $\sigma_N(t) = 1 - \Delta\sigma_N\, e^{-t/\tau}$, where $\Delta\sigma_N$ depends on the fraction of the formed isotropic phase, which tends to zero at the binodal point. Thus, for each concentration the binodal point was determined as the shear rate at which $\Delta\sigma_N$ vanishes (see figure 2(b)). The resulting binodal points are plotted in figure 2(c). This figure constitutes the low concentration branch of the non-equilibrium binodal for the Pb–Peo block copolymer system. The equilibrium I–N binodal, in the absence of flow, is found to be located at $[\mathrm{Pb-Peo}] = 1.7 \pm 0.1\%$. The open star in figure 2 indicates the location of the spinodal at zero shear rate. How this spinodal point was determined will be discussed later.

As we are dealing with a system that can also be described as flexible rods, we know from Chen (1993), for example, that the I–N phase coexistence region is very broad and thus the location of the I–N spinodal can be found at a significantly higher concentration than the I–N binodal. In the case of rigid rods, the collective rotational diffusion becomes very small on approach of the spinodal point, as discussed in section 2. For semi-flexible chains, the rotational motion of the Kuhn segments will become very slow on the approach of the spinodal. We will now employ dynamic experiments to access this slowing down. We want to do this not only on the macroscopic level, i.e. by rheology, but also on the microscopic level, in order to establish a link between the behaviour of Kuhn segments and the measured stress in the system.

5.2. SANS on quiescent and stationary sheared samples

The quiescent dispersion of Pb–Peo micelles has an angle-averaged scattering pattern as plotted in figure 3(a). At low

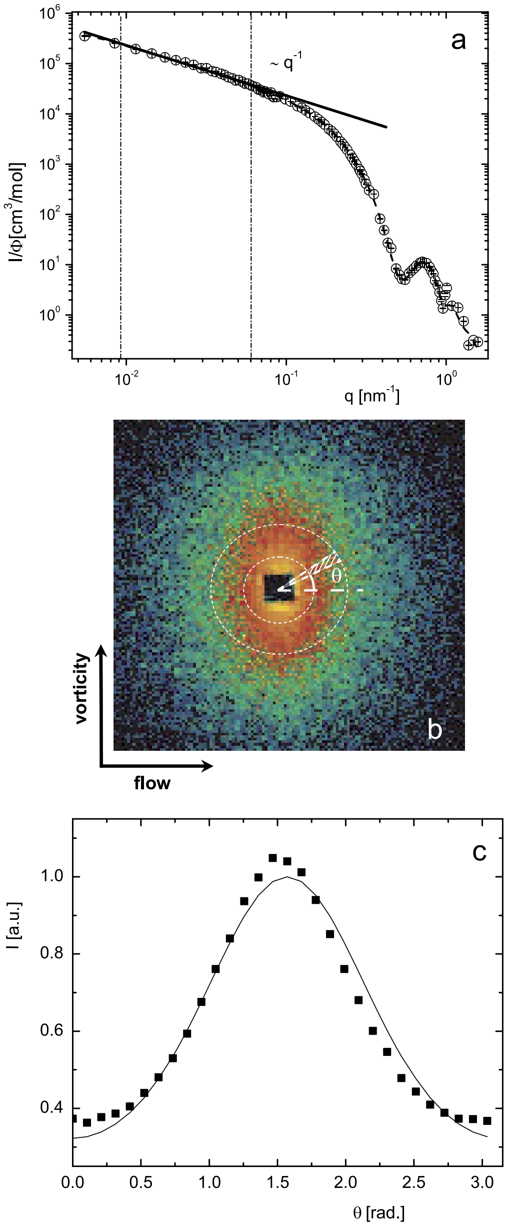

Figure 3. (a) Angle-averaged SANS curve at zero shear. The full line indicates the q range where a q^{-1} dependence is found, typical for rods. (b) Scattering pattern of 1% Pb–Peo in deuterated water at shear rate $\dot{\gamma} = 1\ \mathrm{s}^{-1}$ in the flow-velocity plane. The dashed lines indicate the Q range that is used to obtain the azimuthal intensity profile as plotted in (c). Here θ is the angle with the shear flow and the full line indicates a fit to equation (13).

(This figure is in colour only in the electronic version)

Table 1. Structural micelle characteristics as obtained from fitting of the SANS curve in figure 3.

N_{ag} (nm^{-1})	σ_{core} (nm)	σ_{shell} (nm)	β
26.5	6.4	7.8	3.65

Q values, the scattering curve shows a $I \sim q^{-1}$ dependence, typical for rods. The transition from $I \sim q^{-1}$ to a $I \sim q^{-2}$ dependence that is expected for wormlike micelles is outside the experimental window. This shows that the persistence length of the worms is at least 500 nm, in agreement with previous experiments on the same system (Won *et al* 1999). For this reason the data could be fitted with the form factor of a long cylinder. The details of the fitting procedure are beyond the scope of this paper and will be described elsewhere. The main point is that the cylinders are assumed to have a uniform core and a shell with an exponential density profile, i.e. density $\sim(1-r)\,\mathrm{e}^{(-\alpha r)}$, where $r = \frac{r-\sigma_{\mathrm{core}}}{\sigma_{\mathrm{shell}}}$. From the fitting, the core and shell radii σ_{core} and σ_{shell}, the aggregation number per unit length and the exponent α have been obtained. The numerical values of these parameters are given in table 1. The values for the cylinder cross section is in agreement with that already reported in the literature (Won *et al* 1999).

Figure 3(b) shows a typical scattering pattern of Pb–Peo under shear conditions (with $\dot{\gamma} = 1\ \mathrm{s}^{-1}$), which shows the shear-induced anisotropic structure. This can be more clearly seen in the azimuthal intensity profile, as plotted in figure 3(c), which is obtained from the part of the scattering pattern in figure 3(b) where the scattered intensity is proportional to q^{-1} (the area in between the circles in figure 3(b)). Assuming a Maier–Saupe type of orientation distribution function, the azimuthal scattered intensity $I(Q,\theta)$ from the nematic phase is generally well described by (Picken *et al* 1990)

$$I(Q,\theta) \sim \exp\{\beta P_2(\theta) - 1\}, \qquad (13)$$

where the parameter β describes the width of the intensity profile and P_2 is the second-order Legendre polynomial. The solid line in figure 3(c) shows an example of a fit of the expression in equation (13) with the experimental data as obtained from the scattering pattern in figure 3(b). The scalar order parameter $\langle P_2(\theta)\rangle$ can then be calculated from

$$\langle P_2(\theta)\rangle = \frac{\int_0^{\pi} \exp\{\beta P_2(\theta)\}\, P_2(\theta)\sin(\theta)\,\mathrm{d}\theta}{\int_0^{\pi} \exp\{\beta P_2(\theta)\}\sin(\theta)\,\mathrm{d}\theta}. \qquad (14)$$

In this way, the order parameter $\langle P_2(\theta)\rangle$ can be obtained from scattering data for each shear rate at different concentrations. As expected, flow-induced orientation of the cylindrical micelles is observed.

In Förster *et al* (2005) it is suggested that the shear viscosity is a universal function when plotted against the orientational order parameter, independent of concentration. We indeed find such a behaviour for our Pb–Peo system, as can be seen from figure 4. For the two concentrations of 1 and 2%, the two curves fall on top of each other. Contrary to Förster *et al* (2005), we do not find a linear dependence of the viscosity on the order parameter, probably due to the fact that we also used data at shear rates lower than those where the stress plateau occurs.

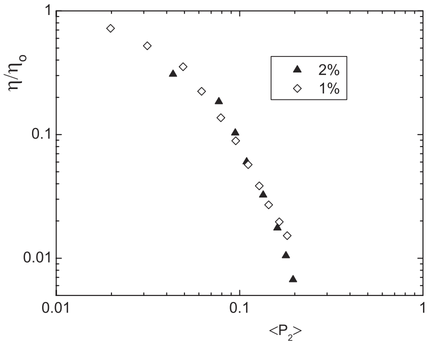

Figure 4. The scaled viscosity η (with η_0 the viscosity at zero shear rate) versus the orientational order parameter $\langle P_2\rangle$.

5.3. Dynamic experiments

Oscillatory shear-rate experiments were performed for concentrations lower and around the I–N equilibrium binodal point, i.e. between 0.5 and 2%. As for steady-state measurements, the order parameter $\langle P_2\rangle$ can be calculated from SANS experiments according to equations (13) and (14) at each point in time during an oscillation. In this way we probe the time dependence of the orientational order parameter $\langle P_2\rangle$. In order to compare and relate the orientational response with the change in the stress the stress response was also recorded and analysed by fast Fourier transform rheology experiments on samples in a somewhat broader concentration range between 0.5 and 2.5%.

In figure 5 we plot the time-dependent response of $\langle P_2\rangle$ ((a) and (b)) and the stress ((c) and (d)) of a 2% sample. In figures 5(a) and (c), the response for different shear amplitudes $\dot\gamma_0$ (see equation (8)) is shown, where the maximum shear rate during an oscillation is kept constant by adjusting the frequency. In figures 5(b) and (d), the response for different frequencies is shown, where again the maximum shear rate during an oscillation is kept constant, but now by adjusting the shear amplitude. The first thing to note is that the order parameter oscillates with twice the frequency of the applied shear rate, even for low shear rates where the stress response is linear in the shear rate. The reason for this is that the scattering experiments probe the flow-vorticity plane, so that the measured order parameter characterizes the orientational order within that plane. As already discussed in section 2, there is no linear response of the order parameter in this plane and the leading response is quadratic in the shear rate. This results in the double-frequency response of the probed projection of orientational order. The experimental trends are in good qualitative agreement with the theoretical calculations based on equations (7) and (1), as can be seen from figure 6, where figure 6(a) should be compared to the experimental results in figure 5(b), and figures 6(b)–5(d). The theoretical curves have the same form as the experimental curves, exhibiting similar trends on changing frequency and shear amplitude. In order to quantify the dynamic response we analyse this response on the basis of the Fourier modes as given in equations (9) and (10) for the stress and (flow-vorticity projected) orientational order parameter $\langle P_2\rangle$, respectively. The experimental phase shifts for the 2% sample are shown in figures 7(a), (c) and (e). The Fourier amplitude ratios that measure the departure from linear response, $|P_2|_4/|P_2|_2$ for $\langle P_2\rangle$ and $|\eta|_3/|\eta|_1$ for the stress, are plotted in figures 7(b), (d) and (f).

As mentioned in the theory section 2, the rate at which a dispersion of rods relaxes close to the spinodal point is determined by the effective diffusion coefficient $D_{\rm eff}$ given by equation (5). There are two unknown parameters in this equation, namely the spinodal concentration, i.e. the concentration where $\frac{L}{d}\phi = 4$, and the rotational diffusion at infinite dilution $D_{\rm r}$. When critical slowing down is at the origin of the difference in dynamic response for various concentrations, we should find scaling when response functions are plotted against effective quantities, like the effective Peclet number in equation (11) and the effective Deborah number in equation (12). In order to test such a scaling for relatively low shear rates, we need to know the concentration where the I–N spinodal in the absence of flow is located. In view of our expression (5) for the effective rotational diffusion coefficient, we will use the following similar form for the effective diffusion coefficient of the Pb–Peo system:

$$D_{\rm r}^{\rm eff} = D_{\rm r}\{1 - [\mathrm{Pb} - \mathrm{Peo}]/C\}, \qquad (15)$$

where, as before, $[\mathrm{Pb} - \mathrm{Peo}]$ is the concentration of $\mathrm{Pb} - \mathrm{Peo}$ and C is a scaling parameter that determines the location of the I–N spinodal. For a given value of the parameter C, the effective Peclet and Deborah numbers are calculated from equations (11) and (12).

As can be seen from figure 9, all experimental data for phase shifts and nonlinear response functions collapse on a single curve when C is taken equal to 3. This is true for both the stress response as well as for the response of the orientational order parameter $\langle P_2\rangle$ (projected on the flow-vorticity plane). This is in accord with the idea that the concentration dependence of the response of both orientational order as well as the stress is related to critical slowing down. Thus, in terms of polymer concentration, the spinodal point is located at $[\mathrm{Pb} - \mathrm{Peo}]_{\rm spin} = 3\%$. The spinodal point is indicated by the open star in figure 2(c). This spinodal concentration seems to be in accord with the somewhat lower binodal concentration of 1.7% in the absence of flow.

The spinodal concentration can be estimated from the length, thickness and volume fraction of the wormlike micelles, neglecting the effect of the flexibility. As discussed before, the structural parameters of the wormlike micelles have been derived from fitting of scattering data (see table 1). In this way we can estimate the location of the I–N spinodal by equating both expressions (5) and (15) for the effective diffusion coefficient. Since $\phi = 2.73 \times [\mathrm{Pb} - \mathrm{Peo}]$, $d = 14.2156$ nm and $L = 1\ \mu$m (L obtained from DLS and microscopy data, to be published) we find that

$$[\mathrm{Pb} - \mathrm{Peo}]_{\rm spin} = \frac{4}{2.73} \times \frac{d}{L} = 2.1\%, \qquad (16)$$

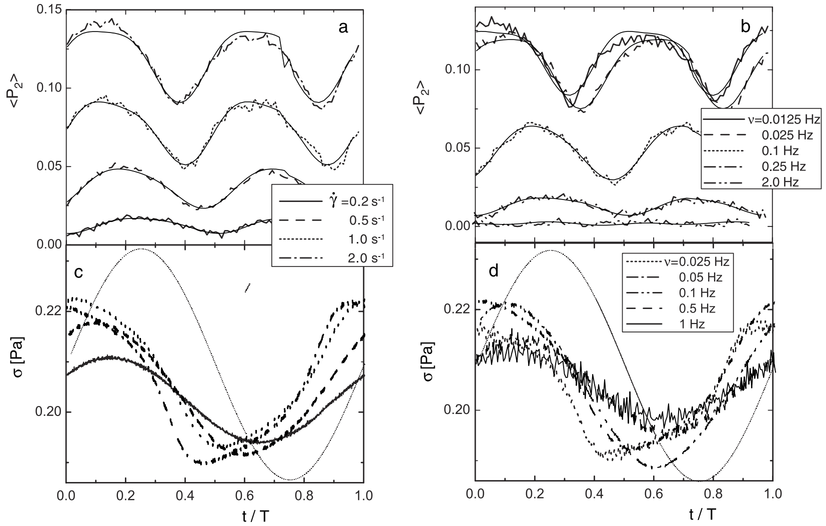

Figure 5. Time-dependent response of the orientational order parameter $\langle P_2 \rangle$ ((a) and (b)) and the stress ((c) and (d)) to an oscillatory shear flow at a shear rate of $\dot{\gamma}_{\max} = 1.0\ \mathrm{s}^{-1}$ ((a) and (c)) and a frequency of 0.05 Hz ((b) and (d)) at a concentration of 2% Pb–Peo. The thin dotted curves indicate the applied shear rate. The time t is scaled with the period T of oscillation.

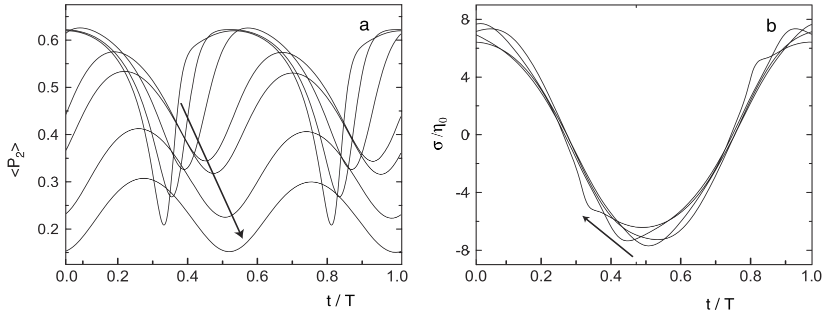

Figure 6. Theoretical predictions for the response of (a) the stress and (b) the order parameter $\langle P_2 \rangle$ for Ω varying from 3 to 60. The arrows indicates increasing Ω. The effective Peclet number is $\mathrm{Pe}_{\mathrm{eff}} = 75$ and the concentration is $\frac{L}{d}\varphi = 3.3$. The time t is scaled with the period T of oscillation.

which, in view of the neglect of flexibility in obtaining this number, is in reasonable agreement with the value obtained from the dynamic experiments.

In order to compare the experimental results with theory, the rotational diffusion at infinite dilution D_{r} needs to be determined. To do so we determine the Deborah number Ω_{eff} for which the limiting values for the phase shifts for $\mathrm{Pe}_{\mathrm{eff}} \rightarrow 0$ as found in the experiments is reproduced. As can be seen in figure 8 there is a reasonable comparison, especially for $\epsilon_2(Pe_{\mathrm{eff}} \rightarrow 0)$, between the theoretical calculation using $\Omega_{\mathrm{eff}} = 24$ and the experimental frequency of 0.05 Hz at a concentration of 2%. Since we know from the scaling that $C = 3$, it follows that $\frac{L}{d}\varphi = 10/3$ for this concentration, and thus, with equation (12), we find that $D_{\mathrm{r}} = 0.04\ \mathrm{s}^{-1}$. This number, together with the dimensionless concentration $\frac{L}{d}\varphi$, was used in the scaling of the frequency and shear rates in figure 9. In this figure, as well as in figure 8, the theoretical validity of the scaling argument is tested by calculating the dynamic response at two different dimensionless concentrations $\frac{L}{d}\varphi = 10/3$ and $5/3$, having the same distance to the spinodal point as the 2% and 1% samples.

The theoretical frequency dependence of phase shifts and nonlinear response functions exhibit the same features as the experimental results, as can be seen from figure 9: the functional form of both is reproduced and the absolute values are in qualitative agreement. Due to the neglect of flexibility, a quantitative agreement is not expected. What is more important, however, is that the functional variation with the effective frequency is the same for both experiment and theory. We can therefore draw the important conclusion that

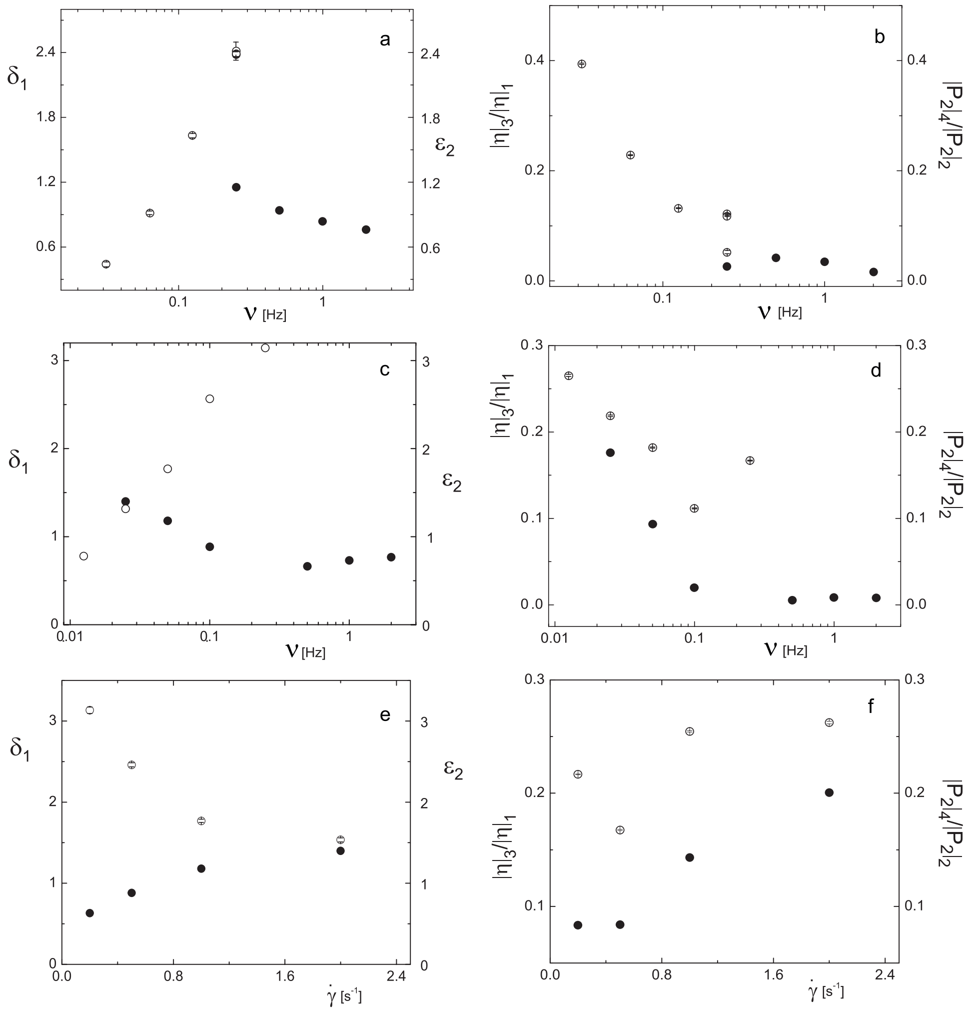

Figure 7. Results of the Fourier analysis using equation (10) for $\langle P_2\rangle(t)$ (open symbols) and equation (9) for the stress (filled symbols) at 1% ((a) and (b)) and 2% ((c)–(f)) Pb–Peo. ((a), (c) and (e)) are plots of the phase shift δ_1 for the stress and ϵ_2 for $\langle P_2\rangle$, while ((b), (d) and (f)) are plots of $|\eta|_3/|\eta|_1$ for the stress and $|P_2|_4/|P_2|_2$ for $\langle P_2\rangle$), which quantities measure the departure from linear response. In ((a)–(d)), the shear rate is fixed to $\dot{\gamma}_{\max} = 4.0\ \mathrm{s}^{-1}$ for 1% Pb–Peo and $\dot{\gamma}_{\max} = 1.0\ \mathrm{s}^{-1}$ for 2% Pb–Peo. In ((e) and (f)) the frequency is fixed to $\nu = 0.05$ Hz.

the scaling with equation (15) in the experiments is justified. In other words, the flow response of the Pb–Peo system scales with the distance from the spinodal point.

The correspondence between theory and experiment is especially satisfactory for the frequency dependence of the phase shift in $\langle P_2\rangle$, ϵ_2 in figure 9(c) and the nonlinearity in the stress, given by $|\eta|_3/|\eta|_1$ in figure 9(b). This correspondence confirms the choice of $D_r = 0.04\ \mathrm{s}^{-1}$. The experimental phase shift δ_1 in the stress, given in figure 9(a), however, shows a more pronounced frequency dependence as predicted by theory. Concerning the phase shifts, it is interesting to note that, at low frequencies, $\langle P_2\rangle$ is in phase with the applied shear field $\dot{\gamma} \propto \frac{\mathrm{d}\gamma}{\mathrm{d}t} \propto \cos(\omega t)$ and $\epsilon_2 = 0$, while at high frequencies $\epsilon_2 \to \pi$. For the stress we observe that at low frequencies $\delta_1 = \pi/2$, corresponding to fluid-like behaviour, while δ_1 decreases with increasing frequency, but never reaches 0, which value corresponds to solid-like behaviour. The variation of ϵ_2 is twice that of δ_1 due to the fact that $\langle P_2\rangle(t) \sim \dot{\gamma}^2$, as discussed before.

The frequency dependence of the nonlinear response functions show that with increasing frequency the system becomes more linear (at the cost of an increasing phase shift). The linear response regime therefore extends up to larger shear rates when the frequency increases. The reason for this is that, at high frequencies, microstructural order is not able any more to fully respond to the external field.

There is a considerable discrepancy between the value of the orientational diffusion coefficient D_r at infinite dilution that one would calculate for the length and thickness of the worms from well-known expressions for stiff rods (Tirado *et al* 1980) and the value found in our experiments. It is unclear

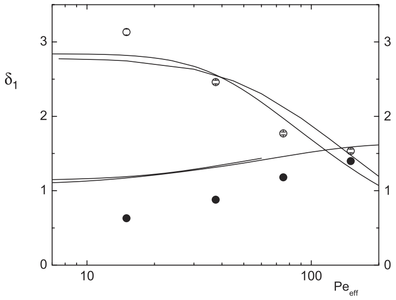

Figure 8. Shear rate dependence of the phase shifts δ_1 and ϵ_2 for the theoretically calculated response of the stress (bottom curves) and the orientational order parameter $\langle P_2 \rangle$ (top curves), respectively, at a scaled volume fraction of $\frac{L}{d}\phi = 10/3$ (solid line) and $\frac{L}{d}\varphi = 5/3$ (dashed line). The effective Deborah number is $\Omega = 24_{\mathrm{eff}}$. The symbols give the experimental response for the stress (solid) and $\langle P_2 \rangle$ (open) at 2% Pb–Peo, scaled with the orientational diffusion coefficient at infinite dilution with a value of $D_{\mathrm{r}} = 0.04\ \mathrm{s}^{-1}$ and $C = 3$.

whether this is the result of the flexibility of the rods. Another source for this discrepancy might be that the theory neglects dynamical correlations. In the derivation of equations (1) and (7), the rod–rod pair-correlation function is taken equal to the Boltzmann exponential of the pair-interaction potential. This is asymptotically exact for very long and thin hard rods for the calculation of thermodynamic quantities of rod suspensions. For dynamical processes (with or without shear flow), however, such an approximation for the pair correlation is approximate, and particularly neglects dynamical correlations. Simulations have shown that such correlations are of importance, at least for fast dynamical processes (Tao *et al* 2006). The simulations show that critical slowing down is enhanced by dynamical correlations. This might explain the above-mentioned discrepancy between theory and experiment. This is a subject for future investigations.

6. Conclusion

The aim of this paper is to find the microscopic mechanism of the strong shear-thinning behaviour of giant wormlike micelles consisting of Pb–Peo block copolymers. The dynamics of the stress is probed by dynamic shear experiments in the linear and nonlinear regimes using Fourier transfer rheology. The dynamics of the orientational order parameter under oscillatory flow is studied with a newly developed time-resolved neutron scattering set-up. It is shown that critical slowing down of orientational Brownian motion due to the vicinity of the isotropic–nematic spinodal is responsible for the shear-thinning behaviour. The response functions for different concentrations are indeed identical when plotted against an effective Deborah number that accounts for critical slowing down. In a certain shear-rate range, shear thinning is so strong that gradient shear banding occurs, where flow profiles have been measured with heterodyne light scattering. The location of the binodal in the shear rate versus concentration plane is determined by step-down rheology, and the spinodal concentration in the absence of flow is obtained from the scaling behaviour of response functions. Both the measured

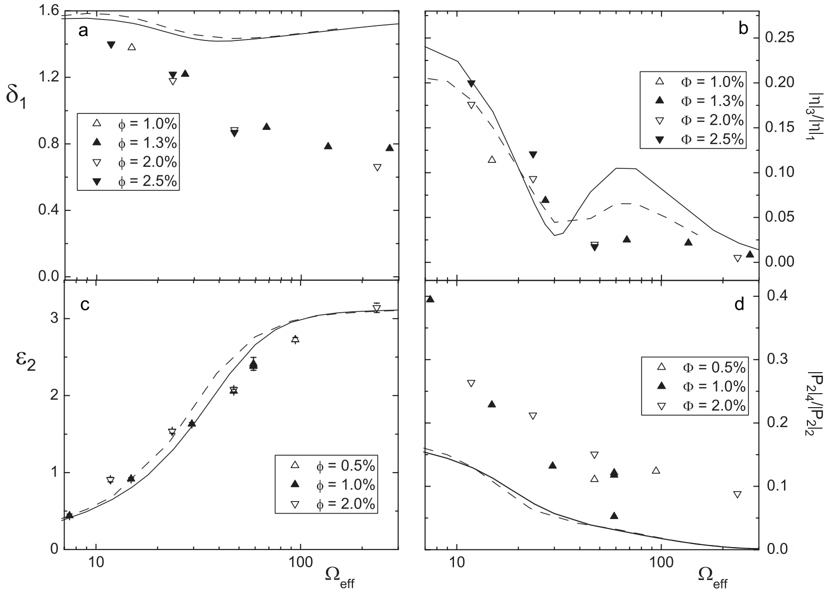

Figure 9. The phase shifts ((a) and (c)) and nonlinearity ((b) and (d)) for the stress ((a) and (b)) and $\langle P_2 \rangle$ ((c) and (d)) versus the Deborah number. The symbols indicate the experiments for different concentrations. The solid lines give the theoretical responses for $\frac{L}{d}\varphi = 10/3$ and the dashed line for $\frac{L}{d}\varphi = 5/3$. For the scaling of the experimental frequency we used a value for the orientational diffusion coefficient at infinite dilution of $D_{\mathrm{r}} = 0.04\ \mathrm{s}^{-1}$ and $C = 3$ was used, see equation (15). $\mathrm{Pe}_{\mathrm{eff}} = 250$ for all data.

linear and nonlinear stress response and order parameter response are in qualitative agreement with a theory for stiff rods that includes critical slowing down on approach of the isotropic–nematic spinodal. The comparison with theory, however, is qualitative since the theory neglects flexibility. Another possible reason for deviations between theory and experiments might be that the theory neglects dynamical correlations, which have been shown by simulations to enhance critical slowing down. In surfactant wormlike micellar systems, shear thinning can also be due to breaking and stress-induced merging of worms. The breaking and merging of worms can give rise to strong shear thinning by itself, and can give rise to shear banding in the absence of critical slowing down, far away from the spinodal. Scission and stress-induced merging probably do not play a role in the Pb–Peo block copolymer system that we studied here.

Acknowledgments

We acknowledge the Transregio Sonderforschungsbereich TR6018 ‘Physics of Colloidal Dispersions in External Fields’ for financial support. We are grateful to Jörg Stellbrink, Peter Lang and Aggeliki Tsigkri for information on the particle characteristics.

References

Allgaier J, Poppe A, Willner L and Richter D 1997 *Macromolecules* **30** 1582

Berret J-F 2004 *Molecular Gels* (Amsterdam: Elsevier) chapter (Rheophysics of Wormlike Micelles)

Briels W J, Mulder P and den Otter W K 2004 *J. Phys.: Condens. Matter* **16** S3965–74

Cates M E and Candau S J 1990 *J. Phys.: Condens. Matter* **2** 6869

Chen Z Y 1993 *Macromolecules* **26** 3419

Denkova A G, Mendes E and Coppens M-O 2008 *J. Phys. Chem.* B **112** 793

Dhont J K G and Briels W J 2003a *Colloid Surface* A **213** 131

Dhont J K G and Briels W J 2003b *J. Chem. Phys.* **118** 1466

Dhont J K G and Briels W J 2008 *Rheol. Acta.* **47** 257

Doi M and Edwards S F 1986 *The Theory of Polymer Dynamics* (Oxford: Clarendon)

Förster S, Konrad M and Lindner P 2005 *Phys. Rev. Lett.* **94** 017803

Keiderling U 2002 *Appl. Phys.* A **74** S1455

Kohlbrecher J and Wagner W 2000 *J. Appl. Cryst.* **33** 804

Lettinga M P and Dhont J K G 2004 *J. Phys.: Condens. Matter* **16** S3929

Lund R, Willner L, Richter D and Dormidontova E E 2006 *Macromolecules* **39** 4566

Manneville S 2008 *Rheol. Acta* **47** 301–18

Olmsted P D 2008 *Rheol. Acta.* **47** 283

Picken S J, Aerts J, Visser R and Northolt M G 1990 *Macromolecules* **23** 3849

Salmon J-B, Colin A and Manneville S 2003 *Phys. Rev. Lett.* **90** 228303

Tao Y-G, Dhont J K G and Briels W J 2006 *J. Chem. Phys.* **124** 134906

Tirado M, Martinez C and Delatorre J G 1980 *J. Chem. Phys.* **73** 1986

Wilhelm M, Maring D and Spiess H 1998 *Rheol. Acta.* **37** 399

Won Y-Y, Davis H T and Bates F S 1999 *Science* **283** 960

Chapter 16

Superposition rheology of shear-banding worm-like micelles

Superposition rheology of shear-banding wormlike micelles

Pierre Ballesta

*Centre de Recherche Paul Pascal, CNRS UPR 8631, Avenue Schweitzer,
F-33600 Pessac, France*

M. Paul Lettinga

Forschungszentrum Jülich, IFF, Weiche Materie, D-52425 Jülich, Germany

Sébastien Manneville[a]

*Centre de Recherche Paul Pascal, CNRS UPR 8631, Avenue Schweitzer,
F-33600 Pessac, France*

(Received 13 February 2007; final revision received 29 May 2007)

Synopsis

Wormlike micelle solutions are submitted to small-amplitude oscillatory shear superimposed to steady shear in the shear banding regime. By imposing a shear oscillation, the interface between high- and low-shear regions oscillates in time. A two-fluid semiphenomenological model is proposed for superposition rheology in the shear banding regime, which allows us to extract a characteristic velocity for the interface dynamics from experiments involving only a standard rheometer. Estimates of the stress diffusion coefficient $\mathcal{D}$ can also be inferred from such superposition experiments. The validity of our model is confirmed by directly recording the interface displacement using ultrasonic velocimetry. © *2007 The Society of Rheology.*
[DOI: 10.1122/1.2750665]

I. INTRODUCTION

During the last decade, wormlike micelle solutions have become a model system to study the so-called "shear banding" phenomenon. Depending on the concentration, most of these surfactant systems constituted of long, cylindrical, semiflexible aggregates undergo a shear-induced transition from a state of entangled, weakly oriented micelles to a state of highly aligned micelles above some critical shear rate $\dot{\gamma}_I$. Such a transition is strongly shear thinning since the viscosity of the aligned state can be orders of magnitude smaller than the zero-shear viscosity of the system. Under simple shear and above $\dot{\gamma}_I$, the system spatially separates into coexisting bands of high and low viscosities corresponding, respectively, to the entangled and aligned states. As the shear rate is increased above $\dot{\gamma}_I$, the shear-induced structure progressively expands in the sample along the velocity

---

[a] Present address: Laboratoire de Physique, CNRS UMR5672, ENS Lyon, 46 allée d'Italie, 69364 Lyon Cedex 07, France; electronic mail: sebastien.manneville@ens-lyon.fr

J. Rheol. 51(5), 1047-1072 September/October (2007) 0148-6055/2007/51(5)/1047/26/$27.00

gradient direction until the system is fully aligned at some shear rate $\dot{\gamma}_N$ (in this work I and N, respectively, stand for isotropic and nematic in reference to the isotropic-to-nematic transition although the precise structure of the shear bands is still unclear). The rheological signature of shear banding is the existence of a horizontal plateau at a constant shear stress $\sigma=\sigma_c$ in the shear stress versus shear rate constitutive curve $\sigma(\dot{\gamma})$, which extends from $\dot{\gamma}_I$ to $\dot{\gamma}_N$. The present paper is restricted to the shear banding scenario described above and referred to as "gradient banding" in the literature. Another situation known as "vorticity banding" may also occur in wormlike micelles, where the system separates into bands bearing different stresses stacked along the vorticity direction, corresponding to a vertical portion in the flow curve, i.e., to a shear-thickening transition. A recent review of the specific rheological properties of wormlike micelles is available in Berret (2005).

The first experimental evidence for a stress plateau in nonlinear rheological measurements was provided by Rehage and Hoffmann (1991) on the CPCl-NaSal system. Further research effort established the generality of this peculiar feature on other wormlike micelle systems [Berret and co-workers (1994, 1997); Soltero and co-workers (1999)]. Theoretically, shear banding was first interpreted in the framework of nonequilibrium phase transitions in liquid crystals [Cates and Milner (1989); Olmsted and Goldbart (1990, 1992)]. Specific features of the wormlike micelles such as polymerlike behavior and reversible breakage were then included by Spenley and co-workers (1993) in connection with the nonlinear rheology of conventional polymers [Cates and co-workers (1993)]. These two different approaches led to a theoretical debate about nonmonotonic constitutive equations and shear banding seen either as a mechanical instability or as a nonequilibrium phase transition [Schmitt and co-workers (1995, 1996); Olmsted and Lu (1997); Porte and co-workers (1997)]. Theoretical and numerical works later focused on including stress diffusion to account for a unique stress selection and for the band dynamics [Dhont (1999); Yuan (1999); Olmsted and co-workers (2000)] and on studying the effects of flow-concentration coupling [Fielding and Olmsted (2003a)] or the possible instabilities inherent to the models [Fielding (2005)].

From the experimental point of view, phase separation under shear was ascertained for the first time by flow birefringence which showed the coexistence of bands of weakly oriented and highly anisotropic material in sheared CTAB solutions close to an isotropic-to-nematic equilibrium transition [Cappelaere and co-workers (1995); Makhloufi and co-workers (1995)]. Early nuclear magnetic resonance measurements confirmed the existence of inhomogeneous flows and the presence of differently sheared regions characterized by different order parameters [Mair and Callaghan (1996); Britton and Callaghan (1997); Mair and Callaghan (1997)] but it is not until recently that the simple shear banding scenario described above received full experimental validation from light scattering and particle tracking velocimetry in the CPCl-NaSal system [Salmon and co-workers (2003); Méndez-Sánchez and co-workers (2003); Hu and Lips (2005)]. In particular the so-called "lever rule" which, in strong analogy with first-order equilibrium phase transitions, gives the proportion α of the aligned state as a function of the shear rate $\dot{\gamma}$ along the stress plateau

$$\dot{\gamma}=(1-\alpha)\dot{\gamma}_I+\alpha\dot{\gamma}_N, \tag{1}$$

appears as a rather robust feature provided that steady state is reached [Salmon and co-workers (2003); Lerouge and co-workers (2004)].

Thus, although the exact nature of shear bands is still under debate, the coexistence of differently sheared bands is now well established [López-González and co-workers (2006)]. Most of latest work on shear banding has concentrated on the local flow dynamics during transients [Lerouge and co-workers (2004); Hu and Lips (2005)], on velocity and birefringence fluctuations and departures from the steady scenario described above [Holmes and co-workers (2003); Becu and co-workers (2004); López-González and co-workers (2004); Lee and co-workers (2005); Yesilata and co-workers (2006)], on interface stability [Lerouge and co-workers (2006)], and on modeling such spatiotemporal dynamics [Radulescu and co-workers (2003); Fielding and Olmsted (2003b, 2004, 2006)].

In this paper we propose to use the parallel superposition technique introduced by Booij (1966a) to investigate shear banding in wormlike micelles and more precisely to access the dynamics of the interface between shear bands. In our opinion, the interest of superposition rheology has been overlooked in the literature. In particular, only a very limited number of papers are devoted to superposition measurements in complex fluids that show strong flow-microstructure coupling, e.g., associative polymers [Tirtaatmadja and co-workers (1997)] or liquid crystalline polymers [Grizzuti and Maffettone (2003)]. Our aim is to show how this technique, which is available on most rheometers, can be used to access the dynamical behavior of shear bands, without having to rely on involved techniques as described above. We first recall the principle of superposition rheology and illustrate it in the case of wormlike micelles sheared below $\dot{\gamma}_I$, i.e., in the homogeneous, entangled state. Then a two-fluid semi-phenomenological model is described for superposition rheology in the shear banding regime in the simple case of infinite parallel plates. This model is extended to account for experimental geometries, namely cone-and-plate, Couette, and Mooney–Couette geometries. The corresponding calculations are gathered in the appendix. Finally, our model is probed experimentally on the well-studied wormlike micellar system CPCl-NaSal through superposition rheology and compared to direct measurements of the interface dynamics using ultrasonic velocimetry in Couette geometry. The results are further discussed and interpreted in terms of the stress diffusion coefficient $\mathcal{D}$, a key parameter in recent theoretical approaches of shear banding.

II. ONE-FLUID SUPERPOSITION RHEOLOGY

Superposition rheology as first introduced by Booij (1966a) is the addition of a small-amplitude oscillatory shear to a main steady shear. The oscillatory shear can be either parallel or perpendicular to the steady shear. Superposition allows one to probe the dynamical response of a shear-driven system and to generalize the notions of viscoelastic moduli to far-from-equilibrium conditions through a perturbation analysis. The properties of the "superposition moduli" and the relationships between "parallel moduli" and "orthogonal moduli" were discussed by Vermant and co-workers (1998) and Dhont and Wagner (2001) and applied to polymer solutions and colloidal suspensions, respectively. Here we focus on parallel superposition which is now available as an option on most recent commercial rheometers.

A. Notations for one-fluid superposition rheology

Let us first introduce the various notations for superposition rheology. In the following we shall use complex notations and assume that the shear rate reads

$$\dot{\gamma} = \dot{\gamma}_1 + \dot{\gamma}_2 e^{i\omega t}. \tag{2}$$

Both $\dot{\gamma}_1$ and $\dot{\gamma}_2$ are taken to be real and positive. If $\dot{\gamma}_2$ corresponds to a perturbation to the steady shear in the linear regime, the shear stress can be written as

$$\sigma = \sigma_1 + \sigma_2 e^{i\omega t}, \tag{3}$$

where σ_1 is real and σ_2 is the complex amplitude of the oscillatory part of the shear stress. The issue of specifying which variable is controlled and which is measured will be addressed below and further discussed in Sec. II B. From Eqs. (2) and (3), two apparent viscosities are defined as

$$\eta = \frac{\sigma_1}{\dot{\gamma}_1}, \tag{4}$$

$$\eta_{\parallel}^{*} = \frac{\sigma_2}{\dot{\gamma}_2}. \tag{5}$$

Since the oscillatory part of the shear is only a linear perturbation of the steady component, η depends only on $\dot{\gamma}_1$ and reduces to the standard shear viscosity found when $\dot{\gamma}_2 = 0$. On the other hand, the complex viscosity $\eta_{\parallel}^{*}$ depends on both $\dot{\gamma}_1$ and ω and allows one to explore the dynamical behavior of the shear-driven system.

When both $\dot{\gamma}_1$ and $\dot{\gamma}_2$ tend to zero, one should recover the usual complex viscosity $\eta^{*}(\omega)$ so that

$$\lim_{\dot{\gamma}_1 \to 0} \eta_{\parallel}^{*}(\omega, \dot{\gamma}_1) = \eta^{*}(\omega). \tag{6}$$

Another useful limit is found by considering vanishing frequencies for a finite $\dot{\gamma}_1$. In that case, $\dot{\gamma}_2$ and σ_2 become steady perturbations so that Eq. (5) reduces to $\eta_{\parallel}^{*} = \mathrm{d}\sigma_1 / \mathrm{d}\dot{\gamma}_1$, which leads to

$$\lim_{\omega \to 0} \eta_{\parallel}^{*}(\omega, \dot{\gamma}_1) = \eta(\dot{\gamma}_1) + \dot{\gamma}_1 \frac{\mathrm{d}\eta}{\mathrm{d}\dot{\gamma}_1}(\dot{\gamma}_1). \tag{7}$$

B. Conventional rheology of wormlike micelles in the low-shear regime

As already reported many times in the literature, semidilute solutions of wormlike micelles present an almost perfect Maxwellian behaviour in the linear regime [Rehage and Hoffmann (1988)]. Such a striking feature was predicted and explained in terms of a reaction-diffusion model by Cates (1987). However, at high frequencies, significant deviations from the Maxwell model may occur due to fast relaxation modes [Fischer and Rehage (1997); Yesilata and co-workers (2006)]. Thus a more thorough description of the low-shear rheology of polymer-like micelles is provided by the Oldroyd-B model [Oldroyd (1953, 1955)] whose linear complex viscosity $\eta^{*}(\omega)$ and nonlinear shear viscosity $\eta(\dot{\gamma})$ read

$$\eta^{*}(\omega) = \eta_0 \frac{1 + i\omega\tau_2}{1 + i\omega\tau_1}, \tag{8}$$

$$\eta(\dot{\gamma}) = \eta_0 \frac{1 + (s_2\dot{\gamma})^2}{1 + (s_1\dot{\gamma})^2}, \tag{9}$$

where τ_1, τ_2, s_1, and s_2 are characteristic times.

In the following, we focus on a wormlike micelle solution made of cetylpyridinium chloride (CPCl, from Aldrich) and sodium salicylate (NaSal, from Acros Organics) dissolved in brine (0.5 M NaCl) with a fixed concentration ratio [NaSal]/[CPCl]=0.5 and a

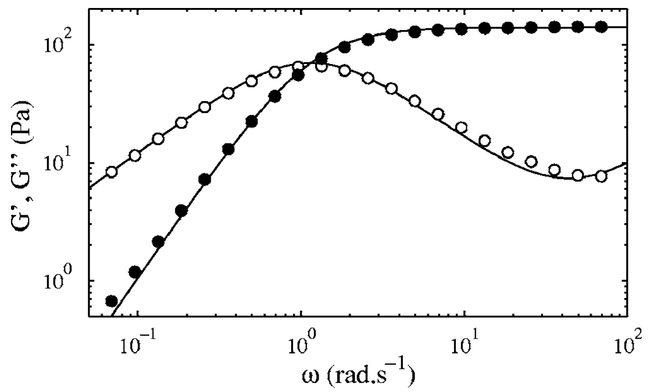

FIG. 1. Linear rheology of an 8% wt CPCl-NaSal solution: storage modulus G' (•) and loss modulus G'' (◦) vs frequency ω. The solid lines correspond to an Oldroyd-B fluid [Eq. (8)] with $\eta_0 = 122$ Pa s, $\tau_1 = 0.87$ s, and $\tau_2 = 0.60$ ms.

total surfactant concentration of 8% wt (unless stated differently) as described by Rehage and Hoffmann (1988); Berret and co-workers (1997). The working temperature is $T = 21$ °C. Figure 1 shows the linear viscoelastic moduli of our micellar solution measured in the Mooney–Couette geometry described below (see Sec. IV A) with a standard stress-controlled rheometer (AR1000, TA Instruments). All the experiments in the present work were performed under controlled shear stress. Both G' and G'' are very well described by the Oldroyd-B model [Eq. (8) with $G' + iG'' = i\omega\eta^*$] which captures the departure of G'' from the ω^{-1}scaling at high frequencies.

The constitutive curve σ vs $\dot{\gamma}$ of the same micellar solution is shown in Fig. 2. As expected the fluid is weakly shear thinning below $\dot{\gamma}_I \simeq 2.2$ s^{-1}. Above $\dot{\gamma}_I$ very strong shear thinning is observed and the stress saturates at a plateau value $\sigma_c \simeq 100$ Pa. This corresponds to the shear banding transition. The solid line in Fig. 2 shows that the nonlinear rheological behavior of our fluid in the low-shear regime is rather well captured by the Oldroyd-B model [Eq. (9)].

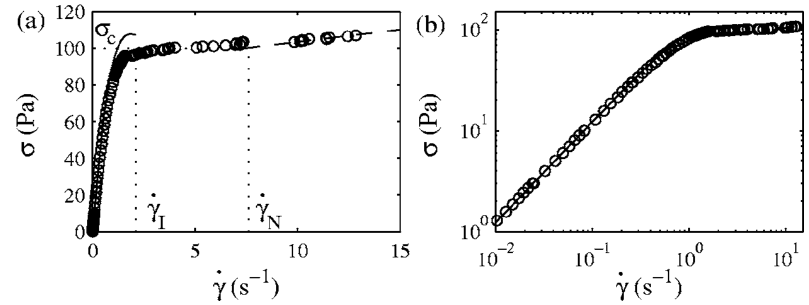

FIG. 2. Nonlinear rheology of an 8% wt CPCl-NaSal solution: shear stress σ vs shear rate $\dot{\gamma}$ (a) in linear scales and (b) in logarithmic scales (right). The solid line corresponds to an Oldroyd-B fluid [Eq. (9)] with $\eta_0 = 122$ Pa s, $s_1 = 0.59$ s, and $s_2 = 0.13$ s. The dashed line is the best fit of the high-shear branch by a Bingham fluid $\sigma = \sigma_B + \eta_B \dot{\gamma}$ with $\sigma_B = 91.7$ Pa and $\eta_B = 1.13$ Pa s. The shear banding regime extends from $\dot{\gamma}_I \simeq 2.2 \pm 0.2$ s^{-1} to $\dot{\gamma}_N \simeq 7.4 \pm 0.4$ s^{-1}.

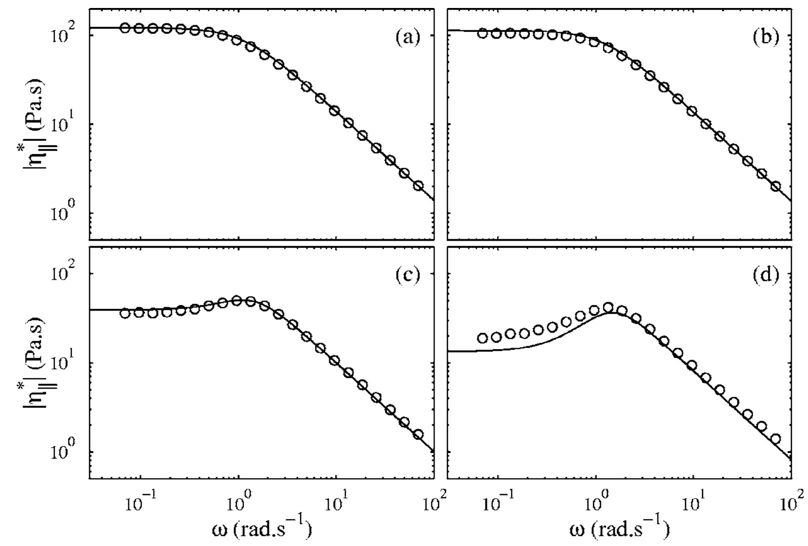

FIG. 3. Superposition rheology of an 8% wt CPCl-NaSal solution in the low-shear regime: $|\eta^*_{\|}(\omega,\dot{\gamma}_1)|$ vs ω for (a) $\dot{\gamma}_1=0$, (b) 0.025, (c) 1.09, and (d) 1.49 s^{-1}. The solid lines correspond to an Oldroyd-B fluid [Eq. (10)] with $\eta_0=122$ Pa s, $s_1=0.59$ s, $s_2=0.13$ s, $\tau_1=0.87$ s, and $\tau_2=0.60$ ms.

C. Superposition rheology of wormlike micelles in the low-shear regime

The superposition rheology of an Oldroyd-B fluid was computed by Booij (1966b) and leads to

$$\frac{\eta^*_{\|}(\omega,\dot{\gamma}_1)}{\eta_0}=\frac{1-\tau_1\tau_2\omega^2(1+s_1^2\dot{\gamma}_1^2)+(3s_2^2-s_1^2+s_1^2s_2^2\dot{\gamma}_1^2)\dot{\gamma}_1^2+i\omega[\tau_1+\tau_2+(\tau_1 s_2^2+\tau_2 s_1^2)\dot{\gamma}_1^2]}{(1+s_1^2\dot{\gamma}_1^2)[(1+i\omega\tau_1)^2+s_1^2\dot{\gamma}_1^2]}. \tag{10}$$

It is easily checked that Eqs. (6) and (7) are recovered from Eq. (10) when the limits $\dot{\gamma}_1\to 0$ and $\omega\to 0$ are considered.

Figure 3 presents superposition measurements in the low-shear regime. The steady-state shear rates $\dot{\gamma}_1$ indicated in the caption of Fig. 3 (and later Figs. 4, 6, and 13) are the values measured by the rheometer. In all our experiments, the amplitude of the oscillatory

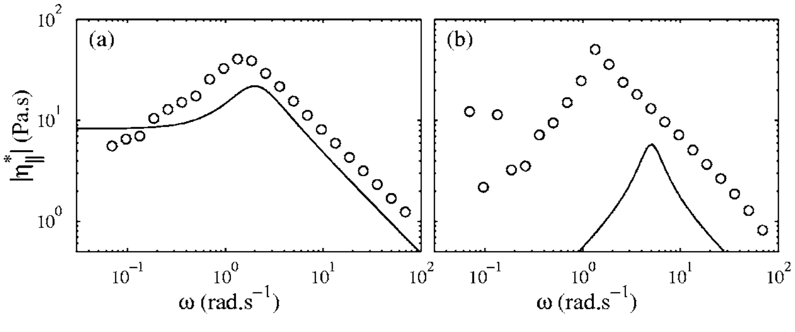

FIG. 4. Superposition rheology of an 8% wt CPCl-NaSal solution in the shear banding regime: $|\eta^*_{\|}(\omega,\dot{\gamma}_1)|$ vs ω for (a) $\dot{\gamma}_1=2.5$ and (b) 7.14 s^{-1}. The solid lines correspond to an Oldroyd-B fluid [Eq. (10)] with $\eta_0=122$ Pa, $s_1=0.59$ s, $s_2=0.13$ s, $\tau_1=0.87$ s, and $\tau_2=0.60$ ms.

part of the shear stress is fixed to $\sigma_2 = 0.5$ Pa, except for Sec. IV B where $\sigma_2 = 1$ Pa. Figure 3 clearly shows that the five parameters inferred from Figs. 1 and 2 yield a good description of $\eta^*_{\parallel}(\omega, \dot{\gamma}_1)$ for all $\dot{\gamma}_1 \lesssim 1.5$ s^{-1} when used in Eq. (10).

III. TWO-FLUID SUPERPOSITION RHEOLOGY: THEORETICAL PREDICTIONS

The above results obtained in the low-shear regime prompt us to use the superposition technique in the shear banding regime. Indeed the CPCl-NaSal system is known to separate into weakly and highly sheared bands as described in the introduction [Berret and co-workers (1997); Porte and co-workers (1997)]. Previous work has shown that the shear banding phenomenon is rather simple in this particular system: the proportion of shear-induced structure is given by the lever rule (1) and no wall slip is detected [Salmon and co-workers (2003); Hu and Lips (2005)]. In the case of our 8% wt CPCl-NaSal solution, the shear banding transition occurs for $\dot{\gamma} > \dot{\gamma}_I \simeq 2.2$ s^{-1} and $\sigma = \sigma_c \simeq 100$ Pa. The value for the critical shear stress is in good agreement with the prediction $\sigma_c = 0.67 G_0$, with $G_0 = \eta_0 / \tau_1$ the plateau modulus [Spenley and co-workers (1993)]. Note, however, that the stress plateau is not perfectly flat at σ_c in Fig. 2. This is most probably due to the curvature of the Mooney–Couette geometry which induces a significant slope of the constitutive curve in the shear banding regime [Radulescu and Olmsted (2000); Salmon and co-workers (2003)]. Such a slope may also arise from flow-concentration coupling [Schmitt and co-workers (1995); Olmsted and Lu (1997); Fielding and Olmsted (2003a)]. However, in the absence of clear experimental evidence for such a mechanism in the literature on the system under study, we shall not refer to concentration coupling effects thereafter. In any case, the slope in the flow curve makes it hard to distinguish between the "stress plateau" and the homogeneous high-shear regime where the system is fully aligned (see also Appendix Sec. B).

Figure 4 shows that the Oldroyd-B model used in the low-shear regime completely fails in describing the complex viscosity $\eta^*_{\parallel}(\omega, \dot{\gamma}_1)$ when $\dot{\gamma}_1 > \dot{\gamma}_I$. This is a strong indication that the system enters the shear banding regime and that the model for superposition needs to be modified. In the following, we discuss a two-fluid model for superposition rheology in the presence of shear banding. This simple model is presented for various geometries, from the most simple geometry (infinite parallel plates) to the more complicated one actually used in our experiments (Mooney–Couette geometry). The detailed calculations for experimental geometries are presented in the Appendix.

A. Infinite parallel plates

Let us first consider the case of two unbounded parallel plates in translation separated by a gap e. We assume that the fluid separates into bands of "isotropic" (I) and "nematic" (N) material. In a superposition experiment in the shear banding regime, the steady component of the shear stress is fixed to $\sigma_1 = \sigma_c$ and the steady component of the shear rate in the isotropic (respectively, nematic) material is simply $\dot{\gamma}_{I1} = \dot{\gamma}_I$ (respectively, $\dot{\gamma}_{N1} = \dot{\gamma}_N$), where $\dot{\gamma}_I$ and $\dot{\gamma}_N$ are the limits of the stress plateau. This leads us to generalize the notations introduced in Sec. II A to the two-fluid case

$$\sigma(t) = \sigma_c + \sigma_2 e^{i\omega t}, \tag{11}$$

$$\dot{\gamma}(t) = \dot{\gamma}_1 + \dot{\gamma}_2 e^{i\omega t}, \tag{12}$$

$$\dot{\gamma}_I(t) = \dot{\gamma}_I + \dot{\gamma}_{I2} e^{i\omega t}, \tag{13}$$

$$\dot{\gamma}_N(t) = \dot{\gamma}_N + \dot{\gamma}_{N2}e^{i\omega t}, \tag{14}$$

$$\eta_I = \frac{\sigma_c}{\dot{\gamma}_I} \quad \text{and} \quad \eta^*_{\|I} = \frac{\sigma_2}{\dot{\gamma}_{I2}}, \tag{15}$$

$$\eta_N = \frac{\sigma_c}{\dot{\gamma}_N} \quad \text{and} \quad \eta^*_{\|N} = \frac{\sigma_2}{\dot{\gamma}_{N2}}. \tag{16}$$

Since the steady shear in each phase is fixed to $\dot{\gamma}_I$ and $\dot{\gamma}_N$, respectively, η_I and η_N are two constants and $\eta^*_{\|I}$ and $\eta^*_{\|N}$ depend only on ω. In other words η_I and η_N are the apparent viscosities of the isotropic and nematic materials under a steady shear stress $\sigma_1 = \sigma_c$, while $\eta^*_{\|I}$ and $\eta^*_{\|N}$ correspond to the dynamical behaviors of the two phases for $\sigma_1 = \sigma_c$.

In the absence of wall slip, the lever rule (1) is a mere consequence of the continuity of the velocity at the interfaces between bands [Salmon and co-workers (2003)] and the proportion of shear-induced structure $\alpha(t)$ obeys

$$\alpha(t) = \alpha_1 + \alpha_2 e^{i\omega t}, \tag{17}$$

$$\dot{\gamma}(t) = (1 - \alpha(t))\,\dot{\gamma}_I(t) + \alpha(t)\,\dot{\gamma}_N(t), \tag{18}$$

$$\dot{\gamma}_1 = (1 - \alpha_1)\,\dot{\gamma}_I + \alpha_1\,\dot{\gamma}_N. \tag{19}$$

Note that the fact that the "instantaneous" lever rule (18) applies at all times actually results from a steady-state approximation of the Navier–Stokes equations, i.e., from assuming that $\rho\partial_t v \ll \partial_z \sigma$. This assumption will be checked below *a posteriori*. Moreover, Eq. (19) leads to the lever rule for the apparent viscosity

$$\frac{1}{\eta} = \frac{\dot{\gamma}_1}{\sigma_c} = \frac{1 - \alpha_1}{\eta_I} + \frac{\alpha_1}{\eta_N}. \tag{20}$$

Using the above notations and restricting the analysis to linear response, it is easily shown that

$$\dot{\gamma}_2 = (1 - \alpha_1)\frac{\sigma_2}{\eta^*_{\|I}} + \alpha_1\frac{\sigma_2}{\eta^*_{\|N}} + \alpha_2\sigma_c\left(\frac{1}{\eta_N} - \frac{1}{\eta_I}\right). \tag{21}$$

In order to get an expression for $\eta^*_{\|} = \sigma_2/\dot{\gamma}_2$ in the shear banding regime, we need to link α_2 and σ_2. We chose to use the reaction-diffusion model proposed by Radulescu and co-workers (1999) that assumes the existence of a single band and shows that the interface between the isotropic and nematic regions moves at a velocity c that only depends on the difference $\sigma(r_c) - \sigma_c$, where r_c is the position of the band, and vanishes for $\sigma(r_c) = \sigma_c$. More precisely, if one assumes the shear-induced structure to be located from $r = 0$ to $r = r_c(t) = \alpha(t)e$, with r being the coordinate across the gap, the model predicts

$$\frac{d\alpha}{dt} = \frac{\sigma(r) - \sigma_c}{e}\left.\frac{dc}{d\sigma}\right|_{\sigma_c} = \frac{\sigma(r) - \sigma_c}{\sigma_c}\frac{c_0}{e} = \frac{\sigma_2 e^{i\omega t}}{\sigma_c}\frac{c_0}{e}, \tag{22}$$

where we have introduced the characteristic velocity c_0 defined by $c_0/\sigma_c = dc/d\sigma|_{\sigma_c}$. Equation (17) then leads to

$$\alpha_2 = \frac{\sigma_2}{\sigma_c}\frac{c_0}{i\omega e}. \tag{23}$$

Experimentally the amplitude $\alpha_2 e$ of the oscillations of the interface position $r_c(t)$ should be accessible through the time-resolved velocimetry techniques mentioned in the introduction provided that the spatial resolution is fine enough. An estimate of c_0 from direct measurements of α_2 using ultrasonic velocimetry will be presented in Sec. IV B. Finally, inserting Eq. (23) into Eq. (21) and using the definition (5) yields

$$\frac{1}{\eta_{\parallel}^{*}} = \frac{1-\alpha_1}{\eta_{\parallel I}^{*}} + \frac{\alpha_1}{\eta_{\parallel N}^{*}} + \frac{\dot{\gamma}_N - \dot{\gamma}_I}{\sigma_c}\frac{c_0}{i\omega e}. \tag{24}$$

Equation (24) shows that the complex viscosity in parallel superposition involves two terms

$$\frac{1}{\eta_L} = \frac{1-\alpha_1}{\eta_{\parallel I}^{*}} + \frac{\alpha_1}{\eta_{\parallel N}^{*}}, \tag{25}$$

$$\frac{1}{\eta_{D_\infty}} = \frac{\dot{\gamma}_N - \dot{\gamma}_I}{\sigma_c}\frac{c_0}{i\omega e}. \tag{26}$$

The first term $\eta_L(\dot{\gamma}_1,\omega)$ corresponds to the "steady" lever rule (20) applied to the complex viscosities $\eta_{\parallel I}^{*}$ and $\eta_{\parallel N}^{*}$ and depends on both $\dot{\gamma}_1$ (through α_1) and ω (through $\eta_{\parallel I}^{*}$ and $\eta_{\parallel N}^{*}$). In principle $\eta_{\parallel I}^{*}(\omega)$ and $\eta_{\parallel N}^{*}(\omega)$ are accessible through superposition measurements in the homogeneous states at $\dot{\gamma}_1 = \dot{\gamma}_I$and $\dot{\gamma}_1 = \dot{\gamma}_N$, respectively [or at least by extrapolation of $\eta_{\parallel}^{*}(\dot{\gamma}_1,\omega)$ when $\dot{\gamma}_1 \to \dot{\gamma}_I^-$ and $\dot{\gamma}_1 \to \dot{\gamma}_N^+$], so that $\eta_L(\omega,\dot{\gamma}_1)$ is known once α_1 is known via Eq. (19).

The second term $\eta_{D_\infty}(\omega)$ accounts for the dynamics of the interface between the two bands and does not depend on $\dot{\gamma}_1$. Note, however, that this "dynamical" term depends on the geometry since e shows up in Eq. (26). Since good approximations of $\dot{\gamma}_I$, $\dot{\gamma}_N$, and σ_c are given by nonlinear rheological measurements, the only unknown in Eq. (26) is c_0. We conclude that superposition rheology in the shear banding regime should provide an experimental means of probing the dynamics of the interface between shear bands through the measurement of c_0. In practice the various parameters involved in Eq. (24) are not that easy to extract from independent measurements. As already pointed out the limits of the stress plateau are not always clear (see Fig. 2). But the largest difficulty probably lies in getting a good approximation for the dynamical behavior of the shear-induced structure $\eta_{\parallel N}^{*}(\omega)$ from superposition measurements at $\dot{\gamma}_1 \gtrsim \dot{\gamma}_N$. Indeed the high-shear branch of the flow curve is sometimes impossible to access due to flow instabilities that tend to expel the sample from the measuring tool at high shear rates [Berret and co-workers (1997); Hu and Lips (2005)]. Still one may argue that $\eta_{\parallel N}^{*}(\omega)$ could also be inferred from superposition experiments in the shear banding regime by looking at the dependence of $\eta_{\parallel}^{*}(\omega,\dot{\gamma}_1)$ on α_1 in Eq. (24). We shall further discuss this point below in Sec. IV C.

A simple way to overcome the difficulty raised by $\eta_{\parallel N}^{*}$ is to focus on the limit $\alpha_1 \to 0$, i.e., just at the onset of shear banding. In this limit Eq. (24) becomes

$$\lim_{\alpha_1 \to 0} \frac{1}{\eta_{\parallel}^{*}} = \frac{1}{\eta_{\parallel I}^{*}} + \frac{\dot{\gamma}_N - \dot{\gamma}_I}{\sigma_c}\frac{c_0}{i\omega e}, \tag{27}$$

where c_0 is the only unknown parameter since $\eta_{\parallel I}^{*}$ is known from measurements in the low-shear regime. Experimentally, α_1 is varied for a given frequency ω. The value at the origin of the linear regression of $1/\eta_{\parallel}^{*}$ vs α_1 is then Eq. (27), from which $1/\eta_{D_\infty}(\omega)$ is determined. Finally, a linear fit of $\eta_{D_\infty}(\omega)$ vs ω yields c_0. This fitting procedure will be tested in Sec. IV A.

To conclude this discussion of Eq. (24), let us check the validity of the "instantaneous" lever rule (18). In the case of oscillating velocity and stress fields, neglecting the time derivative in the Navier–Stokes equation is equivalent to setting $\rho\omega v_2 \ll \sigma_2/e$ where $v_2 \simeq \dot{\gamma}_2 e$. In the low-frequency limit, Eq. (24) yields $\eta_\parallel^* = \sigma_2/\dot{\gamma}_2 \simeq i\omega e\sigma_c/c_0(\dot{\gamma}_N - \dot{\gamma}_I)$ so that the steady-state approximation holds if

$$\rho c_0 e \frac{\dot{\gamma}_N - \dot{\gamma}_I}{\sigma_c} \ll 1. \tag{28}$$

With the typical values $\rho = 10^3$ kg m^{-3}, $c_0 \lesssim 1$ mm s^{-1} (as will be checked experimentally below), $e = 1$ mm, $\dot{\gamma}_N - \dot{\gamma}_I = 10$ s^{-1}, and $\sigma_c = 100$ Pa, the left-hand side of Eq. (28) is about 10^{-4}. Hence, the approximation holds at least in the low-frequency limit of Eq. (24). More generally, the steady-state approximation reads $\rho\omega e^2 \ll |\eta_\parallel^*|$. It can be checked from Figs. 3 and 4 that, for the highest frequencies achieved in our experiments ($\omega \simeq 100$ rad s^{-1}), one always keeps $|\eta_\parallel^*| \gtrsim 1$ Pa s, so that, with $\rho\omega e^2 \lesssim 0.1$, the approximation remains valid.

B. Experimental geometries

Standard experiments use cone-and-plate or Couette geometries (or their combination known as the Mooney–Couette geometry). The changes that the use of such geometries induces in Eqs. (24)–(26) are described in detail in the Appendix. It is shown in Appendix Secs. A and B that the expressions found for $\eta_\parallel^*$ in both the cone-and-plate and the Couette geometries can be written in forms similar to Eq. (24).

In particular, in both cone-and-plate and infinite parallel plates, it is seen from Eq. (23) that α_2 diverges at low frequencies for fixed σ_2, i.e., under controlled stress. Such a behavior is a direct consequence of the highly nonlinear fluid response under controlled stress in flat geometries, where jumps between the two shear branches of the flow curve are expected. Therefore, to ensure that the experiments are conducted inside the stress plateau for all frequencies, superposition rheology in the cone-and-plate geometry requires to work under controlled shear rate, so that α_2 [and thus $\dot{\gamma}_2$ through Eqs. (17)–(19)] always remains a linear perturbation of the steady shear. Since a controlled-stress rheometer is used in the present work and since ultrasonic velocimetry is not available in the cone-and-plate geometry, we shall rather focus on the Couette geometry where the divergence of α_2 does not occur.

More precisely, Appendix Sec. B shows that in the "small-gap approximation," i.e., when the gap e is small enough compared to the radius R_0 of the inner cylinder, the case of a Couette geometry reduces exactly to the case of infinite parallel plates provided that η_{D_∞} is replaced by

$$\frac{1}{\eta_D} = \frac{\dot{\gamma}_N - \dot{\gamma}_I}{\sigma_c} \frac{c_0}{i\omega e + \dfrac{2c_0 e}{R_0}} = \frac{1}{\eta_{D_\infty}} \frac{1}{1 - \dfrac{2ic_0}{\omega R_0}}. \tag{29}$$

This corresponds to the zero-order version of Eq. (A14), i.e., it assumes that both the term of order e/R_0 in Eq. (A16) and the first-order corrective term $1/\eta_\partial$ given by Eq. (A17) can be neglected. As seen in Eq. (A11) the curvature of the Couette geometry prevents α_2 from diverging at low frequencies so that superposition measurements can be performed under controlled stress.

Finally, Appendix Sec. C shows that the case of a Mooney–Couette geometry of height h can be handled by considering the proportions $\epsilon_{\text{co}}=(1+R_0/2h)^{-1}$ and $\epsilon_{\text{cp}}=1-\epsilon_{\text{co}}$ of the surface, respectively, covered by the Couette (co) and by the cone-and-plate (cp) geometries relative to the total surface. In particular, $\eta_{\parallel}^{*}$ is given by the following average of the corresponding viscosities $\eta_{\parallel\text{co}}^{*}$ and $\eta_{\parallel\text{cp}}^{*}$,

$$\eta_{\parallel}^{*} = \epsilon_{\text{co}}\eta_{\parallel\text{co}}^{*} + \epsilon_{\text{cp}}\eta_{\parallel\text{cp}}^{*}. \tag{30}$$

However, to close the problem one has to specify the values of α_1 in the two parts of the geometry. As shown in the Appendix, this leads to serious complications and the interpretation of superposition measurements in the Mooney–Couette geometry requires in principle the full knowledge of the dynamical behaviors $\eta_{\parallel I}^{*}$ and $\eta_{\parallel N}^{*}$ of the high- and low-viscosity materials.

To keep things analytically tractable and although this may be a crude approximation of the actual behavior in the Mooney–Couette geometry, we shall assume that

$$\frac{1}{\eta_{\parallel}^{*}} = \frac{\epsilon_{\text{co}}}{\eta_{\parallel\text{co}}^{*}} + \frac{\epsilon_{\text{cp}}}{\eta_{\parallel\text{cp}}^{*}}, \tag{31}$$

which is consistent with Eq. (30) only for $e/R_0 \ll 1$. Using the effective α_1 found in Appendix Sec. C and given by

$$\alpha_1 = \epsilon_{\text{co}}\frac{R_0}{e}\left(\sqrt{\frac{\sigma_1-\epsilon_{\text{cp}}\sigma_c}{\epsilon_{\text{co}}\sigma_c}}-1\right) + \epsilon_{\text{cp}}\frac{\dot{\gamma}_1-\dot{\gamma}_I}{\dot{\gamma}_N-\dot{\gamma}_I}, \tag{32}$$

together with Eq. (A14) at zero order in e/R_0 for $\eta_{\parallel\text{co}}^{*}$ and Eq. (A6) with $e=R_0\tan\beta$ for $\eta_{\parallel\text{cp}}^{*}$, one finds

$$\frac{1}{\eta_{\parallel}^{*}} = \frac{1-\alpha_1}{\eta_{\parallel I}^{*}} + \frac{\alpha_1}{\eta_{\parallel N}^{*}} + \frac{\dot{\gamma}_N-\dot{\gamma}_I}{\sigma_c}\frac{c_0}{i\omega e}\left(\frac{\epsilon_{\text{co}}}{1-\dfrac{2ic_0}{\omega R_0}} + 2\epsilon_{\text{cp}}\right). \tag{33}$$

Equation (33) is exactly Eq. (24) up to a corrective frequency-dependent term on c_0 that accounts for the Mooney–Couette geometry. Thus under the above assumptions we may still use the data analysis procedure described above in Sec. III A [see Eq. (27)] on experimental data recorded in the Mooney–Couette geometry.

IV. TWO-FLUID SUPERPOSITION RHEOLOGY: EXPERIMENTAL RESULTS

A. Superposition experiments in the Mooney–Couette geometry

Superposition experiments were performed in the shear banding regime on the previous 8% wt CPCl-NaSal solution under controlled stress in a Mooney–Couette geometry with inner radius $R_0=24$ mm, outer radius $R_1=25$ mm, and height $h=30$ mm. Using the notations defined above, this corresponds to $\epsilon_{\text{co}}\simeq 0.7$ so that we cannot neglect the presence of the cone. The small-gap approximation holds since $e/R_0\simeq 0.04$. A solvent trap is used to prevent evaporation and we checked that no significant change of the rheological properties of our micellar solution occurs over the ~8 h maximal duration of our experiments.

Figure 5 shows the experimental $1/\eta_{\parallel}^{*}(\alpha_1)$ data obtained when varying the imposed steady shear stress σ_1 (i.e., the average proportion α_1 of oriented phase) for a given frequency ω. $1/\eta_{\parallel}^{*}(\alpha_1)$ is inferred from the raw data $\eta_{\parallel}^{*}(\dot{\gamma}_1,\omega)$ at fixed ω (see Figs. 4 and 6 for examples of such raw data). To test the robustness of the linear behaviour of $1/\eta_{\parallel}^{*}$ vs α_1 expected from Eq. (33), the data were plotted against α_1 computed from Eq. (A21)

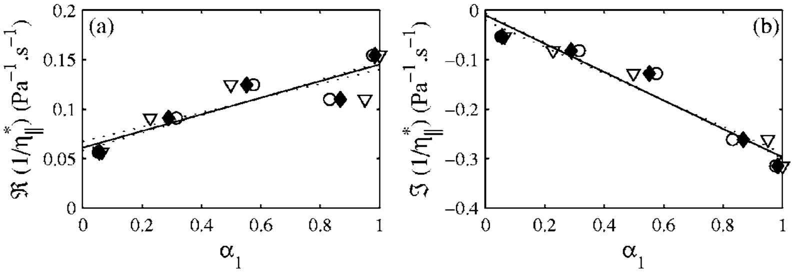

FIG. 5. (a) Real and (b) imaginary parts of $1/\eta_\parallel^*(\dot\gamma_1,\omega)$ vs α_1 deduced from Eq. (A21) (∘), from Eq. (A22) (▽), and from Eq. (A23) (◆). The solid lines are the best linear fits of the ◆ data while the dotted lines show the linear fits obtained using the ○ and ▽ data. The frequency is $\omega=0.26$ rad s^{-1}. The fluid under study is an 8% wt CPCl-NaSal solution.

alone (i.e., taking $\epsilon_{\text{co}}=1$ and neglecting the cone-and-plate part of the geometry, see ∘ symbols), from Eq. (A22) alone (i.e., taking $\epsilon_{\text{cp}}=1$ and neglecting the Couette part of the geometry, see ▽ symbols), and from the full Eq. (A23) with $\epsilon_{\text{co}}=0.7$ and $\epsilon_{\text{cp}}=0.3$ (see ◆ symbols). The quality of the three linear fits are similar and the values of the slopes as well as the intercepts at $\alpha_1=0$ are all very close. We conclude that the linear behavior predicted by Eq. (33) is indeed observed and that the way α_1 is computed is not critical.

In order to use the extrapolation procedure proposed in Sec. III A for Eq. (27), $\eta_{\parallel I}^*$ is taken to be the experimental value for the homogeneous fluid obtained closest to the onset of shear banding. The corresponding data are shown in Fig. 6(a) (∘ symbols, see also the discussion in Sec. IV C). We then calculate $1/\tilde\eta=1/\eta_\parallel^*(\alpha_1\to 0)-1/\eta_{\parallel I}^*$ for various frequencies ω ranging from 0.07 to 70 rad s^{-1}. The real and imaginary parts of $\tilde\eta$ are plotted as a function of ω in Fig. 7.

If Eq. (33) holds, one expects

$$\tilde\eta(\omega)=\frac{\sigma_c}{\dot\gamma_N-\dot\gamma_I}\frac{i\omega e}{c_0}\left(\frac{\epsilon_{\text{co}}}{1-\dfrac{2ic_0}{\omega R_0}}+2\epsilon_{\text{cp}}\right)^{-1}. \tag{34}$$

If one further assumes that $2c_0/\omega R_0\ll 1$, then one should find a range of ω for which $\Im(\tilde\eta)\gg\Re(\tilde\eta)$ and

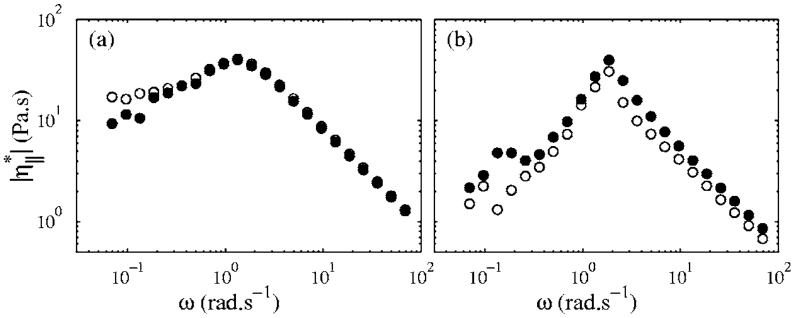

FIG. 6. (a) $|\eta_{\parallel I}^*(\omega)|$ measured closest to the onset of shear banding for $\dot\gamma_1=1.7$ s$^{-1}\lesssim\dot\gamma_I$ (∘) and inferred from the fitting procedure based on Eq. (33) (•). (b) $|\eta_{\parallel N}^*(\omega)|$ measured in the high-shear state for $\dot\gamma_1=11.1$ s^{-1} (∘) and deduced from Eq. (33) (•). The fluid under study is an 8% wt CPCl-NaSal solution.

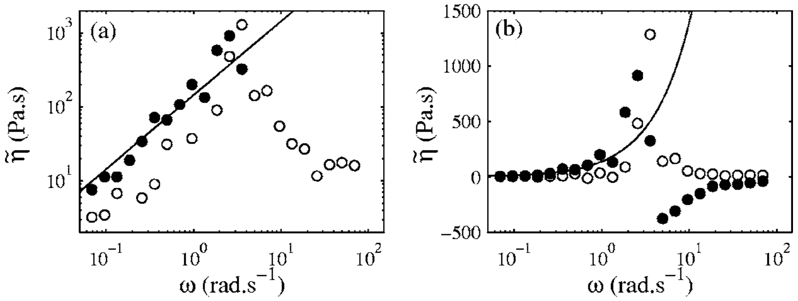

FIG. 7. $\Im(\tilde{\eta})$ (•) and $\Re(\tilde{\eta})$ (○) vs ω in (a) logarithmic scales and (b) semilogarithmic scales. The solid line is the best linear fit of $\Im(\tilde{\eta})$ by Eq. (35) with $\dot{\gamma}_I$=2.2 s^{-1}, $\dot{\gamma}_N$=7.4 s^{-1}, σ_c=100 Pa, e=1 mm, and c_0 =0.1 mm s^{-1}. The fluid under study is an 8% wt CPCl-NaSal solution.

$$\Im(\tilde{\eta}) \simeq \frac{\sigma_c}{\dot{\gamma}_N - \dot{\gamma}_I} \frac{\omega e}{c_0} \frac{1}{1 + \epsilon_{\text{cp}}}. \tag{35}$$

Figure 7(a) shows that $\Im(\tilde{\eta}) \gg \Re(\tilde{\eta})$ for $\omega \simeq 0.07-3$ rad s^{-1} in the experiment. The best linear fit of $\Im(\tilde{\eta})$ vs ω over this range of frequencies yields $c_0(1+\epsilon_{\text{cp}})$ $=0.13\pm0.05$ mm s^{-1} so that $c_0=0.1\pm0.04$ mm s^{-1}. The large uncertainty ($\simeq 40\%$) on the determination of c_0 is mainly due to the uncertainty on $\dot{\gamma}_I$ and $\dot{\gamma}_N$ and therefore on the calculation of α_1. Since $2c_0/\omega R_0 \simeq 0.003-0.1$ for $\omega \simeq 0.07-3$ rad s^{-1}, the approximation leading to Eq. (35) is justified *a posteriori*. These results were obtained with $\dot{\gamma}_I$ =2.2 s^{-1}, $\dot{\gamma}_N$=7.4 s^{-1}, and σ_c=100 Pa, which were estimated independently from nonlinear rheology as explained in Appendix Sec. B. However, at "high" frequencies ($\omega \gtrsim 1$ rad s^{-1}), the terms induced by the curvature of the Mooney–Couette geometry are no longer negligible, so that first-order terms in e/R_0 should be taken into account in Eq. (A14). This most probably explains the observation of negative data for $\Im(\tilde{\eta})$ in Fig. 7(b).

In the last section of this paper we use ultrasonic velocimetry to directly access the dynamics of the interface during superposition experiments and check the validity of the above findings. These experiments were performed on a 6% wt CPCl-NaSal solution (due to technical limitations involving the velocimetry setup and the 8% wt sample). To allow for a direct comparison with velocimetry experiments, Fig. 8 presents the analysis

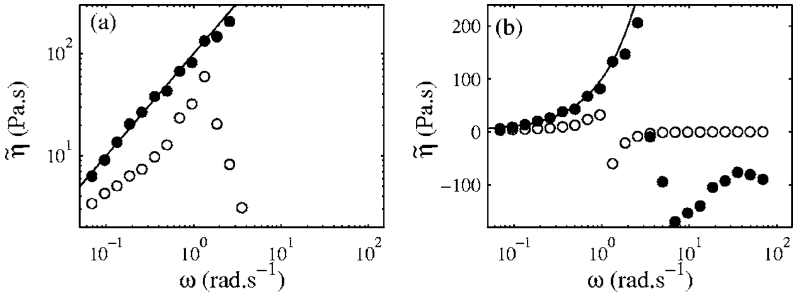

FIG. 8. $\Im(\tilde{\eta})$ (•) and $\Re(\tilde{\eta})$ (○) vs ω in (a) logarithmic scales and (b) semilogarithmic scales. The solid line is the best linear fit of $\Im(\tilde{\eta})$ by Eq. (35) with $\dot{\gamma}_I$=4.0 s^{-1}, $\dot{\gamma}_N$=6.3 s^{-1}, σ_c=68 Pa, e=1 mm, and c_0 =0.31 mm s^{-1}. The fluid under study is a 6% wt CPCl-NaSal solution.

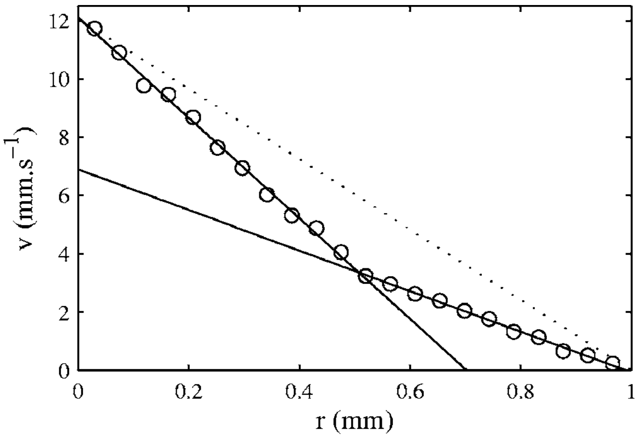

FIG. 9. Velocity profile $v(r)$ (∘) recorded in a 6% wt CPCl-NaSal solution at steady state for $\sigma_1 = 70.5$ Pa (which corresponds to $\alpha_1 \simeq 0.5$). The solid lines represent linear fits of the velocity profile in the high- and low-shear bands. Their intersection yields the position r_c of the interface. The dotted line shows the velocity profile for a Newtonian fluid.

of superposition rheology measurements performed on the 6% wt solution. The results are qualitatively the same as those for the 8% wt sample shown in Fig. 7. The estimate for c_0 in the 6% wt sample is $c_0 = 0.31 \pm 0.15$ mm s^{-1}.

B. Ultrasonic velocimetry during superposition experiments

1. Velocity profile measurements

Superposition experiments in the shear banding regime have shown the possibility of characterizing the dynamics of the interface between shear bands using only a standard rheometer. In this section, the above results and model are confirmed using time-resolved local velocity measurements. To access the velocity field we used the ultrasonic velocimetry technique described in Manneville and co-workers (2004). As shown by Becu and co-workers (2004), this technique allows one to measure the velocity profile of shear-banding wormlike micelles in the gap of a Couette cell with a temporal resolution of about 1 s and a spatial resolution of about 40 μm.

Figure 9 shows a typical velocity profile $v(r)$ measured in a 6% wt CPCl-NaSal solution, where r is the distance from the inner rotating cylinder. As explained in Manneville and co-workers (2004), the fluid was seeded with 1% wt hollow glass spheres (Sphericel, Potters Industries) of mean radius 11.7 μm and density 1.1 in order to provide acoustical scattering. We checked that both linear and nonlinear rheological properties were not significantly affected by the addition of such acoustic contrast agents. Since the velocity profiles are recorded in the Couette part of the Mooney–Couette cell, we shall focus on the model developed in Appendix Sec. B. Let us only recall here Eq. (A11) which gives the complex amplitude $r_2 = \alpha_2 e$ of the interface displacement

$$r_2 = \frac{\sigma_2}{\sigma_c} \frac{R_0^2}{(R_0 + r_1)^2} \frac{c_0}{i\omega + \dfrac{2c_0}{R_0 + r_1}}. \tag{36}$$

In the following, the steady shear stress is fixed to σ_1 such that $\alpha_1 \simeq 0.5$. The steady-state velocity profile of Fig. 9 clearly shows two linear parts that separate the gap into

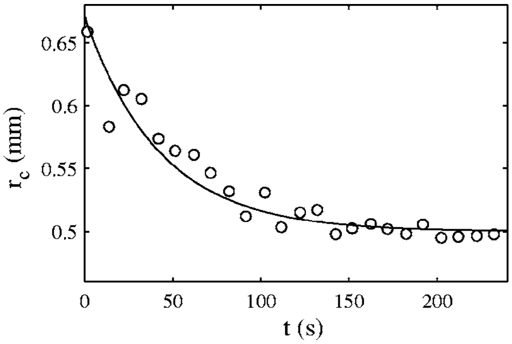

FIG. 10. Position of the interface $r_c(t)$ vs time as the external shear stress is reduced from $\sigma_1+\sigma_2=71.5$ Pa to $\sigma_1=70.5$ Pa at $t=0$. The solid line is the best fit by Eq. (38) with $r_2=0.17$ mm and $c_0=0.28$ mm s^{-1}. The fluid under study is a 6% wt CPCl-NaSal solution.

two shear bands of equal width where the apparent viscosities differ by a factor of about 2. Linear fits in the two shear bands yield the interface position $r_1=\alpha_1 e\simeq 0.5$ mm.

2. Measurement of c_0 in a transient experiment

In the framework of the model proposed by Radulescu and co-workers (1999), the characteristic velocity c_0 can be deduced from transient velocity profile measurements. Indeed by suddenly decreasing the shear stress from $\sigma=\sigma_1+\sigma_2$ to $\sigma=\sigma_1$ at time $t=0$ and by measuring the evolution of the velocity profiles $v(r,t)$ in time, we can easily track the interface position $r_c(t)$. Experimentally σ_2 is fixed such that, by using Eq. (A9), $r_2(\omega=0)=\alpha_2(\omega=0)e\simeq 0.2$ mm. In the small-gap approximation, the equation for the interface position reads

$$\frac{1}{c_0}\frac{dr_c}{dt}=\frac{\sigma(r_c)-\sigma_c}{\sigma_c}=\frac{2}{R_0}[r_1-r_c(t)], \tag{37}$$

which leads to

$$r_c(t)=r_1+r_2 e^{-2c_0 t/R_0}, \tag{38}$$

where $r_2(\omega=0)$ was simply noted r_2. As seen in Fig. 10, the position of the interface $r_c(t)$ is well fitted by Eq. (38) which yields $c_0=0.28\pm0.03$ mm s^{-1}. Comparing with the results of the superposition measurements shown in Fig. 8, one finds that both values are in quantitative agreement, which confirms the relevance and the ability of superposition rheology to extract dynamical information in the shear banding regime. Of course the uncertainty on c_0 given by time-resolved velocimetry is much less than that of the superposition method (but at the cost of using a more involved technique and processing a large amount of ultrasonic data).

The present analysis of the velocity measurements also neglects the first two stages of the band dynamics during the transient, namely low-shear band destabilization and interface reconstruction, as evidenced by Radulescu and co-workers (2003). These initial stages were shown to occur in typically 2 s which is of the order of the temporal resolution of our velocimetry experiments. Thus we only focus on the last dynamical step called "interface travel" in Radulescu and co-workers (2003). In particular, due to the existence of two early relaxation stages, one may argue that the initial position is ill

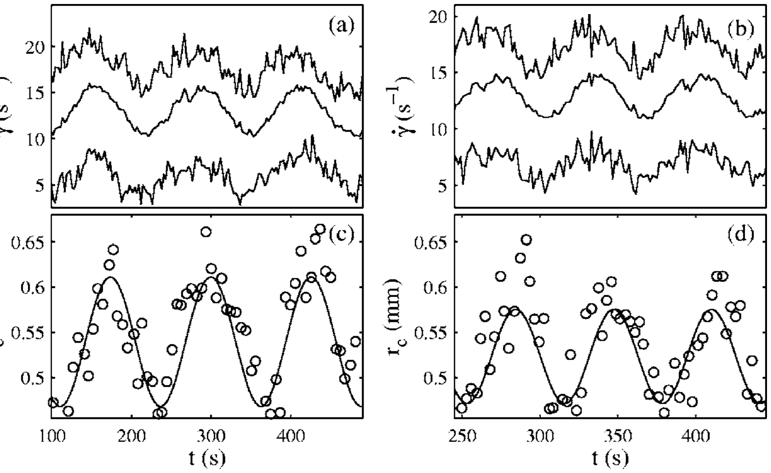

FIG. 11. (a) Local shear rates vs time in the nematic band (top) and isotropic band (bottom) along with the global shear rate recorded by the rheometer (middle) for $\omega=0.05$ rad s^{-1} and (b) $\omega=0.1$ rad s^{-1}. Position of the interface $r_c(t)$ vs time for (c) $\omega=0.05$ rad s^{-1} and (d) $\omega=0.1$ rad s^{-1}. The solid lines are the best fits by sine functions. The fluid under study is a 6% wt. CPCl-NaSal solution submitted to stress oscillations of amplitude $\sigma_2=1$ Pa around the mean value $\sigma_1=70.5$ Pa.

defined and that the interface position after reconstruction may significantly differ from r_1+r_2. This is the reason why r_2 was actually left as a free parameter in Eq. (38).

3. Validation of the model for superposition experiments

Now turning to the superposition experiment, we add an oscillatory shear stress of amplitude σ_2 to a steady shear stress σ_1, and follow the position of the interface in time for various frequencies. Figure 11 presents the measurements of the local shear rates in the two bands and of the interface position $r_c(t)$ versus time for two different frequencies. As expected these various quantities oscillate in time and, in spite of some experimental scatter, fitting $r_c(t)$ by sine functions for various frequencies yields a good estimate for the amplitude $r_2(\omega)=\alpha_2(\omega)e$.

The dots (•) in Fig. 12 show the amplitude $|r_2|$ of the interface oscillations inferred from ultrasonic velocimetry for four different frequencies, while the solid line is calculated using Eq. (36) with the value $c_0=0.28$ mm s^{-1} obtained from the transient experiment. The quantitative agreement between the experimental data and the calculated prediction confirms the generality of Eq. (36) and provides strong support for the model developed in Sec. III. Let us emphasize that in the present case the prediction for $r_2(\omega)$ is obtained without any free parameter since σ_2, r_1, R_0, and e are known experimentally and σ_c is found by nonlinear rheology.

C. Discussion and perspectives

Our main result is that superposition rheology can be used to infer conclusive information on the dynamics of wormlike micelles in the shear banding regime. In particular, superposition measurements lead to an estimate of the velocity c_0 which characterizes the dynamics of the interface between shear bands. The present uncertainty on the estimation of c_0 through superposition rheology alone is of the order of ±40%. In our opinion this relatively large uncertainty is due to the use of a Mooney–Couette cell and to the subsequent approximations needed to process the superposition data in order to recover c_0.

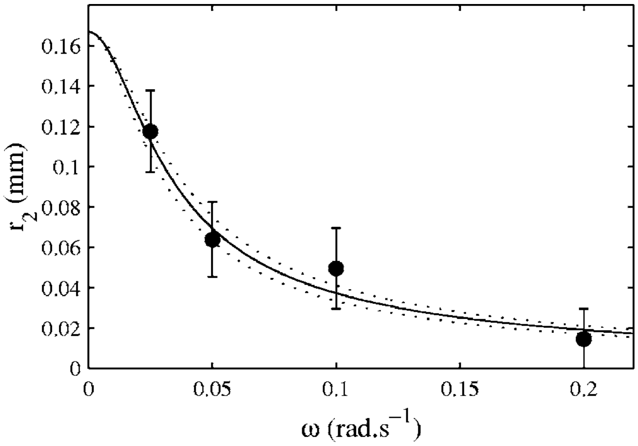

FIG. 12. Amplitude of the interface displacement $|r_2|$ vs ω. The solid line represents the prediction of Eq. (36) where all the parameters $\sigma_2=1$ Pa, $\sigma_c=68$ Pa, $r_1=0.5$ mm, and $c_0=0.28$ mm s^{-1} are known independently. The dotted lines were computed using $c_0=0.25$ (lower curve) and $c_0=0.31$ mm s^{-1} (upper curve) in Eq. (36). They illustrate the sensitivity of the prediction to a 10% variation in c_0, which corresponds to the experimental uncertainty on the fit of Fig. 10. The fluid under study is a 6% wt CPCl-NaSal solution.

Experiments in the cone-and-plate geometry under controlled shear rate should be simpler to process and should provide a better accuracy on c_0. To minimize boundary effects in the concentric cylinder geometry, one could also avoid the use of a Mooney–Couette cell by trapping an air bubble below the inner cylinder.

Let us now discuss the value of c_0 found from the superposition experiments reported above. According to Radulescu and co-workers (2003), c_0 is linked to the diffusion coefficient $\mathcal{D}$ of the stress across the streamlines, a central parameter in recent theoretical approaches of shear banding [Olmsted and co-workers (2000)]. More precisely, one has

$$\left.\frac{d\sigma}{dc}\right|_{\sigma=\sigma_c} = \frac{\sigma_c}{c_0} = KG_0\sqrt{\frac{\tau_1}{\mathcal{D}}}, \tag{39}$$

where $c=ed\alpha/dt$ is the velocity of the interface, K is a dimensionless parameter that depends on the constitutive model, G_0 is the plateau modulus, and τ_1 the main relaxation time already introduced in Sec. II B. Following Radulescu and co-workers (2003), we take $KG_0/\eta_{\|}^{*}(0,\dot{\gamma}_l)\dot{\gamma}_l=0.3$. From the nonlinear rheological measurements of Sec. II B and using Eq. (7), we find $\eta_{\|}^{*}(0,\dot{\gamma}_l)\dot{\gamma}_l\simeq 0.09\sigma_c$. With $c_0=0.1$ mm s^{-1} and $\tau_1=0.87$ s, Eq. (39) yields $\mathcal{D}\simeq 6.3\ 10^{-12}$ m^2 s^{-1}for the 8% wt CPCl-NaSal solution. This corresponds to a stress correlation length $\zeta=\sqrt{\mathcal{D}\tau_1}\simeq 2.3$ μm, which is much larger than the mesh size $\xi \sim (kT/G_0)^{1/3}\simeq 30$ nm of our system. Let us emphasize the fact that ultrasonic velocimetry has provided the same order of magnitude for c_0 at a slightly lower surfactant concentration but with a much better accuracy ($c_0=0.28\pm 0.03$ mm s^{-1} for a 6% wt CPCl-NaSal solution), which confirms that the stress diffusion coefficient estimated from Eq. (39) should be in the range 10^{-12}–10^{-11} m^2 s^{-1} in the system under study.

Such a value of $\mathcal{D}$ differs by two orders of magnitude from the stress diffusion coefficient inferred from transient rheo-optical measurements by Radulescu and co-workers (2003) in various wormlike micelle solutions with 0.3 M CTAB ($\mathcal{D}\simeq 1.2-7.2\times 10^{-14}$ m^2 s^{-1}). Consequently our stress correlation length is about 20 times larger than the estimate found by Radulescu and co-workers (2003), $\zeta\simeq 100$ nm, which was comparable to the mesh size of their micellar network ($\xi\simeq 26$ nm). Since we used the

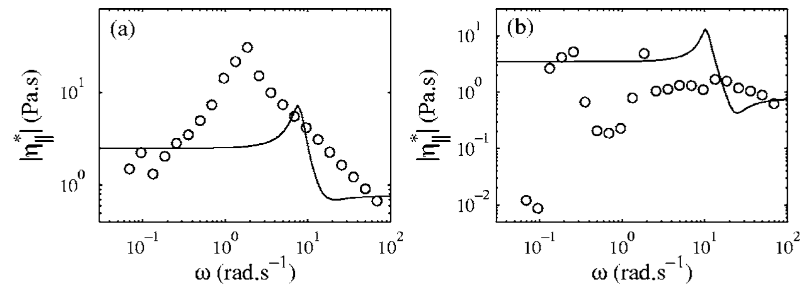

FIG. 13. Superposition rheology of an 8% wt CPCl-NaSal solution in the high-shear regime: $|\eta^*_{\|}(\omega,\dot{\gamma}_1)|$ vs ω for (a) $\dot{\gamma}_1=11.1$ and (b) 15.0 s^{-1}. The solid lines correspond to an Oldroyd-B fluid [Eq. (10)] with $\eta_0=122$ Pa, $s_1=0.59$ s, $s_2=0.13$ s, $\tau_1=0.87$ s, and $\tau_2=0.60$ ms.

CPCl-NaSal system rather than CTAB solutions such a difference may not be too unexpected. For instance the viscosity difference between the two coexisting phases, and hence, the width of the stress plateau, is much smaller in our case $[\tau(\dot{\gamma}_N-\dot{\gamma}_I)\simeq 4.5]$ than in the experiments of Radulescu and co-workers (2003) $[\tau(\dot{\gamma}_N-\dot{\gamma}_I)\simeq 19-80]$. Moreover, the value of K is not only model dependent but could also vary with the average shear rate [Dhont (1999)]. Estimates of $\mathcal{D}$ inferred from Eq. (39) should thus probably be taken with care. In any case, superposition experiments in CTAB solutions, where wider stress plateaus and a better precision on their limits should make the determination of c_0 more accurate, would be very useful in order to confirm the values of $\mathcal{D}$ found by Radulescu and co-workers (2003) in this system.

Besides extracting a value for $\mathcal{D}$, superposition rheology in the shear banding regime would be even more interesting if it could provide some information on the rheological behavior of the nematic phase as suggested in Sec. III A. Indeed information about the structure and dynamics of the shear-induced, oriented phase is often tricky to derive from conventional measurements due to the slope in the flow curve that results from curvature and due to instabilities that occur on the high-shear branch. Here the dynamical behavior $\eta^*_{\|N}(\omega)$ of the shear-induced phase may be recovered by considering the slopes of the linear fits of $1/\eta^*_{\|}$ in Fig. 5 which are equal to $1/\eta^*_{\|I}-1/\eta^*_{\|N}$ according to Eq. (33). The reconstructed $\eta^*_{\|N}(\omega)$ data are presented in Fig. 6(b), where they are compared to superposition data measured at the beginning of the high-shear branch of the flow curve. The fact that the experimental data are systematically lower than the reconstructed data can be easily explained by the distance from the experimental shear rate ($\dot{\gamma}=11.1$ s^{-1}) to the upper limit of the stress plateau ($\dot{\gamma}_N\simeq 7.4$ s^{-1}). Moreover, as shown in Fig. 6(a), which compares experimental data recorded just below $\dot{\gamma}_I$ and the $\eta^*_{\|I}(\omega)$ data reconstructed using the $\alpha_1=0$ limit and $c_0=0.1$ mm s^{-1} in Eq. (33), superposition measurements at the onset of shear banding also yield a very good approximation of the complex viscosity $\eta^*_{\|I}(\omega)$ close to the beginning of the plateau. This allowed us to check the consistency of our fitting procedure and to confirm that superposition rheology provides useful quantitative information on the dynamical behaviors of both the entangled and the oriented states. A deeper analysis and modelling of such behaviors are left for future work.

For the sake of completeness, Fig. 13 shows superposition data obtained on the high-shear branch of the flow curve. Although a simple interpretation of Fig. 13(b) may not be possible due to the occurrence of flow instabilities for $\dot{\gamma}\gtrsim 15$ s^{-1}, these data clearly show that the dynamical behavior of the shear-induced phase totally differs from the initial

Oldroyd-B behavior of the weakly oriented, entangled phase. Such information may turn out to be crucial for the modeling of shear banding since the exact behavior of the fluid at the limits of the stress plateau is usually unknown.

Finally, the influence of normal stresses or flow-concentration coupling in superposition experiments and the way to include them in a model also constitute directions for further research.

CONCLUSION

In this paper we have shown that superposition rheology constitutes a useful tool to access the dynamics of a shear-banded flow. A two-fluid semiphenomenological model was proposed based on the simplest shear banding scenario. This model was shown to provide a good description of the oscillations of the interface between shear bands in CPCl-NaSal wormlike micelle solutions sheared in the Mooney–Couette geometry. In particular an estimate for the stress diffusion coefficient $\mathcal{D}$ was reported for the first time in the CPCl-NaSal micellar system, whose value was shown to be significantly larger than that reported for CTAB systems. Independent measurements of the interface dynamics through local velocimetry experiments nicely corroborated our model without any free parameter. We have shown, however, that a more accurate determination of the characteristic velocity requires a simpler and better controlled geometry. Further experiments, e.g., under controlled shear rate in the cone-and-plate geometry, should allow one to probe even more precisely the dynamics of the shear bands using only a standard rheometer and to infer important information on the dynamical behaviors of the two coexisting phases. The formalisms to use for these experiments are also supplied in the present work.

ACKNOWLEDGMENTS

The authors wish to thank J. Teisseire, A. Colin, F. Molino, and C. Gay for fruitful discussions as well as the “Cellule Instrumentation” of CRPP for technical advice and design of the experiment. This work was cofunded by CNRS, Région Aquitaine, and the SoftComp Network of Excellence, a project of the European Commission developed under the sixth Framework Programme.

APPENDIX: TWO-FLUID CALCULATIONS IN EXPERIMENTAL GEOMETRIES

In this Appendix the detailed calculations for two-fluid superposition rheology are presented in the standard geometries used in the experiments namely cone-and-plate, Couette, and Mooney–Couette geometries.

A. Cone-and-plate geometry

Let us first consider a cone-and-plate geometry of angle $\beta \ll 1$ and maximum radius R_0. In such a geometry and in a homogeneous fluid, the shear rate can be considered as constant throughout the sample. In the shear banding regime, $\dot{\gamma}_1$ and α_1 are still linked by the lever rule (19) so that Eq. (20) remains valid. Moreover, at a given distance r from the axis of the cone, the system is equivalent to an infinite parallel plate geometry of gap $e = r \tan \beta$ for which the shear stress is

$$\sigma(r) = \sigma_c + \eta_{\parallel}^{*}(r)\,\dot{\gamma}_2 e^{i\omega t}, \tag{A1}$$

where $\eta_{\parallel}^{*}(r)$ is computed from Eq. (24) by setting $e = r \tan \beta$. One can then calculate the total stress exerted on the cone from

$$\sigma = \frac{2}{R_0^2}\int_0^{R_0}\sigma(r)r\mathrm{d}r. \tag{A2}$$

In analogy with Eqs. (25) and (26) let us define the two characteristic viscosities

$$\frac{1}{\eta_L} = \frac{1-\alpha_1}{\eta^*_{\|I}} + \frac{\alpha_1}{\eta^*_{\|N}}, \tag{A3}$$

$$\frac{1}{\eta_D} = \frac{\dot{\gamma}_N - \dot{\gamma}_I}{\sigma_c}\frac{c_0}{i\omega R_0 \tan\beta}, \tag{A4}$$

so that η_D corresponds to the dynamical term η_{D_∞} of the complex viscosity [Eq. (26)] with $e=R_0\tan\beta$. With these notations, inserting Eq. (A1) into Eq. (A2) leads to $\sigma=\sigma_c+\eta^*_{\|}\dot{\gamma}_2 e^{i\omega t}$, where

$$\eta^*_{\|} = \eta_L\left[1 - 2\frac{\eta_L}{\eta_D} + 2\frac{\eta_L^2}{\eta_D^2}\ln\left(1+\frac{\eta_D}{\eta_L}\right)\right]. \tag{A5}$$

The above expression for $\eta^*_{\|}$ in the cone-and-plate geometry clearly differs from Eq. (24) obtained for infinite parallel plates. In particular a linear fit of $1/\eta^*_{\|}$ vs α_1 does not seem relevant. As discussed in Sec. III A, one could still use Eq. (A5) to fit $\eta^*_{\|}$ with two free parameters $\eta^*_{\|N}(\omega)$ and $\eta_D(\omega)$. Such a procedure would provide an estimate for $\eta_D(\omega)$ and therefore c_0. Another way to proceed is to notice that in our experiments $\eta_D > \eta_L$, so that

$$\frac{1}{\eta^*_{\|}} \simeq \frac{1}{\eta_L} + \frac{2}{\eta_D}, \tag{A6}$$

which is equivalent to Eq. (24) with $2e=R_0\tan\beta$. In this case the linear regression of $1/\eta^*_{\|}$ may also lead to a good approximation of c_0.

B. Couette geometry

Let us now consider a concentric cylinder geometry (Couette geometry) where the inner cylinder of radius R_0 is rotating while the outer cylinder of radius R_1 remains fixed. This choice is made to be consistent with the experimental section but our model can easily be adapted to any rotational configuration of the two cylinders. The gap between the rotor and the stator is $e=R_1-R_0$. In the Couette geometry the shear stress is *not* homogeneous throughout the whole cell. Under the steady-state approximation already discussed in Sec. III A, the shear stress depends on the distance r from the inner cylinder as

$$\sigma(r) = \frac{\sigma_1 + \sigma_2 e^{i\omega t}}{\left(1+\frac{r}{R_0}\right)^2}, \tag{A7}$$

so that $\sigma_1+\sigma_2 e^{i\omega t}=\sigma(0)$ corresponds to the shear stress at the inner cylinder. Note that the rheometer may rather indicate "average" shear stresses for σ_1 and σ_2 measured in superposition experiments. Since these stresses only differ from the values at the inner cylinder by a geometrical factor of order 1 and since this factor also depends on the way the average is defined, we shall leave out this complication and stick with σ_1 and σ_2 as the values at the inner wall.

In the simple shear banding scenario described in the introduction, the inhomogeneity of σ ensures that only two shear bands separated by a single interface coexist in the gap. More precisely, the shear-induced transition occurs when there exists $0 \leq r_c \leq e$ such that $\sigma(r_c) = \sigma_c$. For $r > r_c$, $\sigma(r) < \sigma_c$ so the fluid remains entangled and in the high-viscosity state, while for $r < r_c$, $\sigma(r) > \sigma_c$ and the fluid is in the shear-induced low-viscosity state. Another consequence of the stress inhomogeneity is that the stress plateau is *not* flat [Radulescu and Olmsted (2000); Salmon and co-workers (2003)]. Indeed the shear-induced state first appears when $\sigma(0) = \sigma_c$ and fills the whole cell when $\sigma(0) = \sigma_c(1 + e/R_0)^2$. When $e/R_0 \ll 1$, this leads to a linear σ vs $\dot\gamma$ curve with slope $d\sigma/d\dot\gamma = 2e\sigma_c/R_0(\dot\gamma_I - \dot\gamma_N)$. In the case of the experimental data shown in Fig. 2, $e/R_0 \simeq 0.04$ and the shear stress is indeed seen to increase linearly in the shear banding regime. However, as already noted, the high-shear branch of the flow curve is hardly distinguishable from the "stress plateau." Still we can take advantage of the existence of a tilted plateau to estimate $\dot\gamma_N$. Fitting the flow curve at high shear rates by a Bingham fluid $\sigma = \sigma_B + \eta_B\dot\gamma$ [as suggested by Salman and co-workers (2003)] and looking for the shear rate corresponding to $\sigma = \sigma_c = 100$ Pa yields $\dot\gamma_N = 7.4 \pm 0.4\ \mathrm{s}^{-1}$ (see dashed line in Fig. 2).

Thus, from Eq. (A7), it is required that $\sigma_c < \sigma_1 \pm \sigma_2 < \sigma_c(1 + e/R_0)^2$ for a superposition experiment to be performed in the shear banding regime at all times. Let us define r_1 such that $\sigma_c = \sigma_1/(1 + r_1/R_0)^2$ and $r_c(t)$ the position of the interface at time t. The model proposed by Radulescu and co-workers (1999) implies that

$$\frac{1}{c_0}\frac{dr_c}{dt} = \frac{\sigma(r_c) - \sigma_c}{\sigma_c} = \left(1 + \frac{\sigma_2}{\sigma_1}e^{i\omega t}\right)\left(\frac{R_0 + r_1}{R_0 + r_c}\right)^2 - 1. \tag{A8}$$

In the linear response, Eq. (A8) leads to $r_c(t) = r_1 + r_2 \exp(i\omega t)$, where

$$r_2 = \frac{\sigma_2}{\sigma_1}\frac{c_0}{i\omega + \dfrac{2c_0}{R_0 + r_1}}. \tag{A9}$$

Since $r_c(t) = \alpha(t)e$, one gets $\alpha(t) = \alpha_1 + \alpha_2 \exp(i\omega t)$ with

$$\alpha_1 = \frac{r_1}{e} = \frac{R_0}{e}\left(\sqrt{\frac{\sigma_1}{\sigma_c}} - 1\right), \tag{A10}$$

$$\alpha_2 = \frac{r_2}{e} = \frac{\sigma_2}{\sigma_c}\frac{R_0^2}{(R_0 + r_1)^2}\frac{c_0}{i\omega e + \dfrac{2c_0 e}{R_0 + r_1}}. \tag{A11}$$

This last equation is tested experimentally through velocity profile measurements in Sec. IV B.

Once the interface motion is known from Eqs. (A10) and (A11), one can go back to the apparent shear rate, i.e., the shear rate averaged over the whole sample

$$\dot\gamma(t) = \dot\gamma_1 + \dot\gamma_2 e^{i\omega t} = \int_0^{r_c(t)} \left\{ \frac{\sigma_1(r)}{\eta_N[\sigma_1(r)]} + \frac{\sigma_2(r)e^{i\omega t}}{\eta^*_{\|N}[\omega, \sigma_1(r)]} \right\} \frac{dr}{e} + \int_{r_c(t)}^{e} \left\{ \frac{\sigma_1(r)}{\eta_I[\sigma_1(r)]} + \frac{\sigma_2(r)e^{i\omega t}}{\eta^*_{\|I}[\omega, \sigma_1(r)]} \right\} \frac{dr}{e}, \tag{A12}$$

where $\sigma_1(r) = \sigma_1/(1 + r/R_0)^2$ and $\sigma_2(r) = \sigma_2/(1 + r/R_0)^2$. Since our superposition experiments are performed under controlled stress, we have noted the viscosities η_I, η_N, $\eta^*_{\|I}$, and $\eta^*_{\|N}$ as functions of the local steady shear stress $\sigma_1(r)$. In principle, knowing the different viscosities (from experimental measurements or extrapolated data as mentioned in Sec. III A), Eqs. (A9) and (A12) allow one to solve for $\dot{\gamma}_1$ and $\dot{\gamma}_2$ and thus to find $\eta^*_{\|} = \sigma_2 / \dot{\gamma}_2$.

In order to get an explicit form for $\eta^*_{\|}$ that we may compare to Eq. (24), we shall assume that the small-gap approximation $e \ll R_0$ holds, which is almost always the case in standard experiments in the Couette geometry. In that case, expanding Eq. (A12) to first-order in e/R_0 and looking for the constant terms leads to

$$\frac{1}{\eta} = \frac{\dot{\gamma}_1}{\sigma_1} = \frac{1-\alpha_1}{\eta_I(\sigma_c)} + \frac{\alpha_1}{\eta_N(\sigma_c)} + \frac{e}{R_0}\left\{ \frac{1}{\eta_I(\sigma_c)}\left[(1-\alpha_1)^2 \frac{\sigma_c}{\eta_I(\sigma_c)} \left.\frac{\partial \eta_I}{\partial \sigma}\right|_{\sigma_c} - 1 + \alpha_1^2 \right] - \frac{\alpha_1^2}{\eta_N(\sigma_c)}\left[\frac{\sigma_c}{\eta_N(\sigma_c)} \left.\frac{\partial \eta_N}{\partial \sigma}\right|_{\sigma_c} + 1 \right] \right\}. \tag{A13}$$

This yields the apparent viscosity η indicated by the rheometer in the shear banding regime (up to some multiplicative factor of order 1 that depends on whether the rheometer actually indicates the shear stress at the inner wall or some average shear stress, as already mentioned above). Note the first order correction in e/R_0 to the case of simple shear given by Eq. (20). By looking for the terms proportional to $\exp(i\omega t)$ in the first-order expansion of Eq. (A12), one finds

$$\frac{1}{\eta^*_{\|}} = \frac{\dot{\gamma}_2}{\sigma_2} = \frac{1}{\eta_L} + \frac{1}{\eta_D} + \frac{1}{\eta_\partial}, \tag{A14}$$

with

$$\frac{1}{\eta_L} = \frac{1-\alpha_1}{\eta^*_{\|I}} + \frac{\alpha_1}{\eta^*_{\|N}}, \tag{A15}$$

$$\frac{1}{\eta_D} = \frac{\dot{\gamma}_N - \dot{\gamma}_I}{\sigma_c} \frac{c_0}{i\omega e + \dfrac{2c_0 e}{R_0}} \left[1 + \alpha_1 \frac{e}{R_0}\left(\frac{1}{i\omega e + \dfrac{2c_0 e}{R_0}} - 2 \right) \right] \simeq \frac{1}{\eta_{D_\infty}} \frac{1}{1 - \dfrac{2ic_0}{\omega R_0}}, \tag{A16}$$

$$\frac{1}{\eta_\partial} = \frac{e}{R_0}\left\{ \frac{1}{\eta^*_{\|I}}\left[(1-\alpha_1)^2 \frac{\sigma_c}{\eta^*_{\|I}} \left.\frac{\partial \eta^*_{\|I}}{\partial \sigma}\right|_{\sigma_c} - 1 + \alpha_1^2 \right] - \frac{\alpha_1^2}{\eta^*_{\|N}}\left(\frac{\sigma_c}{\eta^*_{\|N}} \left.\frac{\partial \eta^*_{\|N}}{\partial \sigma}\right|_{\sigma_c} + 1 \right) \right\}, \tag{A17}$$

where we have dropped the dependence on σ_c of the various viscosities for the sake of clarity. Equation (A14) generalizes Eq. (24) to the case of a small-gap Couette geometry and shows that $\eta^*_{\|}$ now involves three terms: the lever rule η_L, the dynamical component η_D that arises from the motion of the interface, and η_∂ a first-order correction to η_L similar to that found in Eq. (A13) and linked to the stress inhomogeneity. Keeping in mind that the various viscosities in Eq. (24) are taken at $\sigma_1 = \sigma_c$, the case of two infinite parallel plates is easily recovered from Eqs. (A13)–(A17) when $R_0 \to \infty$.

Therefore, in a small-gap Couette geometry, $1/\eta^*_{\|}$ is a second-order polynomial in α_1 whose value for $\alpha_1 \to 0$ is

$$\lim_{\alpha_1 \to 0} \frac{1}{\eta_\parallel^*} = \frac{1}{\eta_{\parallel I}^*} + \frac{\dot{\gamma}_N - \dot{\gamma}_I}{\sigma_c} \frac{c_0}{i\omega e + \dfrac{2c_0 e}{R_0}}. \tag{A18}$$

This is very similar to Eq. (27) so that the same data analysis should lead to the measurement of $\eta_D(\omega)$ and to an experimental determination of c_0.

C. Mooney–Couette geometry

Experimentally, in order to minimize boundary effects due to the finite height of the cylinders, one often uses a composite geometry, called the Mooney–Couette geometry, made of a Couette cell of gap e with a cone-shaped bottom such that $e = R_0 \tan \beta \simeq R_0 \beta$. In a Newtonian fluid and in the small-gap approximation, this geometry ensures that the shear rate remains constant over the whole sample.

Using the results obtained in Appendix Secs. A and B, one can easily construct a model for superposition experiments in the Mooney–Couette geometry of height h by considering the proportions $\epsilon_{co} = (1 + R_0/2h)^{-1}$ and $\epsilon_{\text{cp}} = 1 - \epsilon_{\text{co}}$ of the surface respectively covered by the Couette (co) and by the cone-and-plate (cp) geometries relative to the total surface. The total shear stress is then simply given by $\sigma = \epsilon_{\text{co}} \sigma_{\text{co}} + \epsilon_{\text{cp}} \sigma_{\text{cp}}$, which yields

$$\eta = \epsilon_{\text{co}} \eta_{\text{co}} + \epsilon_{\text{cp}} \eta_{\text{cp}}, \tag{A19}$$

$$\eta_\parallel^* = \epsilon_{\text{co}} \eta_{\parallel \text{co}}^* + \epsilon_{\text{cp}} \eta_{\parallel \text{cp}}^*, \tag{A20}$$

where η_{cp} and $\eta_{\parallel \text{cp}}^*$ are given by Eqs. (20) and (A6), and η_{co} and $\eta_{\parallel \text{co}}^*$ by Eqs. (A13) and (A14). To close this set of equations, one has to specify the values of α_1 in the two parts of the geometry. Since the shear rate is perfectly homogeneous in the cone-and-plate, the steady component of the shear stress acting on the cone is $\sigma_{1\text{cp}} = \sigma_c$ so that the steady component of the shear stress acting on the inner cylinder is $\sigma_{1\text{co}} = (\sigma_1 - \epsilon_{\text{cp}} \sigma_c)/\epsilon_{\text{co}}$. Thus the local proportions of shear-induced structure $\alpha_{1\text{cp}}$ and $\alpha_{1\text{co}}$ are given by

$$\alpha_{1\text{co}} = \frac{R_0}{e} \left(\sqrt{\frac{\sigma_1 - \epsilon_{\text{cp}} \sigma_c}{\epsilon_{\text{co}} \sigma_c}} - 1 \right), \tag{A21}$$

$$\alpha_{1\text{cp}} = \frac{\dot{\gamma}_1 - \dot{\gamma}_I}{\dot{\gamma}_N - \dot{\gamma}_I}. \tag{A22}$$

In the limit $e/R_0 \ll 1$ one can define an effective α_1 for the whole cell:

$$\alpha_1 = \epsilon_{\text{co}} \alpha_{1\text{co}} + \epsilon_{\text{cp}} \alpha_{1\text{cp}} = \epsilon_{\text{co}} \frac{R_0}{e} \left(\sqrt{\frac{\sigma_1 - \epsilon_{\text{cp}} \sigma_c}{\epsilon_{\text{co}} \sigma_c}} - 1 \right) + \epsilon_{\text{cp}} \frac{\dot{\gamma}_1 - \dot{\gamma}_I}{\dot{\gamma}_N - \dot{\gamma}_I}. \tag{A23}$$

With Eqs. (A20), (A6), (A14), (A21), and (A22), one can in principle determine the characteristic velocity c_0 and the dynamical behaviors of the two coexisting phases $\eta_{\parallel I}^*$ and $\eta_{\parallel N}^*$ by fitting $\eta_\parallel^*$ using Eq. (A20) at a fixed ω. However, in practice, such a fit requires to know precisely σ_c, $\dot{\gamma}_I$, and $\dot{\gamma}_N$ together with $\dot{\gamma}_1$ and $\eta_\parallel^*$ for at least four different values of σ_1. As already pointed out, σ_c, $\dot{\gamma}_I$,and $\dot{\gamma}_N$ may be difficult to access and, in a curved geometry, are known to within 10% at best. Therefore, the complexity of the fitting procedure along with the high number of unknowns prevent us to fit experimental data to the full model described above. Moreover the simple data analysis proposed in Sec. III A and based on an extrapolation to $\alpha_1 = 0$ (in order to remove the dependence on the unknown viscosity $\eta_{\parallel N}^*$) is no longer possible in the Mooney–Couette geometry since α_{1cp} and α_{1co} do not go to zero for the same $\dot{\gamma}_1$ or σ_1. Nevertheless, in Sec. III B, it is shown that Eq. (24) along with α_1 calculated from Eq. (A23) may still allow us to estimate c_0.

References

Bécu, L., S. Manneville, and A. Colin, "Spatiotemporal dynamics of wormlike micelles under shear," Phys. Rev. Lett. **93**, 018301 (2004).

Berret, J.-F., Rheology of wormlike micelles: Equilibrium properties and shear banding transition, cond-mat/0406681, in P. Terech and R. Weiss, *Molecular Gels* (Elsevier, New York, 2005).

Berret, J. F., G. Porte, and J.-P. Decruppe, "Inhomogeneous shear flows of wormlike micelles: A master dynamic phase diagram," Phys. Rev. E **55**, 1668–1676 (1997).

Berret, J. F., D. C. Roux, and G. Porte, "Isotropic-to-nematic transition in wormlike micelles under shear," J. Phys. II **4**, 1261–1269 (1994).

Booij, H. C., "Influence of superimposed steady shear flow on the dynamic properties of non-Newtonian fluids I," Rheol. Acta **5**, 215–221 (1966).

Booij, H. C., "Influence of superimposed steady shear flow on the dynamic properties of non-Newtonian fluids II," Rheol. Acta **5**, 222–226 (1966).

Britton, M. M., and P. T. Callaghan, "Two-phase shear band structures at uniform stress," Phys. Rev. Lett. **78**, 4930–4933 (1997).

Cappelaere, E., R. Cressely, and J.-P. Decruppe, "Linear and non-linear rheological behavior of salt-free aqueous CTAB solutions," Colloids Surf., A **104**, 353 (1995).

Cates, M. E., "Reptation of living polymers: dynamics of entangled polymers in the presence of reversible chain-scission reaction," Macromolecules **20**, 2289–2296 (1987).

Cates, M. E., T. C. B. McLeish, and G. Marucci, "The rheology of entangled polymers at very high shear rates," Europhys. Lett. **21**, 451–456 (1993).

Cates, M. E., and S. Milner, "Role of shear in the isotropic-to-lamellar transition," Phys. Rev. Lett. **62**, 1856–1859 (1989).

Dhont, J. K. G., "A constitutive relation describing the shear-banding transition," Phys. Rev. E **60**, 4534–4544 (1999).

Dhont, J. K. G., and N. J. Wagner, "Superposition rheology," Phys. Rev. E **63**, 021406 (2001).

Fielding, S. M., "Linear instability of planar shear banded flow," Phys. Rev. Lett. **95**, 134501 (2005).

Fielding, S. M., and P. D. Olmsted, "Flow phase diagrams for concentrated-coupled shear banding," Eur. Phys. J. E **11**, 65–83 (2003).

Fielding, S. M., and P. D. Olmsted, "Early stage kinetics in a unified model of shear-induced demixing and mechanical shear banding instabilities," Phys. Rev. Lett. **90**, 224501 (2003).

Fielding, S. M., and P. D. Olmsted, "Spatiotemporal oscillations and rheochaos in a simple model of shear banding," Phys. Rev. Lett. **92**, 084502 (2004).

Fielding, S. M., and P. D. Olmsted, "Nonlinear dynamics of an interface between shear bands," Phys. Rev. Lett. **96**, 104502 (2006).

Fischer, P., and H. Rehage, "Rheological master curves of viscoelastic surfactant solutions by varying the solvent viscosity and temperature," Langmuir **13**, 7012–7020 (1997).

Grizzuti, N., and P. L. Maffettone, "Quiescent and flow-induced transitional behavior of hydroxypropylcellulose solutions," J. Chem. Phys. **118**, 5195–5200 (2003).

Holmes, W. M., M. R. Lopez-Gonzalez, and P. T. Callaghan, "Fluctuations in shear-banded flow seen by NMR velocimetry," Europhys. Lett. **64**, 2740 (2003).

Hu, Y. T., and A. Lips, "Kinetics and mechanism of shear banding in an entangled micellar solution," J. Rheol. **49**, 1001–1027 (2005).

Lee, J. Y., G. G. Fuller, N. Hudson, and X-F. Yuan, "Investigation of shear-banding structure in wormlike micellar solution by point-wise flow-induced birefringence measurements," J. Rheol. **49**, 537–550 (2005).

Lerouge, S., M. Argentina, and J.-P. Decruppe, "Interface instability in shear-banding flow," Phys. Rev. Lett. **96**, 088301 (2006).

Lerouge, S., J.-P. Decruppe, and P. D. Olmsted, "Birefringence banding in a micellar solution or the complexity of heterogeneous flows," Langmuir **20**, 11355365 (2004).

López-González, M. R., W. M. Holmes, P. T. Callaghan, and P. J. Photinos, "Shear banding fluctuations and nematic order in wormlike micelles," Phys. Rev. Lett. **93**, 268302 (2004).

López-González, M. R., W. M. Holmes, and P. T. Callaghan, "Rheo-NMR phenomena in wormlike micelles," Soft Mater. **2**, 855–869 (2006).

Mair, R. W., and P. T. Callaghan, "Observation of shear banding in worm-like micelles by NMR velocity imaging," Europhys. Lett. **36**, 719 (1996).

Mair, R. W., and P. T. Callaghan, "Shear flow of wormlike micelles in pipe and cylindrical Couette geometries as studied by nuclear magnetic resonance microscopy," J. Rheol. **41**, 901–924 (1996).

Makhloufi, R., J.-P. Decruppe, A. Ait-Ali, and R. Cressely, "Rheo-optical study of worm-like micelles undergoing a shear banding flow," Europhys. Lett. **32**, 2538 (1995).

Manneville, S., L. Bécu, and A. Colin, "High-frequency ultrasonic speckle velocimetry in sheared complex fluids," Eur. Phys. J.: Appl. Phys. **28**, 361–373 (2004).

Méndez-Sánchez, A. F., J. Pérez-González, L. de Vargas, J. R. Castrejón-Pita, A. A. Castrejón-Pita, and G. Huelsz, "Particle image velocimetry of the unstable capillary flow of a micellar solution," J. Rheol. **47**, 1455–1466 (2003).

Oldroyd, J. G., "The elastic and viscous properties of emulsions and suspensions," Proc. R. Soc. London, Ser. A **218**, 122–132 (1953).

Oldroyd, J. G., "The effects of interfacial stabilizing films on the elastic and viscous properties of emulsions," Proc. R. Soc. London, Ser. A **232**, 567–577 (1955).

Olmsted, P. D., and P. Goldbart, "Theory of the nonequilibrium phase transition for nematic liquid crystals under shear flow," Phys. Rev. A **41**, 4578 (1990).

Olmsted, P. D., and P. Goldbart, "Isotropic-nematic transition in shear flow: State selection, coexistence, phase transitions, and critical behavior," Phys. Rev. A **46**, 4966–4993 (1992).

Olmsted, P. D., and C.-Y. D. Lu, "Coexistence and phase separation in sheared complex fluids," Phys. Rev. E **56**, R55–R58 (1997).

Olmsted, P. D., O. Radulescu, and C.-Y. D. Lu, "Johnson–Segalman model with a diffusion term in cylindrical Couette flow," J. Rheol. **44**, 257–275 (2000).

Porte, G., J. F. Berret, and J. L. Harden, "Inhomogeneous flows of complex fluids: Mechanical instability versus non-equilibrium phase transition," J. Phys. II **7**, 459–472 (1997).

Radulescu, O., and P. D. Olmsted, "Matched asymptotic solutions for the steady banded flow of the diffusive Johnson–Segalman model in various geometries," J. Non-Newtonian Fluid Mech. **91**, 143–164 (2000).

Radulescu, O., P. D. Olmsted, and C.-Y. D. Lu, "Shear banding in reaction-diffusion models," Rheol. Acta **38**, 606–613 (1999).

Radulescu, O., P. D. Olmsted, J.-P. Decruppe, S. Lerouge, J.-F. Berret, and G. Porte, "Time scales in shear banding of wormlike micelles," Europhys. Lett. **62**, 230 (2003).

Rehage, H., and H. Hoffmann, "Rheological properties of viscoelastic surfactant systems," J. Phys. Chem. **92**, 4712–4719 (1988).

Rehage, H., and H. Hoffmann, "Viscoelastic surfactant solutions: Model systems for rheological research," Mol. Phys. **74**, 933 (1991).

Salmon, J.-B., A. Colin, S. Manneville, and F. Molino, "Velocity profiles in shear–banding wormlike micelles," Phys. Rev. Lett. **90**, 228303 (2003).

Schmitt, V., C. M. Marques, and F. Lequeux, "Shear-induced phase separation of complex fluids: The role of flow-concentration coupling," Phys. Rev. E **52**, 4009–4015 (1995).

Soltero, J. F. A., F. Bautista, J. E. Puig, and O. Manero, "Rheology of cetyltrimethylammonium p-toluenesulfonate-water system. 3. Nonlinear viscoelasticity," Langmuir **15**, 1604–1612 (1999).

Spenley, N. A., M. E. Cates, and T. C. B. McLeish, "Nonlinear rheology of wormlike micelles," Phys. Rev. Lett. **71**, 939–942 (1993).

Spenley, N. A., X. F. Yuan, and M. E. Cates, "Nonmonotonic constitutive laws and the formation of shear-banded flows," J. Phys. II **6**, 551–571 (1996).

Tirtaatmadja, V., K. C. Tam, and R. D. Jenkins, "Superposition of oscillations on steady shear flow as a technique for investigating the structure of associative polymers," Macromolecules **30**, 1426–1433 (1997).

Vermant, J., L. Walker, P. Moldenaers, and J. Mewis, "Orthogonal versus parallel superposition measurements," J. Non-Newtonian Fluid Mech. **79**, 173–189 (1998).

Yuan, X.-F., "Dynamics of a mechanical interface in shear-banded flow," Europhys. Lett. **46**, 542–548 (1999).

Yesilata, B., C. Clasen, and G. H. McKinley, "Nonlinear shear and extensional flow dynamics of wormlike surfactant solutions," J. Non-Newtonian Fluid Mech. **133**, 73 (2006).

Chapter 17

Competition between shear banding and wall slip in worm-like Micelles

PRL **103,** 248302 (2009) PHYSICAL REVIEW LETTERS week ending 11 DECEMBER 2009

Competition between Shear Banding and Wall Slip in Wormlike Micelles

M. Paul Lettinga[1,*] and Sébastien Manneville[2]

[1]*IFF, Institut Weiche Materie, Forschungszentrum Jülich, D-52425 Jülich, Germany*
[2]*Laboratoire de Physique, Université de Lyon-École, Normale Supérieure de Lyon-CNRS UMR 5672*
46 allée d'Italie, F-69364 Lyon cedex 07, France

(Received 23 April 2009; published 8 December 2009)

The interplay between shear band (SB) formation and boundary conditions (BC) is investigated in wormlike micellar systems (CPyCl-NaSal) using ultrasonic velocimetry coupled to standard rheology in Couette geometry. Time-resolved velocity profiles are recorded during transient strain-controlled experiments in smooth and sandblasted geometries. For stick BC standard SB is observed, although depending on the degree of micellar entanglement temporal fluctuations are reported in the highly sheared band. For slip BC wall slip occurs only for shear rates larger than the start of the stress plateau. At low entanglement, SB formation is shifted by a constant $\Delta\dot{\gamma}$, while for more entangled systems SB constantly "nucleate and melt." Micellar orientation gradients at the walls may account for these original features.

DOI: 10.1103/PhysRevLett.103.248302 PACS numbers: 83.80.Qr, 47.50.−d, 83.50.Rp, 83.60.−a

During the past two decades, shear banding (SB), i.e., the shear-induced coexistence of macroscopic bands with widely different viscosities, has been evidenced in a large range of complex fluids [1]. Sheared dispersions of surfactant wormlike micelles have attracted considerable attention due to their practical use in industry, but also because they challenged the physicists to address a nonequilibrium problem with concepts from thermodynamics [1–3]. Indeed, rheological measurements show that the flow curve of shear-banding systems, i.e., the measured shear stress σ vs the applied shear rate $\dot{\gamma}$, presents a plateau at a well-defined shear stress $\sigma^\star$ over a given range of shear rates [4], very similar to the plateau in pressure as a function of overall concentration of a demixed system. As for equilibrium phase transitions, it has been suggested that the flow can be either metastable or unstable for SB formation, depending on the applied shear rate [2,5–7]. The formation of two coexisting SB, bearing the local shear rates $\dot{\gamma}_1$ and $\dot{\gamma}_2$ that mark, respectively, the lower and upper limits of the stress plateau, constitutes a pathway for the relaxation of the excess stress in the initially linear flow. Stress relaxation can, however, also occur through apparent wall slip. Slip phenomena are ubiquitous in polymers [8,9] and soft glassy materials [10]. Wall slip has also been reported in shear-thinning wormlike micellar systems [11,12] but its connection with SB has been underexposed. Still, information on the interplay between wall slip and a flow instability like SB are essential for fully understanding the behavior of complex fluids.

In this Letter, wall slip is shown to compete with SB formation by offering an alternative route for stress relaxation. We use tunable boundary conditions (BC) at the walls as an experimental tool to probe the effect of wall slip on the flow behavior of cetylpyridinium chloride/sodium salicylate (CPyCl-NaSal) micellar solutions at 6 and 10 wt% in 0.5 M NaCl brine at 23 °C. We enforce "stick" BC by using a rough sandblasted Plexiglas Couette cell and partial "slip" BC by using a smooth Plexiglas cell [13]. The competition between SB formation and wall slip after shear rate quenches is addressed through simultaneous rheological [14] and time-resolved velocity profiles measurements. For the latter, we use ultrasonic speckle velocimetry (USV) [15] since the sandblasted cell is not transparent and optical techniques as in [16–18] would be too difficult to implement. We show that with slip BC, wall slip occurs only for shear rates larger than the start of the stress plateau for both the concentrations under study. The extent to which SB formation is frustrated by wall slip strongly depends, however, on the degree of micellar entanglement. Very large temporal fluctuations are reported in the more concentrated sample for both BC.

The flow curve of 6 wt% CPyCl-NaSal shown in Fig. 1(a) for stick and slip BC reveals a stress plateau at $\sigma^\star \simeq 75$ Pa that extends from $\dot{\gamma}_1 \simeq 4.5$ to $\dot{\gamma}_2 \simeq 22$ s^{-1}, with a slight tilt due to the curvature of the Couette cell [16]. Interestingly the flow curve for slip BC does not show such a sharp bend at $\dot{\gamma}_1$ as with stick BC. Figure 1(b) presents the stress responses for quenches from $\dot{\gamma}_{\text{init}}$ located in the low shear regime to $\dot{\gamma}_{\text{appl}} = 8$ s^{-1} located in the *beginning* of the stress plateau. In line with earlier experiments [2,7], the stress shows a slow decay after an initial overshoot and a few oscillations. As in Ref. [7], we define the amplitude of this slow relaxation as the *excess* stress $\Delta\sigma = \sigma^M - \sigma^\infty$, where σ^M is the "mechanical" stress at the end of the oscillations and σ^∞ is the steady-state shear stress. Although the initial overshoot is more pronounced for stick BC, the stress responses for $t \gtrsim 10$ s are very similar for both BC. Yet, depending on the BC, velocity profiles display radically different behaviors that persist in the steady state. As seen from Figs. 1(c) and 1(d), linear profiles are recorded just before and after the shear rate quench for both BC. For stick BC, a high SB develops within a few seconds at $\varepsilon = \delta/e \simeq 0.5$, where δ is the width of the SB and e the gap width. The interface then

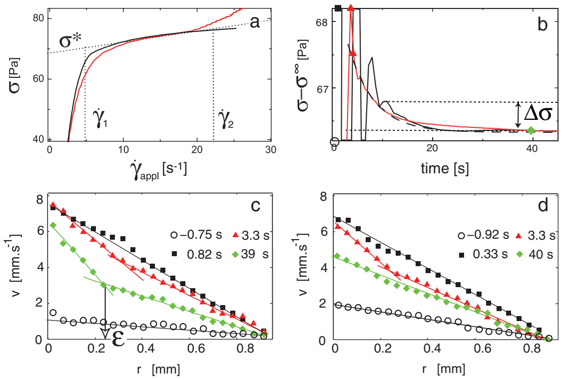

FIG. 1 (color). (a) Steady-state flow curves of 6 wt % CPyCl-NaSal for stick (black) and slip BC (red) for a shear rate sweep of 1200 s. (b) Stress responses $\sigma(t) - \sigma^\infty$ after a shear rate quench to $\dot{\gamma}_{\rm appl} = 8\ {\rm s}^{-1}$ at $t = 0$ for stick (black, $\dot{\gamma}_{\rm init} = 0.8\ {\rm s}^{-1}$) and slip BC (red, $\dot{\gamma}_{\rm init} = 2\ {\rm s}^{-1}$). The dashed line indicates an exponential decay with a characteristic time of 10 s. (c) Velocity profiles $v(r, t)$ for stick BC at various times during the quench shown in (b) [see colored dots in (b)]. r denotes the radial position from the inner rotating cylinder. (d) Same as (c) for slip BC.

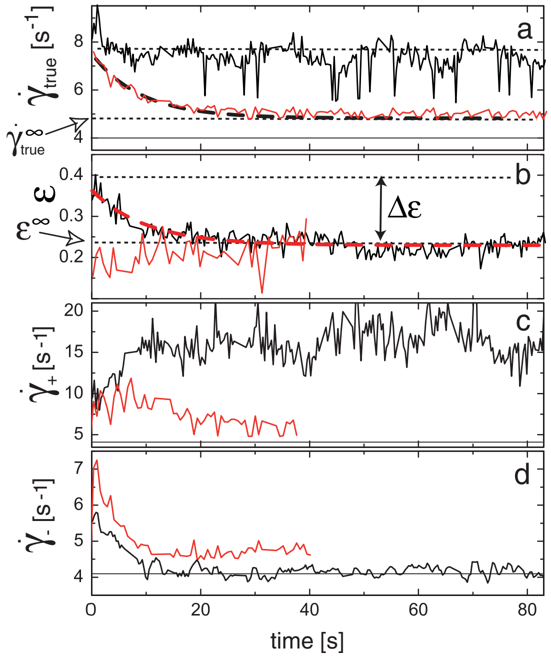

FIG. 2 (color). Analysis of the velocity data corresponding to the shear rate quenches to 8 ${\rm s}^{-1}$ with stick (black) and slip BC (red). (a) True shear rate $\dot{\gamma}_{\rm true}(t)$. (b) Proportion of the high SB $\varepsilon(t)$. (c) Shear rate in the high SB $\dot{\gamma}_+(t)$ and (d) in the low SB $\dot{\gamma}_-(t)$. The dashed lines indicate exponential decays with the same time constant of 10 s.

migrates towards its final position in agreement with previous observations [17]. For slip BC, however, SB do not fully develop [see the velocity profile at $t = 3.3$ s in Fig. 1(d)] and the system rather slips to reach a steady state characterized by a *homogeneous* shear flow with substantial wall slip (about 40%) at the inner cylinder, as in a recent report on DNA dispersions [9].

Figure 2 provides the analysis of the time-resolved velocity measurements after quenches to $\dot{\gamma}_{\rm appl} = 8\ {\rm s}^{-1}$, as in Figs. 1(c) and 1(d). Each velocity profile was analyzed to extract the true shear rate $\dot{\gamma}_{\rm true}(t)$, the proportion of highly sheared material $\varepsilon(t)$, and the local shear rates $\dot{\gamma}_\pm(t)$ in each SB [19]. As noted above our results for *stick* BC are consistent with previous data where no significant wall slip was reported [16,17]. They also reveal two important new features: (i) the presence of noticeable fluctuations in both $\dot{\gamma}_{\rm true}(t)$ and $\dot{\gamma}_+(t)$ while $\varepsilon(t)$ and $\dot{\gamma}_-(t)$ remain roughly constant for $t \gtrsim 30$ s and (ii) the fact that the position of the SB settles with the same dynamics as the shear stress. For *slip* BC, Fig. 2(a) shows that (i) the imposed shear rate $\dot{\gamma}_{\rm appl}$ cannot be sustained although initially $\dot{\gamma}_{\rm true} \simeq \dot{\gamma}_{\rm appl}$ and (ii) wall slip sets in immediately and has the same time constant as the stress relaxation since $\dot{\gamma}_{\rm true}(t)$ and $\sigma(t)$ follow the same decay. Figures 2(b) and 2(c) reveal that shear banding is observed during the buildup of wall slip. A high SB is formed with $\varepsilon \simeq 0.2$ and $\dot{\gamma}_+ \simeq 10\ {\rm s}^{-1}$, a value close to the initial shear rate for stick BC. However, for slip BC, $\dot{\gamma}_+$ rapidly drops and approaches $\dot{\gamma}_-$, which leads to the loss of banding structure [hence the lack of $\varepsilon(t)$ and $\dot{\gamma}_\pm$ data for $t \gtrsim 40$ s] and to linear profiles with $\dot{\gamma}_{\rm true} \simeq 5\ {\rm s}^{-1}$ in the steady state. We conclude that at $\dot{\gamma}_{\rm appl} = 8\ {\rm s}^{-1}$ the excess stress relaxes fully due to wall slip for slip BC, while for stick BC it relaxes by SB formation. Both processes have the same time constants since the decay of $\dot{\gamma}_{\rm true}(t)$ for slip BC is the same as the settling of the SB through $\varepsilon(t)$ for stick BC. As a consequence the stress relaxations for stick and slip BC are also similar [see the dashed line in Fig. 1(b)].

Quenches were repeated as described above for final shear rates $\dot{\gamma}_{\rm appl}$ covering almost the whole stress plateau [20]. Figure 3 presents the steady-state values of the true shear rate $\dot{\gamma}^\infty_{\rm true}$ and the proportion of the high SB ε^∞, as well as the amplitude of the relaxation of $\varepsilon(t)$ [noted $\Delta\varepsilon$ and defined in Fig. 2(b)] and that of the stress relaxation $\Delta\sigma$. As shown by the solid line $\dot{\gamma}_{\rm true} = \dot{\gamma}_{\rm appl}$ in Fig. 3(a), stick BC apply for the sandblasted cell. Moreover the linear behavior of ε^∞ vs $\dot{\gamma}_{\rm appl}$ is consistent with the "lever rule": $\varepsilon^\infty = (\dot{\gamma}_{\rm appl} - \dot{\gamma}_1)/(\dot{\gamma}_2 - \dot{\gamma}_1)$ [see solid line in Fig. 3(b)] with $\dot{\gamma}_1 = 3.4 \pm 0.2\ {\rm s}^{-1}$ and $\dot{\gamma}_2 = 22.4 \pm 0.5\ {\rm s}^{-1}$ in satisfactory agreement with both the flow curve and the steady-state values of the local shear rates $\dot{\gamma}_- = 4.3 \pm 0.3\ {\rm s}^{-1}$ and $\dot{\gamma}_+ = 22 \pm 1\ {\rm s}^{-1}$ measured from the velocity profiles [19]. These observations not only confirm previous results in the absence of wall slip [16–18] but also allow us to evidence the migration of the high SB towards the stator (i.e., $\Delta\varepsilon < 0$) for deep quenches. For slip BC, $\dot{\gamma}_{\rm true} = \dot{\gamma}_{\rm appl}$ only holds when $\dot{\gamma}_{\rm appl} < \dot{\gamma}_1$. Wall slip is

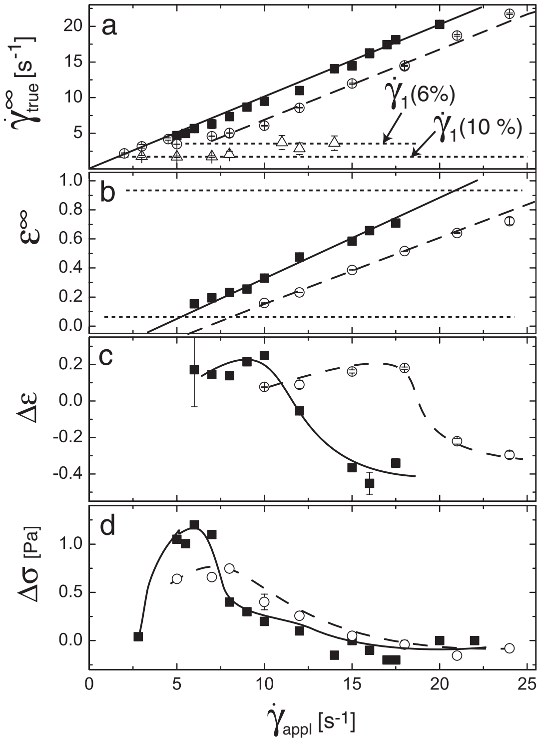

FIG. 3. Steady-state values of (a) the true shear rate $\dot{\gamma}^{\infty}_{\rm true}$ and (b) the proportion of the high SB ε^{∞}, and amplitudes of the relaxations of (c) the proportion of the high SB $\Delta\varepsilon$ and (d) the excess shear stress $\Delta\sigma$ as a function of the imposed shear rate $\dot{\gamma}_{\rm appl}$. Solid (open) symbols refer to stick (slip) BC. All data are for 6 wt % CPyCl-NaSal except for the triangles in (a) which are for 10 wt % CPyCl-NaSal with slip BC. In (a) the solid line is $\dot{\gamma}_{\rm true} = \dot{\gamma}_{\rm appl}$, while the dashed line is $\dot{\gamma}_{\rm true} = \dot{\gamma}_{\rm appl} - 3.4\ {\rm s}^{-1}$ and the dotted lines indicate $\dot{\gamma}_1$ for 6 and 10 wt % CPyCl-NaSal. The dotted lines in (b) show the resolution limit for SB detection [19]. The lines in (c) and (d) are to guide the eye.

observed over the whole stress plateau and $\dot{\gamma}^{\infty}_{\rm true}$ is shifted by a constant $\Delta\dot{\gamma} \simeq 3.4\ {\rm s}^{-1}$ with respect to stick BC. If SB occurs in the presence of wall slip, then one expects ε^{∞} to be shifted by the same amount. Figure 3(b) shows that SB indeed sets in for $\dot{\gamma}_{\rm appl} > \dot{\gamma}_1 + \Delta\dot{\gamma} \simeq 8\ {\rm s}^{-1}$. However, the slope of ε^{∞} vs $\dot{\gamma}_{\rm appl}$ is slightly smaller than for stick BC leading to a shift that increases with $\dot{\gamma}_{\rm appl}$ [see dashed line in Fig. 3(b)]. The same observation holds for Fig. 3(c) where the shift between the $\Delta\varepsilon$ curves is seen to increase up to about 15 s^{-1} for the highest achievable $\dot{\gamma}_{\rm appl}$. This suggests a more subtle influence of wall slip on SB than a mere shift due to the difference between $\dot{\gamma}_{\rm appl}$ and $\dot{\gamma}_{\rm true}$ but remains questionable due to surface instability for very deep quenches. Finally, if one assumes that the viscosity of the slip layer at the rotor does not depend on $\dot{\gamma}_{\rm appl}$ throughout the stress plateau, then a constant $\Delta\dot{\gamma}$ corresponds to some *constant stress* released by wall slip. Figure 3(d) shows that the excess stress $\Delta\sigma$ is most affected by the BC for $\dot{\gamma}_{\rm appl} = 5$–$8\ {\rm s}^{-1}$ (where $\Delta\sigma$ is about twice smaller for slip BC than for stick). At larger $\dot{\gamma}_{\rm appl}$, $\Delta\sigma$ follows roughly the same decay for both BC.

It is interesting to see how the balance between SB and wall slip changes for a more entangled system, e.g., a 10 wt % CPyCl-NaSal sample, as studied by López-González *et al.* [11]. The response to shear rate quenches for this system, where $\sigma^{\star} \simeq 158$ Pa, $\dot{\gamma}_1 \simeq 1.7\ {\rm s}^{-1}$, and $\dot{\gamma}_2 \simeq 20\ {\rm s}^{-1}$ is plotted in Fig. 4. Even in the sandblasted cell where stick BC are supposed to be valid, the true shear rate never coincides with $\dot{\gamma}_{\rm appl}$. Moreover, considerable fluctuations in $\dot{\gamma}_+$ are observed, while $\dot{\gamma}_-$ remains much smoother. For slip BC and $\dot{\gamma}_{\rm appl} = 5\ {\rm s}^{-1}$, we observe that the sample slips to the shear rate $\dot{\gamma}_1$ at the start of the stress plateau where there is no excess stress [see the green line in Fig. 4(a)]. A quench to a higher shear rate of $\dot{\gamma}_{\rm appl} = 8\ {\rm s}^{-1}$ reveals that $\dot{\gamma}_{\rm true}$ jumps from $\dot{\gamma}_1$ to significantly higher values over short time windows indicated by vertical dashed lines in Fig. 4. Velocity profiles also show that, when $\dot{\gamma}_{\rm true} > \dot{\gamma}_1$, a small but detectable high SB forms with $\varepsilon \gtrsim 0.1$ and $\dot{\gamma}_+ \simeq 15$–$20\ {\rm s}^{-1}$. In other words the high-shear state is formed over short periods of time and is unstable over longer times, which is reminiscent of "nucleation and melt" events typical of metastability. Since $\dot{\gamma}_{\rm true} \approx \dot{\gamma}_1$ up to $\dot{\gamma}_{\rm appl} \simeq 12\ {\rm s}^{-1}$ [see open triangles in

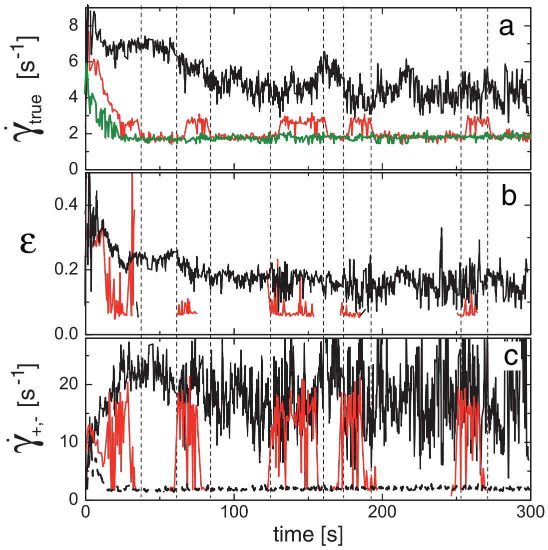

FIG. 4 (color). Responses to shear rate quenches from $\dot{\gamma}_{\rm init} = 0.8\ {\rm s}^{-1}$ to $\dot{\gamma}_{\rm appl} = 8\ {\rm s}^{-1}$ for stick (black) and slip BC (red) in 10 wt % CPyCl-NaSal. (a) True shear rate $\dot{\gamma}_{\rm true}(t)$. The green line is the response to a quench to $\dot{\gamma}_{\rm appl} = 5\ {\rm s}^{-1}$ for slip BC. (b) Proportion of the high SB $\varepsilon(t)$. (c) Shear rate in the high SB $\dot{\gamma}_+(t)$ (solid) and low SB $\dot{\gamma}_-(t)$ (dashed, only stick BC). The vertical dashed lines indicate the times where SB nucleate and melt (see text). The gaps in the slip data in (b) and (c) are due to the lack of SB [19].

Fig. 3(a)], wall slip dominates SB formation over the full accessible part of the stress plateau.

In summary, we established that under slip BC wall slip is observed only for shear rates larger than the start of the stress plateau, i.e., $\dot{\gamma} > \dot{\gamma}_1$. For the 6 wt % sample, SB formation is suppressed by wall slip over the first $\Delta\dot{\gamma} \simeq 3.4\ \mathrm{s}^{-1}$ into the stress plateau, while for higher shear rates stable SB are observed together with partial slip. For 10 wt % CPyCl-NaSal, "nucleation and melt" is observed over the full accessible part of the stress plateau. This has the important implication that for both concentrations wall slip acts as to stabilize the bulk flow.

By combining presently available theories we may interpret our results along the following line of argumentation. Strong gradients in the shear rate can build up at the wall, assuming that wormlike micelles preferentially align with the smooth walls, i.e., that gradients in orientation are intrinsically present at the wall, see Ref. [21]. Orientation gradients grow when the system is quenched into the plateau region, see Refs. [5,6]. The stress that is stored in the system after the quench needs to diffuse in order for the system to relax, see Ref. [22]. These latter two processes should be independent of whether the gradients are present in the bulk or at the wall. Combining these arguments one can explain the observation that no apparent wall slip is observed below the stress plateau because in this region the flow is stable and gradients at the walls or in bulk do not grow. It also follows that the time constants of $\dot{\gamma}_{\mathrm{true}}$ for slip BC and ε for stick BC are comparable in Fig. 2, resulting in similar stress decays [see Fig. 1(b)], since the same stress diffusion is needed in both cases. Once the SB have settled $\dot{\gamma}_- = \dot{\gamma}_1$ holds for the low SB both for stick and slip BC. Fluctuations between both conditions can now easily occur since no stress diffusion is needed. This may account for the difference between the stable low SB and the fluctuating high SB [see Fig. 4(c)], and for the fast formation of the nucleating bands in the more concentrated sample.

To conclude, BC appear to be a crucial control parameter that accounts for some of the fluctuations reported earlier on similar systems [11,12]. The interplay between wall slip and SB formation may have major implications for tuning the flow behavior of complex fluids showing flow instabilities. A full understanding of our experiments still requires a proper combination of the above mentioned theories. The competition between local stress relaxation at the wall via slip and bulk relaxation through SB formation depends on the details of the system, such as the surface treatment and the degree of entanglement in the bulk. A possible microscopic input in the theory could be to mimic surface roughness, i.e., stick BC, by randomizing the alignment of the wormlike micelles at the walls. This is missing from the theoretical work so far. Experiments on a less coarse grained level as was achieved here with USV are also needed to identify micellar orientations at the wall.

The experiments were funded by the SoftComp EU Network of Excellence and performed at CRPP, Pessac, France. The authors thank P. Ballesta and E. Laurichesse for technical help and J. K. G. Dhont, S. Lerouge, and P. D. Olmsted for fruitful discussions.

---

*p.lettinga@fz-juelich.de

[1] D. Roux *et al.*, Europhys. Lett. **24**, 53 (1993); P. T. Callaghan *et al.*, J. Phys. II (France) **6**, 375 (1996); J. van der Gucht *et al.*, Phys. Rev. Lett. **97**, 108301 (2006).
[2] C. Grand *et al.*, J. Phys. II (France) **7**, 1071 (1997).
[3] J.-F. Berret *et al.*, J. Phys. II (France) **4**, 1261 (1994).
[4] H. Rehage and H. Hoffmann, Mol. Phys. **74**, 933 (1991).
[5] J. K. G. Dhont, Phys. Rev. E **60**, 4534 (1999).
[6] P. D. Olmsted *et al.*, J. Rheol. **44**, 257 (2000).
[7] J.-F. Berret, Langmuir **13**, 2227 (1997).
[8] P. P. Drda and S.-Q. Wang, Phys. Rev. Lett. **75**, 2698 (1995).
[9] P. E. Boukany *et al.*, Macromolecules **41**, 2644 (2008).
[10] L. Isa, R. Besseling, and W. C. K. Poon, Phys. Rev. Lett. **98**, 198305 (2007); V. Bertola *et al.*, J. Rheol. **47**, 1211 (2003); J. R. Seth *et al.*, J. Rheol. **52**, 1241 (2008).
[11] M. R. López-González *et al.*, Phys. Rev. Lett. **93**, 268302 (2004).
[12] L. Bécu, S. Manneville, and A. Colin, Phys. Rev. Lett. **93**, 018301 (2004).
[13] Our "smooth" ("rough" respectively) walls have a roughness (average standard deviation of height profiles measured from atomic force microscopy) of 15 nm (0.6 μm respectively).
[14] Rheological data are collected with a stress controlled rheometer (TA Instruments AR 1000) in Couette cells with inner radius 24 mm, outer radius 25 mm, and height 30 mm. A computer-controlled feedback loop is used to apply quenches between constant shear rates and the corresponding stress response $\sigma(t)$ is recorded.
[15] S. Manneville *et al.*, Eur. Phys. J. Appl. Phys. **28**, 361 (2004); USV requires that the acoustically transparent micellar samples be seeded with 0.7 wt % hollow glass spheres (Sphericel, Potters) of mean diameter 6 μm that scatter ultrasound. We checked that this does not significantly affect the rheology of our samples.
[16] J.-B. Salmon *et al.*, Phys. Rev. Lett. **90**, 228303 (2003).
[17] Y. T. Hu and A. Lips, J. Rheol. **49**, 1001 (2005).
[18] E. Miller and J. P. Rothstein, J. Non-Newtonian Fluid Mech. **143**, 22 (2007).
[19] Velocity profiles are linearly extrapolated to estimate the fluid velocities close to the walls $v(0, t)$ and $v(e, t)$, yielding $\dot{\gamma}_{\mathrm{true}}(t) = (v(0, t) - v(e, t))/e$. The intersection and the slopes of linear fits of $v(x, t)$ over the two SB, respectively, yield the position $\delta(t) = e\varepsilon(t)$ of the interface between SB and the local shear rates $\dot{\gamma}_+(t)$ and $\dot{\gamma}_-(t)$. Because of the USV spatial resolution, this fitting procedure cannot ascertain the presence of SB smaller than 80 μm, hence the lack of data points with $\varepsilon \lesssim 0.1$ in Fig. 3(b).
[20] The large shear rate range, as compared to Refs. [17,18], was achieved by using a special lid that reduces the air-sample interface. In this way instabilities of the free surface at high shear rates due to air inclusions are hindered.
[21] J. M. Adams *et al.*, J. Non-Newtonian Fluid Mech. **151**, 101 (2008); L. F. Rossi *et al.*, J. Non-Newtonian Fluid Mech. **136**, 79 (2006).
[22] O. Radulescu *et al.*, Europhys. Lett. **62**, 230 (2003).

Chapter 18

Summary

This Habilitationsschrift treats two main themes: the dynamics and phase separation kinetics of dispersions of colloidal rods *in equilibrium* and *under shear flow.* Part I and II on dispersions of colloidal rods in equilibrium concerns issues that are fundamental to the understanding of lyotropic liquid crystals. In Part I the self-diffusion of rod-like particles throughout the different phases is investigated. It is shown how diffusion is influenced by the different degrees of ordering and, *vise versa*, how the different phases are characterized by the diffusive behavior of the rods. Part II is dedicated to the isotropic-nematic (I-N) phase separation kinetics. Here the interest is to characterize the unstable and meta-stable regions in the bifurcation diagram and the resulting phase separation kinetics. As both are already old issues, at the same time new physical issues arise, like the anomalous diffusion of rods in the smectic phase and the coalescence of nematic droplets. In part III and IV the focus is on the phase behavior and flow behavior of rod-like particles. The goal in part III is very similar to the goal in part II, namely to find the phase boundaries and characterize the phase separation kinetics, but now for a system subjected to shear flow. It is expected that the phase boundaries will shift, because shear flow induces alignment in the system. This is however not straightforwardly the case and the dynamic states of the sheared isotropic and nematic need to be considered. Also flow instabilities are observed, which are caused by the elastic deformation of the biphasic structures. The working horse that we use in part I to III are *fd* viruses, which are the most ideal rods available so far due to the high aspect ratio and stiffness of the rods. In part IV flow instabilities are studied for worm-like 'living' polymers. These are worm-like particles that can break up and recombine and that have a relatively long persistence length. These systems show intriguing similarities and differences with the sheared dispersions of *fd* virus.

The subject of ***Part I*** is ***"Diffusion of rods throughout phase space"***. In chapter 2 and 3 the diffusion around the I-N transition into the nematic phase is studied. The methodology we used for all the papers in Part I, Video Fluorescence Microscopy, is introduced in chapter 2, "*Self-diffusion of rod-like viruses in the nematic phase*". Here a small fraction of viruses is labelled with a fluorescent dye and dispersed in a background of unlabelled rods. The trajectories of individual rods are visualized using fluorescence microscopy from which the diffusion constant is extracted. In chapter 1 we focused on the the diffusion parallel ($D_{\|}$) and perpendicular ($D_{\perp}$) to the nematic director. The ratio ($D_{\|}/D_{\perp}$) increases monotonically with increasing virus concentration. Crossing the isotropic-nematic phase boundary results in increase of $D_{\|}$ and decrease of $D_{\perp}$ when compared to the diffusion in the isotropic phase (D_{iso}).

In chapter 3 we focused on "*Hydrodynamic interactions in dense rod suspensions*". We did this experimentally by comparing the diffusion rate of charged rod-like viruses with and without polymer coating at various ionic strengths. Here we exploited the fact that the surface of the virus can be modified by grafting a polymer layer onto it, together with the fact that the double layer of counter ions can be tuned by the ionic strength of the buffer. Both modifications lead to an effective thicker rod resulting in an I-N phase transition at a lower ionic strength. However, the hydrodynamic interactions will be different because the distance between the surface of two neighboring rods is very different for the two types of modified rods. In computer simulations performed in the group of prof. Gompper in Jülich the hydrodynamic interactions are directly accessed by explicitly simulating the solvent. The anisotropy in the diffusion of rods in the nematic phase is dominated by the effective excluded volume, while the absolute values of the diffusion coefficients are strongly affected by hydrodynamic interactions. In all cases the total diffusion increases after the I-N transition, which can be regarded as a signature of the increase in the positional entropy.

The other two chapters in Part I concern the diffusion of rods in the smectic phase. The main results are presented in chapter 4, "*Self-Diffusion of Rodlike Viruses through Smectic Layers*". It was always thought that in the smectic phase rods behave liquid-like within the layer, while positional entropy in the third direction is lost. We, however, directly visualized at the scale of single particles a significant mass transport between smectic layers, also called permeation. Self-diffusion takes place preferentially in the direction normal to the smectic layers, and occurs by quasiquantized steps of one rod length. This was illustrated by analyzing individual tracks, but also by the distinct peaks at integer rod lengths in the Self-van Hove function, which is the probability to find a particle at position r at time t, given that is was at position 0 at time 0. We calculated the probability of the position of the rod with respect to the middle of the layer, from which the mean potential energy that stabilizes the smectic layers could be inferred, using the Boltzmann factor. Thus diffusion in the smectic phase is a nice example of the diffusion of a Brownian particle in a periodic potential, given that the rods move almost only in the direction parallel to the long axis. Using an exact theory for such a process, we could show that the diffusion rate corresponds with the rate calculated from the diffusion in the nematic state with the lamellar periodic ordering potential that is obtained from the positional distribution function. Note that all of these features cannot be found by scattering techniques. The diffusion within the layer has a glassy character, i.e. it is a subdiffusive process. Thus we concluded that the smectic phase of *fd* viruses consists of layers of glassy rods.

In chapter 5, "*Dynamical and structural insights into the smectic phase of rod-like particles*", we extended the analysis of the diffusion and focus on the subdiffusive character of the transport process. It is shown that the motion of the rods is subdiffusive before the rod has diffused its own length and becomes almost diffusive for longer times. The diffusion perpendicular to the rod also becomes more diffusive, but is still glassy-like. There is a qualitative agreement between the probability density function of displacement at different times, i.e. the self-van Hove function, that was found experimentally with the theoretical predictions based on a dynamical density functional theory.

Part II is dedicated to the "***Isotropic-nematic Phase separation kinetics***". To understand the nature of the I-N and N-I phase transition one has to access the kinetics of these transitions. For this the system needs to be 'quenched' from a stable state to an unstable state. Though this is generally experimentally difficult, we took advantage of the fact that there are two parameter that determine the phase behavior of colloidal rods: position *and* orientation. This means that a quench can also be made by pre-aligning the rods with an external field and studying the response of the system when this nematic stabilizing field is switched off. Performing such quenches at different concentrations within the isotropic-nematic coexistence region will render the system meta-stable or unstable, such that the N-I spinodal and binodal points can be probed. In order to access a wide range of concentrations, the polysaccharide dextran was added to the dispersion, which induces depletion interactions between the rods. This results in an increase in the width of the biphasic region as well as higher contrast between the different phases.

In chapter 6, "*Kinetic pathways of the nematic-isotropic phase transition as studied by confocal microscopy on rod-like viruses*", the main features of the N-I phase separating process are outlined. Here we used confocal microscopy in combination with a shear cell. The contrast in the microscopy is due to differences in birefringence, i.e. polarization confocal microscopy. If the quench is performed at high concentrations then dark spindle-like structures are formed after some induction time. These spindles are atactoids, which means that they are droplets of the isotropic phase in a background of the nematic phase. They are randomly distributed in space but all have the same orientation, namely with the long axis parallel to the director of the nematic, i.e. the direction of the applied field before the quench. The finite induction time and the randomly distributed isotropic nuclei are clear signatures for a nucleation-and-growth process. Hence at high concentrations the system is meta-stable after switching of the field. For quenches at low concentration phase separation immediately sets in and a bicontinuous structure is formed. This is typical for systems that undergo spinodal decomposition. Hence for the low concentrations the system is unstable after the quench. At intermediate concentrations we identified the transition between both demixing processes, where the spinodal point is located. Except for the fact that these experiments show that we have the experimental tools to locate the N-I spinodal, maybe the most fascinating observation of this paper is the late stages of the spinodal decomposition. First, we observed that the bicontinuous structure breaks up in small nematic tactoids, instead of a gradually growing bicontinuous structure. Eventually these tactoids grow, mainly via coalescence. The coalescence process on itself is very interesting because it seems that it can only take place when tactoids have a specific orientation with respect to each other. Also the aspect ratio of the tactoids decreases with increasing size as predicted from theory.

"*Nematic-isotropic spinodal decomposition kinetics of rodlike viruses*" are further studied in chapter 7. Here we used confocal microscopy as well as small-angle light scattering to monitor spinodal decomposition after a shear rate quench. Plotting the eigenvalue $\lambda^{(-)}$, which quantifies the rate of the phase separation, versus the scattering angle k we observed that $\lambda^{(-)}$ approaches a nonzero constant value for $k \to 0$. In contrast, for gas-liquid demixing of spheres the corresponding eigenvalue becomes zero for $k \to 0$. This is due to the fact that for rods a local reorientation is sufficient to start the phase separation, whereas for spheres translational diffusion over finite distances is needed. This corresponds with the theoretical predictions for an initially isotropic phase, where it is shown that concentration fluctuations follow fluctuations in the orientation. Translational diffusion dominates when the concentration of dextran is increased.

The effect of attraction on the kinetics of the I-N transition is studied into more detail in chapter 8, "*Supersaturated dispersions of rodlike viruses with added attraction*". The N-I spinodal points for dispersions of rods with varying concentrations of dextran were obtained again from orientation quenches using cessation of shear flow in combination with small-angle light scattering. We found that the location of the N-I spinodal point is independent of the attraction, which was confirmed by theory. Surprisingly, the experiments showed that also the absolute induction time, the critical nucleus, and the growth rate are insensitive to the attraction if the concentration is scaled to the distance to the phase boundaries, i.e. the binodal points. In addition we also applied concentration quenches using pressure jumps. Here we profit from the compressibility of water, which is about 5 % at 1 kbar. We probed the response with polarization microscopy, birefringence, and turbidity measurements. The full biphasic region could be accessed, resulting in the construction of an experimental analog of the bifurcation diagram.

Part III describes the '***Isotropic-nematic Phase Transition under shear flow*** '. Chapter 9, "*Non-equilibrium phase behaviour of rod-like viruses under shear flow*" , summarizes the main physical phenomena that play a role: The shape of the binodal line, the dynamic behavior of the nematic in shear flow, and the formation of vorticity shear bands. In the following chapters each of these themes is studied in detail.

In chapter 10 the "*Flow Behavior of Colloidal Rodlike Viruses in the Nematic Phase*" is treated. The monodisperse nature of these rods combined with relatively small textural contribution to the overall stress make this a suitable model system to investigate the effect of flow on the nonequilibrium phase diagram. Transient rheological experiments are used to determine the critical shear rates at which director tumbling, wagging, and flow-aligning occurs.

The present model system enables us to study the effect of rod concentration on these transitions. The results are in quantitative agreement with the Doi-Edwards-Hess model. Moreover, we observed that there is a strong connection between the dynamic transitions and structure formation, which is not incorporated in theory.

In chapter 11 "*Attractive Colloidal Rods in Shear Flow*" are studied, focussing on the effect of shear flow on the isotropic-nematic phase transition of attractive colloidal rods. When a biphasic dispersion of rods is sheared, a flow aligned isotropic (paranematic) phase coexists with a tumbling nematic phase, as we know it from chapter 10. The location of binodals and spinodals are determined using small-angle light scattering and step rate rheology experiments. The maximum of the binodal is set by the tumbling-to-aligning transition line. Thus it could be concluded that the collective rotational motion of the nematic phase frustrates the merging of the coexisting regions. This was confirmed by simulations. The phase diagrams in the shear-concentration plane for the various strengths of attractions can be mapped onto a master curve by appropriate scaling, similar to the results presented in chapter 8.

In a part of the biphasic region " *Vorticity banding in rodlike virus suspensions*" are observed, which is the subject of chapter 12. Banding occurs uniformly throughout the cell gap within a shear-rate interval, which depends on the rod concentration. For shear rates below the lower-border shear rate only shear elongation of inhomogeneities, which are formed due to paranematic-nematic phase separation, is observed. Within a small region just above the upper-border shear rate, banding occurs heterogeneously. The kinetics of vorticity banding is essentially different, depending on the morphology of inhomogeneities formed during the initial stages of the paranematic-nematic phase separation, as described in part II. Particle tracking and polarization experiments indicate that the vorticity bands are in a weak rolling flow, superimposed on the applied shear flow. We suggest that the mechanism to explain the origin of the banding instability and the transient stability of the banded state is related to the normal stresses generated by inhomogeneities formed due to the underlying paranematic-nematic phase transition.

The question "*Is vorticity-banding due to an elastic instability?*" is answered in chapter 13. A mechanism similar to the well-known elastic instability for polymer systems (the Weissenberg effect) is proposed, where nonuniform elastic deformation are caused by gradients in the local shear rate. The role of polymer chains is now played by the inhomogeneities due to the underlying paranematic-nematic phase transition. Nonuniform deformation of these inhomogeneities are thus proposed to lead to hoop stresses which give rise to banded structures where there is secondary, weakly rolling flow within each of the bands.

In ***Part IV*** "***Flow instabilities in dispersions of worm-like particles***" are studied for three different systems. These systems can all be categorized as 'living' polymers, which are polymer-like particles that can break up and recombine. They are quite stiff, meaning that the ratio of Kuhn-length over the diameter is at least about 10, so that they can generally be described as "worm-like". All of the three systems show shear band formation, but now in the gradient direction, when submitted to shear flow in the region where there is strong shear-thinning. The origin of this flow instability is different for the different systems.

In chapter 14 the "*Multiple Shear-Banding Transitions in a Supramolecular Polymer Solution*" is studied. This system consists of reversible supramolecular polymers, based on hydrogen bonding. Velocity profiles measured by heterodyne dynamic light scattering indicate three different shear-banding regimes upon increasing shear rate, each with different characteristics. While the first of these regimes has features of a mechanical instability, as for the surfactant wormlike micelles, the second shear-banding regime is related to a shear-induced phase separation and the appearance of birefringent textures, similar to the block copolymer wormlike micelles. The shear-induced phase itself becomes unstable at very high shear rates, giving rise to a third banding regime. This cascade of flow instabilities is very unusual.

"*Dynamic response of block copolymer wormlike micelles to shear flow*", described in chapter 15, is dominated by the proximity of the isotropic-nematic phase transition and hence by the critically slowing down of the rotational diffusion. As in chapter 9 we first determined the location of I-N phase transition lines by rheological step down experiments. To probe the critical slowing down we determined the rheological and structural response to an oscillatory shear flow by means of Fourier transform rheology and time-resolved small-angle neutron scattering experiments, respectively. The equation of motion for rod-like particles linking the order parameter tensor to the the stress tensor is used to interpret the experimental data, both in the linear and nonlinear regimes. Scaling of the dynamic behaviour of the orientational order parameter and the stress is found when critical slowing down due to the vicinity of the isotropic-nematic spinodal is accounted for. Rheological flow curves show also that the sample displays extreme shear thinning behavior on approaching the I-N spinodal. Using heterogeneous dynamic light scattering we confirm that indeed gradient shear bands form close to this spinodal point in a well defined range of shear rates. Thus this system is one of the very few, if not the first, examples of gradient banding due to the critical slowing down of the rotational diffusion.

Far more common is the gradient shear banding in the third system that was studied, i.e. surfactant wormlike micelles, in particular cetylpyridinium chloride/sodium salicylate (CPyCl-NaSal) micellar solutions in 0.5 M NaCl brine. Here shear thinning is mainly related to the cession and recombination kinetics of the worms. In chapter 16 it is described how "*Superposition rheology of shear-banding wormlike micelles*" can be used to verify the existence of shear bands with a standard rheometer. By superimposing a shear oscillation to steady shear in the shear banding regime, the interface between high- and low-shear regions oscillates in time. A two-fluid semi-phenomenological model was proposed for superposition rheology in the shear banding regime, which allowed us to extract a characteristic velocity for the interface dynamics from experiments involving only a standard rheometer. Estimates of the 'stress diffusion coefficient' can also be inferred from such superposition experiments. The validity of our model is confirmed by directly recording the interface displacement using ultrasonic velocimetry coupled to standard rheology in Couette geometry.

The same combination of system and technique was used to study "*Competition between* *shear banding and wall slip in wormlike micelles*" described in chapter 17. In this case time-resolved velocity profiles are recorded during transient strain-controlled experiments in smooth and sandblasted geometries. For stick boundary conditions standard shear banding is observed, although depending on the degree of micellar entanglement temporal fluctuations are reported in the highly sheared band. For slip boundary conditions wall slip occurs only for shear rates larger than the start of the stress plateau. At low entanglement, shear band formation is shifted by a constant, while for more entangled systems shear bands constantly nucleate and melt. This has the important implication that for both concentrations wall slip acts as to stabilize the bulk flow. Micellar orientation gradients at the walls may account for these original features.

Acknowledgement

When I started working in Jülich there was almost nothing except for a set-up from Utrecht that has been moved during my stay for about five times. After spending the first couple of months on reading THE book of Jan Dhont, my boss but mostly my inspirator for all the work presented here and more, I set out repeating experiments of my predecessors. This work was on the behavior of critical mixtures of colloidal spheres and polymers under shear flow. Doing so, I found out how fruitful it is to combine experiment, chemistry, and theory all in one group. Here and in later work I profitted for example a lot from the theoretical support of Hao Wang, who worked in Jülich as a post-doc, and Jan Dhont.

At that time also Zvonimir Dogic came to our group, who wanted to study the behavior of colloidal rods under shear flow. For this he wanted to use the set-up I had been using for my first experiments, so he asked for my help. The rest is 'history', meaning to say that this was actually the starting point of this Habilitationsschrift. It wouldn't have existed in its present form without his expertise and his very observing and deducing mind and the visits to his Lab in the Rowland institute at Harvard and Brandeis. Also it wouldn't have existed without the system he introduced here, i.e. our ideal rods the *fd* virus and the billions of bacteria that have been grown and killed to produce these viruses, and without the technical assistance of Karin Sellinghof who did most of that. In producing a huge amount of light scattering data, profiting of his critical mind and being a good room mate I'm very much indebted to Peter Holmqvist. I thank Kyongok Kang for the careful mapping of the vorticity banding behavior, which was crucial for gaining our present level of understanding of this complex process. The gradient banding experiments we did in Jülich could not have been done without the heterodyne dynamic light scattering that was set-up and operated by Hartmut Kriegs. Although her name pops up only once in all the papers I bundled here, I'm much indebted to my first 'half' PhD student Monika Ratajczyk. She performed an unique and difficult experiment with great determination, supported by our big Grizzly Gerd Meier.

The collaborations between the three 'Joint Soft Matter' groups within the IFF were very fruitful. The input from the simulations by Sebastian Messlinger and Marisol Ripoll from the group of Gerhard Gompper and Roland Winkler gave the microscopic insight that we missed doing our experiments. The group of Dieter Richter provided the link between rods and polymers. I profited from the synthesis facilities and expertise from Lutz Willner and the experimental craftsmanship and nice company in the traveling between Aachen and Jülich of Barbara Lonetti.

The rheological behavior of dispersions plays an important role in this thesis. The person that taught me about rheology and that pointed out the way to understand the complex behavior of sheared liquid crystals is my rheological conscious Jan Vermant from the Katholieke Universiteit Leuven. The Forschungszentrum was so kind to send me for half a year to the Centre Recherche Paul Pascal in Bordeaux. This period turned out to be extremely fruitful, and I am still picking the fruits. Sebastien Manneville was a open-minded host who taught me, together with his student Pierre Ballesta, all about wormlike micelles in combination with ultrasound velocimetry. After five months of playing basketball with Eric Grelet we finally talked science so that in the last few weeks at the CRPP we also started to work on the diffusion of *fd* virus in concentrated phase, which was and still is a pleasant and fruitful collaboration. Going back to my home town of Wageningen, I want to thank Jasper van der Gucht and his coworkers for introducing me in the world of living polymers. Going back to the place where I became a Physicist, Utrecht, I want to thank Didi Derks and Arnout Imhof for teaching me how to do microscopy under flow and Paul van der Schoot and Rene van Roij for gaining theoretical understanding of rods almost at rest.

The work in Jülich has not only be pleasant for the above mentioned reasons but also because of the nice atmosphere in our group, which most probably is connected with the people that work in our group. Here I specially want to thank Marie Göcking, our secretary, and Manolis Stiakakis how takes care that new fields of research are being opened while I'm writing these sentences.

Still, the feeling of opening the door of the institute in the morning cannot be compared with the feeling of opening the door of my home in the evening. The things that happen then are of course private but I am very happy to share them with Juliane Cromme and the three children, Mathilde, Carl and Elisabeth, that we have together.

Scientific Curriculum Vitae

- 1970: Born on 15th of June 1970 in Delft, The Netherlands.
- 1982 - 1988: Gymnasium in Wageningen, The Netherlands.
- 1988 - 1994: Study Experimental physics at University Utrecht, the Netherlands. Specialization Molecular Biophysics in Utrecht and in Bologna, Italy.
- 1994: Guest-scientist at Department for Physical Chemistry, University of Padova, Italy.
- 1994 - 1999: PhD at Department of Molecular Biophysics and the Van ‘t Hoff Laboratory for Physical and Colloidal Chemistry, University Utrecht, the Netherlands.
- 1999 - 2000: Post-doc at Van ‘t Hoff Laboratory for Physical and Colloidal Chemistry, University Utrecht, the Netherlands.
- 2000 - 2001: Post-doc at Forschungszentrum Jülich, Institute for Solid state physics, Soft condensed Matter group, Jülich, Germany.
- 2001: Staff member at Forschungszentrum Jülich, Institute for Solid state physics, Soft condensed Matter group, Jülich, Germany.
- 2005: Visiting researcher for half a year at Centre Recherche Paul Pascal, CNRS, Pessac, France.
- Winter 2011: Habilitation at the Science Faculty of the Heinrich Heine university Düsseldorf.

Recent educational tasks

- Presently supervising two PhD students at the Forschungszentrum Jülich and co-supervising two PhD students in collaboration with the Katholieke Universiteit Leuven (with Jan Vermant) and the University of Oxford (with Dirk Aarts).

At the Heinrich Heine University in Düsseldorf:

- 2010/2011: Ergänzungsvorlesung im Rahmen der Vorlesung Biophysik
- 2010: Ergänzungsvorlesung im Rahmen der Vorlesung Theory of Soft Matter
- 2009/2010: Ergänzungsvorlesung im Rahmen der Vorlesung Biophysik
- 2009/2010: Ergänzungsvorlesung im Rahmen der Vorlesung Einführungin die Physik der Kolloiden: Theorie und Experiment
- 2008/2007: Rheology in the masterprogram of physics

Other tasks:

- 2008: Series of Lectures at Forth institute in Crete, 2008
- Lectures at the IFF-Ferienkurs 2002, 2004, and 2008
- 2008: Two Fachhochschule Students from Jülich (one master thesis)
- 2008: One PhD, graduated November in Poznan
- As a PhD I developed and gave a practical course Molecular Biophysics for Medical biologists.

Funding

At the Forschungszentrum Jülich we are funded directly from the state, for which we have to apply on a five year base. Here I took active part by giving presentations. As a consequence of this funding mechanism, we cannot apply for grants except in the context of international networks. Below I summarize in which networks I am active and what they funded:

- Project leader in the SFB-Transregio 6, Colloids in External fields. This network funded till the present a Post-Doc position over the last eight years.
- One PhD position funded by the International Helmholtz Research School of Biophysics and Soft Matter.
- One travel grand from the Royal Society of science together with Dirk Aarts, University of Oxford.

- Two Post-doc position were funded via the european Netowrk of Excellence SoftComp over the last three years together with Eric Grelet , CRPP, Pessac.

Organization of Workshop

- ’Playing colloidal mikado II’, Université du Luxembourg, Luxembourg, 27-29 May, 2010
- ’Playing colloidal mikado’, University of Oxford, Oxford, 6-8 July, 2009
- Co-chairman of Euromech Colloquium 492, Shear banding in entangled systems University College London, London, September 3-5, 2007.

Referee

Phys. Rev. Lett., Europhys. Lett., Phys. Rev. E, J. Chem. Phys., Rheologica Acta, Soft Matter

Publications

The most important publications are marked in boldface.

Peer reviewed papers:

1. M. P. Lettinga and J. K. G. Dhont and Z. Zhang and S. Messlinger and G. Gompper. Hydrodynamic Interactions in Rod Suspensions with Orientational Ordering. *Soft Matter*, 6:4556-4562, 2010.

2. **M. P. Lettinga and S. Manneville. Competition between Shear Banding and Wall Slip in Wormlike Micelles. *Phys. Rev. Lett.*, 103:248302, 2009.**

3. P. Holmqvist, M. Ratajczyk, G. Meier, H. H. Wensink, and M. P. Lettinga. Supersaturated dispersions of rodlike viruses with added attraction. *Phys. Rev. E*, 80:031402, 2009.

4. Z. Zhang, N. Krishna, M. P. Lettinga, J. Vermant, and E. Grelet. Reversible Gelation of Rod-Like Viruses Grafted with Thermoresponsive Polymers. *Langmuir*, 25:2437-2442, 2009.

5. R. Vavrin, J. Kohlbrecher, A. Wilk, M. Ratajczyk, M. P. Lettinga, J. Buitenhuis and G. Meier. Structure and phase diagram of an adhesive colloidal dispersion under high pressure: A small angle neutron scattering, diffusing wave spectroscopy, and light scattering study. *J. Chem. Phys.*, 130:154903, 2009.

6. J. Gapinski, A. Patkowski, A. J. Banchio, J. Buitenhuis, P. Holmqvist, M. P. Lettinga, G. Meier, and G. Nägele. Structure and short-time dynamics in suspensions of charged silica spheres in the entire fluid regime. *J. Chem. Phys.* , 130:084503, 2009.

7. E. Grelet, M. P. Lettinga, M. Bier, R. van Roij and P. van der Schoot. Dynamical and structural insights into the smectic phase of rod-like particles. *J. Phys.: Condens. Matter*, 20:494213, 2008.

8. **M. Ripoll, P. Holmqvist, R. G. Winkler, G. Gompper, J.K.G. Dhont, and M. P. Lettinga. Attractive Colloidal Rods in Shear Flow. *Phys. Rev.Lett.*, 101:168302, 2008.**

9. B. Lonetti, J. Kohlbrecher, L. Willner, J. K. G. Dhont and M. P. Lettinga. Dynamic response of block copolymer wormlike micelles to shear flow. *J. Phys.: Condens. Matter*, 20:404207, 2008.

10. J. Sprakel, E. Spruijt, M. A. Cohen Stuart, N. A. M. Besseling, M. P. Lettinga and J. van der Gucht. Shear banding and rheochaos in associative polymer networks. *Soft Matter*, 4:1696-1705, 2008.

11. K. Kang, M. P. Lettinga, J. K. G. Dhont. Is vorticity-banding due to an elastic instability? *Rheol. Acta* , 47:499-508, 2008.

12. G. Meier, R. Vavrin, J. Kohlbrecher, J. Buitenhuis, M. P. Lettinga and M. Ratajczyk. SANS and dynamic light scattering to investigate the viscosity of toluene under high pressure up to 1800 bar. *Meas. Sci. Technol.*, 19:034017, 2008.

13. C. F. Rediguieri, O. de Freitas, M. P. Lettinga, and R. Tuinier. Thermodynamic Incompatibility and Complex Formation in Pectin/Caseinate Mixtures. *Biomacromolecules*, 8:3345-3354, 2007.

14. **M. P. Lettinga and E. Grelet. Self-Diffusion of Rodlike Viruses through Smectic Layers. *Phys. Rev. Lett.*, 99:197802, 2007.**

15. P. Ballesta, M. P. Lettinga, and S. Manneville. Superposition rheology of shear-banding wormlike micelles. *J. Rheology*, 51(5):1047-1072, 2007.

16. J. Gapinski, A. Patkowski, A. J. Banchio, P. Holmqvist, G. Meier, M. P. Lettinga, and G. Nägele. Collective diffusion in charge-stabilized suspensions: Concentration and salt effects. *J. Chem. Phys.*, 126:104905, 2007.

17. A. J. Banchio, J. Gapinski, A. Patkowski, W. Häußler, A. Fluerasu, S. Sacanna, P. Holmqvist, G. Meier, M. P. Lettinga, and G. Nägele. Many-body hydrodynamic interactions in Charge-Stabilized Suspensions. *Phys. Rev. Lett.*, 96:138303, 2006.

18. J. Kohlbrecher, G. Meier, and M. P. Lettinga. Colloidal dispersions of octadecyl grafted silica spheres in toluene: A global analysis of small angle neutron scattering contrast variation and concentration dependence measurements. *J. Chem. Phys.*, 125:044715, 2006.

19. J. van der Gucht, M. Lemmers, W. Knoben, N. A. M. Besseling, and M. P. Lettinga. Multiple shear-banding transitions in a supramolecular polymer solution. *Phys. Rev. Lett.*, 97:108301, 2006.

20. **K. Kang, M. P. Lettinga, Z. Dogic, and J. K. G. Dhont. Vorticity banding in rodlike virus suspensions. *Phys. Rev. E*, 74:026307, 2006.**

21. M. P. Lettinga, K. Kang, A. Imhof, D. Derks, and J. K. G. Dhont. Nematic-isotropic spinodal decomposition kinetics of rod-like viruses. *Phys. Rev. E.*, 73:011412, 2006.

22. M. P. Lettinga, K. Kang, A. Imhof, D. Derks, and J. K. G. Dhont. Kinetic pathways of the nematic-isotropic phase transition as studied by confocal microscopy on rod-like viruses. *J. Phys.: Condens. Matter*, 17:s3609-s3618, 2005.

23. P. Holmqvist, M. P. Lettinga, J. K. G. Dhont. Crystallization Kinetics of Colloidal Spheres under Stationary Shear Flow. *Langmuir*, 21:10976-10982, 2005.

24. M. P. Lettinga, E. Barry, and Z. Dogic. Self-diffusion of rod-like viruses in the nematic phase. *Europhys. Lett.*, 71:692-698, 2005.

25. **M. P. Lettinga, Z. Dogic, H. Wang, and J. Vermant. Flow behaviour of colloidal rodlike viruses in the nematic phase. *Langmuir*, 21:8048-8057, 2005.**

26. K. Kang, J. Gapinski, M. P. Lettinga, J. Buitenhuis, G. Meier, M. Ratajczyk, J. K. G. Dhont, and A. Patkowski. Diffusion of spheres in crowded suspensions of rods. *J. Chem. Phys.*, 122:044905, 2005.

27. M. P. Lettinga and J. K. G. Dhont. Non-equilibrium phase behavior of rod-like viruses under shear flow. *J. Phys.: Condens. Matter*, 16:s3929-s3939, 2004.

28. M. P. Lettinga, H. Wang, and J. K. G. Dhont. Microstructural response of a near-critical colloid-polymer mixture to shear flow. *Phys. Rev. E*, 70:061405, 2004.

29. M. P. Lettinga, G. H. Koenderink, B.W.M. Kuipers , E. Bessels, and A. P. Philipse. Rotational dynamics of colloidal spheres probed with fluorescence recovery after photobleaching. *J. Chem. Phys.*, 120(9):4517-4529, 2004.

30. J. K.G. Dhont, M. P. Lettinga, Z. Dogic, T. A. J. Lenstra, H. Wang, S. Rathgeber, P. Carletto, L. Willner, H. Frielinghaus, and P. Lindner. Shear-banding and microstructure of colloids in shear flow, *Faraday Discuss.*, 123:157-172, 2003.

31. G. H. Koenderink, H. Zhang, M. P. Lettinga, G. Nägele, and A. P. Philipse. On the validity of Stokes-Einstein-Debye relations for rotational diffusion in colloidal suspensions. *Faraday Discuss.*, 123:335-355, 2003.

32. H. Wang, M. P. Lettinga, and J. K. G. Dhont. Microstructure of a near-critical colloidal dispersions under stationary shear flow, *J. Phys.: Condens. Matter*, 14:7599-7615, 2002.

33. G. H. Koenderink, H. Zhang, M. P. Lettinga, G. Nägele, and A. P. Philipse. Rotational tracer diffusion in binary colloidal sphere mixtures. *Phys. Rev. E*, 64:022401, 2001.

34. M. P. Lettinga, C. M. van Kats, and A. P. Philipse. Rotational diffusion of tracer spheres in packings and dispersions of colloidal spheres studied with Time-resolved Phosphorescence Anisotropy. *Langmuir*, 16(15):6166-6172, 2000.

35. M. P. Lettinga, M. A. M. J. van Zandvoort, C. M. van Kats, and A. P. Philipse. Phosphorescent colloidal silica spheres as tracers for rotational diffusion studies.*Langmuir*, 16(15):6156-6165, 2000.

36. M. P. Lettinga, H. Zuilhof, and M. A. M. J. van Zandvoort. Phosphorescence and fluorescence characterization of fluorescein derivatives immobilized in various polymer matrices. *Phys. Chem. Chem. Phys.*, 2:3697-3707, 2000.
37. M. P. Lettinga, E. M. Klarenbeek, H. Zuilhof, and M. A. M. J. van Zandvoort. The orientation of the phosphorescence dipole moment of Erytherosine within its molecular frame. *J. Fluorescence*, 9:265-276, 1999.
38. A. Barbon, P. Lettinga, and P.-L Nordio. Analysis of temperature dependent fluorescence polarization for dimethylaminobenzonitrile. *Chemical Physics*, 200:41-47, 1995.
39. M. A. M. J. van Zandvoort, D. Wróbel, P. Lettinga, G. van Ginkel, and Y. K. Levine. Chlorophylls in polymers. I. State of chlorophyll a in unstretched polymer systems. *Photochem. and Photobiol.*, 62:279-289, 1995.
40. D. Wróbel, M. A. M. J. van Zandvoort, P. Lettinga, G. van Ginkel, and Y. K. Levine. Chlorophylls in polymers. II. Pheophytin a in polymer and the influence of stretching on the state of chlorophylls in anhydrous polymer films. *Photochem. and Photobiol.*, 62:290-298, 1995.
41. M. A. M. J. van Zandvoort, D. Wróbel, P. Lettinga, G. van Ginkel, and Y. K. Levine. The orientation of the transition dipole moment of chlorophyll a and Pheophytin a in their molecular frame. *Photochem. and Photobiol.*, 62:299-308, 1995.

Conference Reports:

1. H. J. Wilson and M. P. Lettinga. Euromech Colloquium No. 492: Shear-banding Phenomena in Entangled Systems Appl. Rheol. (2008) Vol. 18, 378-379.

Contributions to Books:

1. M. P. Lettinga. The dynamics of rods in different phases, in Soft Matter From Synthetic to Biological Materials, Vorlesungsmanuskripte für den 39. IFF-Ferienkurs 2008.
2. M. P. Lettinga. Viruses as colloidal model systems, in Physics meets Biology, Vorlesungsmanuskripte für den 35. IFF-Ferienkurs 2004.
3. M. P. Lettinga. Phase Separation Kinetics, in Soft Matter, Complex Materials on Mesoscopic Scales, Vorlesungsmanuskripte für den 33. IFF-Ferienkurs 2002.

PhD Thesis:

PhD thesis: http://www.library.uu.nl/digiarchief/dip/diss/1890435/inhoud.htm

Presentations

2001

- Microscopic origin of the non-linear viscoelastic response of colloidal dispersions. *Institut für Festkörperforschung: Informationsveranstaltung für den Wissenschaftlichen Beirat, FZ-Jülich.* 26.04.2001

- Microscopic origin of the non-linear viscoelastic response of collidal dispersions. *Jülich Soft Matter Seminar in Kerkrade, The Netherlands* 16.11.2001

- Microscopic origin of the non-linear viscoelastic response of collidal dispersions *Katholieke Universiteit Leuven, Belgium: Seminarvortrag* 17.12.2001

2002

- Phase separation kinetics *Soft matter: complex materials on mesoscopic scales; 33. IFF-Ferienkurs , FZ-Jülich* 04.03.2002 - 15.03.2002

2003

- Dynamic behaviour of liquid crystalline fd-virus suspensions in shear flow *Annual European Rheology Conference 2003, Guimaraes, Portugal* 11.09.2003 13.09.2003

- Dynamic behaviour of liquid crystalline fd-virus suspensions in shear flow *SFB-Treffen: Transregio in Mainz* 22.09.2003 23.09.2003

- Non-equilibrium phase behaviour of fd-virus dispersions in shear flow *Rowland Institute at Harvard Cambridge, Massasuchets, USA: Seminarvortrag* 05.11.2003

- Non-equilibrium phase behaviour of fd-virus dispersions in shear flow *Brandeis University Waltham, USA: Seminarvortrag* 12.11.2003

2004

- Viruses as Colloidal Model Systems Physics meets Biology: From Soft Matter to Cell Biology *IFF 35th Spring School 2004, FZ-Jülich* 22.03.2004 02.04.2004

- Non-equilibrium phase behaviour of fd-virus dispersions in shear flow *CODEF - Sonderforschungsbereich: Transregio 6 in Bonn, GSI* 29.03.2004 01.04.2004

- Non-equilibrium phase behaviour of fd-virus, dispersions in shear flow *Technische Universität Berlin: Seminarvortrag* 10.02.2004 12.02.2004

- Non-equilibrium phase behaviour of fd-virus, dispersions in shear flow *Wageningen University: Seminarvortrag* 22.12.2004

- Non-equilibrium phase behaviour of fd-virus, dispersions in shear flow *CRPP Bordeaux, France : Seminarvortrag* 05.11.2004

2005

- Shear band formation in wormlike micelles as studied by ultrasonic velocimetry *SoftComp Meeting: GSI Bonn* 30.10.2005 31.10.2005
- Shear band formation in wormlike micelles as studied by ultrasonic velocimetry *Laboratoire du Future, Pessac, France: Seminarvortrag* 16.09.2005
- The kinetics of the nematic-isotropic phase transition *6th Liquid Matter Conference Utrecht, The Netherlands* 02.07.2005 06.07.2005
- Shear band formation in wormlike micelles as studied by ultrasonic velocimetry *Centre Reserche Paul Pascal, Pessac, France: Seminarvortrag* 21.09.2005
- The phase behavior and shearband formation of attractive rods under shear *2nd Annual European Rheology Conference Grenoble, France* 21.04.2005 23.04.2005
- Flow behaviour of fd-virus and wormlike micelles *KU Leuven: Joint Symposium Rheology of Dutch and Belgium Colloidal Society Leuven, Belgium* 23.10.2005

2006

- Exploring the phase behavior of rod dispersions using external fields *Colloids, Interfaces and Liquid Crystals: 13th Course Erice, Italy* 19.07.2006 25.07.2006
- Real space observation of rod-like viruses in the nematic phase under shear *3rd Annual European Rheology Conference , Hersonisos, Greece* 26.04.2006 29.04.2006
- Diffusion of rodlike viruses throughout the concentration-shear-rate plane *SFB-TR6 Workshop 2006: GSI Bonn* 20.03.2006 22.03.2006
- The dynamics and phase behavior of rodlike viruses *Forschungszentrum Jülich: Zentralbibliothek; Beiratssitzung* 25.09.2006 26.09.2006
- Mesoscopic transport phenomena *TU Eindhoven: Seminarvortrag* 09.06.2006
- Dynamics of rod-like viruses in shear flow *Jülich Soft Matter Days 2006: GSI Bonn* 14.11.2006 17.11.2006

2007

- The dynamics and phase behavior of rod like viruses *Universität des Saarlandes, Saarbrücken: Seminarvortrag* 26.01.2007

- Time-resolved SANS on giant wormlike micelles under shear *American Physical Society Denver, Colorado, USA* 06.03.2007 10.03.2007
- The kinetics and dynamics underlying phase transitions in lyotropic liquid crystals *Mesoscale Modeling for Complex Fluids and Flow Oxford, United Kingdom* 25.06.2007 27.06.2007
- Flow instabilities for living polymers *Katholieke Universiteit Leuven, Belgium: Seminarvortrag* 10.08.2007
- Time-resolve SANS on giant wormlike micelles under shear *SoftComp Meeting in Leuven, Belgium* 31.01.2007 01.02.2007
- The dynamics of colloidal rods in and out of equilibrium *AMOLF, Amsterdam, The Netherlands: Seminarvortrag* 08.10.2007
- The dynamics of colloidal rods in and out of equilibrium *TU Berlin: : Seminarvortrag* 27.11.2007
- Response of PB-PEO wormlike micelles to oscillatory shear flow as probed by Time-resoved SANS *International Soft Matter Conference 2007 in Aachen* 01.10.2007 04.10.2007
- The effect of slip on shear banding CPyCl/NaSal wormlike micelles *Euromech Kolloquium 492 in London, United Kingdom* 03.09.2007 05.09.2007

2008

- The Dynamics of Rods in Different Phases *Soft Matter: From Synthetic to Biological Materials: 39th IFF Spring School 2008 Forschungszentrum Jülich* 03.03.2008 14.03.2008
- The phase behavior of attractive rod-like viruses under shear flow as studied by small angle light scattering *CODEF-II Sonderforschungsbereich Transregio 6 in Bonn, GSI* 30.03.2008 02.04.2008
- The phase behavior of attractive rod-like viruses under shear flow *SoftComp Annual Meeting in Riva del Garda, Italy* 04.05.2008 07.05.2008
- Attractive and repulsive colloidal spheres under shear flow *Universität Konstanz: : Seminarvortrag* 12.08.2008
- The dynamics of colloidal rods in and out of equilibrium *University of Oxford, United Kingdom: : Seminarvortrag* 17.03.2008 21.03.2008

- The dynamics of colloidal rods in and out of equilibrium *Brandeis University, Boston, Massasuchets, USA: Seminarvortrag* 06.06.2008 11.06.2008

- The dynamics of colloidal rods in and out of equilibrium *University of Leeds, Leeds, United Kingdom: : Seminarvortrag* 12.12.2008

2009

- Attractive and repulsive colloidal spheres under shear flow *Universität Mainz: Seminarvortrag* 12.01.2009

- Rods in the smectic phase: 1-D Brownian diffusion in a periodic potential *Deutsche Physikalische Gesellschaft Frühjahrstagung Dresden* 22.03.2009 26.03.2009

- Flow behaviour and dynamics of colloidal rods *Fakultät f. Physik, Universität Düsseldorf: Seminarvortrag* 16.04.2009 16.04.2009

- Using time-resolved SANS to understand the flow behavior of Pb-PEO wormlike micelles *Annual SoftComp Meeting in Venedig, Italy* 03.05.2009 07.05.2009

- Flow behavior and dynamics of colloidal rods *National University in Singapore, Singapore: Seminarvortrag* 22.06.2009

- Supersaturated dispersions of rod-like viruses with added attractions *"Playing Colloidal Mikado" in University of Oxford, United Kingdom* 06.07.2009 08.07.2009

- Wormlike micelles under oscillatory shear as probed by time-resolved SANS *Workshop Soft Matter & Science in Bonn, GSI* 30.11.2009 01.12.2009

- Flow behaviour and dynamics of colloidal rods *Katholieke Universiteit Leuven, Belgium: Seminarvortrag* 17.12.2009